

Finite Element Analysis of the Behaviour of Pile Supported Integral Abutment

by Akshay Sakhare

Thesis submitted in fulfilment of the requirements for
the degree of

Doctor of Philosophy

under the supervision of A/Prof. Sanjay Nimbalkar and
Prof. G. R. Dodagoudar

University of Technology Sydney
Faculty of Engineering and Information Technology (FEIT)

April 2024

CERTIFICATE OF ORIGINAL AUTHORSHIP

I, **Akshay Sakhare** declare that this thesis, is submitted in fulfilment of the requirements for the award of **Doctor of Philosophy**, in the **School of Civil and Environmental Engineering** (*Faculty of Engineering and Information Technology, FEIT*) at the University of Technology Sydney.

This thesis is wholly my own work unless otherwise referenced or acknowledged. In addition, I certify that all information sources and literature used are indicated in the thesis.

I certify that the work in this thesis has not previously been submitted for a degree nor has it been submitted as part of the requirements for a degree at any other academic institution except as fully acknowledged within the text. This thesis is the result of a Collaborative Doctoral Research Degree program with Indian Institute of Technology Madras.

This research is supported by the Australian Government Research Training Program.

Signature:

Date: April 2024

LIST OF PUBLICATIONS

REFEREED JOURNALS BASED ON THE THESIS

1. Sakhare, A., H. Farooq, S. Nimbalkar, and G. R. Dodagoudar (2022) Dynamic behavior of the transition zone of an integral abutment bridge. *Sustainability*, 14 (7), 4118. <https://doi.org/10.3390/su14074118>
2. Sakhare, A., P. Punetha, N. Meena, S. Nimbalkar, and G. R. Dodagoudar (2023) Dynamic behavior of integral abutment bridge transition under moving train loads. *Transportation Geotechnics*, 40, 2023, 100989. <https://doi.org/10.1016/j.trgeo.2023.100989>

Dedicated to

My Parents

मम मातापितरौ समर्पितः

ACKNOWLEDGEMENTS

I express my gratitude to all those who have supported me throughout my Ph.D. journey.

I would like to thank Prof. G. R. Dodagoudar, my supervisor at IIT Madras, for his valuable guidance and support throughout my Ph.D. His way of supervision has provided me with flexibility in the way of working, and his trust has always motivated me to come up with outcomes to match his expectations. He encouraged me and provided various opportunities for travel, collaboration, presentation of my research work, and interdisciplinary learning. He constantly pushed me to strive for excellence in my area of study. His immense support during my tough times has encouraged me in my research work.

I would like to thank A/Prof. Sanjay Nimbalkar, my supervisor at UTS. It was a memorable and enjoyable experience in my Joint Ph.D. program to have worked with him. His monthly review meetings have always kept me on my toes to progress towards my objectives. His constant support during my stay at UTS has comforted me and helped me to work towards my research. It was a real privilege to work with him and the research group at UTS. My time with him has helped me to grow in many ways. I am grateful to him.

I would like to thank the doctoral committee members at IIT Madras: Prof. S. T. G. Raghukanth, Prof. B. Nageswara Rao and Prof. K. V. Gopal Nagendra for their valuable suggestions during my course of research. I would also like to thank panel expert at UTS: Prof. Behzad Fatahi, Prof. Hadi Khabbaz, Dr. Xuzhen He and Dr. Gayathri Danasamy for their valuable insights during my course of research.

I express my sincere thanks to the Head of the Department of Civil Engineering, Prof. Benny Raphael, Head of Lab (Geotechnical Division), Prof. Dali Naidu Arnepalli, other faculty members of the Geotechnical Engineering Division and all office staff at the Department of Civil Engineering for providing all the research facilities and required support. I am grateful to Prof. R. G. Robinson and Prof. V. B. Maji for their support and encouragement during my PhD.

I thank my fellow research collaborators and fellow groupmates Ramanandan, Sundaravel, Deviprasad, Prakash, Piyush, and Naveen at IIT Madras and UTS for stimulating discussion, guidance, and collaborative teamwork. I also would like to thank my friends and lab-mates at IIT Madras and UTS: Arnab, Ambili, Sona, Shalini, Pratyusha, Vikram, Adarsh Chatra, Shivakumar G. Patil, Jitesh Chavda, Dinesh, Sandhya, Menaka, Anandha Raj, Sriram, Adnan, Hafsa, Srikant, Somanath, Mandeep, Prana, Umakant, Yogesh, Saurabh, and Divanshu. I will always value the time spent with them during my PhD journey.

I would like to acknowledge the IIT Madras administration for providing me with their financial support in the form of the MHRD Scholarship. I would also like to thank them for providing me with all the necessary facilities to do my research and on-campus hostel accommodation, student activity facilities, and the beautiful nature of campus.

I would like to thank the Global Engagement Office and Alumni Relations at IIT Madras and the Graduate Research School at UTS for their kind cooperation and facilitation of the Joint Doctoral Degree Program. I would like to acknowledge the support of the collaboration between IIT Madras and the University of Technology Sydney, which helped me pursue a Joint Degree and helped me in approving of extension of stay at UTS during the pandemic. Also, I would like to thank both of my supervisors for approving the extension of my stay at UTS during the pandemic. It has been a fantastic experience working between two research groups across different departments and institutions, thanks to everyone.

I would like to thank the University of Technology Sydney for providing me with UTS Presidents Scholarship and Collaborative Research Degree Scholarship, which helped financially assist my research and stay in Sydney.

Finally, I would like to express my special gratitude to my parents for their constant encouragement, empathy, and patience throughout my Ph.D. candidature. I thank my sister Dr. Rohini for her encouragement and for taking over some of my responsibilities. I thank my brother-in-law, cousins, and extended family for their constant support at various stages.

Akshay T. Sakhare

ABSTRACT

KEYWORDS: Integral abutment bridge, Hypoplastic constitutive model, Finite element analysis, Passive force-displacement relationship, Transition zone, Moving train loading, Cyclic thermal loading, Fragility curves.

Integral Abutment Bridges (IABs) are jointless single or multiple-span bridges having their superstructure cast integrally with their substructure. These bridge types have become a popular across the worldwide because of their well-established advantages over the conventional bridges. Despite several advantages, there are a few challenges associated with the performance of the IABs that must be addressed systematically. These include nonlinear deformation of abutment due to ambient temperature variations, creep, and shrinkage effects which result from a complex interaction between the abutment, soil, and the pile. The performance is also highly sensitive to external loads, geometry, backfill soil, and soil-structure interaction (SSI), and differential movement near the bridge approach. Previous researchers have performed field monitoring, large scale experimental and numerical studies to understand the nonlinear behaviour of the integral abutment bridge (IAB). The soil ratcheting, earth pressure magnitude, distribution and its variation are not consistent among the several instrumented IABs under the ambient seasonal temperature variation and are dependent on many factors that are unique to each site. Most of the numerical studies have used simplified lateral supporting systems to incorporate the SSI effects and predicted the realistic behaviour of the IABs.

In the present study, the behaviour of an integral abutment bridge (IAB) and its passive capacity are evaluated using a nonlinear finite element (FE) analysis adopting hypoplastic constitutive model for the backfill soil under static, cyclic, and thermal loadings. The FE analysis is performed to evaluate the effect of soil ratcheting on the passive capacity of the integral abutment-soil-pile system subjected to cyclic loading. The hysteretic behaviour of the backfill soil is simulated using the hypoplastic constitutive model. Further, the parametric sensitivity analysis of the integral abutment-soil-pile system is carried out to evaluate the passive force-displacement relationships. The response of the IAB is also evaluated under cyclic thermal loading and cyclic longitudinal displacement of the abutment.

The comprehensive studies pertaining to the dynamic behaviour of the transition zone of IAB with approach slab under moving train loads are very limited. The growing usage of high-speed and heavy-haul trains to cater to the rapid hike in the demand for rail transport could significantly affect the performance of the IAB-embankment transitions for railways. Therefore, the performance assessment of these critical regions for railway applications is of paramount importance. Transition zones, such as bridge approaches, are discontinuities along a railway line that are highly prone to differential movement due to rapid variation of support conditions along the track. The concrete approach slabs are often provided before and after the bridges to reduce the differential movement and provide a gradual variation in track stiffness. This study provides greater insights into the dynamic behaviour of the transition zone of the integral abutment railway bridge (IARB) consisting of approach slab under static coupled bogie loading and moving train loads using the FE analyses. Firstly, the FE model is successfully validated with the published field data. Subsequently, the validated model is employed to investigate the influence of parameters such as approach slab geometry (length, thickness, inclination, and shape), backfill soil type, direction of train movement and train speed on the response of the IARB. Results show that the behaviour of the IARB is sensitive to the length of the approach slab, backfill soil type and train speed. The findings will enhance the current understanding of the behaviour of IARBs subjected to static coupled bogie loading and moving train loading and identify the important parameters that influence their performance.

A very few studies are performed on the seismic response analysis of the IABs considering SSI effects. The earlier studies have adopted the p-y curves to simulate the SSI effects and soil behaviour. In this study, the FE analysis is performed to assess the seismic vulnerability of the IAB subjected to site-specific scaled and unscaled ground motions using incremental dynamic approach. The probabilistic seismic demand models (PSDMs) are also developed. The fragility curves are developed for the typical IAB within the framework of performance-based earthquake engineering. These curves can be used in the loss estimation and retrofitting of the IABs.

TABLE OF CONTENTS

| | |
|--|-------|
| ACKNOWLEDGMENTS | i |
| ABSTRACT | iii |
| LIST OF TABLES | ix |
| LIST OF FIGURES | xi |
| ABBREVIATIONS | xvi |
| NOTATIONS | xviii |
| CHAPTER 1 INTRODUCTION | 1 |
| 1.1 General | 1 |
| 1.2 Need for the Present Study | 5 |
| 1.3 Objectives and Scope | 6 |
| 1.4 Organization of the Thesis | 7 |
| CHAPTER 2 REVIEW OF LITERATURE | 9 |
| 2.1 Introduction | 9 |
| 2.2 Passive Earth Pressure Theories and Significance | 9 |
| 2.3 Passive Force-Displacement Relationships | 10 |
| 2.3.1 Duncan and Mokwa hyperbolic method | 10 |
| 2.3.2 Log-spiral hyperbolic method | 11 |
| 2.3.3 Hyperbolic force-displacement relationship | 12 |
| 2.3.4 CALTRANS method | 13 |
| 2.3.5 AASHTO method | 14 |
| 2.3.6 Experimental studies on passive force-displacement relationships | 15 |
| 2.3.7 Numerical studies on passive force-displacement relationships | 19 |
| 2.4 Numerical Modelling of Soil-Structure Interface | 19 |
| 2.5 Hypoplastic Constitutive Model | 20 |
| 2.6 Behaviour of IABs under Thermal Loading | 22 |
| 2.6.1 Field monitoring studies | 22 |
| 2.6.2 Numerical studies | 26 |
| 2.7 Behaviour of Transition Zone of IAB | 28 |
| 2.8 Seismic Behaviour and Fragility Curves of IAB | 29 |

| | | |
|--|--|----|
| 2.8.1 | Fragility curves | 30 |
| 2.9 | A Critical Appraisal of the Reviewed Literature | 33 |
| 2.10 | The Proposed Study | 36 |
| 2.11 | Summary | 38 |
| CHAPTER 3 BEHAVIOUR OF INTEGRAL ABUTMENT BRIDGE UNDER STATIC, THERMAL AND CYCLIC DISPLACEMENT LOADING | | 39 |
| 3.1 | Introduction | 39 |
| 3.2 | Calibration of Hypoplastic Sand Model with Triaxial Test | 39 |
| 3.3 | Validation of FE Models | 43 |
| 3.3.1 | Rollins and Cole (2006) | 43 |
| 3.3.2 | Lemnitzer <i>et al.</i> (2009) | 45 |
| 3.4 | Finite Element Modelling of IAB | 49 |
| 3.5 | Response of IAB under Static Lateral Translation Loading | 52 |
| 3.5.1 | Length of the approach slab | 54 |
| 3.5.2 | Backfill soil type | 56 |
| 3.5.3 | Foundation soil stiffness | 57 |
| 3.6 | Response of IAB under Thermal and Cyclic Loadings | 58 |
| 3.6.1 | FE simulation of cyclic thermal loading | 59 |
| 3.6.1.1 | Results and discussion | 60 |
| 3.6.2 | FE simulation of cyclic longitudinal displacement loading | 68 |
| 3.6.2.1 | Results and discussion | 70 |
| 3.7 | Summary | 75 |
| CHAPTER 4 BEHAVIOUR OF INTEGRAL ABUTMENT UNDER STATIC AND CYCLIC TRAIN LOADING | | 77 |
| 4.1 | Introduction | 77 |
| 4.2 | Validation of FE Model | 79 |
| 4.3 | FE Analysis of the IARB | 81 |
| 4.3.1 | Description of geometry | 81 |
| 4.3.2 | Material properties and constitutive model | 83 |
| 4.3.3 | Interface interactions | 84 |
| 4.3.4 | FE mesh discretisation, boundary conditions and modelling procedure | 86 |
| 4.4 | Parametric Studies: Static Loading | 86 |

| | | |
|---------|---|------------|
| 4.4.1 | Length of the approach slab | 87 |
| 4.4.2 | Thickness of the approach slab | 88 |
| 4.4.3 | Height of the integral abutment | 89 |
| 4.4.4 | Inclination of transition zone | 90 |
| 4.4.5 | Backfill soil type | 92 |
| 4.5 | Equivalent Dynamic Loading: Simulation and Results | 93 |
| 4.5.1 | Variation in thickness and fall in inclination of the approach slab | 95 |
| 4.6 | Behaviour of IARB under Cyclic Train Wheel Loading | 97 |
| 4.7 | Summary | 101 |
| | CHAPTER 5 DYNAMIC BEHAVIOUR OF INTEGRAL ABUTMENT | 103 |
| | BRIDGE TRANSITION UNDER MOVING TRAIN LOADING | |
| 5.1 | Introduction | 103 |
| 5.2 | Finite Element Modelling of IARB | 104 |
| 5.2.1 | Description of geometry | 104 |
| 5.2.2 | Moving train load simulation | 105 |
| 5.2.3 | Material properties and constitutive model | 107 |
| 5.2.4 | Interface interactions | 108 |
| 5.2.5 | FE mesh discretisation, boundary conditions and modelling procedure | 108 |
| 5.3 | Results and Discussion | 110 |
| 5.3.1 | Influence of approach slab geometry | 110 |
| 5.3.1.1 | Length | 110 |
| 5.3.1.2 | Thickness | 113 |
| 5.3.1.3 | Inclination | 114 |
| 5.3.1.4 | Shape | 116 |
| 5.3.1.5 | Stresses at the fixed end of the approach slab | 117 |
| 5.3.2 | Influence of backfill soil type | 119 |
| 5.3.3 | Influence of train speed | 120 |
| 5.3.4 | Influence of train movement direction | 122 |
| 5.3.5 | Influence of multiple axle passages | 123 |
| 5.4 | Summary | 124 |

| | |
|---|-----|
| CHAPTER 6 RESPONSE OF INTEGRAL ABUTMENT BRIDGE UNDER SEISMIC LOADING | 125 |
| 6.1 Introduction | 125 |
| 6.2 Methodology | 125 |
| 6.3 Fragility Analysis | 127 |
| 6.3.1 Selection and scaling of ground motions | 127 |
| 6.3.2 Parameters of fragility function | 131 |
| 6.3.2.1 Intensity measure | 131 |
| 6.3.2.2 Engineering demand parameters | 131 |
| 6.3.3 Definition of damage states | 132 |
| 6.3.4 FE modelling of pile supported integral abutment bridge | 134 |
| 6.3.5 Development of PSDMs | 137 |
| 6.3.6 Development of fragility curves | 140 |
| 6.4 Seismic Earth Pressure on Integral Abutment | 143 |
| 6.5 Horizontal Seismic Coefficient for Pile Supported IAB | 144 |
| 6.6 Summary | 145 |
| CHAPTER 7 SUMMARY AND CONCLUSIONS | 147 |
| 7.1 Summary | 147 |
| 7.2 Conclusions | 149 |
| 7.3 Scope for Further Research | 152 |
| REFERENCES | 155 |
| CURRICULUM VITAE | 175 |
| DOCTORAL COMMITTEE | 176 |

LIST OF TABLES

| Table | Title | Page |
|--------------|---|-------------|
| 2.1 | Summary of medium to large-scale field tests on the passive force-displacement relationships | 18 |
| 2.2 | Summary of field monitored previous studies of IABs | 25 |
| 2.3 | Summary of fragility analysis of structural and geotechnical systems | 32 |
| 3.1 | Hypoplastic soil parameters of Karlsruhe sand (Herle and Gudehus, 1999) | 40 |
| 3.2 | Hypoplastic soil parameters of Toyoura sand (Herle and Gudehus, 1999) | 40 |
| 3.3 | Summary of material properties used for FE simulation (data sourced from Rollins and Cole, 2006; Anoosh <i>et al.</i> , 2007; David <i>et al.</i> , 2014) | 44 |
| 3.4 | Summary of material properties used for FE simulation (data sourced from Lemnitzer <i>et al.</i> , 2009) | 46 |
| 3.5 | Material properties used in FE simulation (data sourced from ¹ Al-Qarawi <i>et al.</i> 2020; ² Gadicherla <i>et al.</i> , 2022) | 50 |
| 3.6 | Hypoplastic soil parameters of Toyoura sand as backfill (Herle and Gudehus, 1999) | 50 |
| 3.7 | Material properties of foundation soils used in FE simulation | 57 |
| 4.1 | Parameters used in the validation of the FE model (adopted from Paixão <i>et al.</i> (2014)) | 80 |
| 4.2 | Material properties used in the FE simulation (data sourced from ¹ Farooq <i>et al.</i> , 2021; ² Al-qarawi <i>et al.</i> , 2020; ³ Li <i>et al.</i> , 2018) | 85 |
| 4.3 | Material properties of different backfill soil types (Bowles, 1996) | 92 |
| 5.1 | Material properties used in the FE simulation (data sourced from ¹ Li <i>et al.</i> 2018; ² Al-Qarawi <i>et al.</i> 2020; ³ Indraratna and Nimbalkar 2013) | 107 |
| 5.2 | Parameters used in dynamic FE simulation | 108 |
| 5.3 | Nominal values and range of parameters considered for parametric studies | 110 |
| 5.4 | Variation of peak tensile stress for different parameters | 118 |
| 5.5 | Material properties of different backfill soils (Bowles, 1996) | 120 |
| 6.1 | Characteristics of acceleration time-histories selected for the study | 130 |
| 6.2 | Components of bridge failure modes and relevant EDPs (Argyroudis and Mitoulis, 2021; Ahmed and Dasgupta, 2022) | 132 |

| | | |
|-----|--|-----|
| 6.3 | Damage states and limit state thresholds for highways and railways assets (Argyroudis and Kaynia, 2014) | 133 |
| 6.4 | Damage states and limit state thresholds for abutment-backfill system (Ahmed and Dasgupta, 2022) | 133 |
| 6.5 | Damage states and limit state thresholds for approach fill settlement (Shao <i>et al.</i> , 2022) | 134 |
| 6.6 | Material properties used in the FE simulation (data sourced from ¹ Al- qarawi <i>et al.</i> , 2020; ² Meena <i>et al.</i> , 2020; ³ Gadicherla <i>et al.</i> , 2022) | 135 |

LIST OF FIGURES

| Figure | Title | Page |
|--------|---|------|
| 1.1 | (a) Conventional Bridge, and (b) Integral Abutment Bridge | 2 |
| 2.1 | Hyperbolic Load-Displacement Curve (Duncan and Mokwa, 2001) | 11 |
| 2.2 | Mobilised Logarithmic-Spiral Passive Wedge (Shamsabadi <i>et al.</i> , 2007) | 12 |
| 2.3 | Hyperbolic Force-Displacement Formulation (Shamsabadi <i>et al.</i> 2007) | 13 |
| 2.4 | Effective Abutment Stiffness (CALTRANS SDC, 2013) | 14 |
| 2.5 | Schematic Representation of PBSD Procedure | 30 |
| 3.1 | Comparison of Drained Triaxial Test Results for Karlsruhe Sand: (a) Deviatoric Stress vs. Axial Strain, and (b) Volume Change Behaviour | 41 |
| 3.2 | Comparison of Drained Triaxial Test Results for Toyoura Sand under Two Confining Pressures: (a) 100 kPa, and (b) 500 kPa | 42 |
| 3.3 | Field Test Setup on Pile Cap (a) Plan, (b) Elevation View, and (c) Foundation Soil Profile (Rollins and Cole, 2006) | 43 |
| 3.4 | 3D FE Model with Mesh Discretisation for Rollins and Cole (2006) Field Test Setup | 44 |
| 3.5 | Comparison of Load-Displacement Plots of FE Results and Field Data for (a) No Backfill, (b) Clean Sand, and (c) Silty Sand | 45 |
| 3.6 | (a) Plan, and (b) Cross-Section View of the UCLA Test Setup (Lemnitzer <i>et al.</i> , 2009) | 46 |
| 3.7 | (a) 3D FE Domain with Discretised Mesh and Boundary Conditions, and (b) Deformed Shape of Backfill after Completion of Simulation | 47 |
| 3.8 | Comparison of Passive Force-Displacement Relationships of FE Results and Field Data | 47 |
| 3.9 | Comparison of 2D and 3D FE Simulation Results of Toyoura Sand for Passive Force-Displacement with UCLA Test Data | 48 |
| 3.10 | Comparison of 2D and 3D FE Simulation Results of Karlsruhe Sand for Passive Force-Displacement with UCLA Test Data | 49 |
| 3.11 | Schematic Representation of Pile-Supported Integral Abutment Bridge | 50 |
| 3.12 | Schematic Representation FE Mesh of the Pile-Supported IAB | 51 |
| 3.13 | Schematic of Geometry and 2D FE Mesh of Abutment Backwall with Backfill Soil | 52 |
| 3.14 | Passive Force-Displacement Relationship for Pile-Supported Integral Abutment with and without Approach Slab and the Abutment Backwall | 53 |
| 3.15 | Variation of Passive Pressure with Depth behind the Integral Abutment and Abutment Backwall | 54 |
| 3.16 | Passive Force-Displacement Relationship for Pile-Supported Integral Abutment for varying Length of Approach Slab | 55 |

| | | |
|------|--|----|
| 3.17 | Vertical Settlement Profile of Backfill Soil from the Pile-Supported Integral Abutment for varying Length of Approach Slab | 56 |
| 3.18 | Passive Force-Displacement Relationship for Pile-Supported Integral Abutment for different Backfill Soil Type | 57 |
| 3.19 | Passive Force-Displacement Relationship for Pile-Supported Integral Abutment for different Foundation Soil Stiffness | 58 |
| 3.20 | Variation of Temperature Loading Considered in FE Simulation | 60 |
| 3.21 | Horizontal Displacement of Integral Abutment Top and Bottom for Kim and Laman (2010) Temperature Loading | 61 |
| 3.22 | Horizontal Displacement of Integral Abutment Top and Bottom for Civjan <i>et al.</i> (2013) Temperature Loading | 61 |
| 3.23 | Variation of Soil Pressures for Medium and Dense Sands for 5 Years of Kim and Laman (2010) Temperature Loading | 62 |
| 3.24 | Variation of Soil Pressures for Medium and Dense Sands for 5 Years of Civjan <i>et al.</i> (2013) Temperature Loading | 62 |
| 3.25 | Variation of Passive Force for Medium and Dense Sands for 5 Years of Kim and Laman (2010) Temperature Loading | 63 |
| 3.26 | Variation of Passive Force for Medium and Dense Sands for 5 Years of Civjan <i>et al.</i> (2013) Temperature Loading | 63 |
| 3.27 | Deformed Mesh of Backfill Soil and Variation of Void Ratio for (a) Dense Sand, and (b) Medium Sand after 5 Years of Simulation for Kim and Laman (2010) Temperature Loading | 64 |
| 3.28 | Deformed Mesh of Backfill Soil and Variation of Void Ratio for (a) Dense Sand, and (b) Medium Sand after 5 Years of Simulation for Civjan <i>et al.</i> (2013) Temperature Loading | 65 |
| 3.29 | Vertical Settlement of Backfill Soil at Different Points for Kim and Laman (2010) Temperature Loading | 66 |
| 3.30 | Vertical Settlement Profile of Backfill Soil from Integral Abutment for Kim and Laman (2010) Temperature Loading | 66 |
| 3.31 | Vertical Settlement of Backfill Soil at Different Points for Civjan <i>et al.</i> (2013) Temperature Loading | 67 |
| 3.32 | Vertical Settlement Profile of Backfill Soil from Integral Abutment for Civjan <i>et al.</i> (2013) Temperature Loading | 67 |
| 3.33 | Field Data of Horizontal Displacement of SR-18 Bridge | 69 |
| 3.34 | Applied Sinusoidal Displacement at the Top of the Integral Abutment in the FE Simulation | 69 |
| 3.35 | Variation of Passive Pressure at the bottom of Abutment with Number of Years for Thermal Displacement of SR-18 Bridge | 70 |
| 3.36 | Vertical Settlement of Backfill Soil at Different Points for Cyclic Longitudinal Displacement of the IAB | 71 |
| 3.37 | Variation of Passive Pressure with Number of Cycles of Sinusoidal Displacement Loading | 72 |

| | | |
|------|--|---------|
| 3.38 | Variation of Passive Force with Number of Cycles of Sinusoidal Displacement Loading | 72 |
| 3.39 | Vertical Settlement of Backfill Soil at Different Points with Number of Cycles of Sinusoidal Displacement Loading | 73 |
| 3.40 | Vertical Settlement Profile of Backfill Soil from the Integral Abutment with Number of Cycles of Sinusoidal Displacement Loading | 74 |
| 3.41 | Deformed Mesh of Backfill Soil and Variation of Void Ratio for (a) Dense Sand, and (b) Medium Sand after 20 Cycles of Sinusoidal Displacement Loading | 75 |
| 4.1 | Schematic Representation of Integral Abutment Railway Bridge | 78 |
| 4.2 | FE Model for Validation with Field Data Reported by Paixão <i>et al.</i> (2014) | 80 |
| 4.3 | Comparison of Predicted Rail Displacement with Field Data Reported by Paixão <i>et al.</i> , (2014) | 81 |
| 4.4 | (a) Schematic Geometry of IARB with Approach Slab (all units in m), and (b) Train Loading (Q_w) Configuration Showing Distance between Axles (in m) | 82 |
| 4.5 | Discretised FE Mesh of the IARB with Approach Slab | 86 |
| 4.6 | Variation of Track Displacement for Different Lengths of Approach Slab | 88 |
| 4.7 | Variation of Track Displacement with Thickness of Approach Slab | 89 |
| 4.8 | Variation of Track Displacement with Height of Integral Abutment | 90 |
| 4.9 | Schematic Representation of Fall in Inclination of Approach Slab | 91 |
| 4.10 | Variation of Track Displacement with Fall in Inclination of Approach Slab | 91 |
| 4.11 | Variation of Vertical Displacement with Depth for Different Backfill Soils | 93 |
| 4.12 | Variation of Displacement at the Top of Ballast due to Change in Train Velocity | 94 |
| 4.13 | Variation of Track Displacement with (a) Thickness, and (b) Fall in Inclination of Approach Slab | 96 |
| 4.14 | Variation of Ballast Displacement (a) at 1 st , 5 th , 10 th , 24 th , 50 th , and 100 th Cycle across the FE Domain, and (b) with Number of Cycles of Loading | 98 |
| 4.15 | Variation of Vertical Displacement with Depth at Different Locations along the Track at (a) Embankment, (b) Interface between the Embankment and Transition Zone, and (c) Middle of the Transition Zone | 99, 100 |
| 4.16 | Variation of Vertical Displacement with Depth at Different Locations along the Track for 24 th Cycle of Train Loading | 101 |
| 5.1 | Schematic Geometry of Integral Abutment Railway Bridge | 104 |
| 5.2 | (a) Alfa Pendular Train Configuration with Distance between Axles (in m) and approximate Axle Loads (in kN) (Paixao <i>et al.</i> , 2014), and (b) Variation of Wheel Load with Time at Different Loading Nodes | 106 |

| | | |
|------|--|-----|
| 5.3 | FE Mesh of a Typical IARB with Approach Slab | 109 |
| 5.4 | Mesh Sensitivity Analysis for IARB Model | 109 |
| 5.5 | Variation of Vertical Displacement with Distance along the Track for Different Lengths of Approach Slab | 111 |
| 5.6 | Variation of Contact Stress above Backfill along the Track for Different Lengths of Approach Slab | 112 |
| 5.7 | Variation of Peak Tensile Stress on the Rail along the Length of the Track for Different Lengths of Approach Slab | 113 |
| 5.8 | Variation of Peak Track Displacement along the Approach Slab Length for Different Thicknesses | 114 |
| 5.9 | Reduction in Peak Track Displacement for Different Fall in Inclination of Approach Slab | 115 |
| 5.10 | Variation of Vertical Stress along the Depth of Ballast Layer at: (a) $x = 1.2$ m, (b) $x = 3$ m, and (c) $x = 4.8$ m | 115 |
| 5.11 | Variation of Vertical Displacement along the Length of Track for Different Shapes of the Approach Slab | 117 |
| 5.12 | Variation of Peak Tensile Stress at the Fixed End of Approach Slab for Different Thicknesses | 118 |
| 5.13 | Variation of Track Displacement along the Length of Track for Different Backfill Soils | 120 |
| 5.14 | Effect of Train Speed on Track Displacement at (a) Embankment, (b) Middle of Approach Slab, and (c) Bridge | 121 |
| 5.15 | Variation of Track Displacement along the Length of Track for Different Train Movement Directions | 122 |
| 5.16 | Variation of Peak Vertical Stress along the Length of Track for Different Train Movement Directions | 123 |
| 5.17 | Variation of Vertical Track Displacement in Embankment, Bridge, and Middle of Transition Zone for Multiple Axle Passages | 124 |
| 6.1 | Schematic of the Fragility Analysis Procedure | 127 |
| 6.2 | Average Response Spectrum and Response Spectra of the Ten Selected Ground Motions | 128 |
| 6.3 | Time-Histories of the Selected Broadband Type Ground Motions | 128 |
| 6.4 | Time-Histories of the Selected Pulse Type Ground Motions | 129 |
| 6.5 | Schematic Representation of Pile-Supported Integral Abutment Bridge | 134 |
| 6.6 | FE Mesh of Pile-Supported Integral Abutment Bridge | 136 |
| 6.7 | PSDM for Permanent Vertical Displacement of Backfill of the IAB | 138 |
| 6.8 | PSDM for Approach Fill Settlement of the IAB | 139 |
| 6.9 | PSDM for Longitudinal Displacement of Abutment-Backfill System | 139 |
| 6.10 | Fragility Curves for Pile-Supported IAB for PVDB: Highway Infrastructure | 141 |

| | | |
|------|---|-----|
| 6.11 | Fragility Curves for Pile-Supported IAB for PVDB: Railway Infrastructure | 142 |
| 6.12 | Fragility Curves for Pile-Supported IAB for Approach Fill Settlement | 142 |
| 6.13 | Fragility Curves for Pile-Supported IAB for Longitudinal Displacement of Abutment-Backfill System | 143 |
| 6.14 | Variation of Soil Pressure on (a) Left Integral Abutment, and (b) Right Integral Abutment | 143 |
| 6.15 | Variation of Horizontal Seismic Coefficient with PGA for the Typical Pile-Supported IAB | 144 |

ABBREVIATIONS

| | | |
|--------------------|---|---|
| 2D | - | Two-dimensional |
| 2.5D | - | Two-and-half-dimensional |
| 3D | - | Three-dimensional |
| AASHTO | - | American Association of State Highway and Transportation Officials |
| ABS | - | Abutment Backfill System |
| API | - | American Petroleum Institute |
| AREMA | - | American Railway Engineering and Maintenance-of-way Association |
| ATC | - | Applied Technology Council |
| BE | - | Train is Moving from the Bridge to Embankment |
| BEM | - | Boundary Element Method |
| BM | - | Bending Moment |
| C3D8 | - | Eight Node Continuum Elements with Full Integration |
| C3D8R | - | 8-Node Linear Brick Element, Reduced Integration with Hourglass Control |
| CBM | - | Cement Bound Mixture |
| CCDF | - | Complementary Cumulative Distribution Function |
| CCDFs | - | Complementary Cumulative Distribution Functions |
| CINPE4 | - | One-Way Plane-Strain Infinite Elements |
| CPE4 | - | 4- Noded Bilinear Plane-Strain Element with Full Integration |
| CPE4R | - | 4-Noded Bilinear Plane-Strain Quadrilateral Elements with Reduced Integration |
| DAF | - | Dynamic Amplification Factor |
| DM | - | Damage Measure |
| DP | - | Drucker-Prager |
| DS | - | Damage State |
| DV | - | Damage Variable |
| EB | - | Train is Moving from the Embankment to Bridge |
| EDP | - | Engineering Demand Parameter |
| EDPs | - | Engineering Demand Parameters |
| EHFD | - | Extended Hyperbolic Force-Displacement |
| FD | - | Finite Difference |
| FE | - | Finite Element |
| FEA | - | Finite Element Analysis |
| FEM | - | Finite Element Method |
| FEMA | - | Federal Emergency Management Agency |
| FHWA | - | Federal Highway Administration |
| GEO | - | Geotechnical |
| HFD | - | Hyperbolic Force-Displacement |
| HP pile/ H-pile | - | Steel Pile with H Shaped Section |

| | | |
|-------|---|---|
| HS | - | Hardening Soil |
| HST | - | High-Speed Train |
| IA | - | Integral Abutment |
| IAB | - | Integral Abutment Bridge |
| IABs | - | Integral Abutment Bridges |
| IARB | - | Integral Abutment Railway Bridge |
| IAs | - | Integral Abutments |
| IB | - | Integral Bridge |
| IBs | - | Integral Bridges |
| IDA | - | Incremental Dynamic Analysis |
| IM | - | Intensity Measure |
| IS | - | Indian Standard |
| LE | - | Linear Elastic |
| LRFD | - | Load And Resistance Factor Design |
| LSH | - | Log-Spiral Hyperbolic |
| MC | - | Mohr-Coulomb |
| MSE | - | Mechanically Stabilized Earth |
| NCHRP | - | National Cooperative Highway Research Program |
| PBEE | - | Performance-Based Earthquake Engineering |
| PBSD | - | Performance-Based Seismic Design |
| PEER | - | Pacific Earthquake Engineering Research |
| PGA | - | Peak Ground Acceleration |
| PGD | - | Peak Ground Displacement |
| PSDA | - | Probabilistic Seismic Demand Analysis |
| PSDM | - | Probabilistic Seismic Demand Model |
| PSDMs | - | Probabilistic Seismic Demand Models |
| PVDB | - | Permanent Vertical Displacement of the Backfill |
| RIM | - | Railway Infrastructure Managers |
| SDC | - | Seismic Design Criteria |
| SF | - | Shear Force |
| SSI | - | Soil-Structure Interaction |
| SSSI | - | Seismic Soil-Structure Interaction |
| STR | - | Structural |
| UCD | - | University of California Davis |
| UCLA | - | University of California Los Angeles |
| UGM | - | Unbound Granular Material |
| UMAT | - | User MATerial, User defined MATerial |

NOTATIONS

| | | |
|------------|---|--|
| A_e | - | Effective abutment wall area |
| a | - | Parameters of linear regression |
| b | - | Length of structure, Parameters of linear regression |
| C | - | Coefficient |
| c' | - | Effective cohesion |
| D | - | Euler stretching rate |
| D_i | - | i^{th} damage state |
| D_R | - | Damping ratio |
| E | - | Young's modulus |
| E_c | - | Young's modulus of the uncracked concrete |
| E_{cc} | - | Young's modulus of the cracked concrete |
| E_{ij} | - | Interslice forces |
| e_{c0} | - | Critical void ratio |
| e_{d0} | - | Minimum void ratio |
| e_{i0} | - | Maximum void ratio |
| F | - | Matsuoka-Nakai stress factor |
| F_{ih} | - | Mobilised failure surface |
| F_{ult} | - | Maximum abutment force |
| f_{ck} | - | Characteristic compressive strength |
| f_d | - | Pyknotropy factor |
| f_s | - | Barotropy factor |
| G | - | Shear modulus |
| $G(a b)$ | - | Complementary cumulative distribution function |
| g | - | Spectral acceleration |
| H | - | Backwall height, Thickness of each soil layer |
| H_r | - | Reference backwall height |
| h | - | Height of the backfill soil |
| h_a | - | Thickness of the approach slab |
| h_b | - | Thickness of the ballast layer at the free end of the slab |
| h_e | - | Effective height of the backwall or diaphragm |
| h_s | - | Granulate hardness |
| i | - | Inclination of the approach slab |
| K_{50} | - | Average soil stiffness |
| K_{abut} | - | Longitudinal stiffness of the abutment |
| K_{eff} | - | Effective abutment stiffness |
| k_h | - | Horizontal seismic coefficient |
| k_p | - | Coefficient of passive earth pressure |
| L | - | Second-order constitutive tensors, Length of the bridge span, and Length of the approach slab |
| M | - | Ovesen-Brinch Hansen correction factor |

| | | |
|---------------------------|---|---|
| N | - | Fourth-order constitutive tensors |
| n | - | Exponent, Mode number |
| $P[a b]$ | - | Probability of a conditioned on b |
| $P_f(\cdot)$ | - | Probability of exceeding a particular damage state |
| P_p | - | Passive earth pressure, Passive force |
| P_{ult} | - | Ultimate passive resistance |
| Q_w | - | Individual train wheel axle loads |
| R_f | - | Failure ratio |
| R_i | - | Strength-reduction factor |
| S_D | - | Median value of the seismic demand parameter in terms of an IM |
| T | - | Approach slab thickness, Temperature |
| \dot{T} | - | Stress rate |
| \hat{T} and \hat{T}^* | - | Deviator stresses |
| u | - | Pore water pressure |
| V | - | Velocity of the train |
| V_s | - | Shear wave velocity |
| w_e | - | Projected width of the backwall or diaphragm |
| y | - | Displacement |
| y_{max} | - | Maximum displacement |
| α | - | Parameter controlling the dependency of peak friction angle, Coefficient of thermal expansion, Rayleigh coefficient, and Constitutive coefficient |
| α_{iw} | - | Intermediate mobilised inclination of failure plane at wall-soil interface |
| β | - | Parameter influences the size of the response envelope and Rayleigh coefficient |
| β_c | - | Uncertainty in the resistance capacity |
| β_D | - | Uncertainty in the earthquake input motion demand, Lognormal standard deviation |
| β_{as} | - | Uncertainty in the definition of damage state |
| β_{tot} | - | Total lognormal standard deviation |
| ΔE_{ij} | - | Horizontal component forces |
| ΔT | - | Temperature change from reference temperature |
| Δ_{eff} | - | Effective longitudinal abutment displacement at idealized yield |
| Δ_{gap} | - | Width of the gap between the abutment backwall and superstructure |
| γ | - | Unit weight |
| δ | - | Interface friction angle and Abutment displacement |
| δ_{av} | - | Approach fill settlement |
| δ_h | - | Horizontal displacement of the backfill |
| δ_{iw} | - | Intermediate mobilised wall-soil interface friction angle |
| δ_v | - | Vertical displacement of the backfill, Vertical track displacement, and Permanent vertical displacement of the backfill |

| | |
|------------------|---|
| δ_v^b | - Vertical displacement at ballast top |
| δ_v^r | - Rail deflection |
| δ_v^p | - Peak track displacement |
| δ_{av} | - Vertical displacement of the approach fill settlement |
| δ_h | - Lateral displacement |
| $\dot{\epsilon}$ | - Strain tensor |
| μ | - Interface friction coefficient |
| ν | - Poisson's ratio |
| ρ | - Density of soil |
| σ | - Total stress |
| σ' | - Effective stresses |
| $\dot{\sigma}$ | - Stress tensor |
| σ_c^p | - Peak contact stress |
| σ_v^p | - Peak vertical stress |
| σ_x^p | - Peak tensile stress |
| σ_z^p | - Peak vertical stress |
| ϕ_c | - Critical friction angle |
| ϕ' | - Friction angle of the soil |
| ϕ_i | - Intermediate mobilised soil interface friction angle |
| $\varphi(\cdot)$ | - Standard normal cumulative distribution function |
| ψ | - Dilation angle |
| ω_m | - First natural frequency |
| ω_n | - Third natural frequency |

CHAPTER 1

INTRODUCTION

1.1 GENERAL

Traditionally, a relief system in the bridges consists of expansion joints, roller supports, and other structural releases, provided to permit thermal expansion and contraction, creep and shrinkage as shown in Figure 1.1(a). The simply supported bridges after a few years of service suffer from various problems affecting the sustainability of bridges. Expansion joints will fail to function properly due to elastomeric glands get filled with dirt, rock fragments and trash, leak of de-icing chemicals through the expansion joints and seal, and salt-laden runoff water leading to the corrosion of underlying structural elements. Bridge deck joints are subjected to continual wear and heavy impact loads. The jointed rigid pavements subjected to higher pressures due to temperature variations result in immovable deck joints therefore they will be subjected to severe damages. Over the years, these problems have resulted in the increased cost of maintenance or replacement of faulty expansion joints, along with the initial cost of their design, manufacture, and installation. To overcome all the above disadvantages, civil engineers have continued to use integral abutment bridges for the past two decades (Mistry, 2005).

Integral bridges (IBs) or integral abutment bridges (IABs) are defined as bridges with no expansion joints between the superstructure and the supporting abutments as shown in Figure 1.1(b). If the bridge has no bearings, it is often referred to as a fully integral bridge (IB) or integral abutment bridge (IAB). The IABs are jointless single or multiple-span bridges having their superstructure cast integrally with their substructure. Generally, these bridges include capped pile stub abutments. Piers for the IAB may be constructed either integrally with or independently of the superstructure. The IAB has several advantages such as lower maintenance cost, simple and more economical construction, added redundancy and capacity during seismic events, improved ride quality etc. (Ooi *et al.*, 2010). The benefits of IABs have been widely accepted in the past several decades around the world. Maruri and Petro (2005) and White *et al.* (2010) surveyed the construction experience of IABs across America and European countries,

respectively. There are approximately 9000 fully integral abutment and 4000 semi-integral abutment bridges in the United States (Maruri and Petro, 2005).

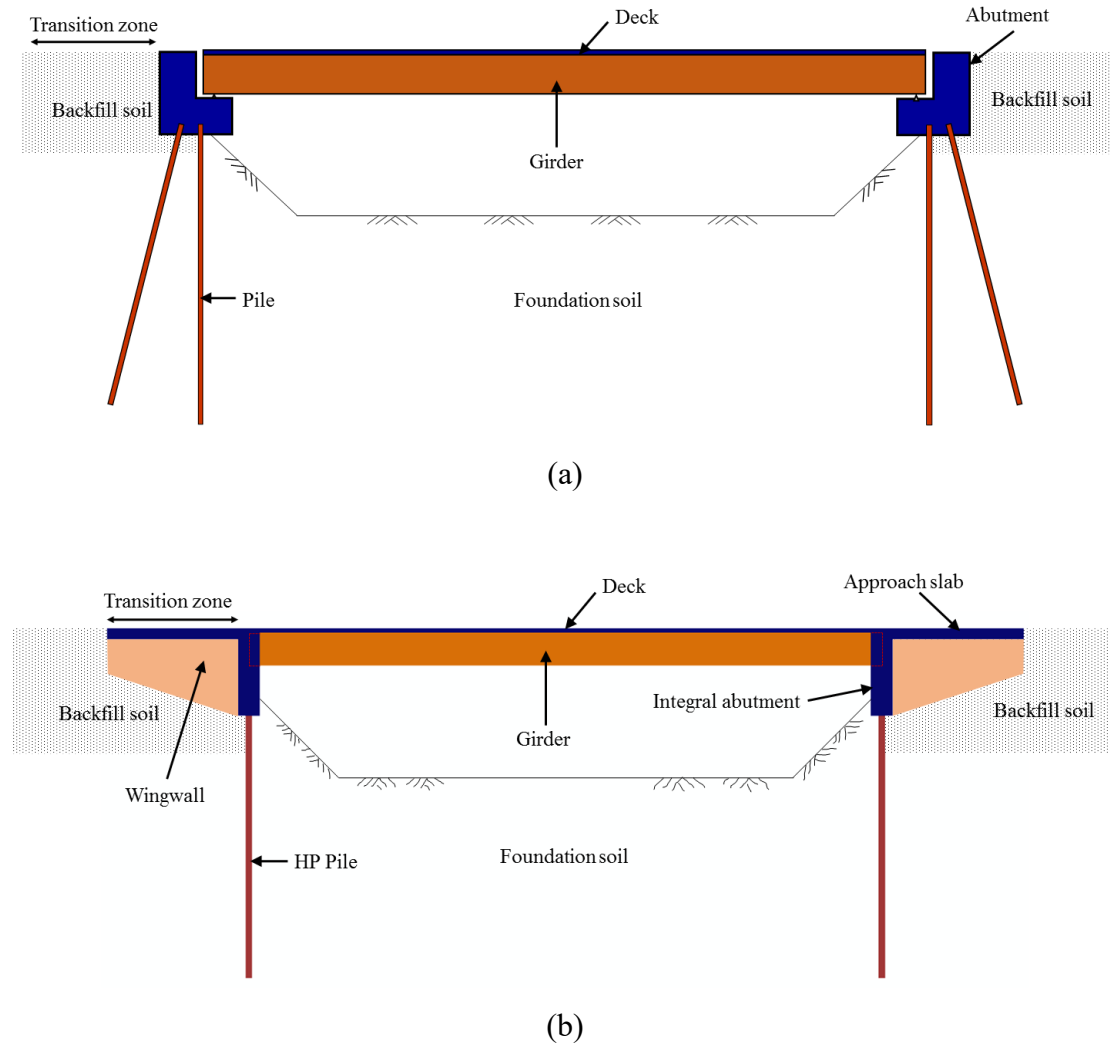


Fig. 1.1 (a) Conventional Bridge, and (b) Integral Abutment Bridge.

Despite having many significant advantages over the conventional bridges; there are some concerns about the high unit stress of the IAB, which arises from the elimination of joints due to thermal expansion and contraction, concrete creep and shrinkage, and differential settlement. The excessive lateral movement of the IAB can lead to the following problems: reduced axial pile capacity, wingwall rotation, and cracking, formation of plastic hinges in piles, excessive settlement of the approach fill, and formation of void behind the abutment leading to erosion of the soil by water entry. In addition, live loads on the bridge move the abutment towards the backfill and cause variation in the earth pressure against the abutment. If the bridge is skewed, the lines of

action of the lateral soil loads on opposite abutments will not coincide. These lateral loads will cause unbalanced moments in a horizontal plane (Ooi *et al.*, 2010).

The pile-supported integral abutment (IA) undergoes complex, cyclic loading/unloading history in response to changes in the ambient temperature. The integral abutments (IAs) respond in a nonlinear way because of nonlinearities of the abutment-soil-pile system interaction and construction joint between the abutment and backwall, even though the other structural components remain elastic. Soil-structure interaction (SSI) analysis of bridges presents a challenge to both the geotechnical and structural engineers. Previous researchers have conducted large-scale field testing, field monitoring of IABs, analytical and numerical modelling on IABs to capture the nonlinear behaviour of the IAs considering the SSI effects. Several analytical studies, laboratory and large-scale field testing have been conducted to develop the passive force-displacement relationship for abutment/backwall subjected to pushover and cyclic loading (Duncan and Mokwa, 2001; Arsoy, 2004; Cole and Rollins, 2006; Xu *et al.*, 2007; Shamsabadi, 2007; Lemnitzer *et al.*, 2009; Mei *et al.*, 2009; Wilson and Elgamal, 2010; Lovell, 2010; Bloodworth *et al.*, 2012; Rollins and Jessee, 2013; Smith, 2014; Ni *et al.* 2018; Al-qarawi *et al.*, 2020). The previous researchers have instrumented and field monitored the IABs for the in-situ behaviour such as abutment displacement, backfill pressure, abutment and girder rotation, pile and girder moment and axial force due to thermal seasonal temperature variations (Fennema *et al.* 2005; Khodair and Hassiotis, 2005; Brena *et al.*, 2007; Lovell, 2010; Ooi *et al.*, 2010; Kim and Laman, 2012; Huntley and Valsangkar, 2013, 2014, 2018; Civjan *et al.*, 2013; Kong *et al.*, 2015). Over the years many studies have been performed using numerical method to understand and simulate the behaviour of IABs for thermal seasonal temperature variations and passive force-displacement relationship (Khodair and Hassiotis, 2005; Shamsabadi, 2007; Civjan *et al.*, 2007; Pugasap *et al.*, 2009; Kim and Laman, 2010; Zordan *et al.*, 2011; Kalayci *et al.*, 2012; David *et al.*, 2014; Khasawneh, 2014; Quinn and Civjan, 2017; Al-qarawi *et al.*, 2020; Abdullah and Naggar, 2023). The present study will address the issues associated with the behaviour of integral abutment-soil-pile system by adopting the advanced constitutive model for backfill soil under static, cyclic, and thermal loadings.

The nonlinear behaviour of the integral abutment-soil-pile system due to concrete creep and shrinkage, thermal expansion and contraction, and differential settlement of the

IAB leads to excessive settlement of the backfill soil in the transition zone. The differential movement is also due to a change in the support conditions at the transition zone between the IAB and embankment. The major problems with railway track transition zone are differential settlement, enhanced dynamic load, and accelerated track deteriorations. These issues might prove detrimental, especially for the IABs supporting the railway lines. The bridge approach slabs constructed with reinforced concrete connected to the bridge deck and abutment are used to achieve a smooth transition of the track stiffness and reduction in maintenance requirements. A few researchers have analysed the behaviour of the transition zone behind the bridge abutment (Briaud, 1997; Cai *et al.* 2005; Kerokoski, 2006; Rodrigues *et al.* 2011; Varandas *et al.*, 2011; Burdet *et al.*, 2015), however, most of the existing studies have considered the transition zone of the conventional bridges.

Over the years, the importance of SSI analysis of bridges has increased due to cyclic and seismic loadings which cause relative movement of the structure with soil. Past earthquakes have caused severe damages to bridges and a few bridges have even collapsed (Wood, 2015). The pattern and severity of damage to a particular bridge can vary depending on the type of bridge structure and supporting system, including the foundation and ground conditions. The seismic performance of IABs is better than conventional bridges. Mitoulis (2020) has summarised the advantages and disadvantages of the IABs. However, major challenges are associated with the seismic response and design of the IABs such as behaviour of integral abutment and its serviceability, and influence of backfill soil on the overall seismic response. Similarly, Ahmed and Dasgupta (2022) presented a review paper on the seismic limit states of the IAB and provided the procedures for the development of probabilistic seismic demand models (PSDMs) and fragility curves. A few studies conducted on the seismic behaviour of the IABs have resulted in development of the PSDMs and fragility curves for the various engineering design parameters (EDPs) of the IABs (Frosch *et al.*, 2009; Argyroudis *et al.*, 2018; Tsinidis *et al.*, 2019; Ahmed and Dasgupta, 2022; Kozak *et al.*, 2022). The current study also addresses the seismic behaviour of the IABs considering the SSI effects and the PSDMs and fragility curves are established for the varying value of intensity measure.

1.2 NEED FOR THE PRESENT STUDY

The preceding discussion suggests that accurate modelling and analysis can predict the realistic behaviour of IABs. Most of the studies on the IABs have used simple foundation springs or simplified lateral supporting systems and considered the SSI effects accordingly. In general, the simplifications are not sufficient and appropriate to obtain the accurate estimate of the structural and soil response and performance, especially when the highly nonlinear soil behaviour is expected. The practical realistic solution involving the SSI requires the use of rigorous numerical techniques such as finite element method (FEM), finite difference method (FDM), and boundary element method (BEM) which are capable of accurately representing the nonlinear, inelastic behaviour of both the soils and structural elements. A reliable prediction of performance of the integral abutment (IA) soil system depends on the use of well-defined structural and geotechnical models that can account for the SSI effects and uncertainties in soil properties. The previous researchers have adopted the Mohr-Coulomb (MC) and hardening soil (HS) constitutive models for modelling the response of backfill soils and accordingly the passive force-displacement relationships are established. In the present study, a hypoplastic sand constitutive model based on the critical state concept is used to model the backfill soil. This model can capture the nonlinear and complex soil behaviour under cyclic loading compared to the MC and HS models. Most of the studies have simulated the behaviour of IABs under ambient seasonal temperature variation, however, they concentrated on the performance of individual components of the bridge.

Nonlinear behaviour of the backfill soil is influenced by the differences in loading and unloading histories, loading rate and interaction between the bridge superstructure and the surrounding soil. In the previous studies, the backfill soil was simulated using nonlinear Winkler spring model. Several earlier researchers have performed the field monitoring of the IABs and provided the conflicting reports on the observation of the soil ratcheting phenomenon, with some noting its presence and others indicating its absence. A comprehensive examination of the soil ratcheting behaviour necessitates a meticulous analysis, involving the development of a detailed two-dimensional (2D) or three-dimensional (3D) finite element (FE) model of the abutment-soil-pile system. This model integrates a soil stress-strain model that is dependent on the loading path.

The primary purpose of the transition zone is to provide a smooth transition between the higher stiffness (bridge) to lower stiffness (embankment) by gradual variation and

vice versa. Approach slabs are effective ways to provide a smooth transition from the superstructure component to embankment and they reduce the settlements significantly. The studies related to the dynamic behaviour of the transition zone of an integral abutment railway bridge (IARB) with approach slab are very limited. Most of the previous studies have dealt with the behaviour of transition zones of the conventional bridges with approach slab only. In IABs, the approach slab is monolithically connected with the integral abutment in comparison to the conventional bridges with doweled connection. The growing usage of high-speed and heavy-haul trains to cater to rapid hike in the demand for rail transport may significantly affect the performance of the IAB-embankment transitions for railways. Therefore, the assessment of performance of these critical regions for railway applications is paramount under realistic train loadings.

Numerical studies on seismic vulnerability assessment of IABs considering SSI effects and representing backfill and foundation soils using continuum elements are very limited. Most of the previous studies are concerned with the structural behaviour, where the interaction between the integral abutment-soil system and pile-soil at the foundation are simulated using nonlinear Winkler springs. A very few studies are reported regarding the development of PSDMs and fragility curves for the IABs within the framework of performance-based earthquake engineering (PBEE). All the above issues are addressed systematically in the current investigation.

1.3 OBJECTIVES AND SCOPE

The aim of the present study is to investigate the behaviour of pile-supported integral abutment bridge with approach slab using nonlinear finite element analysis. The specific objectives of the study are:

1. To evaluate the passive capacity and behaviour of the integral abutment-pile backfill system of the integral abutment bridges adopting hypoplastic constitutive model for the backfill soil under static, cyclic, and thermal loadings,
2. To carry out parametric sensitivity analysis of the integral abutment-pile backfill system to establish the passive force-displacement relationships,
3. To evaluate the dynamic behaviour of the transition zone of an integral abutment bridge subjected to static coupled bogie loading and moving train loading, and

4. To develop the probabilistic seismic demand models and fragility curves for a typical integral abutment bridge within the framework of performance-based earthquake engineering.

The scope of the present study is limited to the development of passive force-displacement relationships for the pile-supported integral abutment backfill system subjected to static, cyclic, and thermal loadings. The effect of water table and moisture variation is not included in this study. The backfill soil is treated as homogeneous, and its temporal variability is not considered in the study. The integral abutment bridge structure is simulated as linear elastic material and the effect of creep and shrinkage is not considered. The finite element method is used as the numerical tool to assess the overall behaviour of the integral abutment-pile backfill system.

1.4 ORGANISATION OF THE THESIS

The contents of the thesis are presented in seven chapters which are organised as follows:

Chapter 1 presents an overview of the research topic, encompassing the background and objectives of the current investigation. Chapter 2 presents a comprehensive review of the literature on the passive force-displacement relationship for abutment-soil systems, the behaviour of IABs under ambient temperature variations, the behaviour of transition zone of the IARB under the train loading and seismic excitation. A brief description of the hypoplastic constitutive model is given. A review on the development of fragility curves for the IABs is also provided at the end. Finally, a critical appraisal of the reviewed literature is presented followed by the protocol of the proposed study.

Chapter 3 presents the development of passive force-displacement relationships for the integral abutment-pile backfill system subjected to static lateral translational loading. The parametric sensitivity analysis is also conducted by varying the parameters such as approach slab length, density of backfill soil and foundation soil stiffness. The soil ratcheting phenomenon due to cyclic thermal loading is evaluated. The behaviour of the integral abutment-pile backfill system and variation of soil pressure under thermally-induced expansion loading are also studied and presented.

Chapter 4 presents the behaviour of the transition zone of the IARB under static and cyclic coupled bogie train loadings. The FE model validation is carried out using the results of the field study conducted on the transition zone. The parametric sensitivity

analysis is conducted by varying the parameters such as the geometry of the approach slab, backfill soil type, and height of the integral abutment. The equivalent dynamic train loading is simulated by the dynamic amplification factor for different train speeds.

Chapter 5 presents the results of dynamic behaviour of the transition zone of the IARB under moving train loading. The parametric sensitivity analysis is also conducted by varying the parameters such as the influence of approach slab geometry, backfill soil type, influence of train speed, and influence of train movement direction. The influence of multiple axle passages of the moving train on the response transition zone is investigated and results are presented in the chapter.

Chapter 6 presents the development of PSDMs and fragility curves for the pile-supported integral abutment bridge. The target spectrum corresponding to seismic Zone IV and for Type I rock or hard soil is used and accordingly the recorded ground motions are obtained from the Pacific Engineering Earthquake Research (PEER) ground motion database. The ten unscaled ground motions are scaled to the required intensity measures (IMs) having successively increasing values and accordingly the response of the integral bridge is evaluated using the incremental dynamic analysis (IDA). The engineering demand parameters (EDPs) considered in the study are permanent vertical displacement of the backfill, approach fill settlement, and longitudinal displacement of the abutment-soil system. These EDPs are used to develop the PSDMs and fragility curves.

Chapter 7 summarises the present study and gives the conclusions. A scope for future research on the behaviour of pile-supported integral abutment bridge is also presented in the chapter. A list of references is given at the end.

CHAPTER 2

REVIEW OF LITERATURE

2.1 INTRODUCTION

This chapter presents the state-of-the-art review on the behaviour of integral abutment-soil-pile system considering interaction effects under static, cyclic and thermal, moving train, and seismic loadings. The different methods available for estimating the passive force-displacement relationships for the abutment-soil systems are briefly reviewed. In the literature, many studies have been performed on the laboratory-scale experiments, large-scale experiments, and numerical simulations to investigate the behaviour of abutment-soil interaction and the passive force-displacement relationships are presented. The behaviour of the IABs under the seasonal ambient temperature variation leads to contraction and expansion of the deck and girder. A detailed review of the previous studies involving the field monitoring of IABs and numerical simulations of the IABs under thermal loading is presented. The previous studies on the behaviour of transition zone of the IAB under moving train loading have also been reviewed and presented. A review of the seismic performance of the IABs is presented at the end followed by the development of PSDMs and fragility curves within the framework of PBEE. A critical appraisal of the reviewed literature is presented along with the protocol of the proposed study.

2.2 PASSIVE EARTH PRESSURE THEORIES AND SIGNIFICANCE

As the IABs expand and contract due to thermal loading, the integral abutment is pushed towards the approach fill which in turn induces passive resistance. This passive resistance imparts compressive load to bridge superstructure through the abutment. Passive earth pressures play a key role in soil-structure interactions. The development of a passive resistance when the abutment moves towards the soil depends on the amount and direction of the movement, strength and stiffness of the soil, friction and/or adhesion between the structure and soil, and shape of the structure. These factors have a major influence on the magnitude of the passive earth pressure. The classical methods to analyse the passive behaviour of abutment walls are Coulomb's method, Rankine's method, and the passive trial wedge method. Other methods include the composite and

non-composite log spiral methods. In the composite logarithmic spiral method, the failure surface is divided into a logarithmic spiral and a linear part as suggested by Terzaghi (1943). The non-composite logarithmic spiral method assumes a single arc of the log-spiral to represent the entire failure surface. Passive pressures in composite and non-composite logarithmic spiral methods are evaluated either by force equilibrium or moment equilibrium. The passive earth pressure for a given depth (h) is expressed as

$$P_p = \gamma h K_p + 2c' \sqrt{K_p} \quad (2.1)$$

where P_p is the passive earth pressure, K_p is the coefficient of passive earth pressure, c' is the cohesion of the backfill soil, γ is the unit weight of the backfill and h is the height of the backfill soil. The seismic passive earth pressure is evaluated by the Mononobe-Okabe method, which is a straightforward extension of the Coulomb sliding wedge theory. Mylonakis *et al.* (2007) proposed a closed-form stress plasticity solution essentially an approximate yield line approach, based on the theory of discontinuous stress fields. This model incorporates the multiple stress fields in the backfill for the region near the ground surface, wall-soil interface, and the transition zone between them. Passive earth pressure coefficient can be evaluated with and without earthquake loading by integrating the stress field expressed as a linear function of the depth measured from the ground surface. Steedman and Zeng (1990) proposed a simple and more realistic pseudo-dynamic method to evaluate the seismic passive earth pressure which was improved by Choudhary and Nimbalkar (2005).

2.3 PASSIVE FORCE-DISPLACEMENT RELATIONSHIPS

The different methods available to estimate the mobilised passive capacity of the bridge abutments with respect to the abutment displacement are reviewed and presented in this section.

2.3.1 Duncan and Mokwa Hyperbolic Method

Duncan and Mokwa (2001) developed an excel spreadsheet computer program called PYCAP based on log-spiral theory. It approximated the passive resistance with deflection variation by a hyperbolic relationship as shown in Figure 2.1. The expression for P_p involving the hyperbolic relationship and the expression for P_{ult} are given as

$$P_p = \frac{y}{\left[\frac{1}{K_{max}} + R_f \frac{y}{P_{ult}} \right]} \quad (2.2)$$

$$P_{ult} = (E_p)(M)(b) \quad (2.3)$$

where P_p is the passive resistance at any displacement y , P_{ult} is the ultimate passive resistance by log-spiral method, E_p is the passive resistance per unit length, M is the Ovesen-Brinch Hansen correction factor for 3D effects, b is the length of structure perpendicular to the plane of analysis, K_{max} is the initial stiffness corresponding to the initial slope of the load-displacement curve, R_f is the failure ratio defined as the ratio of the ultimate passive resistance to the hyperbolic asymptotic value of the passive resistance. For hyperbolic stress-strain curves, the R_f is ranging from 0.75 to 0.95 as reported by Duncan and Chang (1970).

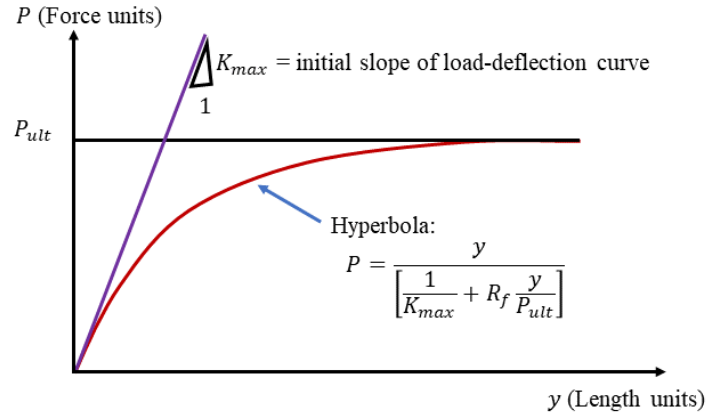


Fig. 2.1 Hyperbolic Load-Displacement Curve (Duncan and Mokwa, 2001).

2.3.2 Log-Spiral Hyperbolic Method

Shamsabadi *et al.* (2007) adopted the limit equilibrium method along with the mobilised logarithmic-spiral (LS) failure surfaces coupled with the modified hyperbolic (H) stress-strain relation for the evaluation of passive force on the abutment. This approach is referred to as the LSH method, which estimates the nonlinear passive force-displacement relationship for the abutment as a function of wall displacement and backfill soil material properties. Figure 2.2 depicts the mobilised logarithmic spiral failure surfaces including the geometry and forces acting on the slice and the same is used to estimate the passive capacity of the abutment. Summation of the horizontal

component forces (ΔE_{ij}) yields the mobilised horizontal passive capacity F_{ih} associated with the mobilised failure surface i as follows:

$$F_{ih} = \frac{\sum_{j=1}^n \Delta E_{ij}}{1 - \tan \delta_{iw} \tan(\alpha_{iw} + \phi_i)} \quad (2.4)$$

where ΔE_{ij} is the horizontal component resulting from interslice forces E_{ij} and $E_{(i+1)j}$ acting at the sides of slice j , E_{ij} is the intermediate mobilised force of slice, δ_{iw} is the intermediate mobilised wall-soil interface friction angle, ϕ_i is the intermediate mobilised soil interface friction angle and $\alpha_{iw} = \theta_{il} + \alpha_{il}$ is the intermediate mobilised inclination of failure plane at wall-soil interface (from horizontal). Shamsabadi *et al.* (2007) evaluated the passive capacity by the LSH method and compared the results with the eight experimental nonlinear force deformation full-scale tests, centrifuge model tests and small-scale laboratory tests of the abutments and pile caps with different backfills.

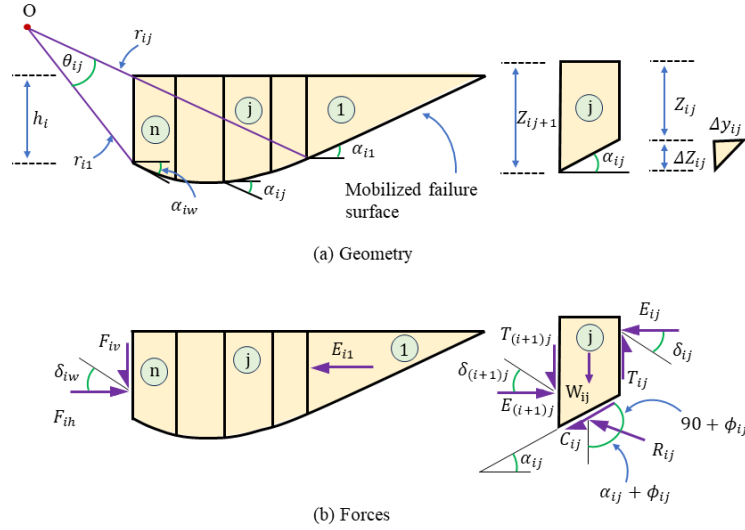


Fig. 2.2 Mobilised Logarithmic-Spiral Passive Wedge (Shamsabadi *et al.*, 2007).

2.3.3 Hyperbolic Force-Displacement Relationship

Shamsabadi *et al.* (2007) proposed a simplified hyperbolic force-displacement (HFD) relationship as shown in Figure 2.3 for the passive force-displacement of abutment backwall. The HFD relationship is a function of three quantities: average soil stiffness (K_{50}), maximum abutment force (F_{ult}) and maximum displacement (y_{max}). The passive force acting on the abutment is expressed as

$$F(y_i) = \frac{Cy}{1 + Dy} \quad (2.5)$$

where $C = \left(2K_{50} - \frac{F_{ult}}{y_{max}}\right)$ and $D = 2\left(\frac{K_{50}}{F_{ult}} - \frac{1}{y_{max}}\right)$. The average abutment stiffness is expressed as $K_{50} = F_{ult}/2y_{50}$, wherein y_{50} is the displacement at half of the maximum abutment force. For various backwall heights, the HFD model was extended by modifying the terms C and D in Equation 2.5 as $C = a(H/H_r)^n$ and $D = b$, where $(H/H_r)^n$ is a backwall height adjustment factor in which H is the backwall height, H_r is the reference backwall height ($H_r=1$) and n is a dimensionless exponent. The extended HFD (EHFD) relation is given as

$$F(y) = \frac{ay}{1 + by} \left(\frac{H}{H_r}\right)^n \quad (2.6)$$

where a and b are the two parameters used for representing the HFD curves.

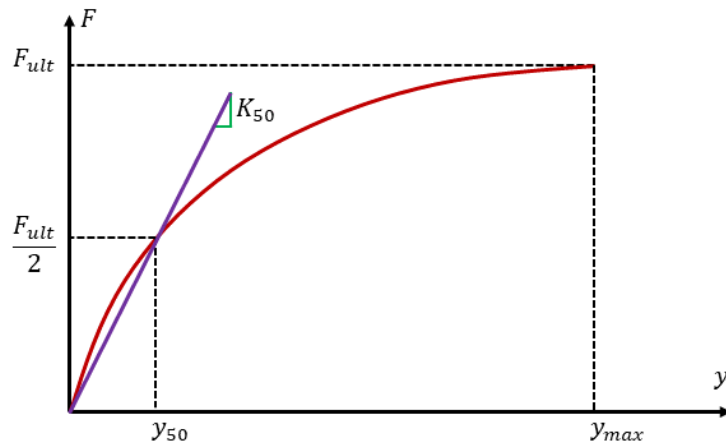


Fig. 2.3 Hyperbolic Force-Displacement Formulation (Shamsabadi *et al.* 2007).

2.3.4 CALTRANS Method

Caltrans Seismic Design Criteria (SDC) (2013) suggest a bilinear approximation of the passive force-displacement relationship as shown in Figure 2.4. The relationship is governed by two parameters, initial stiffness of the abutment (K_i) and ultimate passive force (P_{ult}). The CALTRANS suggests initial stiffness values of 28.7 and 14.35 MN/m per unit width of the abutment wall for the embankment fill material meeting and not

meeting the requirements of the standard specifications respectively. The initial stiffness is adjusted proportional to the backwall/diaphragm height as follows:

$$K_{abut} = K_i \times w_e \times \left(\frac{h_e}{1.7} \right) \quad \text{S.I. units} \quad (2.7)$$

where K_{abut} is the longitudinal stiffness of the abutment under longitudinal translation towards the backfill and h_e and w_e are the effective height and projected width of the backwall or diaphragm for seat and diaphragm abutments, respectively, Δ_{gap} is the width of the gap between the abutment backwall and superstructure, Δ_{eff} is the effective longitudinal abutment displacement at the idealized yield and K_{eff} is the effective abutment stiffness. The magnitude of the ultimate passive force resisting the longitudinal displacement is estimated as follows:

$$P_{ult} = A_e \times 239 \times \left(\frac{h_e}{1.7} \right) \quad (\text{m, kN}) \quad (2.8)$$

where A_e is the effective abutment wall area, $A_e = h_e \times w_e$.

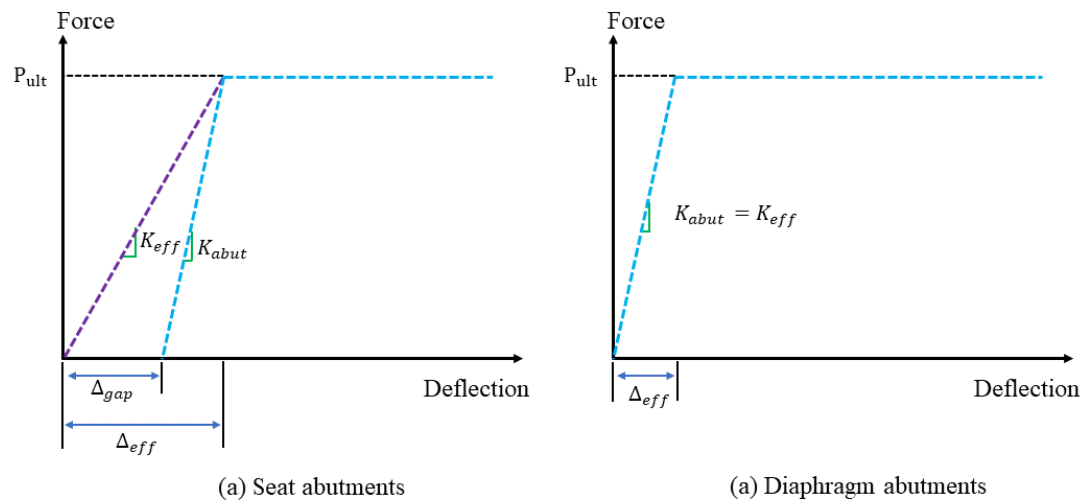


Fig. 2.4 Effective Abutment Stiffness (CALTRANS SDC, 2013).

2.3.5 AASHTO Method

The guidelines given by AASHTO (2015) prescribe a bilinear variation of the passive force-displacement relationship. The AASHTO does not prescribe the value for either abutment stiffness or ultimate passive force. The ultimate passive force is estimated from the log-spiral theory and the displacement is obtained corresponding to the

maximum passive earth pressure (Clough and Duncan, 1991). It is noted that the usage of log-spiral theory and soil type based on the value of maximum displacement for the characterisation of passive force-displacement relationship is the special feature of the AASHTO method.

2.3.6 Experimental Studies on Passive Force-Displacement Relationships

The various researchers have performed laboratory scale, small scale and large-scale field tests to predict the passive earth pressure and to develop the passive force-displacement relationship. A few of those studies are reviewed and presented.

Xu *et al.* (2007) evaluated the magnitude of lateral earth pressure behind a full-height frame integral bridge backfilled with Leighton Buzzard sand and a glass ballotini by radial strained controlled stress path testing using a triaxial cyclic loading system. The magnitude of the earth pressure coefficient continued to increase with the cycles of cyclic loading and it was found that the coefficient is more sensitive to particle shape than the density of sand. Loose backfills also eventually approach passive pressure tendency as with the other densities but these are not recommended due to large settlement and serious serviceability problems. The laboratory results were compared with the field monitoring data.

Cosgrove and Lehane (2003) conducted the experiment on a laboratory scale model of an abutment with loose backfill to understand the cyclic rotation/translation behaviour of the IAB due to temperature variations. The distribution of displacements and strains within the backfill is recorded using an optical measurement technique. The degree of volumetric contraction of sand mass in the vicinity of the abutment is influenced by abutment rotation and a few such rotations. The larger increase in lateral stress on the abutment is noticed because of strain hardening of the loose backfill due to repeated cyclic straining.

Maroney *et al.* (1994) and **Romstad *et al.* (1995)** tested two one-half end diaphragms to failure at the University of California, Davis (UCD) and monitored their behaviour to assess the validity of the assumptions often used in bridge design. The tests involved two different abutment heights and pushed against each other by a hydraulic ram. Yolo loam (clayey soil) and sand are used as backfills for the west and east abutments, respectively. The smaller abutment was tested to failure longitudinally under a displacement controlled test. Subsequently, a load test was performed on the large

abutment to failure under load control in the transverse direction. The results of the tests were compared with the Caltrans design equation. The failure surface has defined the wedge length which was nearly two times the height of the abutment.

Bozorgzadeh (2007) performed a lateral load test on a half-scale bridge abutment model at the University of California, San Diego. The objective of the experimental program was to examine the effects of parameters on longitudinal stiffness and capacity of the abutment. The parameters considered are different backfill soil, backfill height, restraining vertical movement of the wall, and pre-existing weak planes or cut slopes. Tests were performed on two different types of abutments, four tests on diaphragm abutment replicating seat-type abutment behaviour and a system test on the backwall separated from the seat (stemwall) and wingwalls. Clayey and silty sands were chosen as the backfill soils. The FE simulations of the tests were performed using Plaxis adopting the MC and HS constitutive models for the backfill. Based on the experimental study, it is concluded that the vertical movement of the wall had a significant effect on the post-peak behaviour of the abutments. It is recommended not to use the highly simplified models which provide inaccurate predictions for the behaviour of abutments.

Rollins and Cole (2006) and **Cole and Rollins (2006)** performed a series of seven cyclic lateral load tests on a pile cap supported by 4×3 pile group driven into a cohesive soil deposit. Load versus deflection and backbone curves for four different backfill soils and with no backfill are presented. The surcharge produced by the backfill soil had essentially no effect on the lateral soil-pile resistance. A gap formed between the pile cap and backfill soil affected significantly the load-deflection behaviour. The observed sliding surface geometry was in good agreement with that predicted by the log spiral theory. The measured passive resistances were compared with Rankine's, Coulomb's, and log spiral theories, and with the US Navy and Caltrans curves. A cyclic-hyperbolic model was developed to account for the passive force-deflection relationship for cyclic loading conditions and the corresponding limitation of the model was presented.

Jessee (2012) and **Rollins and Jessee (2013)** performed lateral load tests to investigate the passive force-displacement curves for skewed bridges. Tests were performed on backwalls with skew angles of 0, 15, 30, and 45° having backfill of densely compacted sand. Results indicate that with the increase in skew angle the passive force decreases significantly. A 50% reduction was noted for a skew angle of 30°. The reduction of passive force may be due to the involvement of a smaller part of the backfill soil in

mobilisation. The horizontal displacement necessary to develop the peak passive force was still between 2 to 4% of the wall height and has not changed with the skew angle. A reduction factor was introduced as a function of the skew angle to calculate the passive capacity at different skew angles. The experimental results for various skew angles were compared with the analytical studies of Shamsabadi *et al.* (2006). The skewed failure surface appears to be parallel to the abutment, but no specific correlation between the angles of the failure surface and the abutment wall was reported by the authors. The measured passive force-displacement curves were compared with Duncan and Mokwa (2001) and Shamsabadi *et al.* (2007), but none of the methods could depict the decrease in the post-peak passive force.

Wilson and Elgamal (2009) conducted full-scale shake table tests on bridge abutment to measure the lateral passive earth pressure under static and dynamic loading scenarios. In the static scenario, the recorded passive earth resistances were presented in the form of force-displacement backbone curves and these results were compared with the log-spiral theory, Caltrans method and AASHTO models. In the dynamic scenario, the measured dynamic thrusts for both the at-rest and passive pressure conditions were presented in the form of force-time histories and force-acceleration relationships.

Table 2.1 summarises the medium to large-scale field tests conducted by various researchers on the passive force-displacement relationships.

Table 2.1 Summary of medium to large-scale field tests on the passive force-displacement relationships.

| Study | Abutment Height (m) | Mode of Movement | Δ/h | Backfill Soil Type | Abutment Type | Abutment Foundation | Skew Angle (°) |
|---|---------------------|--------------------------|-------------------|--|-------------------|---------------------|------------------|
| Maroney <i>et al.</i> (1994); Romstad <i>et al.</i> (1995) | 1.68, 2.06 | Translation | 0.025 | Yolo Loam (clayey soil) | Integral abutment | Concrete piles | 0 |
| Duncan and Mokwa (2001) | 1.067 | Translation | 0.03 | Sandy silt (ML) and sandy clay (CL) | Anchor block | None | 0 |
| Rollins and Spark (2002) | 1.22 | Translation | 0.06 | Sandy gravel | Pile cap | Steel piles | 0 |
| Rollins and Cole (2006) | 1.12 | Translation | 0.035 to 0.052 | Clean sand, Fine gravel, Coarse gravel, Silty sand | Pile cap | Concrete piles | 0 |
| Bozorgzdeh (2007) | 1.68, 2.3 | Translation | 0.03 | Silty sand | Abutment | None | 0 |
| Stewart <i>et al.</i> (2007); Lemnitzer <i>et al.</i> (2009) | 1.67 | Translation | 0.03 | Silty sand | Backwall | None | 0 |
| Wilson (2009); Wilson and Elgamal (2009) | 1.7 | Translation | 0.027 | Silty sand | Abutment | None | 0 |
| Jessee (2012); Rollins and Jessee (2013) | 1.68 | Translation | 0.02 to 0.04 | Sand | Backwall | None | 0, 15, 30, 45 |
| Marsh (2013); Marsh <i>et al.</i> (2013) | 1.68 | Translation | 0.03 to 0.04 | Sand | Pile cap | Steel piles | 0, 15, 30 |
| Frank (2013) | 1.74 | Translation, Rotation | 0.05 | Sand | Pile cap | Steel piles | 0, 15, 30 |
| Smith (2014) | 0.91, 1.74 | Translation, Rotation | 0.048 | Sand | Pile cap | Steel piles | 0, 45 |
| Rollins <i>et al.</i> (2017) | 1.68 | Translation | 0.034 | Sand, Geofoam inclusion | Pile cap | Steel piles | 0 |

2.3.7 Numerical Studies on Passive Force-Displacement Relationships

Many researchers have attempted to evaluate the passive force-displacement relationship through numerical simulations. Arsoy (2004) investigated the mode of abutment movement as pure translation and rotation by using the fundamental stress-strain behaviour of granular backfill materials. Author evaluated the passive pressure using the log-spiral theory and strain in the backfill using the method proposed by Rowe (1954). The author has proposed the charts for displacement dependent passive earth pressure. Shamsabadi *et al.* (2010) used the FE simulations to replicate the UCLA and UCD abutment tests. The 2D and 3D FE simulations were carried out using Plaxis program with 15-node triangular elements and 15-node tetrahedral elements, respectively. The behaviour of the backfill soil was simulated using the HS model and the interface between the abutment and soil was simulated using the interface elements. The lateral force-displacement curves have been evaluated and compared with the field data and LSH method and are found to be matching well. Wilson and Elgamal (2010) conducted two large-scale experiments on dense sand to evaluate the mobilisation of passive earth pressure. The FE simulations were also carried out with a 2D plane-strain model in the Plaxis and the material parameters adopted were obtained from the triaxial and direct shear tests of Lemnitzer *et al.* (2009). The simulations were conducted in accordance with the experiments and the results were found to be in good agreement. Shamsabadi and Rollins (2014) used a 3D FE model developed in Plaxis and simulated the large-scale abutment tests performed by Marsh (2013). The abutment wall and backfill soil were modelled and simulated as plate and continuum elements, respectively. The backfill soil was modelled using HS model. Ni *et al.* (2018) proposed a design framework to evaluate the displacement-dependent lateral earth pressure on the retaining wall. This framework is an extension of the work by Mei *et al.* (2009). The parameters influencing the model are the effective friction angle and abutment displacement. The lateral earth pressure obtained by the proposed was compared with that reported in the literature.

2.4 NUMERICAL MODELLING OF SOIL-STRUCTURE INTERFACE

A proper modelling of contact surfaces using FE simulations has been developed over the years in the literature. The consideration of interfaces in numerical analysis is often made using simplified Coulomb friction, and the same is implemented widely in geotechnical engineering using the master and slave concepts. Majority of the interface models developed in the geotechnical engineering have used the elastoplastic framework. The Mohr-Coulomb friction

model is the most commonly used interface model. The general form of the interface model is expressed as

$$\dot{\boldsymbol{\sigma}} = f(\dot{\boldsymbol{\varepsilon}}) \quad (2.9)$$

where $\dot{\boldsymbol{\sigma}}$ is the stress tensor and $\dot{\boldsymbol{\varepsilon}}$ is the strain tensor. For evaluating the stress tensor, the following are required:

- A yield criterion to distinguish between elastic and plastic behaviour. For interface model, the yield criterion is used to estimate the stick behaviour.
- A plastic potential to describe the evolution of the yield surface.
- A hardening and/or softening rules.
- A compliance tensor, which governs the adhesion behaviour.

2.5 HYPOPLASTIC CONSTITUTIVE MODEL

The major characteristics of hypoplastic constitutive equations are the simple formulations and a few parameters based on nonlinear tensors. The initial hypoplastic model (Gudehus, 1996; Wolffersdorff, 1996; Kolymbas, 2000) is a tensor function of strain rate having two linear and nonlinear terms with four material parameters, which can be determined by a triaxial test. The state variables considered in the basic models are only the stress tensor. Wu *et al.* (1996) introduced the void ratio as an additional state variable into the model. Classical hypoplasticity theory has the major advantage of being able to model the soil behaviour in the absence of yield surface, plastic potential, and flow rule. The general form of the hypoplastic constitutive model is expressed as

$$\dot{\boldsymbol{T}} = f_s (\boldsymbol{L} : \boldsymbol{D} + f_a \boldsymbol{N} \|\boldsymbol{D}\|) \quad (2.10)$$

This equation relates the objective stress rate $\dot{\boldsymbol{T}}$ to the Euler stretching rate \boldsymbol{D} . In Equation 2.10, \boldsymbol{L} and \boldsymbol{N} are the second and fourth-order constitutive tensors and \boldsymbol{L} is linear and \boldsymbol{D} is the strain rate (stretching) tensor, $\|\boldsymbol{D}\|$ is the norm of the strain rate, defined as $\sqrt{\boldsymbol{D} : \boldsymbol{D}}$. The functions \boldsymbol{L} and \boldsymbol{N} must be isotropic to remain invariant under rigid body rotations. Von Wolffersdorff extended the basic form of the model by incorporating a predefined limit state surface according to Matsuoka-Nakai (1974). The second-order constitutive tensor \boldsymbol{L} and the fourth-order constitutive tensor \boldsymbol{N} are defined as

$$\boldsymbol{L} = f_s \frac{1}{\hat{\boldsymbol{T}} : \hat{\boldsymbol{T}}} \left(F^2 \boldsymbol{I} + a^2 \hat{\boldsymbol{T}} \otimes \hat{\boldsymbol{T}} \right) \quad (2.11)$$

$$N = f_s f_d \frac{a \cdot F}{\hat{T} : \hat{T}} (\hat{T} + \hat{T}^*) \quad (2.12)$$

where $\hat{T}^* = \hat{T} - \frac{1}{3}$ and $\hat{T} = T / \text{tr}T$ is the deviator stress, F denotes the Matsuoka-Nakai stress factor in the model and is given by

$$F = \sqrt{\frac{1}{8} \tan^2 \psi + \frac{2 - \tan^2 \psi}{2 + \sqrt{2} \tan \psi \cos 3\theta}} - \frac{1}{2\sqrt{2}} \tan \psi \quad (2.13)$$

The constitutive coefficient α is defined as

$$\alpha = \frac{\sqrt{3}(3 - \sin \phi_c)}{2\sqrt{2} \sin \phi} \quad (2.14)$$

where ϕ_c is the critical friction angle. The Lode angle θ is defined as

$$\cos 3\theta = -\sqrt{6} \frac{\text{tr}(\hat{T}^* \cdot \hat{T}^* \cdot \hat{T}^*)}{[\hat{T}^* : \hat{T}^*]^{3/2}} \quad (2.15)$$

The barotropy factor, f_s controls the influence of the mean stress, and is expressed as

$$f_s = \frac{h_s}{n} \left(\frac{e_i}{e} \right)^\beta \frac{1 + e_i}{e_i} \left(\frac{-\text{tr}(T)}{h_s} \right)^{1-n} \cdot \left[3 + a^2 - a\sqrt{3} \left(\frac{e_{i0} - e_{d0}}{e_{c0} - e_{d0}} \right)^\alpha \right]^{-1} \quad (2.16)$$

The pyknotropy factor, f_d controls the influence of the relative density, and is expressed as

$$f_d = \left(\frac{e - e_d}{e_c - e_d} \right)^\alpha \quad (2.17)$$

where e_d , e_c and e_i are the limiting void ratios. With increase in mean pressure, these void ratios decrease until the limiting values e_{d0} , e_{c0} and e_{i0} are reached:

$$\frac{e_d}{e_{d0}} = \frac{e_c}{e_{c0}} = \frac{e_i}{e_{i0}} = \exp \left[- \left(\frac{\text{tr}(T)}{h_s} \right)^n \right] \quad (2.18)$$

In the present study, the hypoplastic constitutive model is implemented in ABAQUS by user defined material subroutine (UMAT).

2.6 BEHAVIOUR OF IABs UNDER THERMAL LOADING

The integral abutment bridge superstructure will expand and contract under the thermal temperature variation daily. In the absence of expansion joints, the bridge must accommodate the abutment movements, hence the flexible foundations are being adopted for the IABs. The most common foundation for the IABs are single rows of steel H-pile. Over the years, to understand the behaviour of the IABs under thermal loading, previous researchers have instrumented, and field monitored the behaviour of IABs. The field monitored response data of the IABs and changes noted in the following quantities have been observed: (1) abutment displacement, (2) backfill pressure, (3) abutment rotation, (4) girder rotation, (5) girder bending moment, (6) girder axial force, (7) pile moment, (8) pile axial force, and (9) strain in approach slab. The increase of passive earth pressure under cyclic loading at constant abutment displacement is called the soil ratcheting phenomenon. The previous studies have reported the soil ratcheting based on the data of the field observation and a few of these studies are reviewed.

2.6.1 Field Monitoring Studies

The field monitoring studies are essential to investigate and justify the design and construction aspects, adopted structural design parameters, joint connection effects, and considered stress relief mechanisms during the life of the bridge structures. These studies are performed considering the short-term and long-term effects of the temperature loadings on the behaviour of IABs. In this section, a few publications related to the field monitoring studies are reviewed and presented.

Hassiotis and Xiong (2007) conducted field observation studies of the Scotch Road integral abutment. The design parameters of interest considered were the flexural behaviour of piles, soil-pressure distribution behind the abutment, displacement, and rotation of the superstructure due to thermal loading. Over the 4 years of field observation, it was noted that the passive earth pressure coefficient was found to increase continuously. The earth pressure distribution behind the abutment and variation of earth pressure coefficient with relative displacement for every year was compared with Rankine's theory, National Cooperative Highway Research Program (NCHRP) guidelines, British code, and England *et al.* (2000).

Ooi *et al.* (2010) monitored the drilled shaft-supported integral abutment bridge from foundation installation to in-service behaviour for 45 months in Kahuku town, Oahu, Hawaii. The observed bridge movement represented the cumulative effects of several events including the compaction-induced movements, deep-seated soil movement, superstructure loading,

hydrodynamic loading, concrete creep and shrinkage, and thermal expansion and contraction of the superstructure. Based on the monitoring of the IAB, it was suggested that the staged construction analysis should be used to obtain a predeflected profile of the frame when the subsurface soil is soft and highly plastic clay. The loads measured at the top of the drilled shafts were significantly higher than the working loads. The drilled shaft translated and rotated at the interface with the abutment and the measured moment is less than the cracking moment at all strain gauge locations but the moment derived from the inclinometer provided a conflicting trend.

Kim and Laman (2012) conducted seven years of field monitoring of 4 IABs in Pennsylvania, USA. The monitoring was made for the abutment displacement, backfill pressure, abutment rotation, girder rotation, girder bending moment, girder axial force, pile moment, pile axial force, and strain in the approach slab. The monitored results included the mean, maximum, and minimum envelopes. The abutment displacements of all the four IABs under thermal loading were highly nonlinear and irreversible during the monitoring period. The passive earth pressure at the abutment top and bottom exhibited a clear difference in the first year but these pressure differences became smaller over time and passive pressure ratcheting was not observed. The design guidelines were recommended in line with the available codal provisions.

Huntley and Valsangkar (2013) conducted three years of field monitoring of two-span pile-supported integral abutment bridge near Fredericton, New Brunswick, Canada. The SSI effects of abutment walls subjected to thermal cyclic loading were investigated. The plot of stress ratio over the monitoring period were compared with the traditional Coulomb's and Rankine's earth pressure theories. It was noted that these theories were not the best to predict the earth pressure for integral abutments. The field observation data as reported by the authors was contradictory to some findings already reported in the literature regarding the soil ratcheting. However, the authors reported that a definite conclusion cannot be drawn based on the 3 years of field monitoring of the present structure. The comparison was made with the other field instrumented integral bridge abutment structures which reported soil ratcheting. The presence of earth pressure ratcheting was not consistent among the instrumented bridges reported in the literature. In conclusion, the earth pressure magnitude, distribution, and behaviour over the time were quite variable from structure to structure, as these were dependent on many factors such as the type of backfill, degree of compaction, magnitude of wall movement, movement mode and foundation type and others that were unique to each site.

Table 2.2 summarises the field monitored previous studies on the IABs and indicates whether soil ratcheting was observed or not. From the table it is observed that the soil ratcheting phenomenon is not consistent among the observations made in the previous studies.

Table 2.2 Summary of field monitored previous studies of IABs.

| Study | | Number of Spans | Monitoring Period | Backfill Soil Type | Number of Piles | Skew Angle (°) | Soil Ratcheting |
|--|-----------------------------------|-----------------|-------------------|-----------------------------------|-----------------|----------------|-----------------|
| Khodair and Hassiotis (2005), Hassiotis and Xiong (2007) | | 2 | 4 years | Porous fill (AASHTO T27) | 19 | 15 | Observed |
| Fennema <i>et al.</i> (2005) | | 3 | 4 months | Clay | 8 | 0 | - * |
| Huang <i>et al.</i> (2005) | | 3 | 7 years | Granular soil | - | 0 | Observed |
| Brena <i>et al.</i> (2007) | | 3 | 3 years | Granular soil | 8 | 0 | Observed |
| Frosch <i>et al.</i> (2009), Lovell (2010) | Soundbound I-65 over SR-25 bridge | 2 | 10 years | Granular soil | 6 | 25 | Observed |
| | SR-18 bridge | 5 | 6.7 years | Dense sand | 5 | 8 | Observed |
| | US-231 bridge | 3 | 3.5 years | Dense sand | 7 | 33.8 | Observed |
| Ooi <i>et al.</i> (2010) | | 1 | 45 months | Well graded gravel | 5 | 0 | Not observed |
| David <i>et al.</i> (2010) | | 1 | 15 months | Well graded sand with some gravel | 4 | 35 | - * |
| Kim and Laman (2012) | Bridge No. 109 | 4 | 2.5 years | Granular soil | 12 | 0 | Observed |
| | Bridge No. 203 | 3 | 7 years | Granular soil | 8 | 0 | Not observed |
| | Bridge No. 211 | 1 | 5 years | Granular soil | 12 | 0 | Not observed |
| | Bridge No. 222 | 1 | 6 years | Granular soil | 9 | 0 | Not observed |
| Kirupakaran <i>et al.</i> (2012) (2015) | | 3 | 3.5 years | Sand | 7 | 10 | Observed |
| Huntley and Valsangkar (2013) (2014) | | 2 | 3 years | Loose granular soil | 15 | 0 | Not observed |
| Kong <i>et al.</i> (2015) | | 11 | 3 years | Sand | 4 | 0 | Not observed |

* Soil ratcheting was not specifically reported.

2.6.2 Numerical Studies

Several researchers have conducted numerical simulations for thermal loading to predict the behaviour of IABs for different parameters mentioned in the field monitored studies. Most of the previous studies have adopted the nonlinear Winkler spring to simulate the behaviour of backfill soil behind the abutment and foundation soil surrounding the pile. In the previous studies, the priority was given to the behaviour assessment of bridge superstructure rather than modelling the nonlinear behaviour of backfill and foundation soils considering the hysteresis response under cyclic thermal loading. A few studies have incorporated the nonlinear behaviour of the soil by continuum modelling. The parametric studies have been carried out by various researchers by varying the H-pile orientation with respect to strong axis and weak axis, H-pile sections, span of the bridge, height of the abutment, the applied abutment longitudinal displacement and rotation, and backfill soil type. Following are the some of the studies which used the numerical simulation for thermal loading on the IABs. They are Faraji *et al.* (2001), Dicleli *et al.* (2003), Fennema *et al.* (2005), Paul *et al.* (2005), Civjan *et al.* (2007), Huang *et al.* (2008), Ooi *et al.* (2010), Kim and Laman (2010), Zordan *et al.* (2011), Zhao *et al.* (2011), David *et al.* (2014), Erhan and Dicleli (2014), Kirupakaran *et al.* (2015), LaFave *et al.* (2016), Kirupakaran and Muraleetharan (2017), Quinn and Civjan (2017), Abdel-Fattah *et al.* (2018) and Abdullah and Nagggar (2023). A few of these publications are briefly reviewed and presented.

Khodair and Hassiotis (2005) used the 3D FE model to simulate the pile-soil interaction of the IAB subjected to thermal loading. Two load cases were considered in the model: one is the temperature and the other one is the field monitored IAB data. The nonlinear response of the soil is modelled using solid continuum models according to the Mohr-Coulomb criterion. The pile-soil interaction is modelled using the surface-to-surface contact algorithm in ABAQUS/Standard. The FE model was validated with the results of the field monitored studies and compared with the finite difference and LPILE results. A parametric analysis was conducted to study the effect of the size of the galvanized steel sleeve on the magnitude of the pressure transferred to the surrounding soil and MSE wall.

Dicleli (2005) conducted static pushover analyses of the integral bridge to study the effect of different geometric, structural, and geotechnical parameters on the performance of the abutment-backfill system. The nonlinear behaviour of the piles and abutment-soil interaction under positive thermal variations are incorporated in the 2D modelling using SAP 2000

software. The results of the pushover analyses have been used to propose the design equations to determine the maximum forces in the abutments and maximum length of the integral bridges based on the strength of the abutments.

Pugasap *et al.* (2009) performed the 2D and 3D FE simulations to predict the long-term behaviour of the IAB using ANSYS software and compared the results with the three field instrumented IABs which were monitored for three years. The seasonal thermal loading derived time-dependent strains have been incorporated in the FE model by age adjusted effective modulus method. The Winkler nonlinear springs were adopted to model the SSI effects. The four analyses cases were evaluated over 10- and 100-year simulation periods to examine the relative magnitude of the time-dependent and elastoplastic effects on the long-term performance of the IABs.

Quinn and Civjan (2017) conducted a parametric study to determine the optimum pile orientation of a single-span IAB using 3D FE analysis by SAP 2000 software. Parameters considered in the study are bridge length, skew angle, pile web orientation, and temperature variations. The optimal pile orientation and its design are dependent on the in-situ construction temperature, maximum and minimum design temperatures, and backfill conditions. The 3D FE analysis is recommended to account for the transverse pile moments which are critical for the bridges with skew angles greater than 15°.

Rodriguez *et al.* (2011) investigated the response of abutments and reinforced concrete piers of the integral railway bridge using ABAQUS for thermal cycles and braking load from the trains under 0.15g earthquake event. A variation of peak earth pressure coefficient with the number of cycles of wall rotation for thermal loading is evaluated. The force-displacement evolution and crack width development in circular and rectangular piers, relative pier ground motion and displacement in the longitudinal and transverse directions, and distribution of braking load in piers and abutment and response of the integral abutment to the ground motion are reported in their study.

Al-qarawi *et al.* (2020) investigated the lateral soil pressure and soil settlement through experimental and numerical studies. A 2D plane-strain numerical model was used to simulate the SSI in a pile-supported IAB subjected to cyclic loading which simulated the thermal ambient temperature variations. The effect of EPS geofom inclusion with and without backfill soil was investigated. The use of EPS geofom inclusion is found to be effective and significant in reducing the lateral earth pressure and magnitude of approach settlement.

2.7 BEHAVIOUR OF TRANSITION ZONE OF IAB

The nonlinear response of the abutment-soil-pile system induced by concrete creep, shrinkage, and thermal expansion and contraction results in the excessive settlement of the backfill soil in the transition zone of the IAB. This movement arises from alterations in support conditions at the transition zone between the IAB and the embankment. The major problems with railway track transition zone are differential settlement, enhanced dynamic load, and accelerated track deteriorations (Punetha, 2022). This issue might prove detrimental, especially for the IABs supporting railway lines. From past studies it is noted that the increased maintenance and repair costs of the transition zone are two to four times higher than that associated with the other parts of the track (Asghari *et al.* 2021). The transition zone is considered as the most vulnerable section of the railway track. The settlement in the transition zone can be reduced by making changes in the track components such as superstructure and substructure. The implementation of changes in both components is to be made gradually so that the changes from high stiffness to less stiffness should be smooth and vice versa.

The bridge approach slab is one of the effective ways of reducing the problems in the transition zone, recommended by the American railway engineering and maintenance-of-way association (AREMA). The bridge approach slabs are constructed of reinforced concrete connected to the bridge deck and abutment through a doveled connection, continuous top reinforcement between the bridge and transition slab (partial connection), and cast monolithically with rigid connection (Burdet *et al.*, 2015). The purpose is to achieve a smooth transition of track stiffness and a reduction in maintenance requirements. Many previous researchers have worked on the behaviour of the transition zone behind the bridge abutment (Briaud, 1997; Cai *et al.* 2005; Kerokoski, 2006; Varandas *et al.*, 2011; Burdet *et al.*, 2015 and many more) and these studies are conducted on the conventional bridges. Zakeri and Ghorbani (2011) demonstrated the effectiveness of this approach through the implementation of gradual adjustments in track stiffness. This was achieved by constructing the approach slab with varying thicknesses in the transition zone. Varandas *et al.* (2011) focused on railway passage over the box-culvert transition located in a soft soil region. Extensive monitoring comprising of both short-term and long-term measurements and simulations using 3D FE models have successfully provided the reliable railway transition. The authors have obtained the increased settlement of the ballast layer in the transition zone. Cai *et al.* (2005) performed a numerical analysis to investigate the effect of subgrade settlement on the structural performance of the transition approach slab. However, their study was only focused on the transition zone for the road pavements. Punetha

(2022) summarised in detail the previous research on the track transition zone associated problems and their effect on railway operations. Punetha (2022) has also investigated the response of ballast track in the transition zone by analytical, geotechnical rheological track model and studied the improved performance by using cellular geoinclusions. Author has recommended mitigation measures for improvement in the performance of the transition zone. In the present study, the dynamic behaviour of the transition zone of the IAB under moving train loading is investigated thoroughly.

2.8 SEISMIC BEHAVIOUR AND FRAGILITY CURVES OF IAB

The integral abutment construction without the support bearing, has eliminated the most common problem associated with the conventional bridge construction, that is the unseating of the superstructure from the support bearing. In the absence of expansion joints and bearings, the lateral movement of the bridge due to thermal expansion and contraction and seismic excitation must be accommodated by the abutments and piles. The integral abutment construction provides a better seismic resistance with increased redundancy as compared to the conventional bridge construction (Frosch *et al.*, 2009). A comprehensive review on the seismic response of integral abutment bridges covering various aspects such as integral abutment-backfill interaction and seismic design based on evidence was provided by Mitoulis (2020). The author has reviewed the previous studies and presented the current state of knowledge in the earthquake resistant design of IABs and impact of backfill soil behaviour on the seismic response. The realistic simulation of backfill soil behaviour is one of the important factors in the seismic design of integral abutments taking into account the abutment-backfill interaction. Dhar and Dasgupta (2019) reviewed the past three-decades of studies on the seismic soil-structure interaction (SSSI) effects on the behaviour of IABs. For a better understanding of the SSSI effects on the IABs, the authors have recommended the need of numerical and experimental studies. In this section, some of the previous studies conducted on the seismic behaviour of IABs are reviewed.

Frosch *et al.* (2009) carried out four major tasks as part of FHWA report: (i) Development of a series of design ground motions representing current estimates of the seismic hazard in Indiana, (ii) Evaluation of field data collected during an existing long-term integral abutment bridge monitoring project to estimate the relationship between abutment movements and earth pressures, (iii) Laboratory testing of current and proposed details of the abutment-pile connection to estimate displacement capacity, and (iv) Construction of analytical models to

estimate seismic displacements of the abutment. Finally, the authors have provided seismic design recommendations for the IABs.

Khodair and Ibrahim (2013) studied the seismic behaviour of two span IAB with approximately 15° skew angle considering dynamic vehicular live load and ground motion using 3D FE analysis with SAP 2000 software. The EI Centro earthquake record was used as the ground motion with a peak ground acceleration (PGA) of 0.27 g. The results were compared with the analytical studies and experimental results reported by Dehne and Hassiotis (2003).

2.8.1 Fragility Curves

The Performance-Based Seismic Design (PBSD) procedure consists of hazard, structural response, damage, and loss analyses. The hazard, system response, physical damage and loss are expressed in terms of intensity measure (IM), engineering design parameter (EDP), damage measure (DM), and decision variable (DV). The schematic representation of the PBSD procedure is depicted in Figure 2.5.

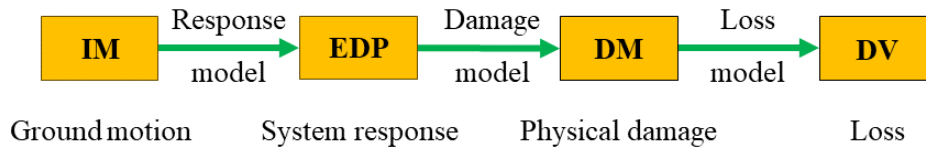


Fig. 2.5 Schematic Representation of PBSD Procedure.

The uncertainties in the intensity of the earthquake, ground motion parameters, structural behaviour, physical damage, and losses are considered in the Pacific Earthquake Engineering Research (PEER) performance-based earthquake engineering (PBEE) framework. The PEER centre has developed a PBEE methodology, and the general form of the framework equation is given as

$$\lambda(DV) = \iiint G(DV|DM)|dG(DM|EDP)||dG(EDP|IM)||d\lambda(IM)| \quad (2.19)$$

where $G(a|b)$ is a complementary cumulative distribution function (CCDF) for a conditioned on b . The three CCDFs from left to right in the above equation result from loss, damage, and response models, whereas $d\lambda(IM)$ is obtained from the mean seismic hazard curve. The evaluated loss hazard can be seen as the weighted average of all possible earthquake, ground motion, damage, and loss scenarios (Kramer, 2014). For practical applications, when all

variables are continuous, the triple integral of Equation 2.19 can be solved through numerical integration, and is represented as

$$\begin{aligned}\lambda_{DV}(dv) &= \sum_{k=1}^{N_{DM}} \sum_{j=1}^{N_{EDP}} \sum_{i=1}^{N_{IM}} P[DV > dv | DM = dm_k] \\ &\quad \times P[DM > dm_k | EDP = edp_j] \\ &\quad \times P[EDP > edp_j | IM = im_i] \Delta\lambda_{IM}(im_i)\end{aligned}\tag{2.20}$$

where $P[a|b]$ describes the probability of a conditioned on b , N_{IM} , N_{EDP} and N_{DM} are the number of increments of IM, EDP and DM respectively. The hazard curves for EDP, DM and DV can be computed by de-aggregating the above framing equation as

$$\lambda_{EDP}(edp) = \sum_{i=1}^{N_{IM}} P[EDP > edp | IM = im_i] \Delta\lambda_{IM}(im_i)\tag{2.21a}$$

$$\lambda_{DM}(dm) = \sum_{j=1}^{N_{EDP}} P[DM > dm | EDP = edp_j] \Delta\lambda_{EDP}(edp_j)\tag{2.21b}$$

$$\lambda_{DV}(dv) = \sum_{k=1}^{N_{DM}} P[DV > dv | DM = dm_k] \Delta\lambda_{DM}(dm_k)\tag{2.21c}$$

The above equations can be interpreted in the same way as the seismic hazard curves obtained from probabilistic seismic hazard analysis (PSHA). The PBSM can be implemented in engineering practice in various ways. It can be implemented at the response level (Equation 2.21a) which would allow the evaluation of the mean annual rate of exceedance in terms of EDPs at different response hazard levels. In the response level implementation, development of probabilistic relationship between the IM and EDP is called probabilistic seismic demand model (PSDM). The probabilistic seismic demand models (PSDMs) are used to evaluate the fragility or conditional probability of exceeding the design limit state thresholds for a given level of IM. There are a few studies reported in the literature for the development of seismic fragility curves for the IABs. Most of the studies have incorporated the nonlinear Winkler spring to simulate the abutment-backfill system and pile-soil system. The previous studies reported in the literature on the development of fragility curves for different structural and geotechnical systems are summarised in Table 2.3.

Table 2.3 Summary of fragility analysis of structural and geotechnical systems.

| Author(s) | Structure Type | Engineering Design Parameters | Intensity Measure |
|---------------------------------|------------------------------|--|-------------------------------|
| Hwang <i>et al.</i> (2000) | Highway bridges | Capacity to demand ratio | PGA |
| Mackie and Stojadinovic (2005) | Highway bridges | Bearing deformations, moment, shear force, stress, strain, energy | PGA, PGV, PGD, S _a |
| Nielson (2005) | Highway bridges | Column ductility and bearing deformations | PGA |
| Jeong and Elnashai (2007) | Bridges and RC frames | Displacement and drift ratio | PGA |
| Argyroudis <i>et al.</i> (2013) | Cantilever bridge abutments | Settlement of backfill | PGA |
| Zakeri <i>et al.</i> (2014) | Concrete box-girder bridges | Column, abutment displacement, shear key, bearing transverse | PGA |
| Choine <i>et al.</i> (2015) | Integral and jointed bridge | Column, abutment, shear key, elastomeric bearing and deck unseating | PGA |
| Simon and Vigh (2016) | Precast multi-girder bridge | Pier flexure and shear, Monolithic joint longitudinal and transverse deformation, backfill deformation | PGA |
| Mangalathu (2017) | Box-girder bridges | Column curvature ductility, displacement, and rotation | S _a |
| Argyroudis <i>et al.</i> (2018) | Pre-stressed concrete bridge | Permanent vertical displacement of backfill soil | PGA |
| Zamiran and Osouli (2018) | Cantilever retaining wall | Relative wall displacement | PGA |
| Shao <i>et al.</i> (2022) | Highway bridges | Approach fill settlement | PGA |
| Ahmed and Dasgupta (2022) | Multispan continuous IAB | Response of pier, bearing, pile-soil system, abutment-backfill system | PGA |

2.9 A CRITICAL APPRAISAL OF THE REVIEWED LITERATURE

The IABs have become popular bridge types because of their well-established advantages of reducing maintenance costs, particularly those associated with bridge expansion joints. The IABs have also been widely accepted across the world because of their many advantages over the traditional bridges with relief systems (Mistry, 2005). Based on the survey conducted by Maruri and Petro (2005) and White *et al.* (2010) on the design practices and designers' experiences and understanding, they found many similarities in design assumptions and construction practices, yet significant differences in the design philosophy, method of practice and analysis of IABs have been identified. Though the IABs are emerging bridges, yet they have some concerns with high unit stress due to thermal expansion and contraction, concrete shrinkage and creep, differential settlement, and excessive lateral movements (Ooi *et al.*, 2010). Despite these concerns with the IABs, the practitioners are adopting them over the conventional bridges in most cases.

The abutments of the integral bridges, i.e., the integral abutments (IAs) undergo complex, cyclic loading and unloading responses to changes in the ambient temperature. The IAs will respond in a nonlinear manner because of the nonlinearities of the abutment-soil-pile system due to multiple interactions. The backfill soil behaviour is hysteretic in nature under cyclic loading. The nonlinear behaviour of the backfill soil is due to the differences in loading and unloading and soil ratcheting (i.e., an increase of soil pressure under cyclic loading at constant wall displacement). The nonlinear behaviour is further complicated by the dependencies on the load history and load rate (Civjan *et al.* 2013). Hassiotis and Xiong (2007) reported the soil ratcheting and measured passive pressure. It was noted that the measured pressure was higher than the design pressure. However, Civjan *et al.* (2013) reported no indication of the soil ratcheting and backfill pressures were consistent across the abutment in the straight bridge, but they were highly variable with the maximum pressure being twice for the 15° skew bridge. Kim and Laman (2012) monitored the behaviour of four IABs. A few of the bridges indicated an increase in the backfill pressures while others did not. Huntley and Valsangkar (2013) reported that the Coulomb's and Rankine's methods are not the best approaches to predict the earth pressure for the integral abutments. The soil ratcheting was observed by some of the researchers such as Huang *et al.* (2005), Brena *et al.* (2007), Frosch *et al.* (2009), Lovell (2010), and Kirupakaran *et al.* (2012,

2015). However, a few researchers such as Ooi *et al.* (2010) and Kong *et al.* (2015) have not observed the soil ratcheting in the field monitoring of IABs. It is noted that the soil ratcheting is not consistent among the several instrumented IABs. The earth pressure magnitude, distribution, and behaviour over time are quite variable from structure to structure, as these are dependent on many factors that are unique to each site. England *et al.* (2000) specifically noted the potentially serious concern of the soil ratcheting associated with the IABs. A few researchers (Clayton *et al.*, 2006, Xu *et al.*, 2007) have addressed the soil ratcheting by performing stress path testing of the backfill soil sample. These studies reported that soil ratcheting was noticed in sand backfills, however no ratcheting was observed in the clay specimens. It is noted that a thorough analysis of the soil ratcheting behaviour would require a detailed 2D or 3D FE modelling of the abutment-soil-pile system incorporating a load path-dependent soil stress-strain model (Frosch *et al.* 2009). Therefore, in the present study, an attempt is made to use the 2D FE analysis to evaluate the effect of soil ratcheting on the passive capacity of the integral abutment-soil-pile system subjected to cyclic loading. It is also proposed to evaluate the passive capacity of the integral abutment-pile backfill system of the IABs using nonlinear FE analysis under static, cyclic, and thermal loadings. The hysteretic behaviour of the backfill soil is simulated using an advanced constitutive model, i.e., the hypoplastic constitutive model.

Arsoy (2004) derived analytical results for backfill pressures behind the integral abutments and pointed out the importance of considering the deformations developed due to translation and rotation of the abutment. The analytically obtained deformation behaviour of the abutment supported by piles differs from the experimentally evaluated behaviour under translation and rotation. The amount of translational/rotational interaction depends on the relative rotational stiffness of the superstructure and substructure components. The realistic analysis and design of IAB require numerical modelling that accounts for the entire structure including actual restraint provided by the superstructure and incorporates the SSI effects at piles and abutments correctly. Previous studies have addressed the issue of numerical modelling considering the SSI effects by p-y curves with nonlinear Winkler springs distributed along the pile and abutment length. A few studies have used guidelines established by the American Petroleum Institute (API) for pile-soil interaction and NCHRP guidelines for abutment-soil interaction. However, a few researchers such as Shamsabadi *et al.* (2010), Wilson and Elgamal (2010), and Shamsabadi and Rollins (2014) have evaluated the passive

force-displacement relationships by adopting the continuum modelling of backfill soil and the abutment was represented as the backwall without piles. The hysteresis behaviour of backfill soil simulated by the MC and HS models. The results are compared with the large-scale field experiments and analytical studies and are in good agreement. A few more guidelines have been developed to address the effect of SSI on the abutment-pile-soil system using the LSH model. The results of Duncan and Mokwa (2001), Clough and Duncan (1991), Rollins and Cole (2006) and many others have also been used in the formulation of guidelines. Moreover, limited studies are performed on the behaviour of abutment-pile-soil system using continuum modelling. Specifically, to simulate the nonlinear behaviour of the backfill, advanced constitutive relations are needed to evaluate accurately the passive capacity of the integral abutment. Hence, in the present study, it is proposed to carry out the parametric sensitivity analysis of the integral abutment-soil-pile system to establish the passive force-displacement relationships for the IAB.

Behaviour of the transition zone of the IAB is considered as the most vulnerable section of the railway track. The cost of repair and maintenance of the transition zone was 2 to 4 times higher than the open track (Asghari *et al.* 2021). Punetha (2022) developed a novel computational methodology to evaluate the performance of transition zone of the ballasted railway tracks under train-induced repeated loading. Punetha (2022) has also summarised the primary challenges involved in the transition zone of the railway tracks such as factors affecting track deterioration, modelling of the transition zone, and the effect of principal stress rotation on the transition zone. The reduction in the settlement of the transition zone is achieved through a gradual reduction in stiffness from higher values at the bridge and to lower values at the open track by improvising the superstructure and substructure. The approach slab is effective in diminishing the problems in the transition zone as outlined by AREMA. The approach slab in the IABs is monolithically connected with the integral abutment. Previous studies on the performance of transition zones, such as Varandas *et al.* (2011), Zakeri and Ghorbani (2011), Cai *et al.* (2005) and Asghari *et al.* (2021) are concentrated mainly on the conventional bridges. As the convention bridges are designed as rigid and provide lateral support to the backfill soil and foundation. In the case of IABs, abutment and piles are designed to be flexible to accommodate the expansion and contraction and the involvement of abutment-backfill system and pile-foundation soil system interactions. All these issues play an important role in the behaviour of IABs. The approach slab in

the conventional bridges is not rigidly connected with the abutment. Hence, the response of the transition zone of the IABs are expected to be different. The existing studies related to the transition zone of the IABs are mostly on the highway bridges, however the studies related to the transition zone of the IABs used for railways are very limited. Therefore, in the present study, an attempt is made to evaluate the dynamic behaviour of the transition zone of the integral abutment railway bridge (IARB) with an approach slab under a moving train loading.

A very few studies are performed on the seismic evaluation of the IABs considering SSI effects. Wood (2009) summarised the recent experimental and analytical studies on the passive capacity of different wall types during earthquake loading. The same results have been used for the analysis of IABs. The performance studies of IABs to earthquakes in New Zealand and California are reported by Wood (2015). The IABs have performed well during small to medium earthquake shaking intensity as compared to the conventional bridges, however under high seismic intensity, the IABs have suffered partial damages (Wood, 2015). For ground motions with larger intensity, the nonlinear behaviour of the bridge may not be consistently captured by the simplified models. Detailed modelling of the soil-bridge interaction is essential for an accurate assessment of the behaviour of the IAB (Erhan and Dicleli, 2014). Most of the studies have adopted the PEER developed PBEE framework for the development of fragility curves considering different EDPs for the convention bridges. These studies listed in Table 2.3 have adopted the nonlinear Winkler springs (p-y curves) to simulate the SSI effects and soil behaviour. Limited studies are reported (Argyroudis *et al.*, 2013, 2018) on the development of fragility curves for the IABs with soil behaviour modelled as a continuum. In the present study, it is proposed to use the finite element analysis for the seismic vulnerability assessment of the IABs subjected to site-specific ground motions. The PSDMs and fragility curves are developed for the typical IAB within the framework of PBEE.

2.10 THE PROPOSED STUDY

As part of the current study, research gaps are identified through a thorough critical appraisal of the reviewed literature. The hysteric behaviour of the backfill soil (Toyoura sand) of the IAB will be modelled using a hypoplastic constitutive model. The hypoplastic sand constitutive model will be calibrated with the triaxial test results. The 2D FE model development of the experimental setup will be developed, and the results

of this model will be validated with the large-scale field test conducted on the abutment backwall. This field test was performed to develop the passive force-displacement relationship. Later, the 2D FE analyses of the abutment backwall will be performed for the assessment of passive capacity and to develop the passive force-displacement relationships for the typical abutment subjected to translational and rotational movements. Further, the FE model development will be made for the pile-supported integral abutment with an approach slab subjected to static lateral displacement and accordingly the passive force-displacement relationships will be developed. The effect of varying length of the approach slab, backfill soil type, and foundation soil stiffness on the response of the integral abutment-pile-backfill system will be assessed and the corresponding passive force-displacement relationships will be evaluated. The effect of ambient temperature variation on the integral abutment bridge will also be simulated using 2D FE analysis. The data for simulating the ambient temperature variation is obtained from the published literature on the field monitoring of IABs. The behaviour of the integral abutment-pile-backfill system under cyclic displacement, which is equivalent of the induced thermal loading, will be studied and accordingly the responses of the system will be assessed. The soil ratcheting phenomenon will also be studied as part of the assessment of IAB under cyclic and thermal loadings.

The dynamic response of the transition zone of the IARB will be evaluated under the static, cyclic coupled bogie train loading and moving train loading. The parametric sensitivity analysis will be carried out by varying the parameters such as the geometry of the approach slab, backfill soil type, influence of train speed, influence of train movement direction, and height of the integral abutment. The dynamic train loading effect will be simulated by the dynamic amplification factor for different train speeds. In the FE model of the IARB, a simulation of hundred repetitive cycles of coupled bogie train loading will be considered and accordingly the response of the IARB will be evaluated. The impact of multiple axle passages of the moving train on the IARB will be investigated. The seismic vulnerability assessment of the typical IAB will be carried out considering continuously varying intensity measure (i.e., PGA) and accordingly the PSDMs and fragility curves will be developed for the pile-supported integral abutment bridge using the incremental dynamic analysis (IDA).

2.11 SUMMARY

In this chapter, a concise examination of the literature is presented, focusing on classical passive earth pressure theories, their significance, and the force-displacement relationships. The section on passive force-displacement relationships briefly covers a range of analytical methods, experimental studies (including laboratory and field medium to large-scale investigations), and numerical studies conducted by previous researchers. The literature pertaining to the behaviour of Integral Abutment Bridges (IABs) under ambient temperature variations is summarized, encompassing the field monitoring of IABs and numerical studies. A review on the importance of transition zone behaviour for bridges is summarised. A brief review on the previous studies of seismic behaviour of IABs is also presented. The performance-based seismic design methodology is discussed as outlined in the PBEE framework. A compilation of the previous studies attempted on the development of fragility curves for different structures is also presented. A critical appraisal of the reviewed literature is presented, and the research gaps are highlighted. The proposed study is outlined at the end.

In the next chapter, the FE model developed is attempted and is validated with field test results. The results of the FE studies on the behaviour of pile-supported integral abutment bridge subjected to static, cyclic and thermal loadings are presented.

CHAPTER 3

BEHAVIOUR OF INTEGRAL ABUTMENT BRIDGE UNDER STATIC, THERMAL AND CYCLIC DISPLACEMENT LOADING

3.1 INTRODUCTION

The behaviour of the integral abutment-soil-backfill system exhibits a complex nonlinear response under thermal and seismic loadings. The lateral capacity of the pile-supported integral abutment is a major factor in the design of IABs. The ambient temperature fluctuation leads to the expansion and contraction of the bridge superstructure longitudinally and transversely. The nonlinear behaviour depends on the several factors such as backfill soil type, abutment-soil interaction, pile-soil interaction, stiffness of foundation soil, length of the bridge span, height of the integral abutment, and many more. The longitudinal displacements are resisted by the soil surrounding the integral abutment which in turn generates the stresses in the bridge superstructure. Understanding the behaviour of integral abutment-soil-backfill system under lateral push, cyclic and thermal loadings is very essential for the reliable design of the IABs. In this chapter, the passive force-displacement relationships for the IAB are evaluated using pushover analysis. The behaviour of the integral abutment-soil-backfill system under cyclic thermal loading is evaluated. The behaviour of the integral abutment-pile-backfill system under cyclic displacement, which is equivalent of the induced thermal loading is studied and accordingly the responses of the system are assessed. The soil ratcheting phenomenon is also be studied as part of the assessment of IAB under cyclic and thermal loadings.

3.2 CALIBRATION OF HYPOPLASTIC SAND MODEL WITH TRIAXIAL TEST

The hypoplastic constitutive model is calibrated with a triaxial test for the backfill behaviour. The triaxial test is a standard test in soil mechanics in which a cylindrical specimen is loaded in radial and axial directions. For hypoplastic sand constitutive model, an UMAT subroutine is implemented in ABAQUS and validated with the results of Herle and Gudehus (1999) and Verdugo and Ishihara (1996). The stress-strain

behaviour of the Karlsruhe and Toyoura sands under different confining pressures is used in the study. Finite element drained triaxial tests are simulated using the UMAT on the Karlsruhe and Toyoura sand samples. Eight node continuum elements with full integration (C3D8) are used to model the soil elements. The hypoplastic soil parameters of the Karlsruhe and Toyoura sands are given in Tables 3.1 and 3.2, respectively. The stress-strain curves for the Karlsruhe sand are plotted for three different confining pressures, 300, 600, and 800 kPa with an initial void ratio of 0.56. The stress-strain curves for the Toyoura sand are plotted for confining pressure of 100 kPa with an initial void ratio having different values: 0.917, and 0.831. Similarly, for 500 kPa confining pressure with an initial void ratio having different values: 0.886, and 0.810, the stress-strain curves are plotted.

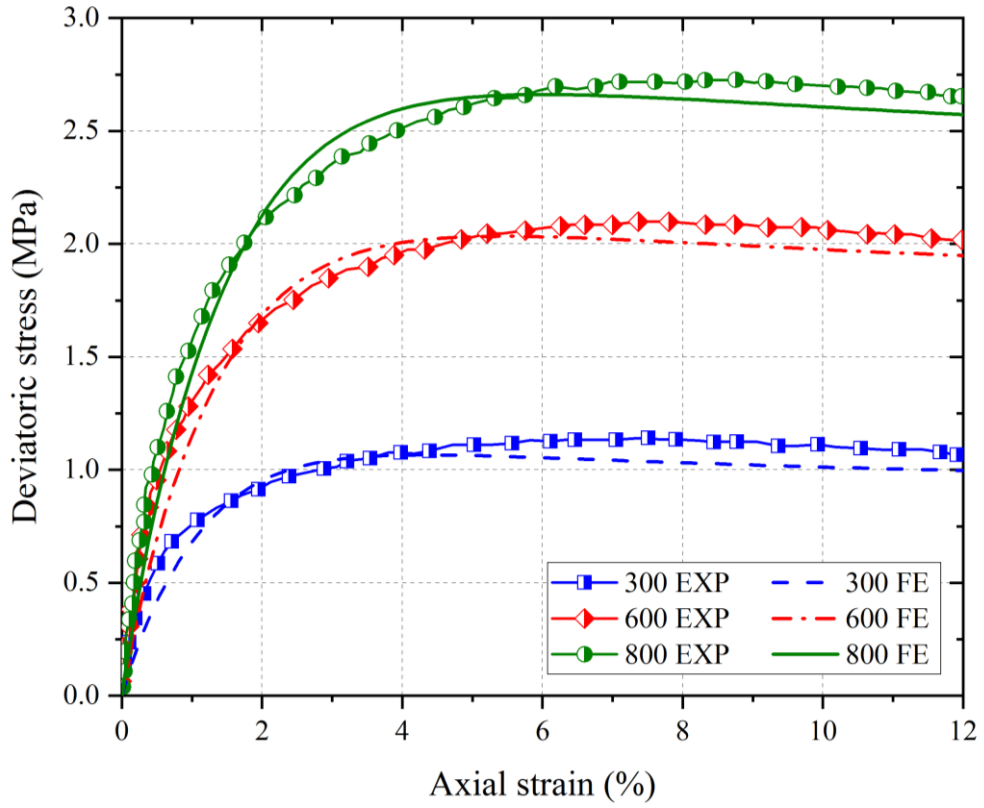
Table 3.1 Hypoplastic soil parameters of Karlsruhe sand (Herle and Gudehus, 1999).

| ϕ_c (°) | h_s (MPa) | n | e_{d0} | e_{c0} | e_{i0} | α | β |
|--------------|-------------|------|----------|----------|----------|----------|---------|
| 30 | 5800 | 0.28 | 0.53 | 0.84 | 1.0 | 0.06 | 2 |

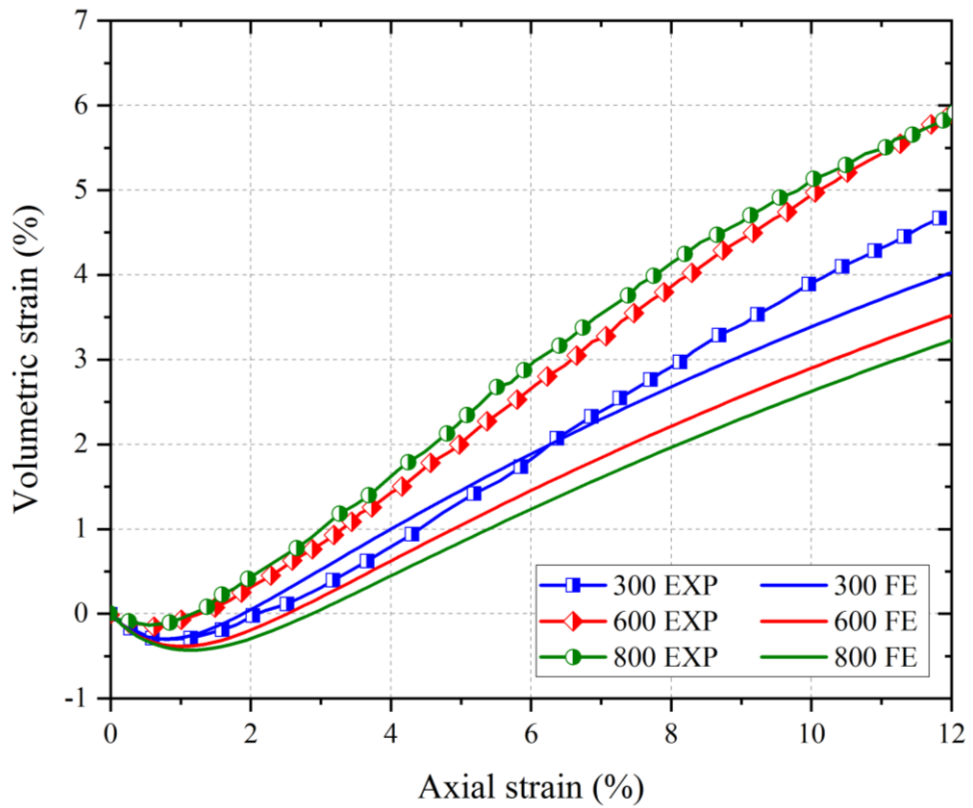
Table 3.2 Hypoplastic soil parameters of Toyoura sand (Herle and Gudehus, 1999).

| ϕ_c (°) | h_s (MPa) | n | e_{d0} | e_{c0} | e_{i0} | α | β |
|--------------|-------------|------|----------|----------|----------|----------|---------|
| 30 | 2600 | 0.27 | 0.61 | 0.98 | 1.1 | 0.14 | 3 |

The FE results of the Karlsruhe sand under three different confining pressures are compared with the triaxial compression test results and are shown in Figure 3.1. It is seen that the FE results obtained from ABAQUS match reasonably well. The FE results of the Toyoura sand under two confining pressures and for three different values of initial void ratios are compared with the triaxial compression test results and are shown in Figure 3.2. It is observed that the FE simulation results of the Toyoura sand are in good agreement with triaxial test data. Hence, the UMAT can capture the behaviour of the soil under different confining pressures and initial void ratios.

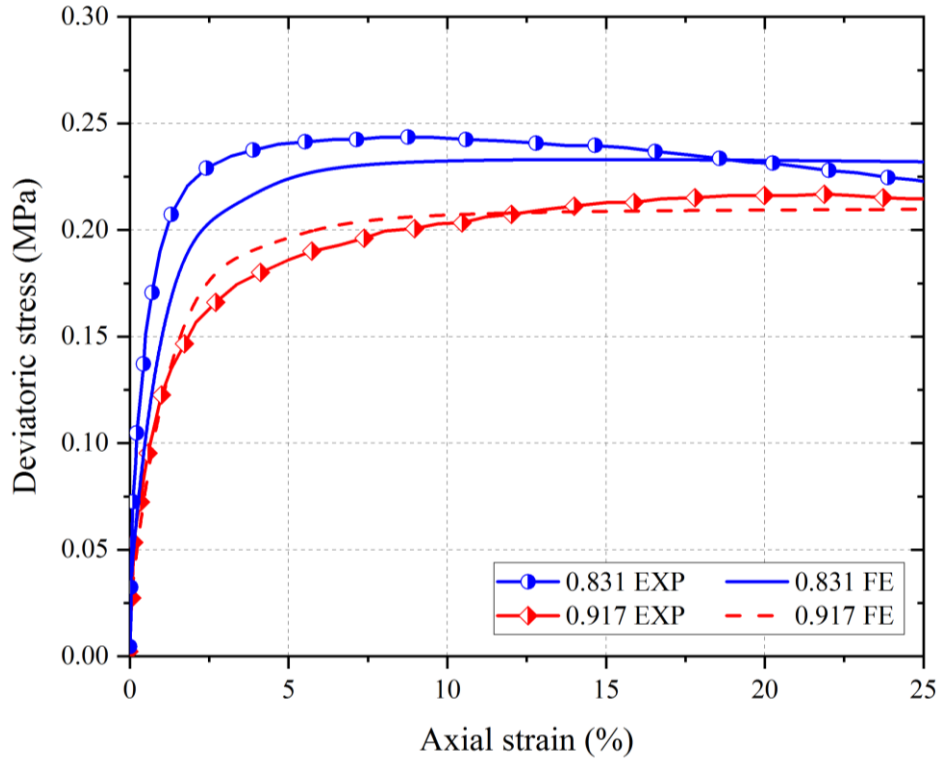


(a)

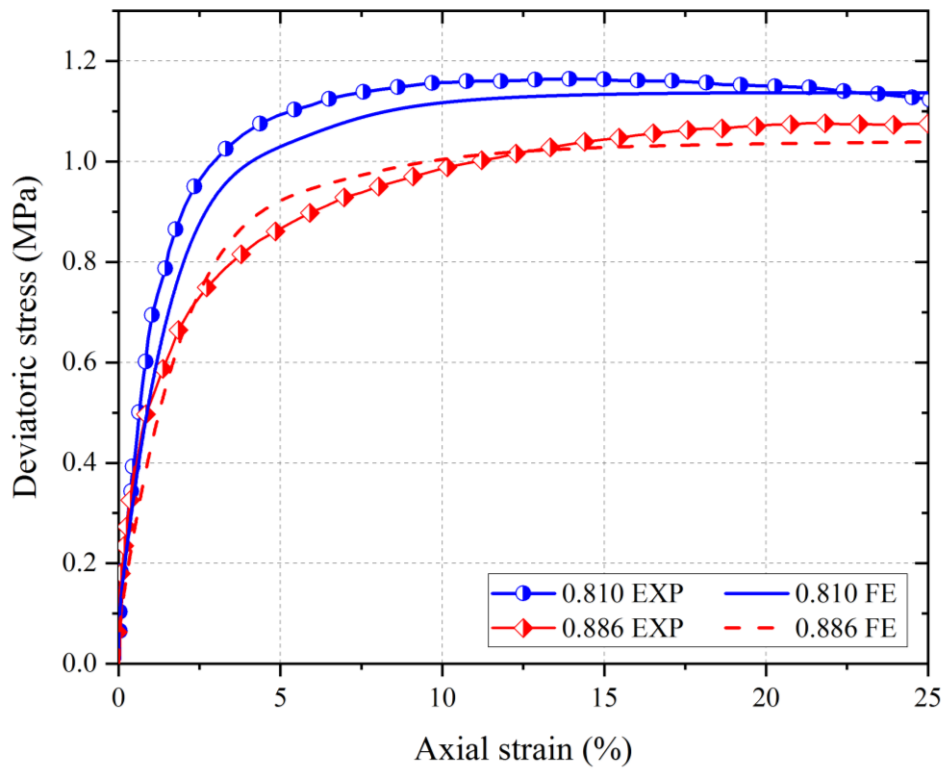


(b)

Fig. 3.1 Comparison of Drained Triaxial Test Results for Karlsruhe Sand: (a) Deviatoric Stress vs. Axial Strain, and (b) Volume Change Behaviour.



(a)



(b)

Fig. 3.2 Comparison of Drained Triaxial Test Results for Toyoura Sand under Two Confining Pressures: (a) 100 kPa, and (b) 500 kPa.

3.3 VALIDATION OF FE MODELS

In this section, the finite element (FE) models of the pile group and abutment backwall system are validated with the large-scale field tests conducted to evaluate the lateral passive capacities of the pile cap and abutment backwall. The Mohr-Coulomb (MC) material model is used to simulate the behaviour of backfill soil and the lateral resistance of the pile cap with and without backfill is assessed. The MC and hypoplastic constitutive models are used to simulate the response of the backfill soil in the case of abutment backwall system and the passive capacity is evaluated and compared with the field results.

3.3.1 Rollins and Cole (2006)

Rollins and Cole (2006) performed a series of full-scale static lateral load tests on a pile cap with dimensions 5.18 m × 3.05 m and a height of 1.12 m resting on a 4 × 3 pile group driven into a cohesive soil profile. Pile group consisted of 324 mm diameter 12 steel pipe piles driven closed ended to a depth of 12.2 m, as shown in Figure 3.3. The loads were applied through two 4.45 MN capacity hydraulic jacks on the pile cap. The lateral resistance of the pile cap was investigated for four different backfills, which were clean sand, fine gravel, coarse gravel, and silty sand as well as for no backfill condition. The corresponding backfill soil properties are given in Table 3.3.

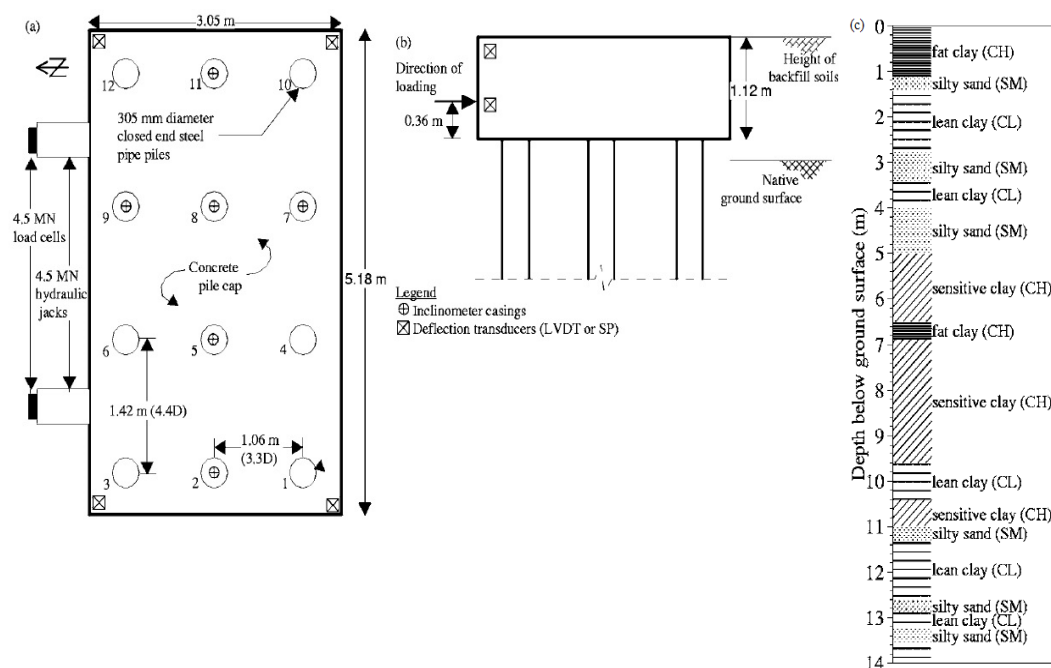


Fig. 3.3 Field Test Setup on Pile Cap (a) Plan, (b) Elevation View, and (c) Foundation Soil Profile (Rollins and Cole, 2006).

Table 3.3 Summary of material properties used for FE simulation (data sourced from Rollins and Cole, 2006; Anoosh *et al.*, 2007; David *et al.*, 2014).

| Material | Bulk Unit Weight, γ (kN/m ³) | Cohesion, c (kPa) | Friction, ϕ (°) | Interface Friction Angle, δ (°) | Young's Modulus, E (MPa) | Poisson's Ratio, ν |
|---------------------|---|---------------------|----------------------|--|----------------------------|------------------------|
| Clean sand | 16.18 | 0 | 39 | 30.03 | 37.1 | 0.27 |
| Silty sand | 16.57 | 7.2 | 27 | 20.25 | 38.3 | 0.35 |
| Reinforced concrete | 24.00 | - | - | - | 31000 | 0.20 |

The three-dimensional (3D) FE model of the pile cap resting on 12 piles, backfill soil, and natural soil assembly model is shown in Figure 3.4. The behaviour of backfill and natural foundation soils is simulated using MC material model, and the pile cap and pile are simulated as linear elastic behaviour. The FE model is discretised with an 8-node linear brick element, reduced integration with hourglass control (C3D8R) and the entire mesh consists of 103,662 elements. Standard boundary conditions are applied, with fixed support at the bottom and roller support on the sides.

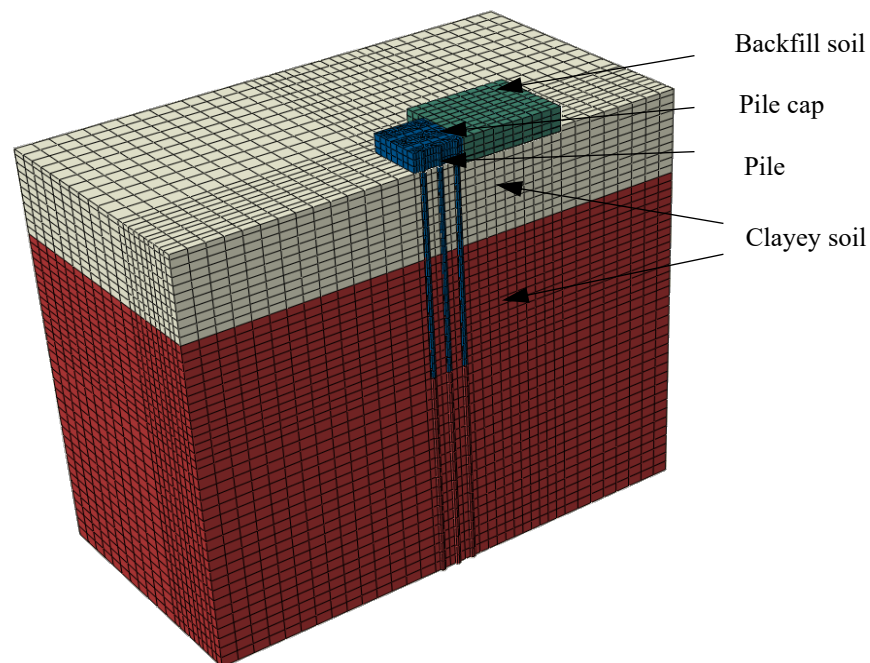


Fig. 3.4 3D FE Model with Mesh Discretisation for Rollins and Cole (2006) Field Test Setup.

The analysis for static loading on the pile cap is performed for two cases such as no backfill and with backfill (clean sand and silty sand). The load-displacement plots are obtained using the FE simulation and are compared with field data for the condition of

without backfill and with backfill having two different soils as in Figure 3.5. It is noted that the FE results are in good agreement with the field data.

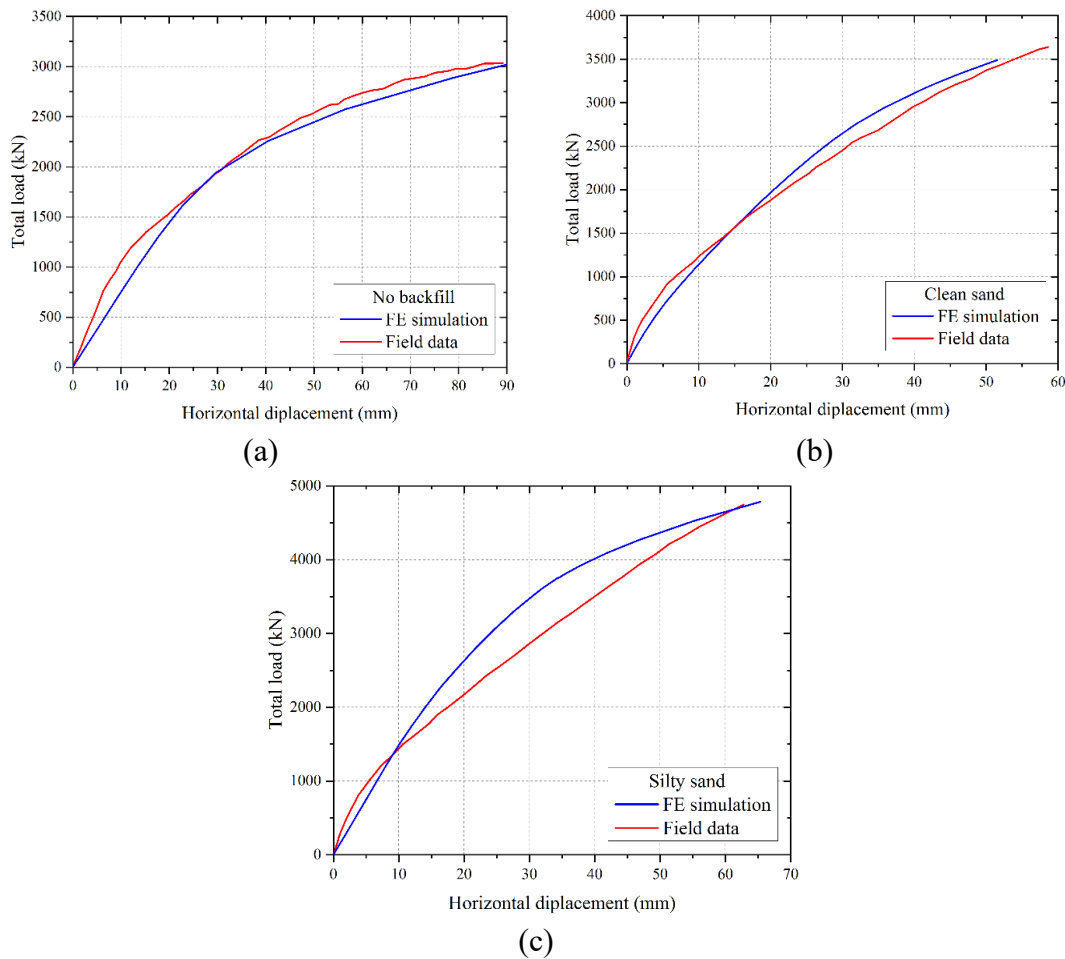


Fig. 3.5 Comparison of Load-Displacement Plots of FE Results and Field Data for (a) No Backfill, (b) Clean Sand, and (c) Silty Sand.

3.3.2 Lemnitzer *et. al.* (2009)

Stewart *et al.* (2007) performed a full-scale cyclic lateral load test of an abutment backwall with dimensions 2.6 m (height) by 4.5 m (width) by 0.9 m (thick) at the University of California, Los Angeles (UCLA). A well-graded sand with silt (SW-SM) as per unified soil classification, compacted to 96% is used as the backfill soil in the test. The plan and cross-section view of the test setup are shown in Figure 3.6. Five hydraulic actuators in horizontal and diagonal configurations between the backwall and the reaction block are used to apply the controlled backwall displacement in the horizontal direction. Triaxial compression tests were performed on the backfill soil specimens. The failure envelopes were constructed using the deviatoric stress-axial strain curves and the MC strength parameters were obtained and are given in Table 3.4.

The FE simulation of the UCLA test is performed in the present study using the MC constitutive model to simulate the behaviour of the backfill soil and the abutment backwall is modelled as a linear elastic one. The FE domain is discretised using 8-node linear brick elements with full integration (C3D8) and the entire mesh consists of 3,040 elements as shown in Figure 3.7(a). Standard boundary conditions are applied, with fixed support at the bottom and roller support on the sides as shown in Figure 3.7(a).

Table 3.4 Summary of material properties used for FE simulation (data sourced from Lemnitzer *et al.*, 2009).

| Material | Bulk Unit Weight, γ (kN/m ³) | Cohesion, c (kPa) | Friction Angle, ϕ (°) | Interface Friction Angle, δ (°) | Young's Modulus, E (MPa) | Poisson's Ratio, ν |
|---------------------|---|---------------------|----------------------------|--|----------------------------|------------------------|
| Silty sand | 19.81 | 14 | 39 | 14 | 43.1 | 0.30 |
| | | 24 | 40 | | | |
| Reinforced concrete | 24.00 | - | - | - | 31000 | 0.20 |

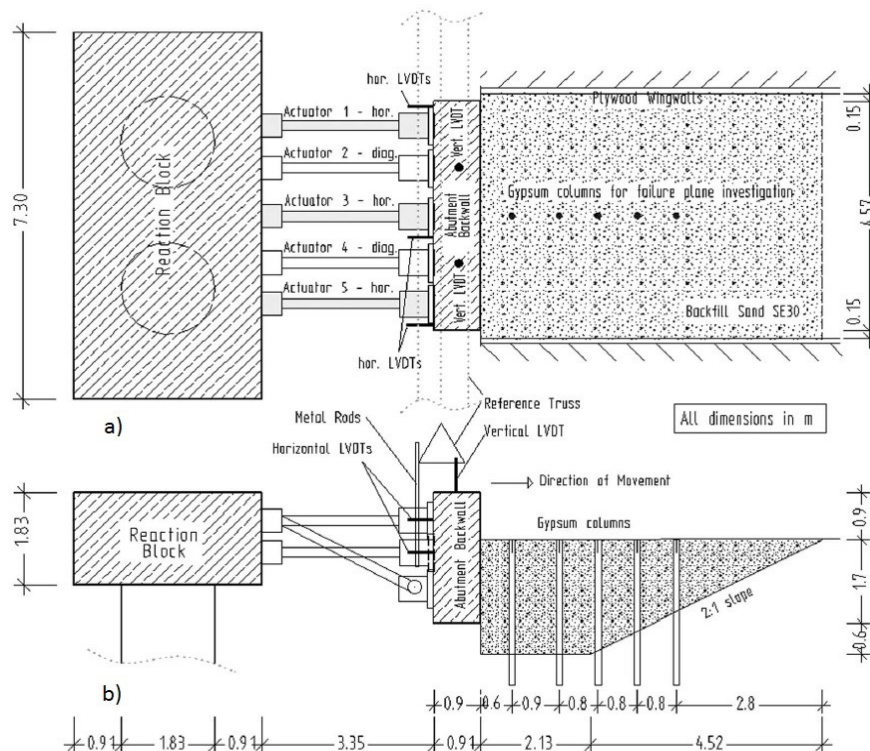


Fig. 3.6 (a) Plan, and (b) Cross-Section View of the UCLA Test Setup (Lemnitzer *et al.*, 2009).

The deformed shape of FE domain of the backfill after the completion of the lateral load simulation is shown in Figure 3.7(b). The comparison of passive force-displacement relationships obtained by FE simulation and the UCLA test data is shown in Figure 3.8.

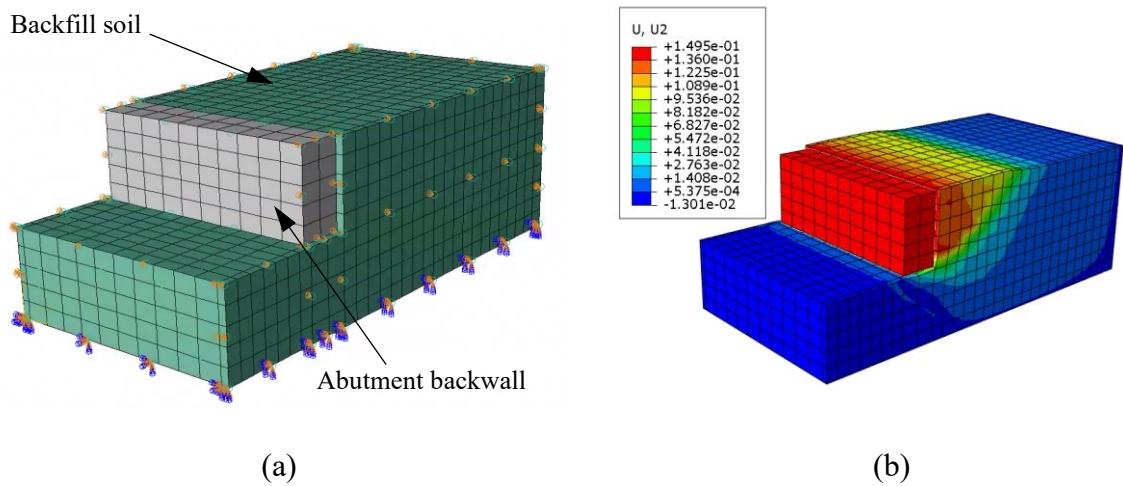


Fig. 3.7 (a) 3D FE Domain with Discretised Mesh and Boundary Conditions, and (b) Deformed Shape of Backfill after Completion of Simulation.

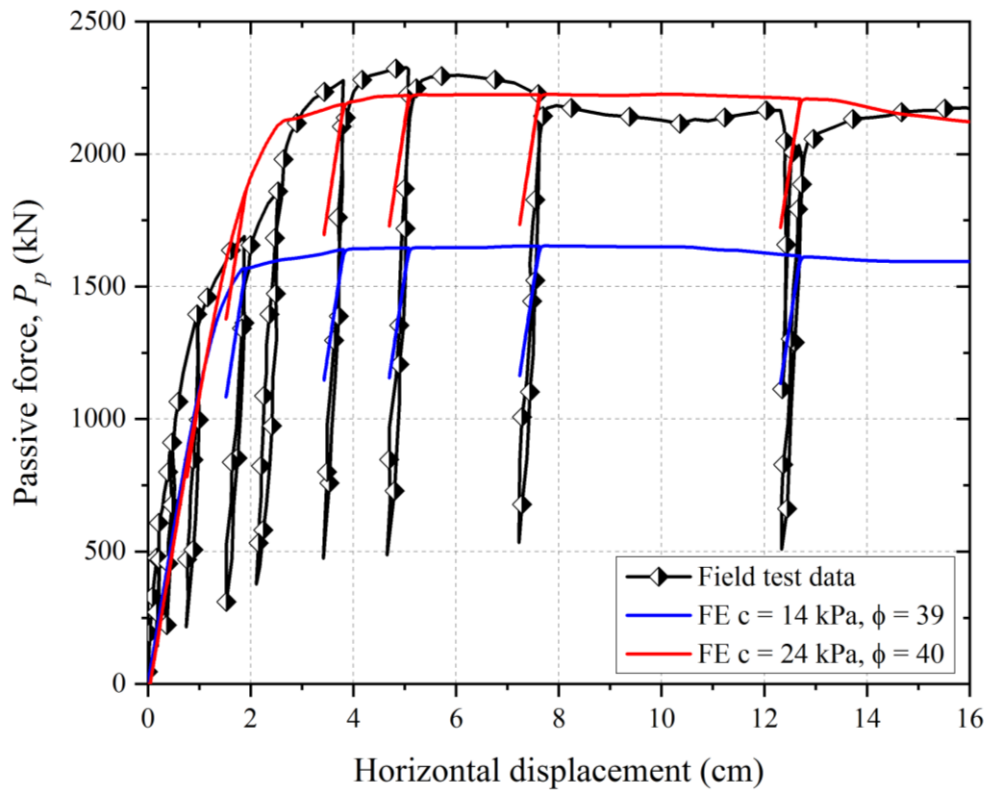


Fig. 3.8 Comparison of Passive Force-Displacement Relationships of FE Results and Field Data.

The two sets of shear strength parameters of the soil are used in the FE simulations, out of which one with a cohesion of 24 kPa and friction angle of 40° provided a good match with respect to the peak passive capacity and initial stiffness.

The 2D and 3D FE simulations of the UCLA test are carried out using the Toyoura and Karlsruhe sands as the backfill soil. The hypoplastic sand constitutive model is used to model the backfill soil. The hypoplastic soil parameters of the Karlsruhe and Toyoura sands are given in Tables 3.1 and 3.2, respectively. The passive force-displacement relationships are obtained using the FE simulation for the Toyoura and Karlsruhe sands and are compared with the UCLA test data as shown in Figures 3.9 and 3.10. The FE results have shown a reasonable agreement with the field data. The basic hypoplastic model for the backfill can provide a reasonable match with the peak passive force of the field data. The 2D FE simulation of the UCLA test reduces the computation time in predicting the behaviour of the integral abutment-pile-backfill system. Hence, it is concluded that for the analysis of IABs, the 2D FE simulations are reliable, therefore in the present study, the response assessment of the IABs is performed using the 2D FE analysis under static, cyclic and thermal loadings.

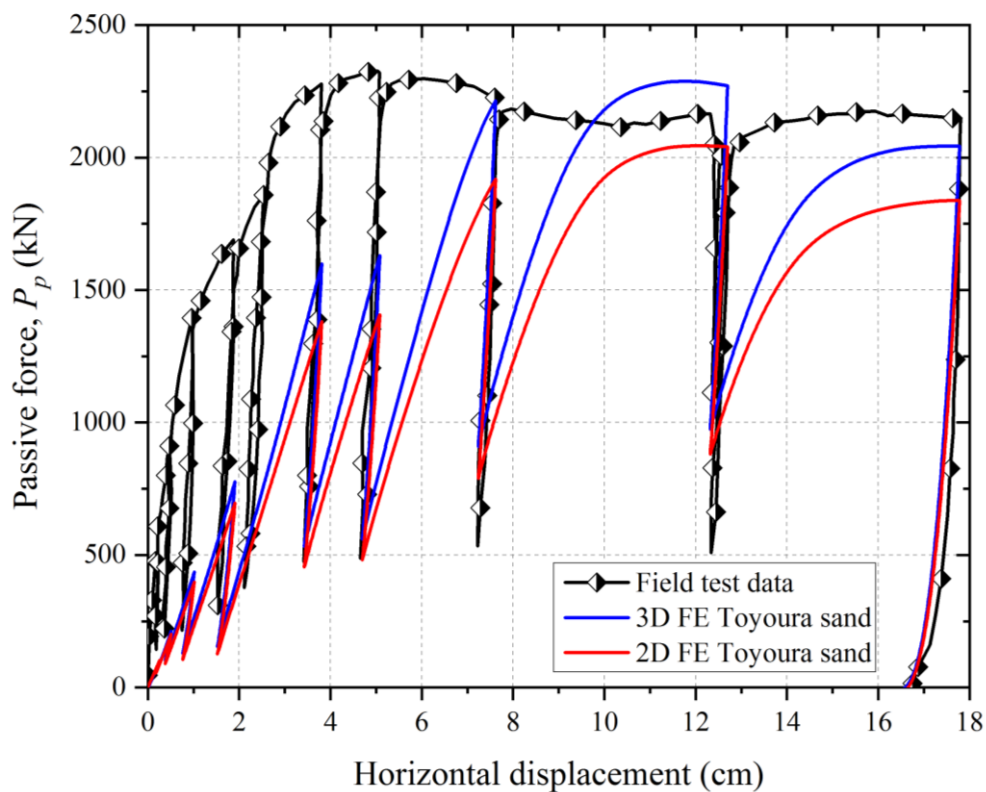


Fig. 3.9 Comparison of 2D and 3D FE Simulation Results of Toyoura Sand for Passive Force-Displacement with UCLA Test Data.

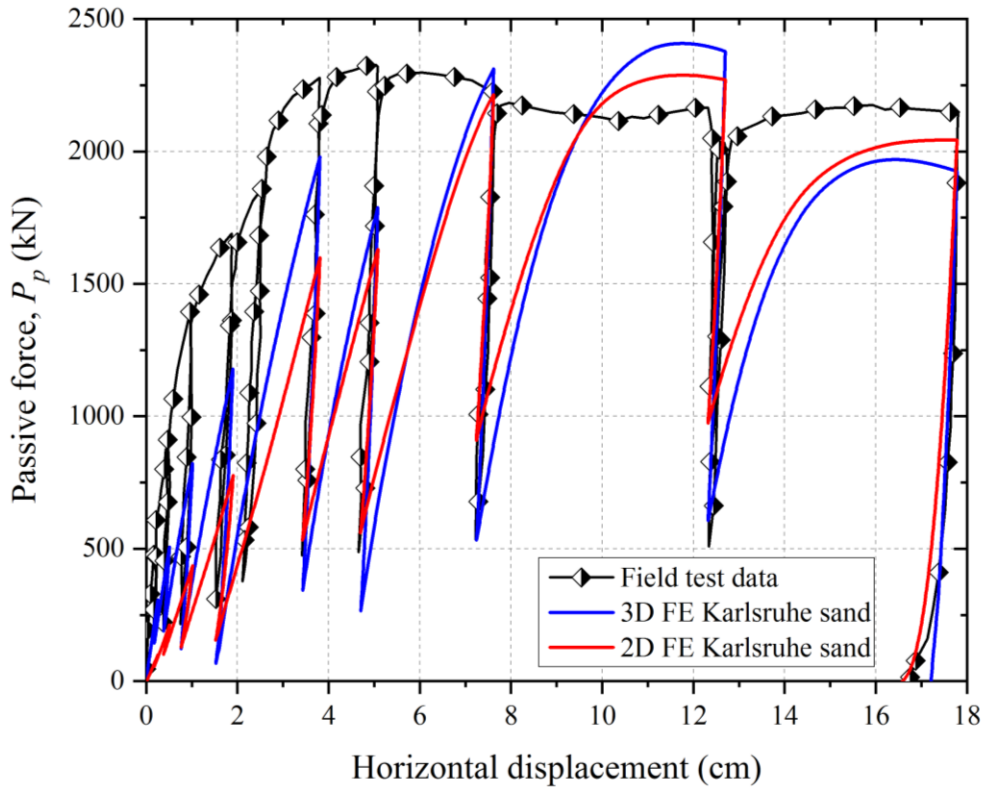


Fig. 3.10 Comparison of 2D and 3D FE Simulation Results of Karlsruhe Sand for Passive Force-Displacement with UCLA Test Data.

3.4 FINITE ELEMENT MODELLING OF IAB

In the present study, the IAB with an approach slab is modelled using FE based program ABAQUS. Figure 3.11 shows the two-dimensional (2D) plane-strain FE model of the single span pile-supported IAB and the same is used in the simulations. The geometry and dimensions of the various components of the pile-supported IAB on the rock are selected based on the Middlesex bridge located at Vermont, United States from the published data (Kalayci, 2012). A single-span, integral abutment bridge having a span of 43 m length and an approach slab of length = 6 m and thickness of 380 mm is adopted in the present study. The steel H-pile is modelled as having a thickness of 0.3 m and a length of 12 m, and the pile is socketed in the bedrock for a depth of one meter. The IAB has a deck slab of thickness = 220 mm, steel girder has a depth of 1.25 m. The integral abutment height of 4 m is chosen with a thickness of 1 m. Behind the integral abutment, the backfill soil has a depth of 4.5 m and a length of 60 m. The foundation soil of 11.5 m and bedrock of 30 m in depths are used. The material properties adopted in the study are given in Tables 3.5 and 3.6. The backfill soil behaviour is simulated using the hypoplastic constitutive model. The behaviour of foundation soil and rock is

simulated using the Mohr-Coulomb model. The integral abutment, approach slab, steel H-Pile, and deck and girder are modelled as linear elastic in the simulations.

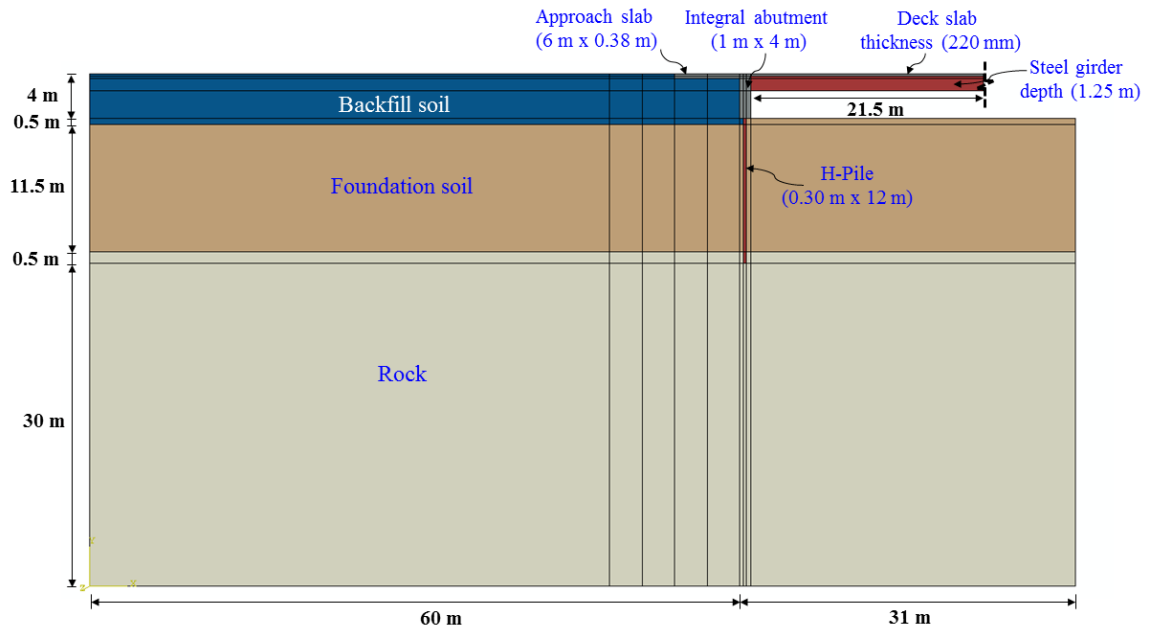


Fig. 3.11 Schematic Representation of Pile-Supported Integral Abutment Bridge.

Table 3.5 Material properties used in FE simulation (data sourced from ¹Al-Qarawi *et al.*, 2020; ²Gadicherla *et al.*, 2022).

| Component | Material Model | Density, ρ (kg/m ³) | Young's Modulus, E (MPa) | Poisson's Ratio, ν | Friction Angle, ϕ' (°) | Dilation Angle, ψ (°) | Cohesion, c' (kPa) |
|--|----------------|--------------------------------------|----------------------------|------------------------|-----------------------------|----------------------------|----------------------|
| Foundation soil ¹ | MC | 1,682 | 30 | 0.3 | 20 | 1 | 20 |
| Backfill soil | Hypoplastic | 1,835 | - | - | - | - | - |
| Rock ² | MC | 2,100 | 720 | 0.35 | 21 | 1 | 115 |
| Integral abutment, deck and approach slab (reinforced concrete) ¹ | LE | 2,385 | 30,000 | 0.25 | - | - | - |
| HP pile (steel) ¹ | LE | 7,951 | 200,000 | 0.3 | - | - | - |

Table 3.6 Hypoplastic soil parameters of Toyoura sand as backfill (Herle and Gudehus, 1999).

| ϕ_c (°) | h_s (MPa) | n | e_{d0} | e_{c0} | e_{i0} | α | β |
|--------------|-------------|------|----------|----------|----------|----------|---------|
| 30 | 2600 | 0.27 | 0.61 | 0.98 | 1.1 | 0.14 | 3 |

The soil-structure interaction between the integral abutment-backfill soil, pile-foundation soil, and approach slab-backfill soil is simulated using the Coulomb friction model available in ABAQUS. The normal and tangential contact behaviours are simulated using the surface-to-surface interaction by employing the master-slave concept. The normal contact behaviour is simulated as ‘*hard contact*’ in which the normal stresses are transferred under compression. The tangential contact is simulated using a penalty friction algorithm available in ABAQUS.

The 2D plane-strain FE model of the IAB is discretised using a 4-noded bilinear plane-strain element with full integration (CPE4), as shown in Figure 3.12. The entire FE model consists of 16,651 elements with an average size of each element = 0.5 m. The standard boundary conditions are adopted in which the fixed conditions are along the bottom boundary and the roller supports are at the sides of the FE domain. The mesh sensitivity studies are also performed with different mesh sizes. The FE domain adopted in the present study has provided the stable results for the adopted boundary conditions. Various approaches to transform 3D problem to 2D are equivalent area, equivalent flexural stiffness, and equivalent elastic modulus (Meena *et al.*, 2020). In this study, the 2D FE analysis with equivalent elastic modulus is preferred over the 3D analysis to limit the required computational time, however, the 2D analysis has provided reasonably accurate results. There are some limitations associated with the 2D modelling approach such as, inability to realistically simulate the pile supported integral abutment with approach slab. The 2D models with plane-strain elements will simulate the behaviour of integral abutment and approach slab properly. However, the plane-strain elements used for the pile provide reasonably good results in comparison with the beam elements (Ooi *et al.*, 2010).

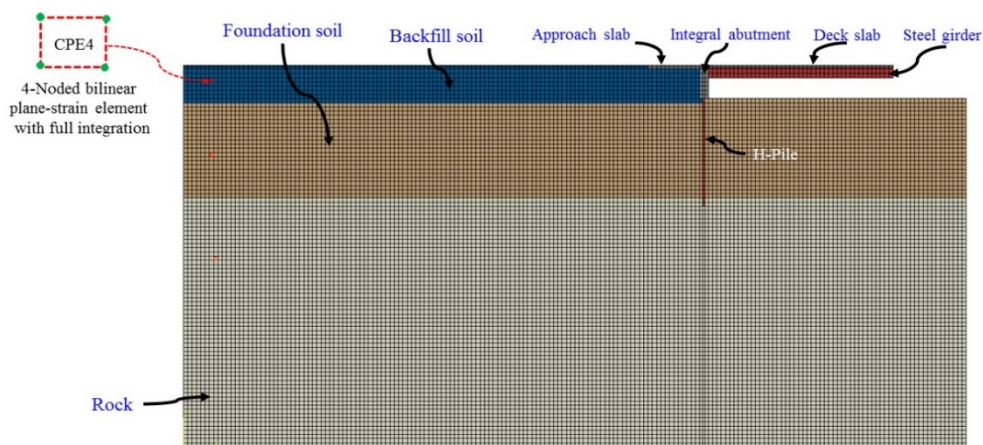


Fig. 3.12 Schematic Representation FE Mesh of the Pile-Supported IAB.

3.5 RESPONSE OF IAB UNDER STATIC LATERAL TRANSLATION LOADING

In the present study, the lateral translation displacement is applied to the 2D FE model of the IAB at the top of the integral abutment to the entire depth of the girder including the deck slab (a total depth = 1.45 m). Then the FE simulations are performed. In the next case, a 2D FE model of the abutment backwall system is considered like the one adopted in the UCLA test (See in Figure 3.13) and is subjected to pure translation and pure rotation independently and accordingly the simulations are performed. The behaviour of the abutment backwall is compared with the pile-supported IAB with and without the approach slab subjected to the lateral translation loading at the top of the abutment. The lateral translation displacement of 0.3 m towards the backfill is applied for the case of abutment backwall system and pile-supported integral abutment system. In both the cases, the backfill soil type considered is the Toyoura sand with medium density. The material parameters used for the 2D FE model of the pile-supported integral abutment system are given in Table 3.5. The behaviour of the Toyoura sand is simulated using the hypoplastic sand constitutive model and the corresponding parameters are given in Table 3.6.

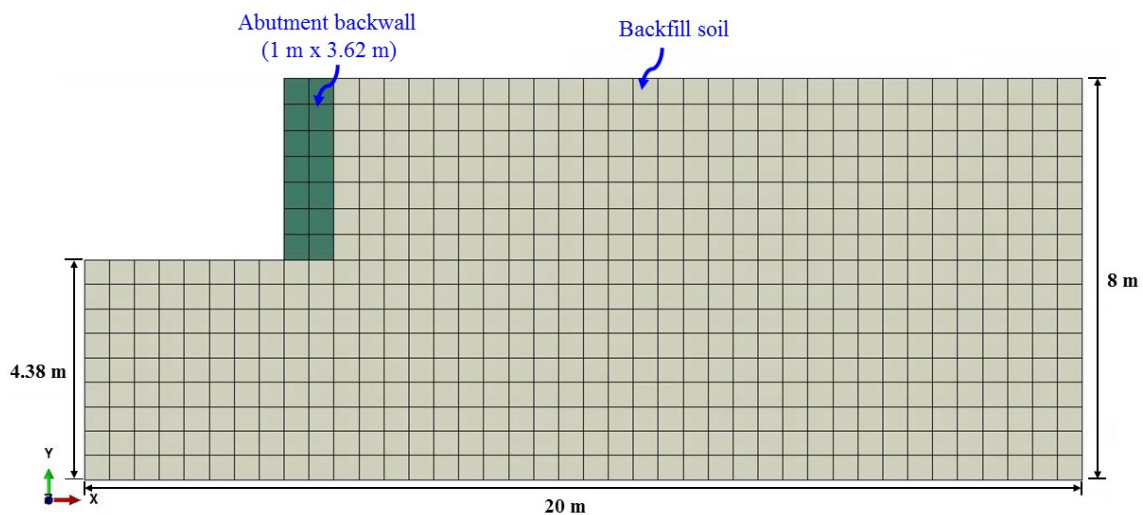


Fig. 3.13 Schematic of Geometry and 2D FE Mesh of Abutment Backwall with Backfill Soil.

Figure 3.14 shows the comparison of the passive force-displacement relationships for the pile-supported integral abutment with and without approach slab subjected to lateral translation at the top of the abutment and the abutment backwall subjected to pure

translation and rotation separately. The behaviour of the pile-supported integral abutment with approach slab is found to be in line with the case of pure translation behaviour of the abutment backwall. The magnitude of the passive force at the end of 0.3 m displacement is found to be higher for the integral abutment with approach slab when compared to the integral abutment without approach slab and the abutment backwall. The pure rotational behaviour of the abutment backwall has developed the least passive force-displacement response. The soil pressure variation behind the pile-supported integral abutment and the abutment backwall is shown in Figure 3.15.

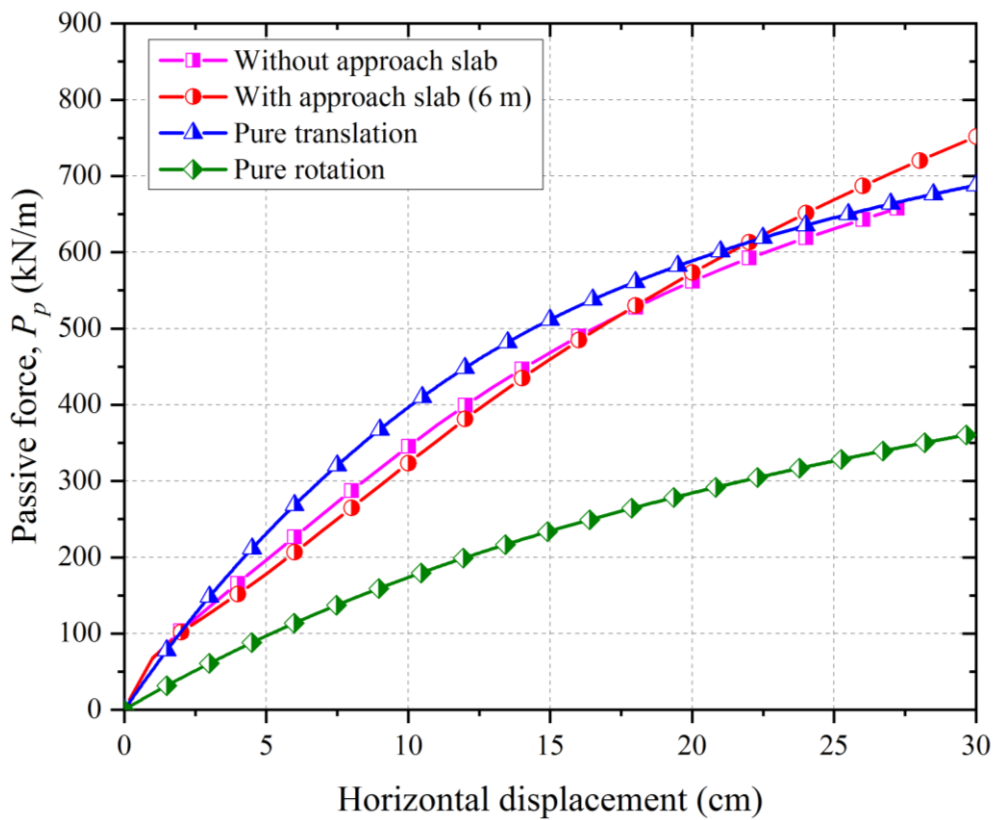


Fig. 3.14 Passive Force-Displacement Relationship for Pile-Supported Integral Abutment with and without Approach Slab and Abutment Backwall.

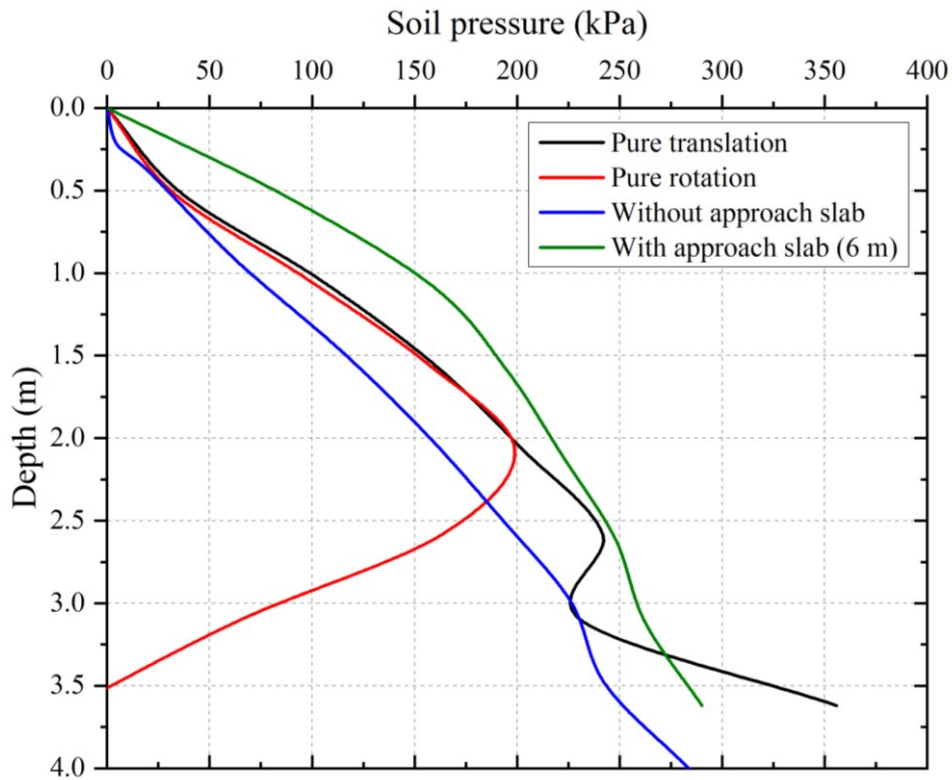


Fig. 3.15 Variation of Passive Pressure with Depth behind the Integral Abutment and Abutment Backwall.

The variation of passive pressure behind the pile-supported integral abutment under static translation at the top of the abutment is in line with the abutment backwall subjected to pure translation. The variation of passive pressure from the top to the middle of the integral abutment is observed to be higher for the integral abutment with the approach slab than the integral abutment without the approach slab and the abutment backwall. However, the variation of passive pressure at the bottom of the integral abutment also depends on the foundation soil stiffness and the distance of closer vicinity to the bottom of the integral abutment. Further, the parametric studies are carried out by varying the length of the approach slab, backfill soil type, and foundation soil stiffness and the results are presented below.

3.5.1 Length of the Approach Slab

The length of the approach slab is considered as 3 m, 6 m, and 9 m. The effect of varying length of the approach slab on the passive force-displacement relationship for the pile-supported integral abutment is evaluated and depicted in Figure 3.16. The variation in the length of the approach slab is found to have the least effect on the passive force-displacement relationships. The pushover analysis is performed on the pile-supported

integral abutment for varying length of the approach slab, and it is noted that the backfill soil is found to experience a considerable heave or the upward vertical displacement behind the abutment as shown in Figure 3.17. For the applied lateral translation, it is observed that the abutment without the approach slab has generated a backfill soil heave just behind the integral abutment. With the presence of the approach slab, the heave is developed at the end of the approach slab in the backfill. The magnitude of the backfill soil heave developed for the integral abutment with the approach slab is higher than that for the integral abutment without the approach slab. The magnitude of the backfill soil heave is found to increase with the increase in the length of the approach slab at the end tip of the approach slab.

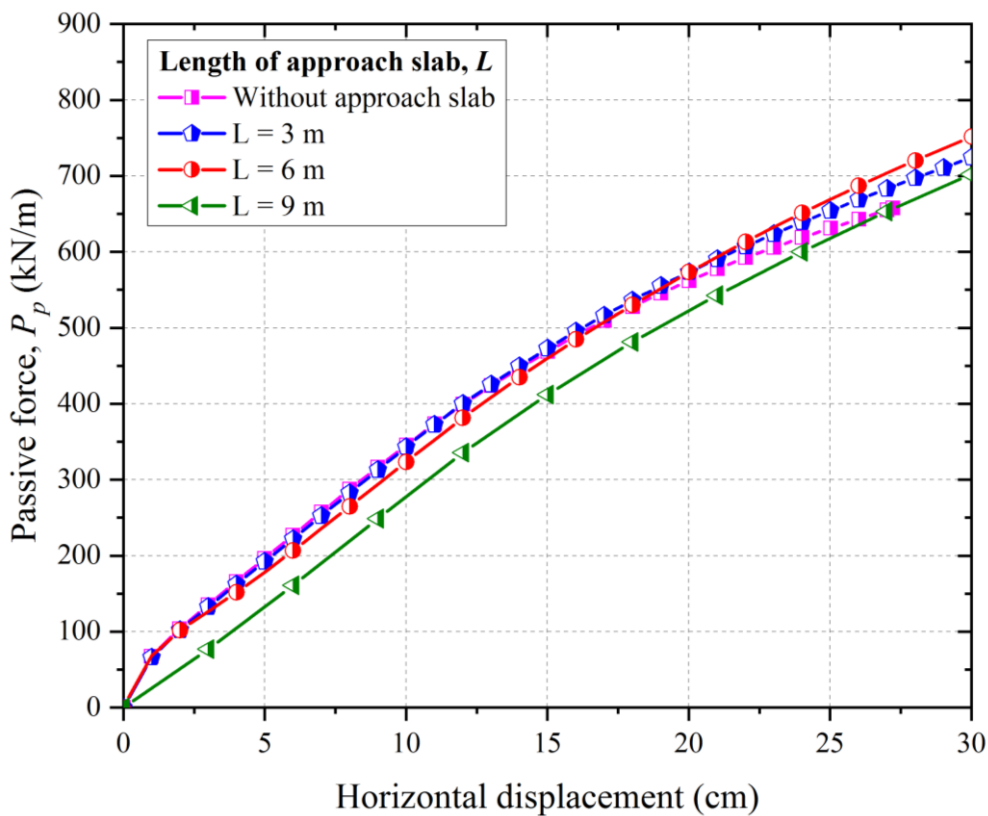


Fig. 3.16 Passive Force-Displacement Relationship for Pile-Supported Integral Abutment for varying Length of Approach Slab.

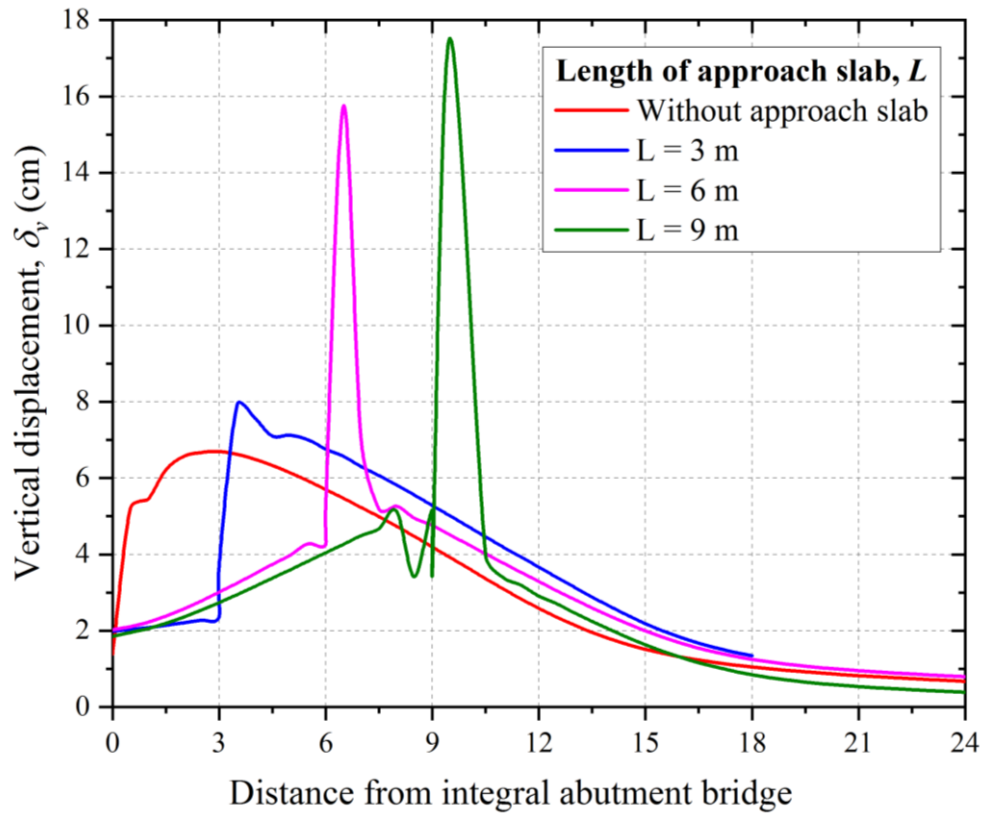


Fig. 3.17 Vertical Settlement Profile of Backfill Soil from the Pile-Supported Integral Abutment for varying Length of Approach Slab.

3.5.2 Backfill Soil Type

The effect of backfill soil type variation such as loose, medium, and dense conditions are simulated considering the different void ratios for the Toyoura sand in FE analysis. The initial densities considered for the loose, medium, and dense sands are expressed in terms of void ratios respectively as 0.980, 0.831 and 0.65. The corresponding relative densities are 24.48%, 54.9% and 91.8%. The effect of using different backfill soils on the passive force-displacement relationships for the pile-supported integral abutment is depicted in Figure 3.18. It is observed from the figure that with increase in the relative density of the backfill soil, the passive force increases. It is noted that the highest and lowest passive forces are generated for the cases of dense and loose sands, respectively.

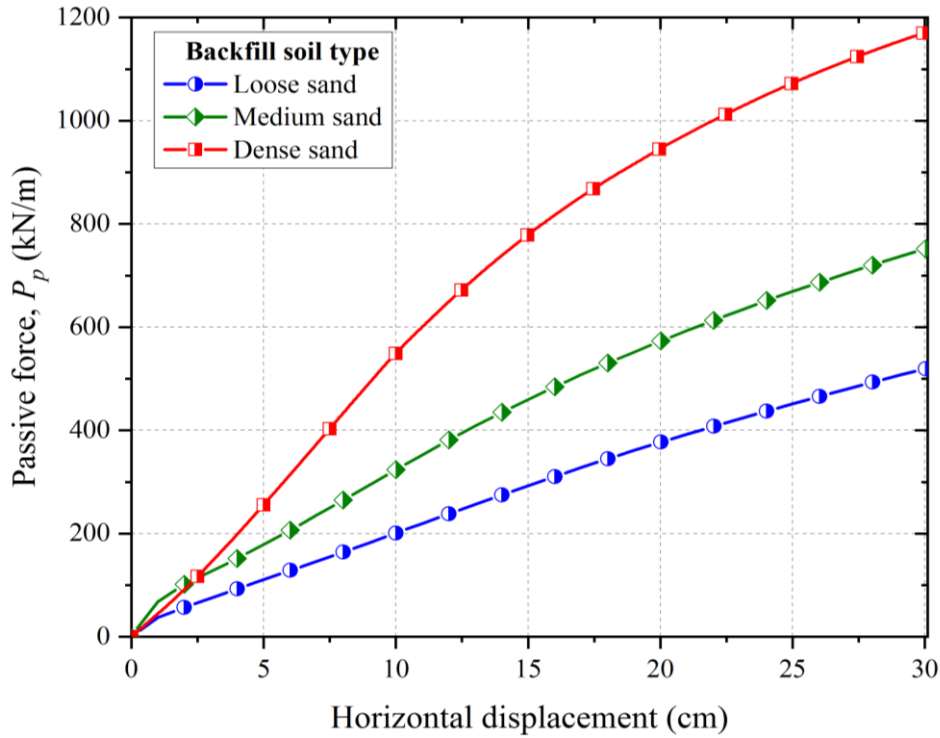


Fig. 3.18 Passive Force-Displacement Relationship for Pile-Supported Integral Abutment for different Backfill Soil Type.

3.5.3 Foundation Soil Stiffness

The effect of varying foundation soil stiffness such as soft clay, medium stiff clay and stiff clay is considered and accordingly the FE simulations are performed. The backfill soil type considered in the simulation is the Toyoura medium sand. The material properties of the foundation soil considered in the FE simulation are given in Table 3.7. The effect of varying foundation soil stiffness on the passive force-displacement relationships for the pile-supported integral abutment is evaluated and is depicted in Figure 3.19. It is observed from the figure that the variation in the foundation soil stiffness has a negligible influence on the passive force-displacement relationship. Similar observations have also been made by Khasawneh (2014).

Table 3.7 Material properties of foundation soils used in FE simulation.

| Foundation Soil | Material Model | Density, ρ (kg/m ³) | Young's Modulus, E (MPa) | Poisson's Ratio, ν | Friction Angle, ϕ' (°) | Dilation Angle, ψ (°) | Cohesion, c' (kPa) |
|-------------------|----------------|--------------------------------------|----------------------------|------------------------|-----------------------------|----------------------------|----------------------|
| Soft clay | MC | 1,682 | 30 | 0.3 | 20 | 1 | 20 |
| Medium stiff clay | MC | 1800 | 45 | 0.3 | 28 | 1 | 48 |
| Stiff clay | MC | 2030 | 70 | 0.3 | 35 | 5 | 100 |

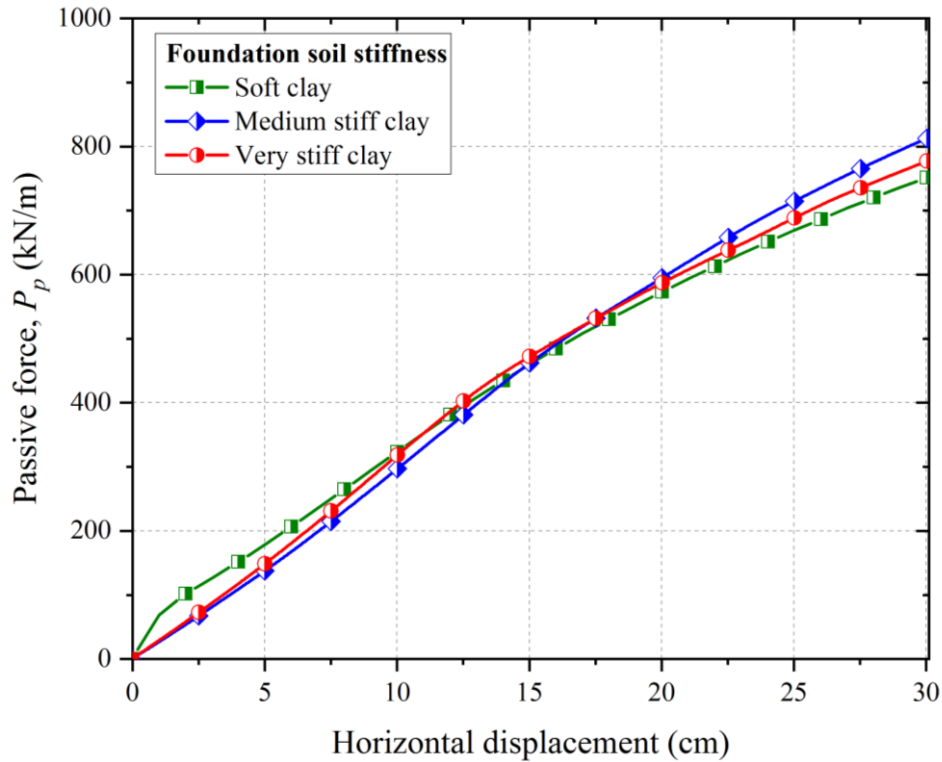


Fig. 3.19 Passive Force-Displacement Relationship for Pile-Supported Integral Abutment for Different Foundation Soil Stiffness.

3.6 RESPONSE OF IAB UNDER THERMAL AND CYCLIC LOADINGS

The IAB actively undergoes expansion and contraction under seasonal temperature variations. The lateral displacement induced by the thermally induced loading can be obtained by the field monitoring of IABs. These lateral displacements of the bridge superstructure are transferred to the soil surrounding the bridge substructure such as the abutments and piles. The resistance developed by the soil such as the passive pressure in turn generates the stresses in the bridge superstructure. To predict the nonlinear behaviour of the integral abutment-pile-backfill system under the cyclic thermal loading, the FE analyses are needed which also incorporate the SSI effects. The abutment displacement (δ) is evaluated for simple expansion and contraction of the deck and girder due to temperature variation by following the equation:

$$\delta = \alpha L \Delta T \quad (3.1)$$

where α = coefficient of thermal expansion for the deck and girder, L = length of the bridge span and ΔT = temperature variation from the reference temperature value present during the construction.

3.6.1 FE Simulation of Cyclic Thermal Loading

In the present study, the values of coefficients of thermal expansion adopted for the reinforced concrete deck and steel girder are $9 \times 10^{-6}/^{\circ}\text{C}$ and $13 \times 10^{-6}/^{\circ}\text{C}$, respectively. Half of the bridge span length is taken into consideration in the FE model of the bridge span adopting symmetry boundary condition. The temperature fluctuation induced by the cyclic thermal loading is calculated using Equation 3.2 (Kim and Laman, 2010; 2012). The cyclic thermal loading in the FE model is applied as a sinusoidal temperature variation:

$$T(t) = T_m + A \sin(\omega t + \phi) \quad (3.2)$$

where T_m = annual mean temperature, A = annual temperature amplitude, ω = frequency (2π , cyclic frequency is 1 Hz), t = analysis time (year) and ϕ = phase lag. A total of two temperature variations are considered in the study using Equation 3.2. The first temperature variation adopted in the FE simulation is as per Kim and Laman (2010). They reported the temperature variation for Bridge No. 203 and the same is used in the study. The maximum, minimum and reference temperatures given for Bridge No. 203 are 24.2, -9.2 and 7.5 °C, respectively. The second temperature variation considered in the study is as per Civjan *et al.* (2013). Equation 3.2 is used to generate the temperature variation matching with the field monitoring data of East Montpelier bridge. The maximum, minimum and reference temperatures used for East Montpelier bridge are 34.1, -20.5 and 7.8 °C, respectively. The cyclic thermal loading for 5 years is generated from Equation 3.2 and is depicted in Figure 3.20. The generated cyclic thermal loadings are applied to the deck and steel girder in the 2D FE model of the IAB. The backfill soil considered is the Toyoura sand and is modelled using the hypoplastic sand model. Two relative densities (54.9% and 91.8%) are considered for the backfill soil and the corresponding void ratios are 0.831 and 0.65, which represent respectively the medium and dense sands. The occurrence soil ratcheting phenomenon is also investigated through FE simulations.

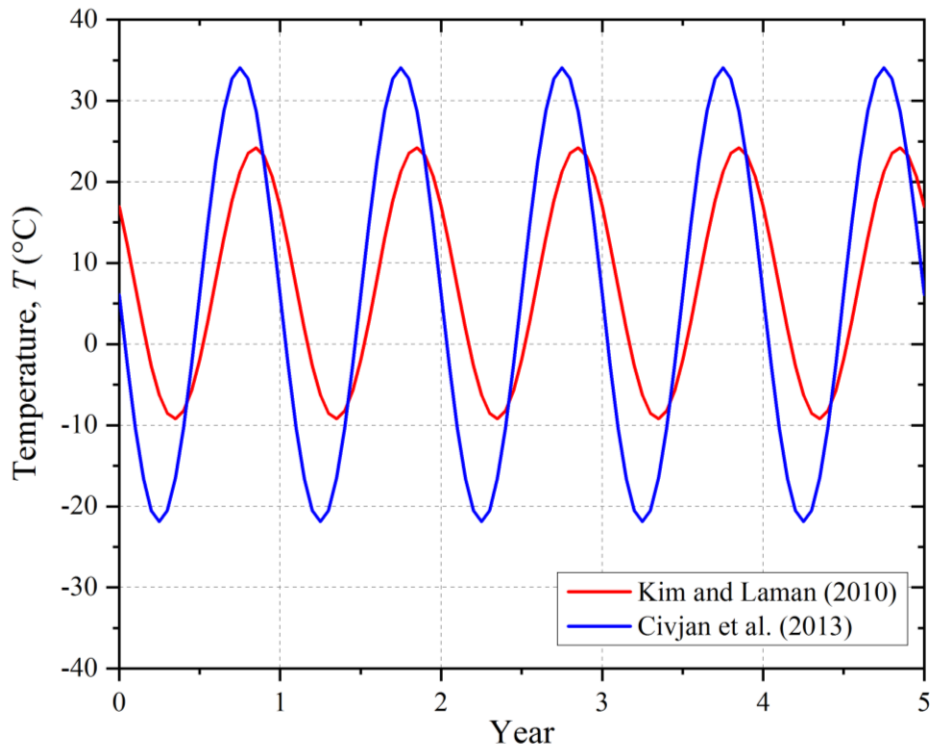


Fig. 3.20 Variation of Temperature Loading Considered in FE Simulation.

3.6.1.1 Results and discussion

In the 2D FE model of the pile-supported integral abutment bridge, the temperature variation is applied to the deck and girder. The change in temperature from the reference temperature will induce the longitudinal expansion and contraction movement through the integral abutment. The monolithic connection of the integral abutment with the deck and girder will induce the horizontal displacements at the top of the abutment and bottom of the abutment as shown in Figures 3.21 and 3.22 for the two considered temperature variations. From the figures it is observed that the changes in the temperature of about 16.7 °C and 26.3 °C from the reference temperature have induced the sinusoidal longitudinal displacements at the top of the abutment having peak value of 6.11 mm and 10.88 mm, respectively. The difference between the longitudinal displacements at the top and bottom of the integral abutment is approximately 1 mm, which is very marginal. These induced displacements have generated the soil pressure in the backfill soil.

The variation of soil pressure at the bottom of the integral abutment for 5 years of cyclic thermal loading is shown in Figures 3.23 and 3.24. The figures also depict the variation of soil pressure for the two types of backfill soils considered in the study. The variation

of total passive force behind the integral abutment for the medium and dense sands is depicted in Figures 3.25 and 3.26 for 5 years of cyclic thermal loading.

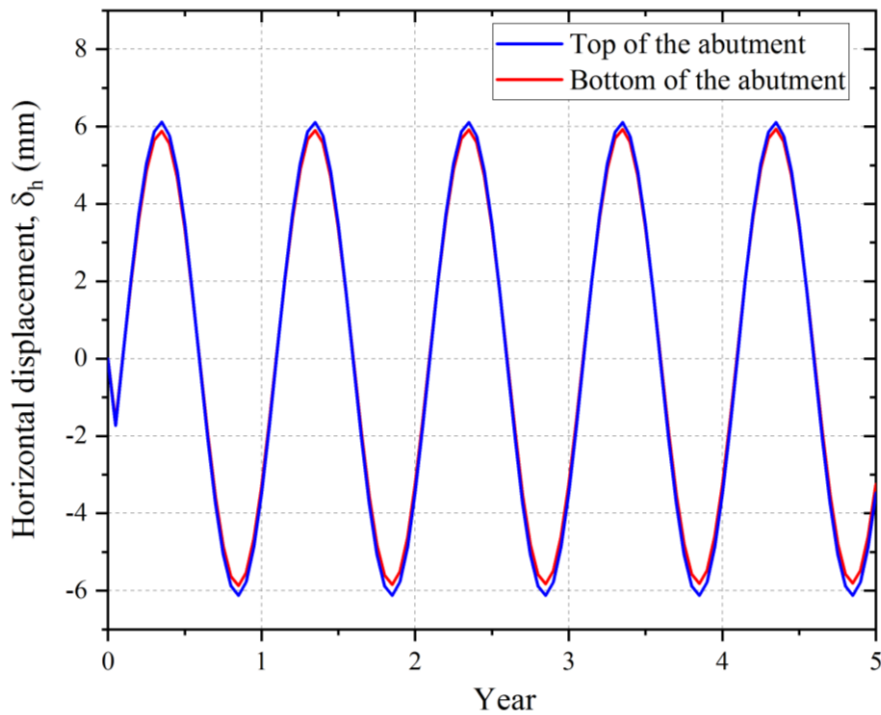


Fig. 3.21 Horizontal Displacement of Integral Abutment at Top and Bottom for Kim and Laman (2010) Temperature Loading.

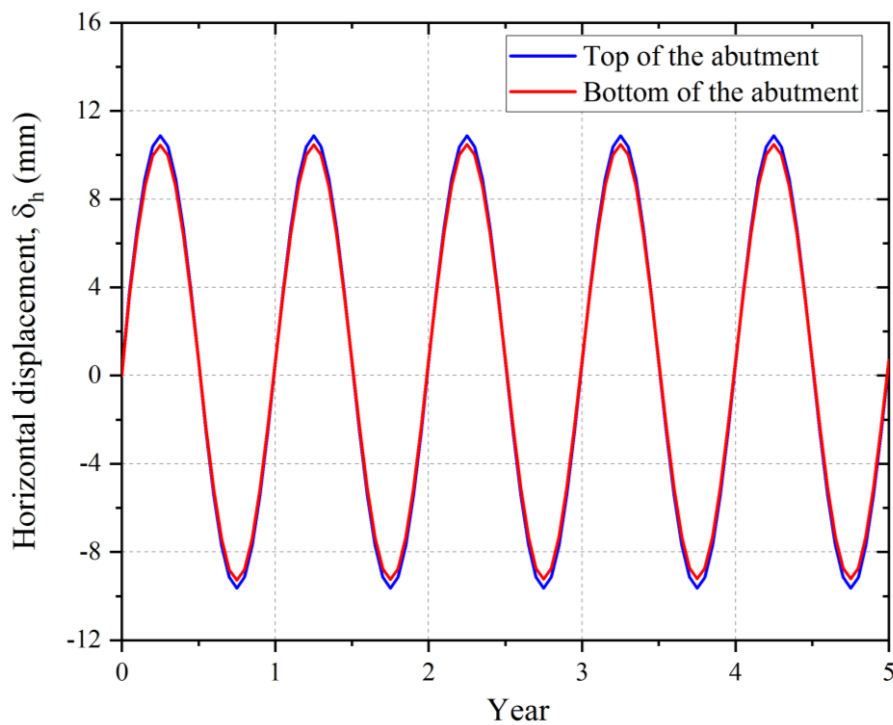


Fig. 3.22 Horizontal Displacement of Integral Abutment at Top and Bottom for Civjan *et al.* (2013) Temperature Loading.

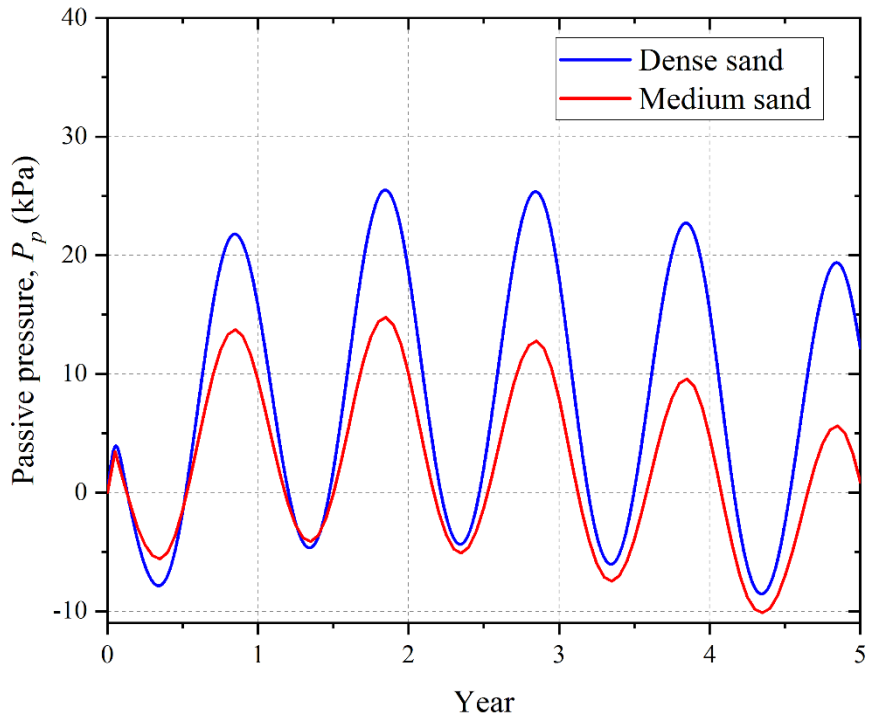


Fig. 3.23 Variation of Soil Pressure for Medium and Dense Sands for 5 Years of Kim and Laman (2010) Temperature Loading.

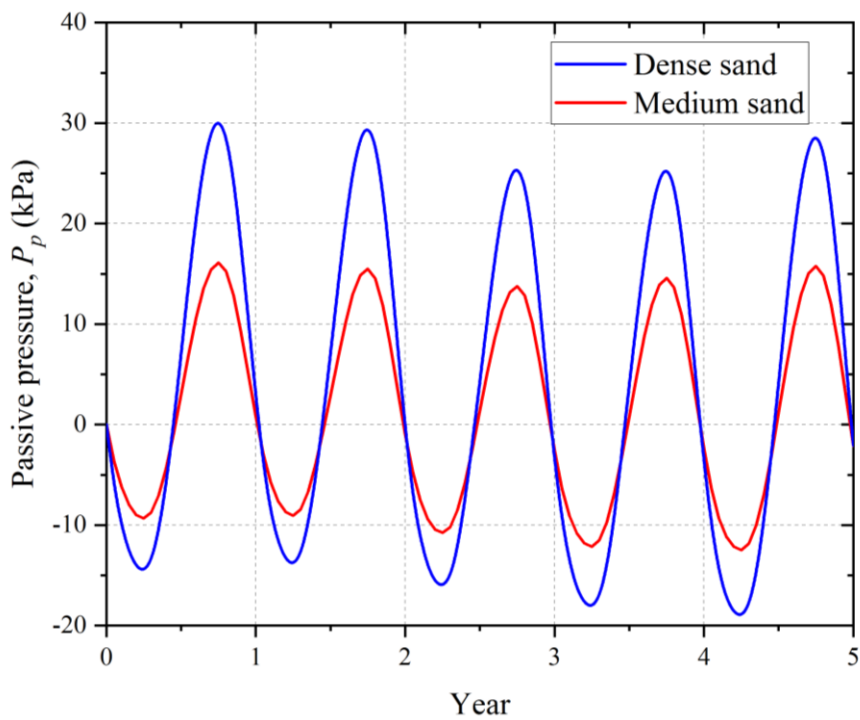


Fig. 3.24 Variation of Soil Pressure for Medium and Dense Sands for 5 Years of Civjan *et al.* (2013) Temperature Loading.

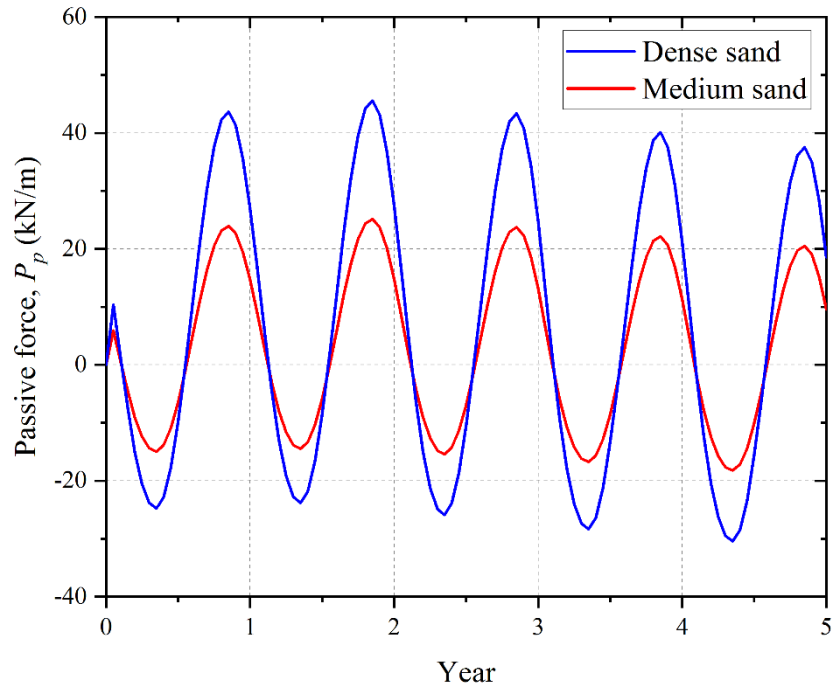


Fig. 3.25 Variation of Passive Force for Medium and Dense Sands for 5 Years of Kim and Laman (2010) Temperature Loading.

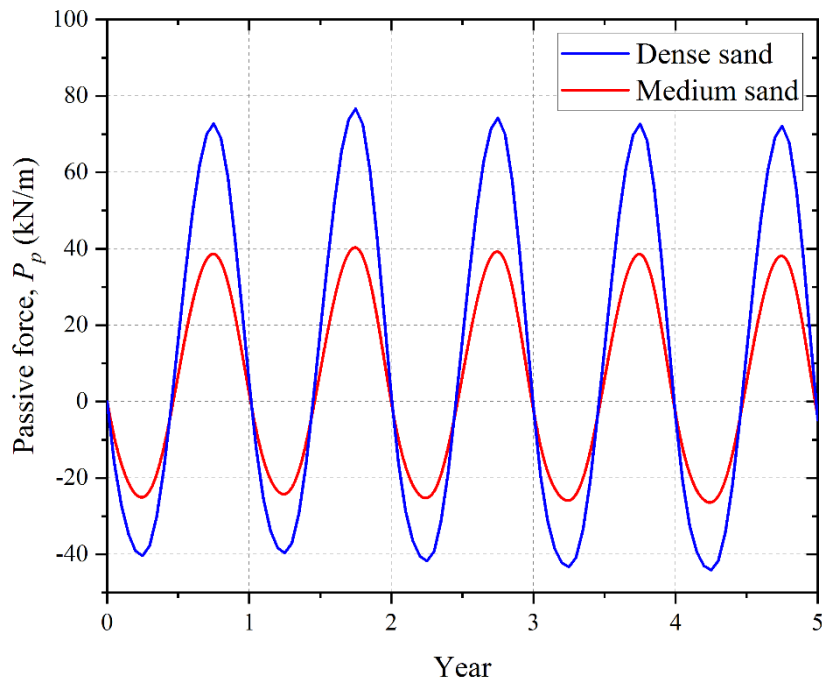
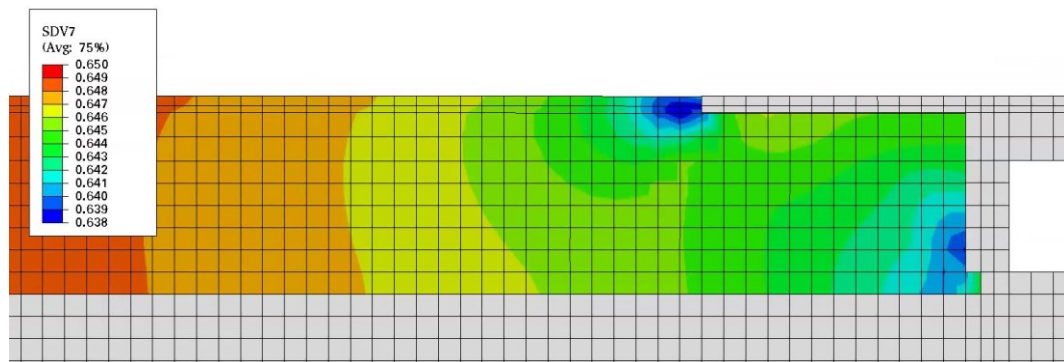


Fig. 3.26 Variation of Passive Force for Medium and Dense Sands for 5 Years of Civjan *et al.* (2013) Temperature Loading.

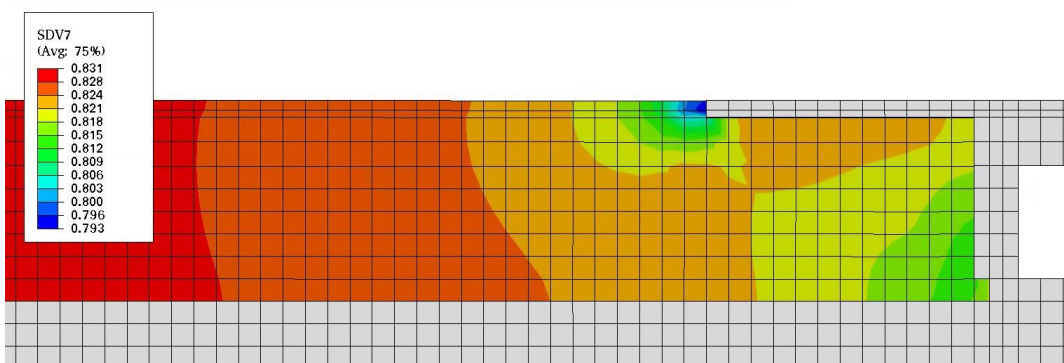
The soil ratcheting phenomenon has not been observed for the cyclic thermal loading cases given by Kim and Laman (2010) and Civjan *et al.* (2013). The soil pressures and passive forces are found to be constant throughout the 5 years of duration. A significant

increase of soil pressure is not observed, although slight variations are observed. It is seen that the simulation of cyclic thermal loading has generated constant longitudinal displacement over the 5-year period, however it has induced a significant settlement in the backfill. The backfill soil is found to readjust and compact with the increase in the number of cycles of the longitudinal displacement.

After 5 years of simulation studies, the deformed mesh and variation of void ratios across the backfill soil for Kim and Laman (2010) and Civjan *et al.* (2013) temperature loadings are shown in Figures 3.27 and 3.28, respectively. From the figures, it is observed that the compaction of the backfill is significant near the integral abutment and at the interface of the approach slab tip and backfill soil. It is seen the backfill soil is densified more near the bottom of the integral abutment and interface between the backfill soil and tip of the approach slab. Far away from the integral abutment, the variation in the void ratio is found to be the least. The densification of backfill soil is predominant in the case of medium sand. The foundation soil stiffness is found to have a significant influence on the densification of the backfill soil.



(a)



(b)

Fig. 3.27 Deformed Mesh of Backfill Soil and Variation of Void Ratio for (a) Dense Sand, and (b) Medium Sand after 5 Years of Simulation for Kim and Laman (2010) Temperature Loading.

The variation of backfill soil settlement with the number of cycles of cyclic thermal loading is studied using FE simulations. Figure 3.29 shows the vertical settlement of the backfill soil at three different points i.e., Point A, Point B and Point C for 5 years of temperature loading of Kim and Laman (2010). The figure has provided the results for both the medium and dense sands for the simulation period.

Figure 3.30 depicts the variation of vertical settlement profile of the backfill soil behind the abutment for the temperature loading of Kim and Laman (2010). In the figure, the settlements of the backfill are evaluated along the red marked line on the approach slab and on the backfill. The figure shows the backfill soil settlement occurred below the approach slab, at the interface of the backfill and approach slab and further away from the approach slab.

Similarly, Figure 3.31 shows the vertical settlement of the backfill soil at three different points for 5 years of temperature loading of Civjan *et al.* (2013). Figure 3.32 depicts the variation of vertical settlement profile of the backfill soil behind the abutment for the temperature loading of Civjan *et al.* (2013).

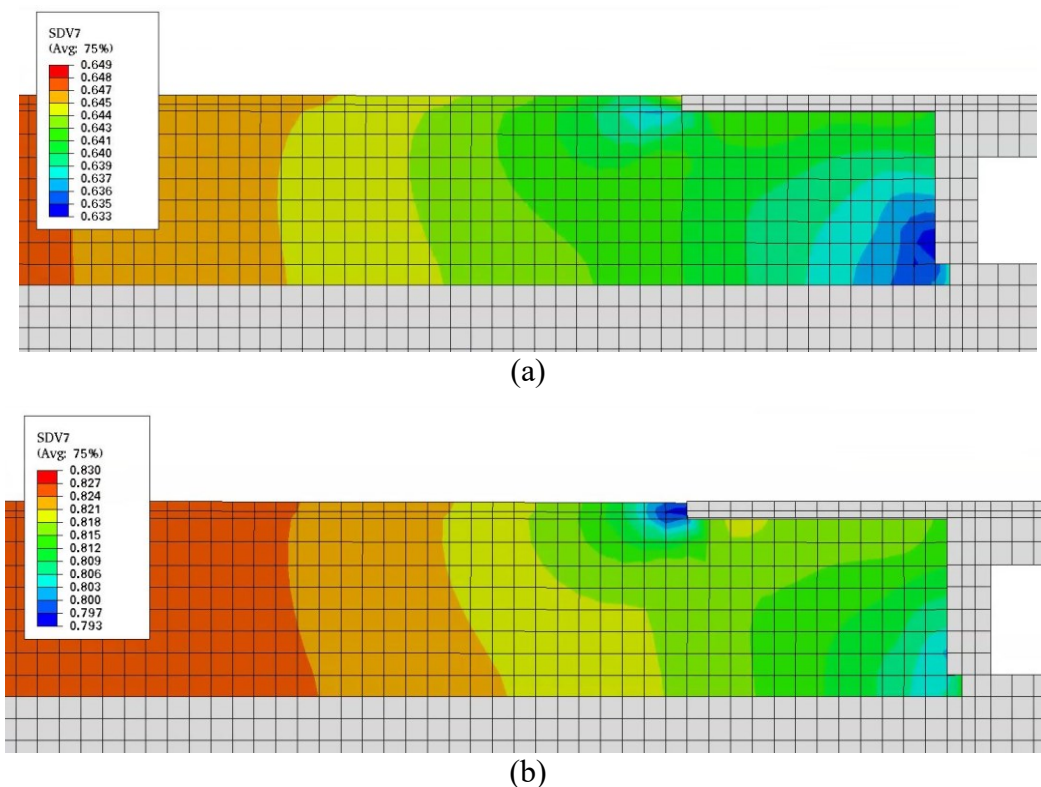


Fig. 3.28 Deformed Mesh of Backfill Soil and Variation of Void Ratio for (a) Dense Sand, and (b) Medium Sand after 5 Years of Simulation for Civjan *et al.* (2013) Temperature Loading.

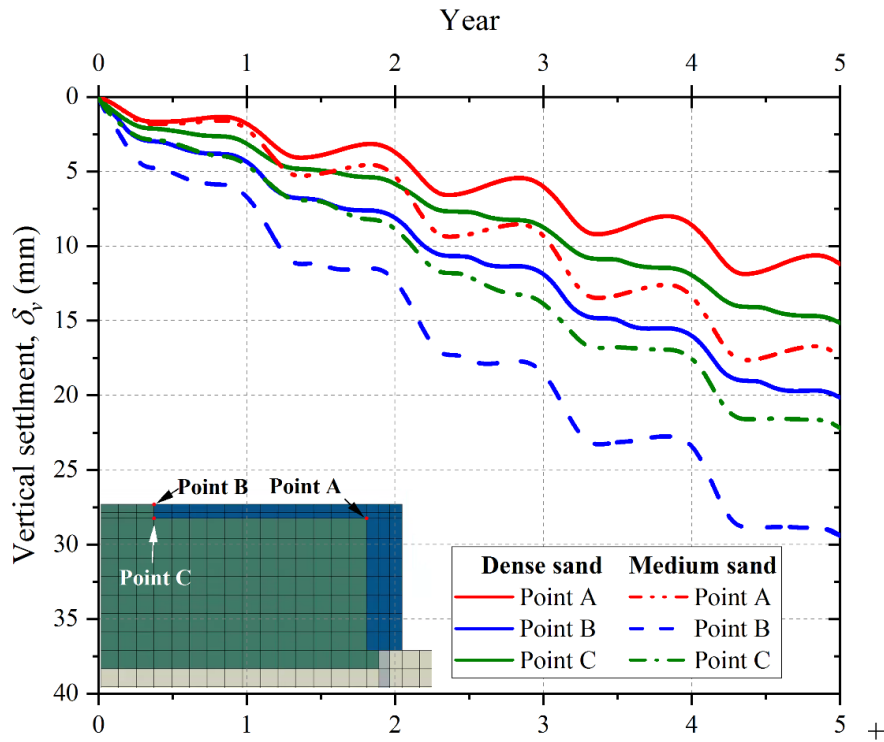


Fig. 3.29 Vertical Settlement of Backfill Soil at Different Points for Kim and Laman (2010) Temperature Loading.

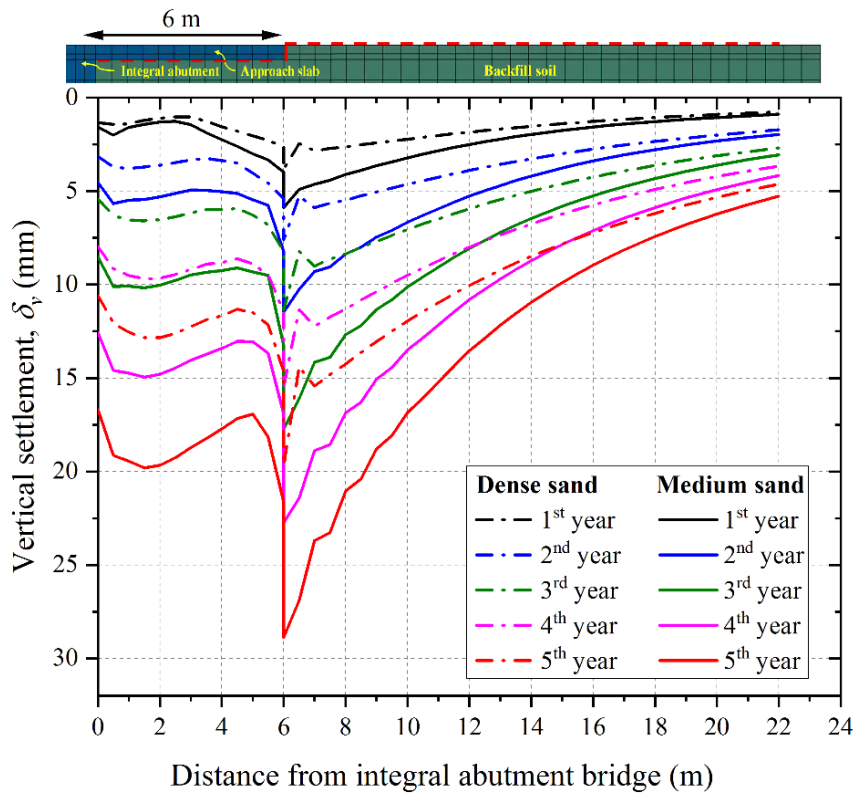


Fig. 3.30 Vertical Settlement Profile of Backfill Soil from Integral Abutment for Kim and Laman (2010) Temperature Loading.

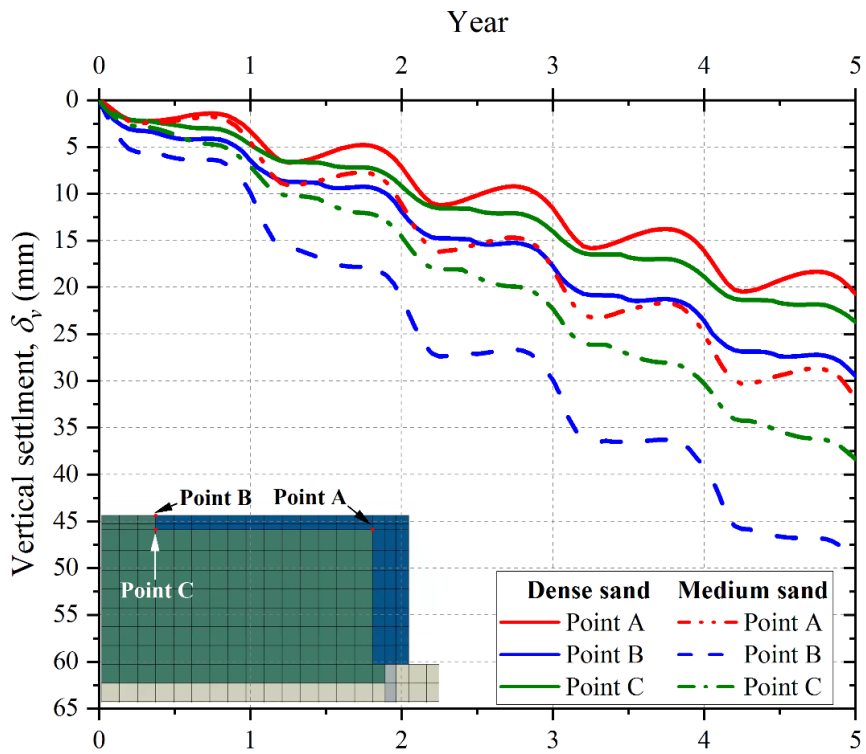


Fig. 3.31 Vertical Settlement of Backfill Soil at Different Points for Civjan *et al.* (2013) Temperature Loading.

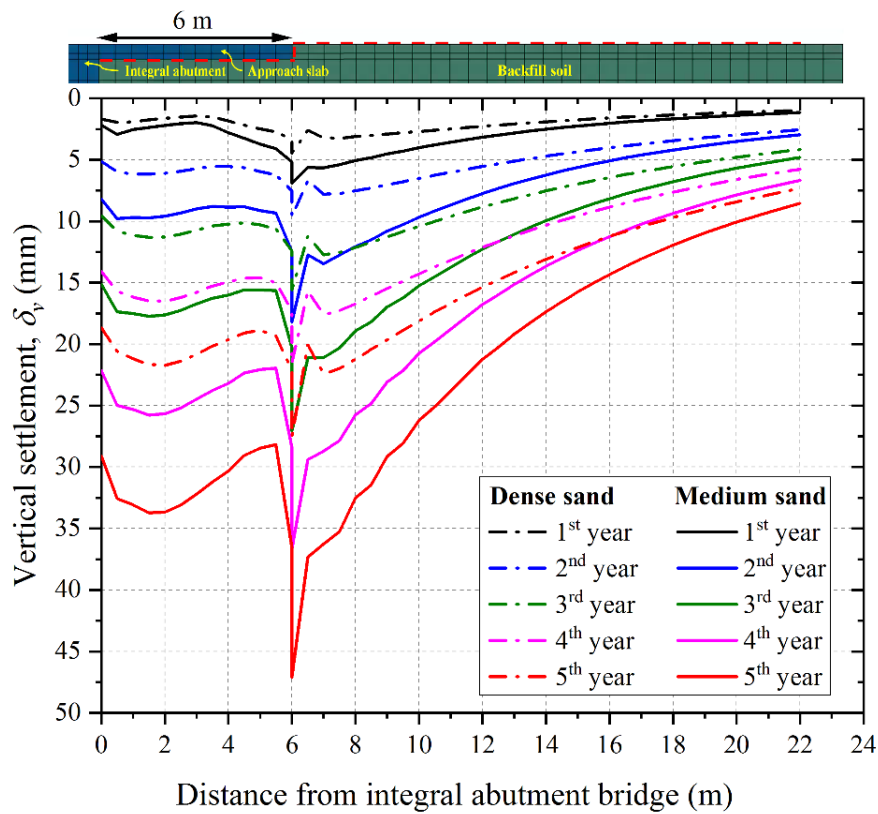


Fig. 3.32 Vertical Settlement Profile of Backfill Soil from Integral Abutment for Civjan *et al.* (2013) Temperature Loading.

The increase in the number of cycles of cyclic thermal loading has led to the increase in the settlement of the backfill soil behind the integral abutment. The maximum settlement of the backfill soil is observed at the approach slab tip, i.e., Point C. The presence of approach slab in the IAB is responsible for the increased settlement of the backfill soil farther away from the integral abutment. In the absence of the approach slab, the increased settlement would have generated just behind the integral abutment. It is noted that, higher is the length of the approach slab farther away is the maximum settlement from the integral abutment. The type of backfill soil has a significant influence on the settlement of the backfill soil. From the above figures, it is observed that the higher backfill settlements are observed for the case of medium sand. The sagging in the settlement profile is noticed below the middle portion of the approach slab. Based on the results of the FE simulations, it is recommended to have the backfill of dense sand for the IABs.

3.6.2 FE Simulation of Cyclic Longitudinal Displacement Loading

In the present study, two cases of thermally induced cyclic longitudinal displacement loadings are adopted and the same are used in the FE simulations. In the first case, the field monitored data of 6.5 years for SR-18 over the Mississinewa River IAB (Lovell, 2010) located in Marion, Indiana, United States, used in the simulations. The abutment cyclic longitudinal displacement data of the above bridge obtained for seasonal temperature variations is depicted in Figure 3.33. In the second case, a sinusoidal abutment displacement of amplitude ± 20 mm for 20 cycles is considered and the same is shown in Figure 3.34. This sinusoidal displacement loading is used in the FE simulation to represent the thermally induced displacement. The sinusoidal displacement loading is applied at the top of the integral abutment to the depth of the steel girder. In the FE simulation of sinusoidal displacement loading, two backfill soil types such as medium and dense sands are considered. In the FE analysis of SR-18 bridge, cyclic longitudinal displacement is applied, and the medium sand is considered as the backfill soil. In both the cases of FE simulations, the backfill soil behaviour is simulated using the hypoplastic sand constitutive model and the occurrence of soil ratcheting phenomenon is investigated.

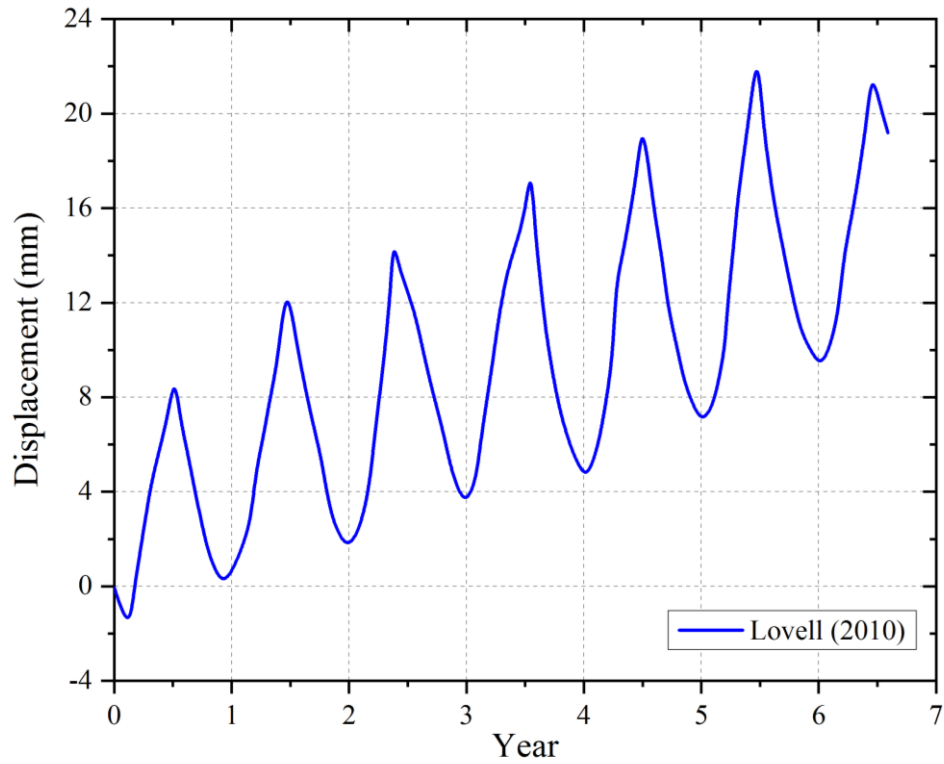


Fig. 3.33 Field Data of Horizontal Displacement of SR-18 Bridge.

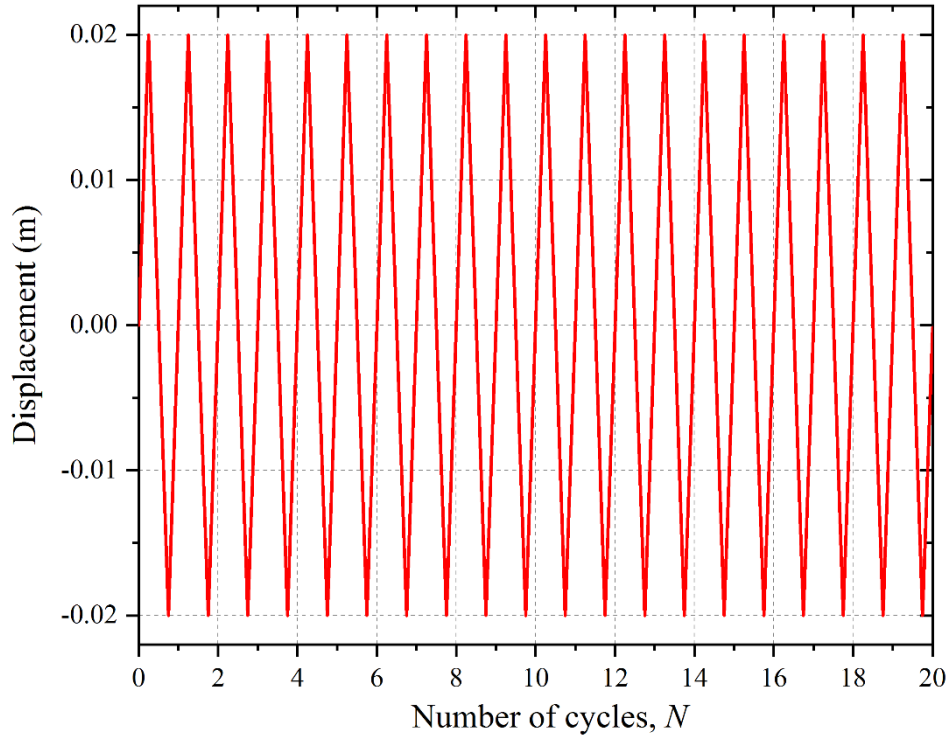


Fig. 3.34 Applied Sinusoidal Displacement at the Top of the Integral Abutment in the FE Simulation.

3.6.2.1 Results and discussion

In the present study, the backfill consists of the Toyoura sand having an initial void ratio of 0.831 and a relative density of 55% which represents the medium dense condition and the cyclic loading as shown in Figure 3.33 used and the FE simulations are performed for the IAB (See Figure 3.11). The variation of passive pressure behind the integral abutment at the bottom is depicted in Figure 3.35. The magnitude of soil pressure is found to increase for the initial three years and later a steady state pressure is observed for the remaining years. The increased soil pressure is attributed to the increased cyclic longitudinal displacement for the initial three years and thereafter the effective peak displacement remained constant. Similar observations were also made for the SR-18 bridge. It is noted that the soil pressure is not continuously increasing with the increase in the number of cycles of cyclic longitudinal displacement. Hence, the presence of soil ratcheting phenomenon is not observed in the FE simulations.

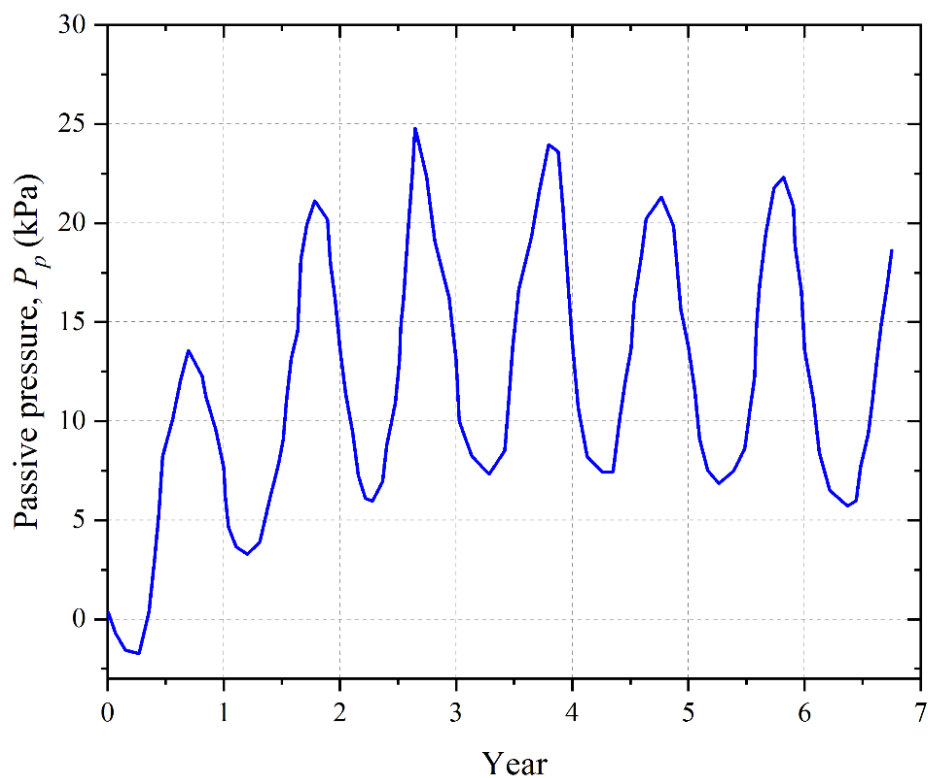


Fig. 3.35 Variation of Passive Pressure at the bottom of Abutment with Number of Years for Thermal Displacement Loading of SR-18 Bridge.

The variation of backfill soil settlement with the number of cycles of cyclic longitudinal displacement is also studied using the FE simulation. Figure 3.36 shows the vertical settlement of the backfill soil at three different points i.e., Point A, Point B and Point C

for 6.5 years of cyclic longitudinal displacement data of SR-18 bridge. The figure shows a similar trend that was observed in the previous section. With the increase in the number of cycles of longitudinal displacement the increase in the vertical settlement of the backfill soil is observed. The maximum settlement of the backfill is observed at the tip of the approach slab as in the figure.

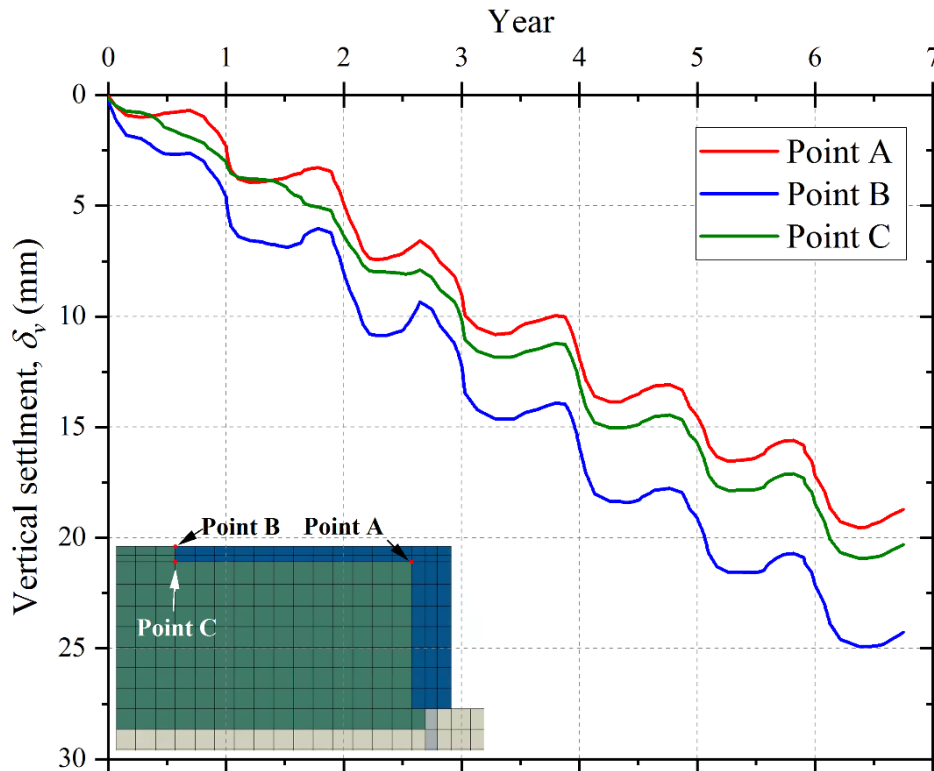


Fig. 3.36 Vertical Settlement of Backfill Soil at Different Points for Cyclic Longitudinal Displacement of the IAB.

The 2D FE analysis of the pile-supported integral abutment is studied. A sinusoidal displacement of amplitude ± 20 mm for 20 cycles, which represents the seasonal temperature variation, is applied at the top of the abutment to the entire depth of the steel girder. The variation of passive pressure and vertical settlement of the backfill soil are evaluated. The passive pressure generated at the bottom of the integral abutment for the sinusoidal displacement is shown in Figure 3.37. Similarly, the total passive force generated behind the integral abutment for the cases of medium and dense sand backfills is shown in Figure 3.38.

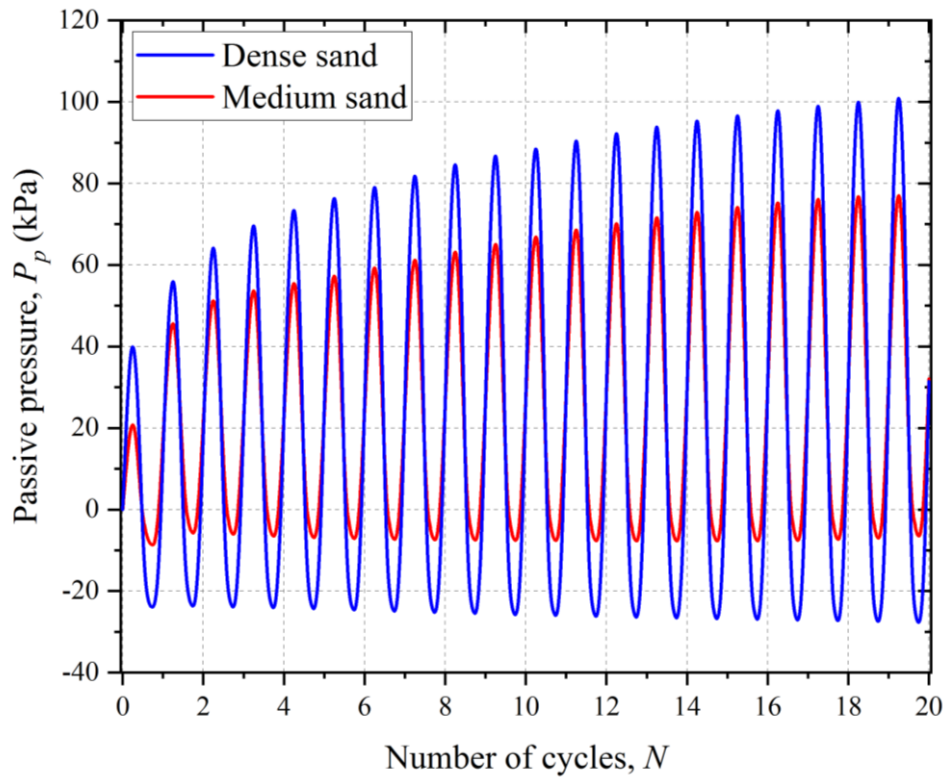


Fig. 3.37 Variation of Passive Pressure with Number of Cycles of Sinusoidal Displacement Loading.

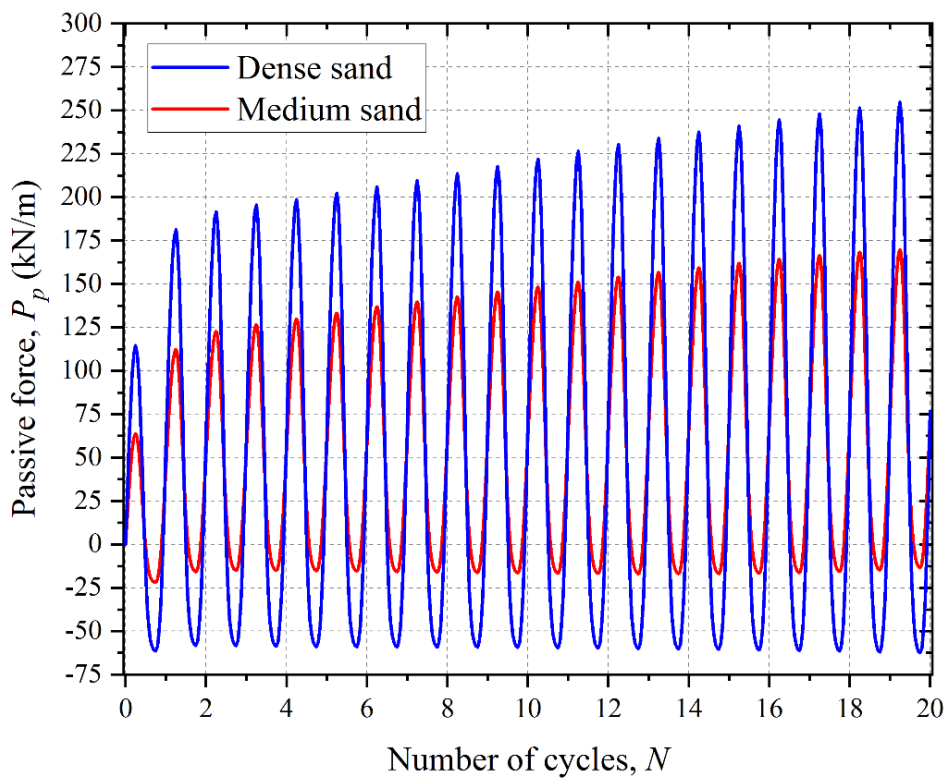


Fig. 3.38 Variation of Passive Force with Number of Cycles of Sinusoidal Displacement Loading.

An increase in the passive pressure at the bottom of the integral abutment with the number of cycles of sinusoidal displacement is observed (See Figure 3.37). A similar trend is also observed in the passive force generated behind the integral abutment (See Figure 3.38). The passive force and passive pressure are observed to be higher for the dense sand backfill. The soil ratcheting phenomenon is observed in both the cases of backfills for the sinusoidal displacement loading.

Figure 3.39 shows the vertical settlement of the backfill soil at three different points i.e., Point A, Point B and Point C for the 20 cycles of sinusoidal displacement for both the backfills. The vertical settlement of the backfill soil increases with the number of cycles of sinusoidal displacement. Figure 3.40 depicts the variation of vertical settlement profile of the backfill soil behind the abutment for the 20 cycles of sinusoidal displacement. From the above figures, it is observed that the higher (68.75%) backfill settlements are observed for the case of medium sand backfill. The backfill soil settlement for the medium sand increases drastically with the number of cycles of sinusoidal displacement.

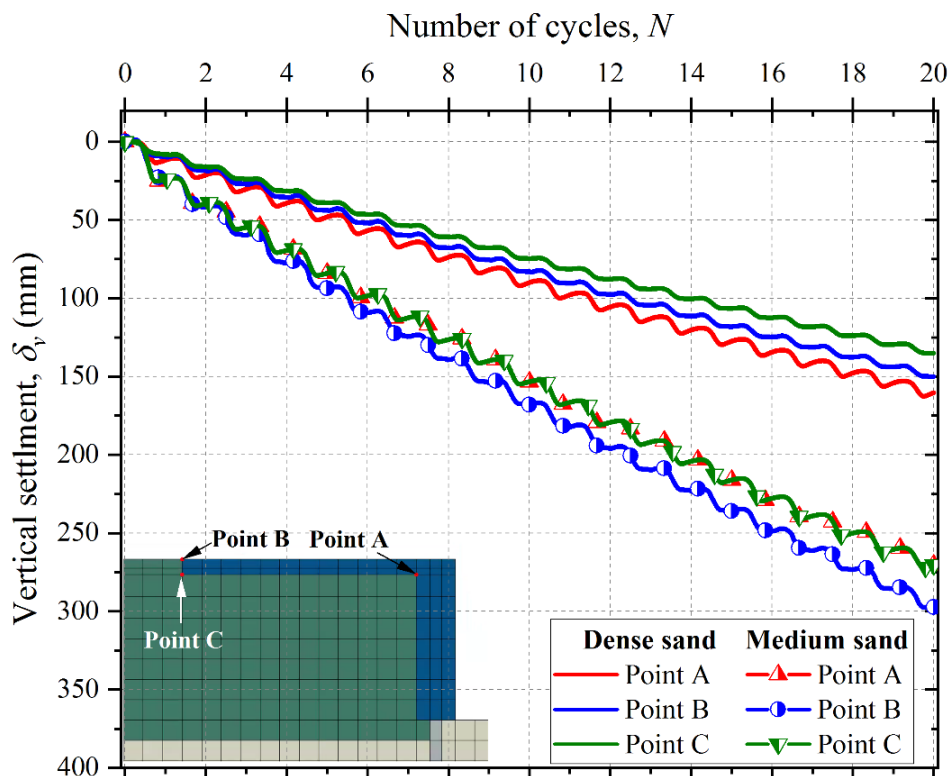


Fig. 3.39 Vertical Settlement of Backfill Soil at Different Points with Number of Cycles of Sinusoidal Displacement Loading.

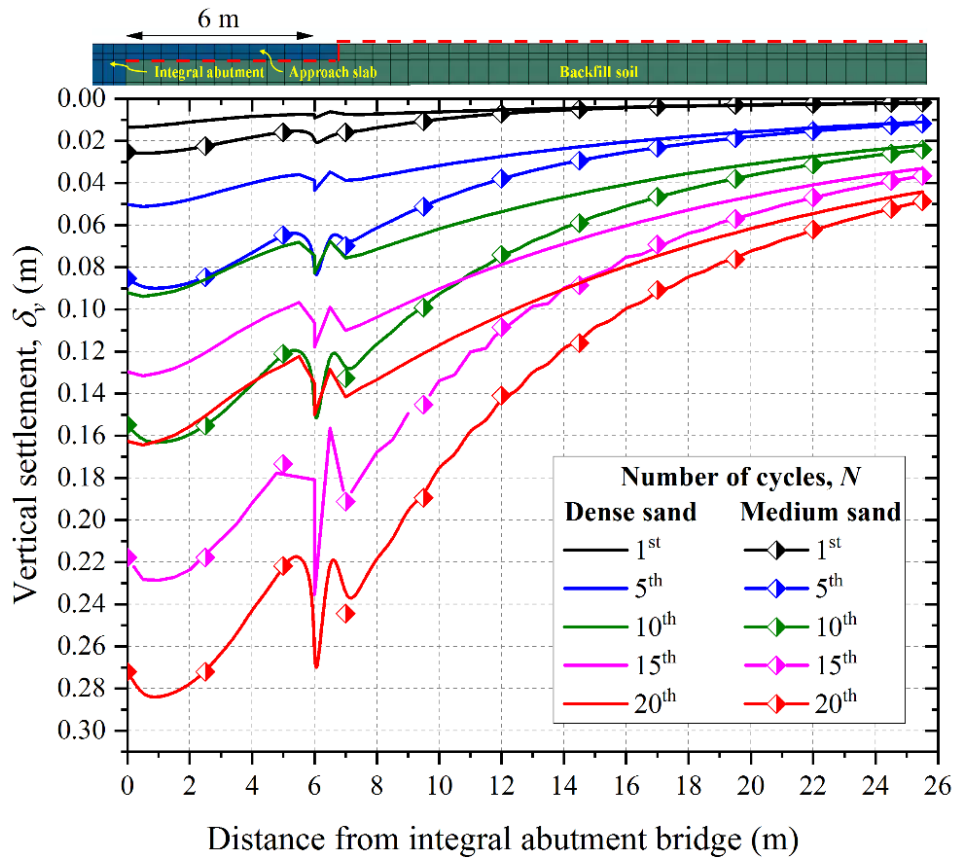
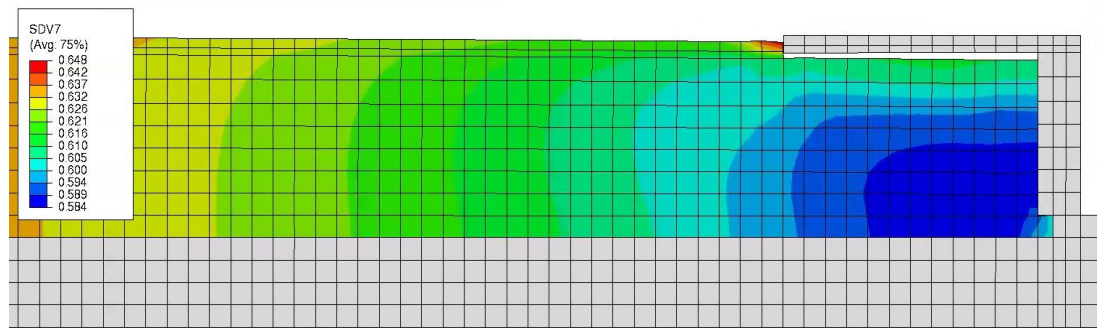
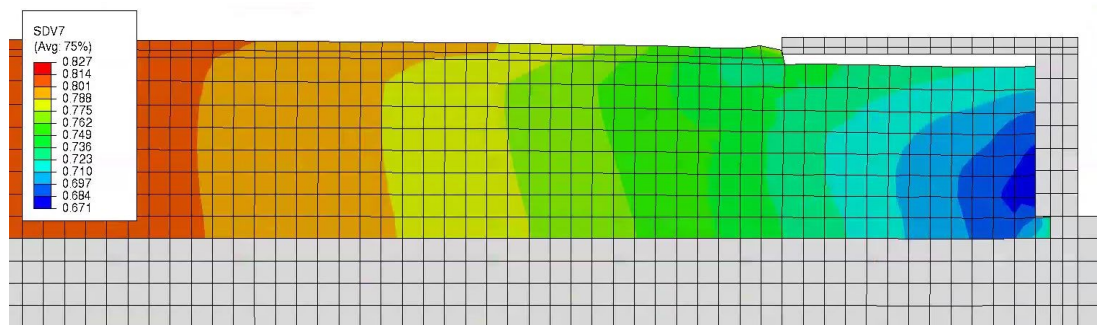


Fig. 3.40 Vertical Settlement Profile of Backfill Soil from the Integral Abutment with Number of Cycles of Sinusoidal Displacement Loading.

The variation of void ratio in the backfill is evaluated after the 20 cycles of sinusoidal displacement for medium and dense sand backfills and is shown in Figure 3.41. It is seen that the backfill soil settlement below the approach slab for the medium sand is very high. The variation of void ratio in the backfill soil beneath the approach slab for the dense sand backfill is minimal as in the figure. The variation of vertical settlement profile of the dense sand backfill behind the abutment for the 20 cycles of sinusoidal displacement is found to be similar as that observed by Al-qarawi *et al.* (2020).



(a)



(b)

Fig. 3.41 Deformed Mesh of Backfill Soil and Variation of Void Ratio for (a) Dense Sand, and (b) Medium Sand after 20 Cycles of Sinusoidal Displacement Loading.

3.7 SUMMARY

The behaviour of pile-supported integral abutment bridge with approach slab subjected to static, cyclic, and thermal loadings is investigated in the chapter. The hypoplastic constitutive model was used to simulate the hysteresis behaviour of the backfill soil. The hypoplastic sand constitutive model for the Toyoura and Karlsruhe sands is validated with the drained triaxial test results. The FE model of the abutment backwall is validated with the large-scale field test conducted on the abutment backwall. The passive force-displacement relationships are developed considering the cyclic loading and are compared with the experimental results. The passive force-displacement relationships for the abutment backwall are developed considering pure translation and pure rotation loadings separately. These results are compared with the integral abutment-pile-backfill system analysed under static translation loading. The effect of variation in approach slab length, backfill soil type and foundation soil stiffness on the passive force-displacement relationships is evaluated.

The FE simulations of the IAB are carried out for the two cases. In the first case, the cyclic thermal loading is applied at the deck and steel girder and in the second case, the thermally induced abutment displacement obtained from the field monitored data and sinusoidal cyclic displacements are applied to the bridge superstructure. The occurrence of soil ratcheting phenomenon is investigated by simulating the backfill soil behaviour using the hypoplastic constitutive model. The effect of backfill soil type on the vertical settlement of the backfill and variation of soil pressure behind the integral abutment is investigated.

In the next chapter, the behaviour of transition zone of the IAB under static, cyclic and equivalent dynamic coupled bogie loadings are analysed and the results are presented.

CHAPTER 4

BEHAVIOUR OF INTEGRAL ABUTMENT BRIDGE TRANSITION UNDER STATIC AND CYCLIC TRAIN LOADING

4.1 INTRODUCTION

The railway track near the abutment deteriorates more quickly than the other track components. The subtle transition zone, characterised by variations in track stiffness and track settlement resulting from irregular train-track interaction and increased dynamic loading, stands as a key factor contributing to this degradation (Banimahd, 2008; Banimahd *et al.*, 2012; Li *et al.*, 2005). Vertical stiffness, which is determined by the track modulus and track irregularity, plays a pivotal role in responding to dynamic forces (Dahlberg, 2010). An augmentation in vertical stiffness mitigates settlement, while a reduction in vertical stiffness triggers resonance (Sanudo *et al.*, 2016). The train-track irregularities in the transition section are typically more pronounced, resulting in diminished passenger comfort, elevated risk of derailling, and accelerated wear and tear on both the train and track components. Prior research has indicated that implementing various measures, such as the use of long and thick sleepers, concrete approach slabs, additional rails, improved subgrade drainage, and other mitigation techniques, can effectively enhance the stiffness adaptation and reduce uniform settlement in the transition zone (Shan *et al.*, 2013; Nimbalkar *et al.*, 2012). This method may not be effective for all the transition zones due to the highly site-specific nature of the differential movement issues (Coelho and Hicks, 2015). To enhance the performance of the transition zone, Railway Infrastructure Managers (RIM) recommend the implementation of a well-compacted backfill consisting of multiple layers of diverse materials between the embankment and the bridge (Paixao *et al.*, 2014). The dominant factor governing an efficient design includes reducing the faults and irregularities of the transition zone (Giannakos and Tsoukantas, 2012).

The schematic representation of a typical H-pile supported integral abutment bridge (IAB) for railways, in which, the deck slab and girder are casted monolithically with the abutment is shown in Figure 4.1. The integral abutment bridges (IABs) are dynamically more stable structures with improved passenger safety and comfort and

much-reduced construction and maintenance costs (Kunin and Alampalli, 2000). The approach slabs are often used to achieve a smooth transition in track stiffness and consequent reduction in maintenance requirement (Burke Jr., 2009). In the IAB, one end of the approach slab is fixed to the integral abutment, and the other is supported on the embankment (see Figure 4.1), thereby providing a gradual change in track stiffness along the length. The transition zones with approach slabs lacks deeper understanding of their behaviour under moving train loads and the influence of parameters such as approach slab geometry and embankment soil properties are the reasons for poor performance. Therefore, it is imperative to understand the behaviour of IAB-embankment transition zones with approach slabs for the safe operation of trains and to identify the critical parameters affecting their performance.

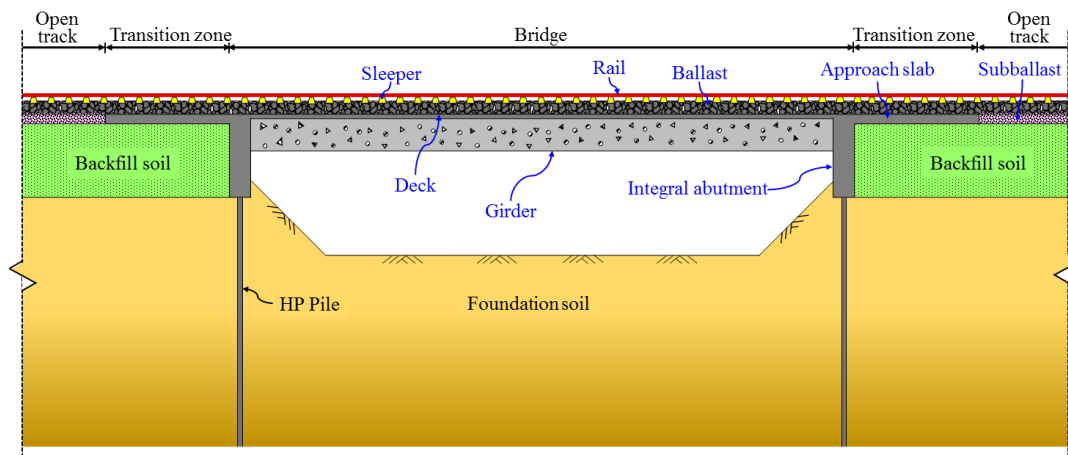


Fig. 4.1 Schematic Representation of Integral Abutment Railway Bridge.

The dynamic behaviour of monolithic structures based on the surface interactions revealed that the pile stability and backfill characteristics are able to influence the abutment behaviour, which in turn affects the transition zone (Pak *et al.*, 2017). However, most of these studies have only focused on the transition zones of the IABs adopted for highways, and the studies related to the IABs for railways are relatively scarce. The behaviour of an IAB-embankment transition for highways and railway tracks can be significantly different, given the differences in the track/pavement structure and the loading conditions (Huang *et al.*, 1984). Additionally, the growing usage of high-speed and heavy-haul trains to cater to the rapidly increasing demand for rail transport may significantly affect the performance of the IAB-embankment transitions for railways. Therefore, an understanding of the dynamic behaviour of these critical regions for railway applications is of paramount importance. Although the field

investigations are reliable tools for understanding the behaviour of transition zones, they are generally expensive and time-consuming. The numerical modelling approach offers a cost-effective alternative to investigate the performance of transition zones in integral abutment railway bridges (IARBs) under the train loading. Several researchers have attempted to study the behaviour of transition zones using numerical techniques such as finite element (FE) analyses (Rodriguez *et al.*, 2011; Cai *et al.*, 2005). The studies pertaining to the dynamic behaviour of the IARB with transition approach slab under the train loading are still very limited.

In the present study, the two-dimensional (2D) FE model of the integral abutment railway bridge (IARB) with an approach slab is developed using ABAQUS. The IARB system is subjected to static and cyclic train loadings and the SSI effects are considered in the analysis. Firstly, the FE model is validated by comparing its response with the field data reported in the published literature. Subsequently, the influence of various parameters such as the approach slab geometry (length, thickness, and inclination) and influence of backfill soil type on the performance of the IARB transition zone is explored. The dynamic effects of different train speeds are simulated using the equivalent dynamic load considering the dynamic amplification factor (DAF) and these dynamic loads are applied at the specific locations of the FE domain. The different approach slab geometries are considered and its responses to equivalent dynamic train loading are evaluated. The repetitive cyclic train wheel loading acting during the passage of entire train is modelled using an equivalent static loading and accordingly the FE simulations have been performed and the results are presented in the chapter.

4.2 VALIDATION OF FE MODEL

The accuracy of the developed 2D FE model of the transition zone and abutment of the bridge is validated by comparing the field investigation data reported by Paixão *et al.* (2014). The field investigated bridge is located at the southern approach side of the railway bridge over the Sado river in Portugal. The transition zone includes two wedge-shaped engineered fills of cement bound mixture (CBM) and unbound granular material (UGM), with CBM behind the abutment and UGM located between the CBM and embankment. Figure 4.2 shows the 2D FE model of this transition zone along with the dimensions of different components. The model is 70 m in length, including the UGM, CBM and abutment. The model is discretised using 4-noded bilinear plane-strain quadrilateral elements with reduced integration (CPE4R), and the entire mesh consists

of 4,544 elements. Standard boundary conditions are applied with fixed support at the bottom, and roller support and symmetric boundary conditions at the left and right side of the model, respectively. Table 4.1 provides the values of the parameters used in the simulation, which are the same as that reported by Paixão *et al.* (2014).

Figure 4.3 shows a comparison of the vertical rail displacement predicted using the FE model with that measured in the field during a single passage of the Alfa Pendular train at two different locations (at $x = 0.9$ m and 14.7 m from the abutment). It is apparent from the figure that the FE model predictions are consistent with the field measurements at both $x = 0.9$ m and 14.7 m. The vertical displacement of the rail is higher at $x = 14.7$ m (track supported by UGM) as compared to $x = 0.9$ m (track supported by CBM). This difference in displacement is due to the different material stiffness at $x = 0.9$ m and 14.7 m. Thus, the FE model accurately predicts the gradual reduction in rail displacement as the train moves from the embankment towards the bridge abutment.

Table 4.1 Parameters used in the validation of the FE model (adopted from Paixão *et al.* (2014)).

| Component | Young Modulus, E (MPa) | Poisson's Ratio, ν | Rayleigh Coefficients | | Density, ρ (kg/m ³) |
|--------------------------------|--------------------------|------------------------|-----------------------------|-------------------------------|--------------------------------------|
| | | | α (s ⁻¹) | β ($\times 10^{-3}$ s) | |
| Rail (steel) | 210×10^3 | 0.35 | – | – | 7850 |
| Sleeper (reinforced concrete) | 30×10^3 | 0.25 | – | – | 6360 |
| Ballast | 130 | 0.20 | 8.52 | 0.4 | 1530 |
| Subballast | 200 | 0.30 | 8.52 | 0.4 | 1935 |
| Capping layer | 3020 | 0.30 | 8.52 | 2.6 | 1935 |
| UGM | 1030 | 0.30 | 8.52 | 2.6 | 1935 |
| CBM | 10×10^3 | 0.30 | 8.52 | 0.4 | 2200 |
| Embankment soil | 80 | 0.30 | 8.52 | 2.9 | 2040 |
| Abutment (reinforced concrete) | 30×10^3 | 0.25 | – | – | 2500 |

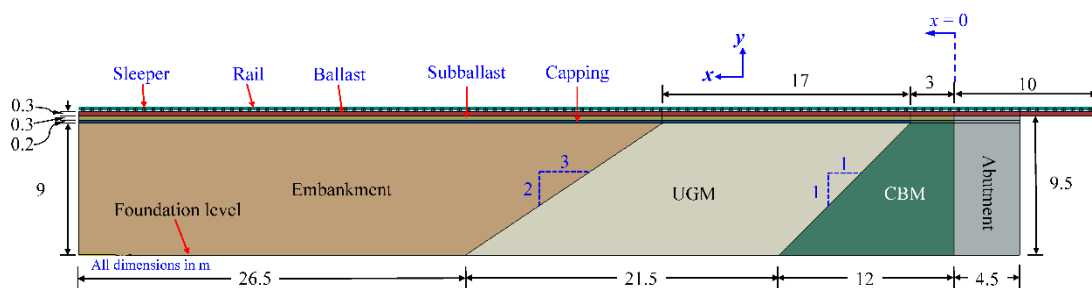


Figure 4.2 FE Model for Validation with Field Data Reported by Paixão *et al.* (2014).

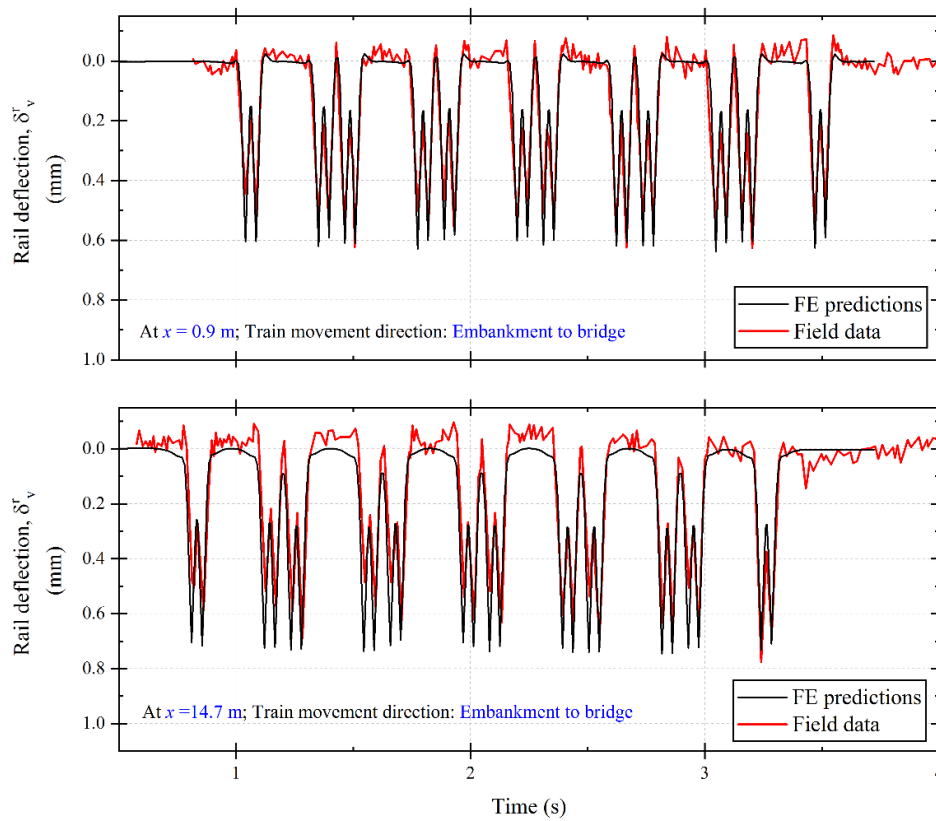


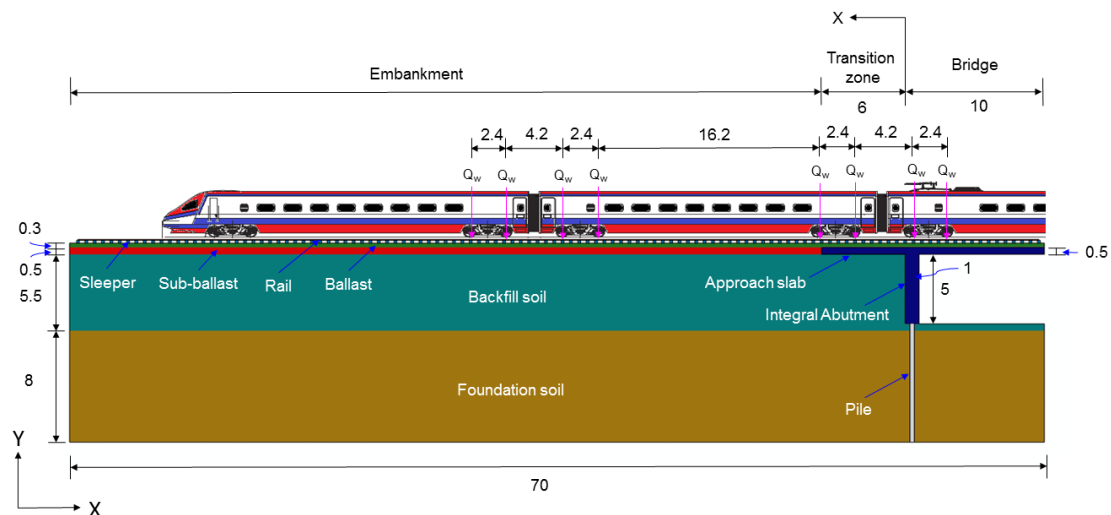
Figure 4.3 Comparison of Predicted Rail Displacement with Field Data Reported by Paixão *et al.*, (2014).

4.3 FE ANALYSIS OF THE IARB

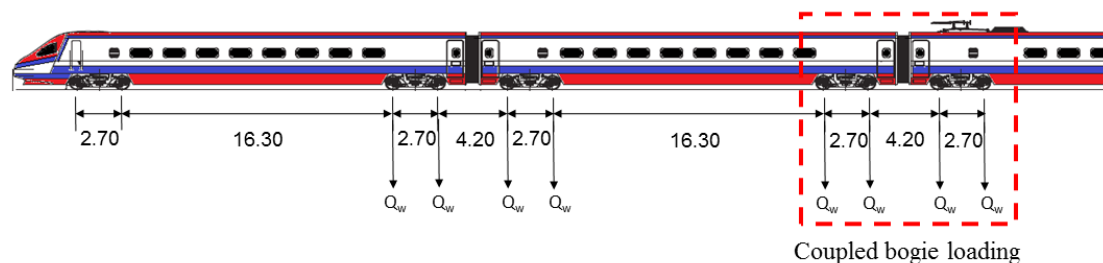
4.3.1 Description of Geometry

The 2D FE model of the IARB is developed using the software package ABAQUS, considering the different components of the train–track–abutment–pile system as shown in Figure 4.4(a). The geometry and dimensions of the various components of the IARB are selected based on the published data on the existing railway bridge transitions (Al-qarawi *et al.*, 2020). The total length of the model is 70 m, with 116 sleepers equally spaced at 0.6 m intervals. An approach slab is provided to allow a smooth transition of the track stiffness. The IARB consists of a steel girder of 1.5 m depth, a deck slab of 0.5 m thickness, and the integral abutment is supported on the H-piles. The width and height of the abutment are taken as 1 m and 5 m, respectively. The H-pile is 8 m long and is firmly socketed into the bedrock. The railway track comprises a steel rail supported by concrete sleepers resting on the ballast bed, which overlies the subballast layer, approach slab or deck slab, depending on the location. The rail is modelled as a rectangle with a moment of inertia equivalent to that of a UIC 60 steel rail standard

with a weight per meter as 60 kg. The height and width of concrete sleepers are taken as 0.2 m and 0.2 m, respectively. The substructure of the railway track in the embankment portion consists of ballast, subballast, backfill and foundation soils. The thickness of the ballast and subballast layers are considered as 0.3 m and 0.5 m, respectively. Figure 4.4(b) shows the configuration of the Alfa Pendular train, which is used to replicate the train-induced loads (Paixão *et al.*, 2014). In this study, the train coupled bogie loading is simulated by applying a point load at the top of the rail above each sleeper (known as loading node), whose magnitude is Q_w equal to 100 kN, is a representative load for the train with an axle load of 20 tonnes. In the FE analysis, the static train coupled bogie loading is emulated by preserving the individual train wheel axle loads (Q_w) spaced at specific configurations, as illustrated in Figure 4.4(b). The coupled bogie loadings are applied as static loading and cyclic loading separately at the specific points in the different zones such as embankment, transition zone and bridge.



(a)



(b)

Fig. 4.4 (a) Schematic Geometry of IARB with Approach Slab (all units in m), and (b) Train Loading (Q_w) Configuration Showing Distance between Axles (in m).

4.3.2 Material Properties and Constitutive Model

The calibration process incorporates the determination of the adequate properties of the different components as included in the FE model. Table 4.2 lists the values of the material properties used in the FE simulations. These values are chosen based on the existing literature and published technical reports. The rail, sleeper, integral abutment, approach slab and H-pile are modelled using the linear elastic model. The behaviour of backfill and foundation soils is simulated using the Mohr-Coulomb material model. The behaviour of the ballast and subballast is simulated using the Drucker-Prager model with a non-associated flow rule (Li *et al.*, 2018; Leshchinsky and Ling, 2013). The material damping in the FE model is captured using Rayleigh damping, and the values of damping coefficients, ‘ α ’ and ‘ β ’ for each of the track materials are determined using the following equations (Chopra, 2007):

$$\alpha = \frac{2D_R \omega_m \omega_n}{\omega_m + \omega_n} \quad (4.1)$$

$$\beta = \frac{2D_R}{\omega_m + \omega_n} \quad (4.2)$$

where D_R is the damping ratio, ω_m and ω_n are the first and third natural frequencies (in rad/s). The first and third natural frequencies for each substructure layer can be computed using the following equation (Kramer, 1996):

$$\omega_n = \frac{\pi V_s}{2H} (2n - 1) \quad (4.3)$$

where V_s and H are the shear wave velocity and thickness of each soil layer, respectively; n is the mode number. Generally, the frequencies corresponding to first mode of a layer and a higher mode referring to the predominant frequency of input motion are considered. In this study, the first and third modes ($n = 1$ and 3) are used to evaluate the natural frequencies. The shear wave velocity (V_s) is calculated using the following equation:

$$V_s = \sqrt{\frac{G}{\rho}} \quad (4.4)$$

where G is the shear modulus and ρ is the density of each soil layer. The shear modulus (G) is determined using the equation:

$$G = \frac{E}{2(1 + \nu)} \quad (4.5)$$

where E is the Young's modulus and ν is the Poisson's ratio of the soil layer. Table 4.2 gives the dynamic parameters of various layers considered in the FE simulation.

4.3.3 Interface Interactions

The soil-structure interaction between the integral abutment-backfill soil, pile-foundation soil, sleeper-ballast, and approach slab-ballast is simulated using the Coulomb friction model available in ABAQUS. The normal and tangential contact behaviours are simulated using surface-to-surface interaction by employing the master-slave concept. The normal contact behaviour is simulated as '*hard contact*' in which the normal stresses are transferred under compression. The tangential contact is simulated using a penalty friction algorithm for which the interface friction coefficient between the two surfaces is evaluated by:

$$\mu = \tan \delta \quad (4.6)$$

where δ is the interface friction angle and is determined as (Potyondy 1961):

$$\tan \delta = R_i \tan \varphi' \quad (4.7)$$

where φ' is the friction angle of the soil, R_i is the strength-reduction factor (assumed as 2/3 in the present study). For interfaces like the ones adopted here, the past studies have used a value of R_i in the range of 0.5-1 (Ooi *et al.* 2010; Donna *et al.* 2018).

Table 4.2 Material properties used in the FE simulation (data sourced from ¹Farooq *et al.*, 2021; ²Al-qarawi *et al.*, 2020; ³Li *et al.*, 2018).

| Material | Constitutive Model | Density, ρ (kg/m ³) | Young's Modulus, E (MPa) | Poisson's Ratio, ν | Friction Angle, ϕ' (°) | Dilation Angle, ψ (°) | Cohesion, c' (kPa) | Rayleigh Coefficients | |
|---|--------------------|--------------------------------------|--------------------------|------------------------|-----------------------------|----------------------------|----------------------|-----------------------------|-------------|
| | | | | | | | | α (s ⁻¹) | β (s) |
| Rail ³ | LE | 7,700 | 206,000 | 0.3 | - | - | - | - | - |
| Sleepers ³ | LE | 2,350 | 25,500 | 0.2 | - | - | - | - | - |
| Ballast ¹ | DP | 1,600 | 110 | 0.3 | 40 | 5 | 1 | 8.52 | 0.0004 |
| Sub-Ballast ¹ | DP | 2,220 | 400 | 0.25 | 35 | 2 | 1 | 8.52 | 0.0004 |
| Backfill soil ² | MC | 1,835 | 35 | 0.35 | 38 | 8 | 6 | | |
| Foundation soil ² | MC | 1,682 | 30 | 0.3 | 20 | 1 | 20 | 1.355 | 0.001 |
| Integral abutment (Concrete) ² | LE | 2,385 | 30,000 | 0.25 | - | - | - | - | - |
| HP pile ² | LE | 7,951 | 200,000 | 0.3 | - | - | - | - | - |
| Approach slab ² | LE | 2,385 | 30,000 | 0.25 | - | - | - | - | - |

Note: LE: Linear elastic; DP: Drucker-Prager; MC: Mohr-Coulomb

4.3.4 FE Mesh Discretisation, Boundary Conditions and Modelling Procedure

The 2D plane-strain FE model of the IARB transition zone is discretised using a 4-noded bilinear plane-strain element with reduced integration (CPE4R) and hourglass control, as shown in Figure 4.5. The entire FE mesh consists of 3,348 elements. The element size of 0.1 m is assigned to the rail, sleeper, ballast, subballast, approach slab and integral abutment. An element of size of 0.2 m is used for backfill and foundation soils. The standard boundary conditions are adopted in the FE model. The roller supports are applied on the lateral sides and a fixed boundary condition at the bottom. The integral abutment is supported by 8 m long H-pile, firmly socketed into the rock. An implicit FE analysis is performed to simulate the static and cyclic train wheel loadings to study the behaviour of the IARB transition zone in the following steps: (a) geostatic step: The effective stresses ($\sigma' = \sigma - u$, where σ is the total stress and u is the pore water pressure) in the model are generated by gravity loading ($g = 9.81 \text{ m/s}^2$). The settlement that is resulted due to the gravity loading is equated to zero in ABAQUS. (b) Static and cyclic train loads are applied at the specific points in the various zones such as embankment, transition zone and bridge.

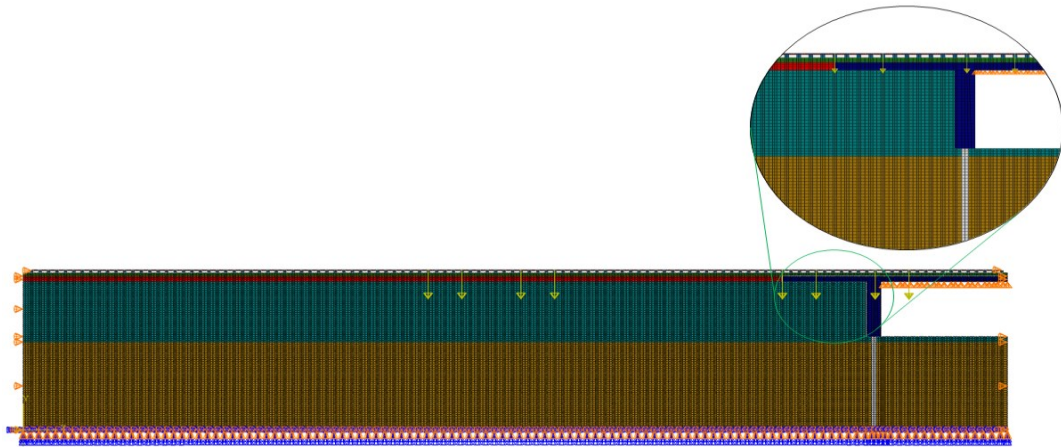


Fig. 4.5 Discretised FE Mesh of the IARB with Approach Slab.

4.4 PARAMETRIC STUDY: STATIC LOADING

The efficacy of the transition zone in effective load transfer and reducing the track settlement is determined by conducting the parametric studies. The influence of parameters such as approach slab geometry (length, thickness, and inclination) and backfill soil type on the behaviour of track is explored. The thickness and length of the

approach slab for practical considerations and development of design aids is usually varied from 300 to 900 mm and 3 to 18 m, respectively (Shi, 2006). Therefore, in the present study, three thicknesses are chosen: 300, 500, and 700 mm. Similarly, the lengths of the approach slab are chosen as 6, 9, 12, and 15 m. The backfill soil types considered in the study are loose, medium, and dense states to evaluate the effectiveness of the backfill in reducing the track displacements. The dynamic effects of various train speeds are simulated using the DAF as given in the document of equivalent dynamic wheel load method. The higher train speeds above 220 km/h will induce the critical velocity effects, which in turn significantly increases the dynamic train load. Hence the train speeds with DAF considered for the simulation studies are 60, 100, 150, and 200 km/h.

4.4.1 Length of the Approach Slab

The length of the approach slab is varied as 6, 9, 12, and 15 m by keeping the thickness of approach slab constant as 500 mm. The backfill soil type considered is medium sand. The influence of the varying length of the approach slab on the track displacement is illustrated in Figure 4.6. The maximum displacement of track occurs when the length of the approach slab is equal to 6 m, albeit the track section at the transition zone–embankment intersection shows larger track displacement than the rest of the transition zone. The track displacement decreases by 5.4% and 8.56% with the increase in the length of the approach slab from 6 m to 9 m at the middle of transition zone and interface of transition zone and embankment. However, for the further increased length of the approach slab to 12 m and 15 m, the change in the track displacement found to be very least. It is noted from the results that the track section at the transition–embankment intersection is the most vulnerable. However, the varying length of the approach slab does not affect the track displacement at the transition–embankment intersection. The track displacement is found to be maximum and minimum at the embankment (open track) and bridge. It is seen that the transition zone track displacement is found to lie between the displacements of embankment and bridge. Similar observations have also been made by Coelho *et al.* (2011).

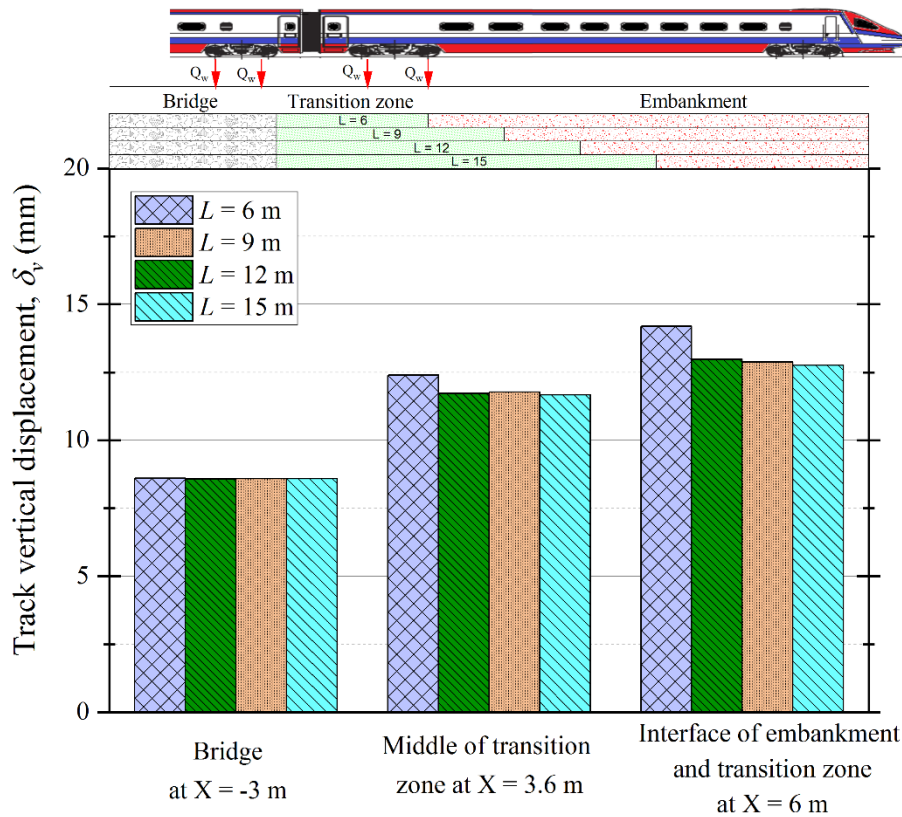


Fig. 4.6 Variation of Track Displacement for Different Lengths of Approach Slab.

4.4.2 Thickness of the Approach Slab

The thickness of approach slab is varied from 300 to 700 mm by keeping the length of the approach slab constant as 6 m. The backfill soil considered is the medium sand. Figure 4.7 shows the track displacement with varying thickness of the approach slab at the bridge, middle of the transition zone, and interface of the transition zone–embankment section. Maximum track displacement observed at the interface of the transition zone-embankment when the thickness of the approach slab is 300 mm. The track displacement at middle of the approach slab decreases by 8.23% and 4.5% for the increase in approach slab thickness from 300 mm to 500 mm and 500 mm to 700 mm respectively. Similarly, at the interface of transition zone and embankment, the track displacement is observed to decrease by 5.3% and 4.9% for the increase in approach slab thickness from 300 mm to 500 mm and 500 mm to 700 mm respectively. This fact highlights the advantage of augmenting the thickness of the approach slab in mitigating the track displacement, particularly at the most crucial section of the track. It is noted that the increased thickness of the approach slab does not affect the track displacement at the bridge section.

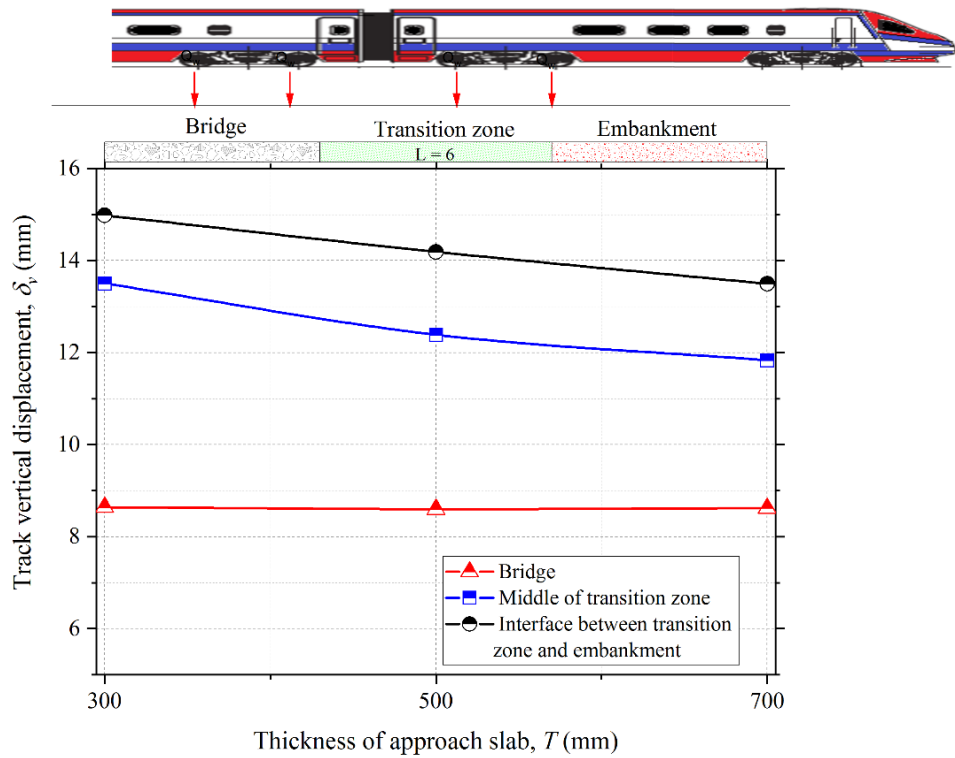


Fig. 4.7. Variation of Track Displacement with Thickness of Approach Slab.

4.4.3 Height of the Integral Abutment

The height of the integral abutment is varied as 3, 4, and 5 m to evaluate the track displacement. The approach slab length and thickness are kept constant as 6 m and 500 mm. The backfill soil considered is the medium sand. The track displacement with the variation in heights of the integral abutment is depicted in Figure 4.8. The track displacement increases with the increase in the height of the integral abutment, notably at the embankment. At the interface of the transition zone–embankment, the transition zone, and at the bridge section, the predominant increasing trend in the track displacement is not observed. The increase in the height of the integral abutment causes a minor difference in the track displacement at the transition zone due to the train load transfer from the ballast layer to the approach slab and further to the integral abutment resting on H-pile. The compression of the backfill soil is higher at the embankment zone than at the transition zone, as the train loading is transferred from the ballast to the sub-ballast and then to the backfill soil.

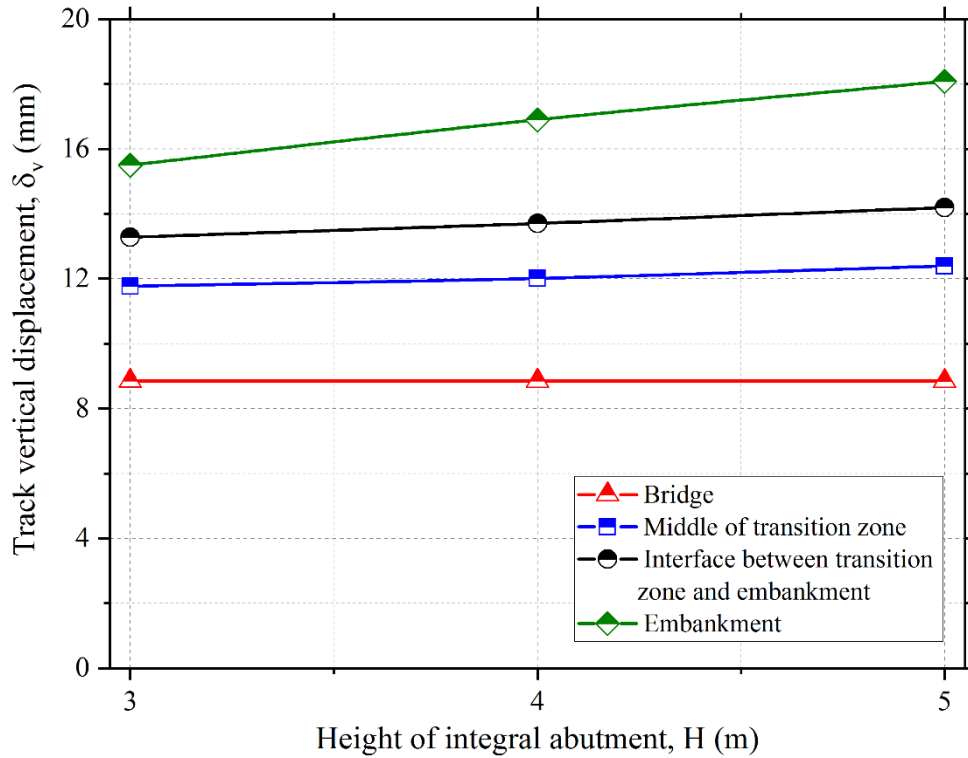


Fig. 4.8 Variation of Track Displacement with Height of Integral Abutment.

4.4.4 Inclination of Transition Zone

The fall in inclination of the approach slab is varied as 0%, 2%, 3% and 5% to investigate its influence on the performance of the track transition. In the analysis, the thickness of the approach slab (h_a) is kept constant as 500 mm, and the thickness of the ballast layer at the free end of the slab (h_b) is increased by Δh for the length of approach slab (L) (see Figure 4.9). The fall in inclination (i) of the approach slab is expressed in Equation 4.8:

$$i = \frac{\Delta h}{L} \quad (4.8)$$

The backfill soil considered is medium sand. Figure 4.10 shows the variation of the track displacement with fall in inclination of the approach slab at the transition zone. The approach slab is responsible for reducing the track displacement. The increase in the fall of the inclination resulted in the reduction of the track displacement at the critical sections. However, the track displacement at the bridge is unaffected with the fall in the inclination of the approach slab because there are no geometrical changes at the bridge.

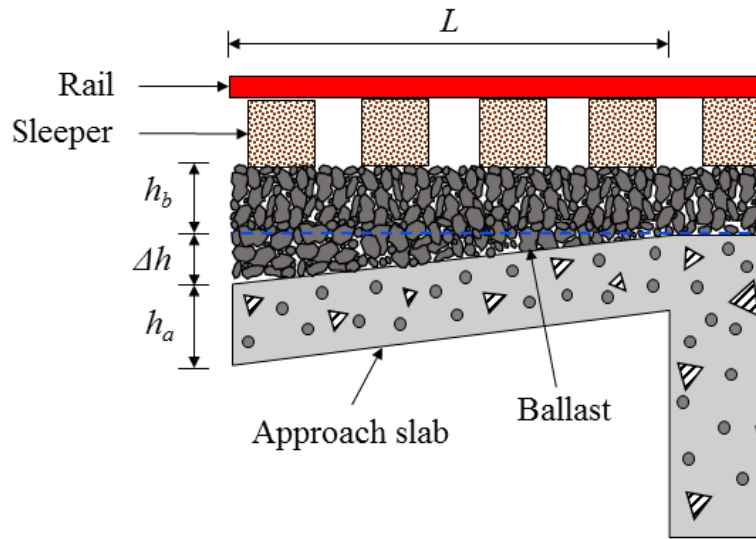


Fig. 4.9 Schematic Representation of Fall in Inclination of Approach Slab.

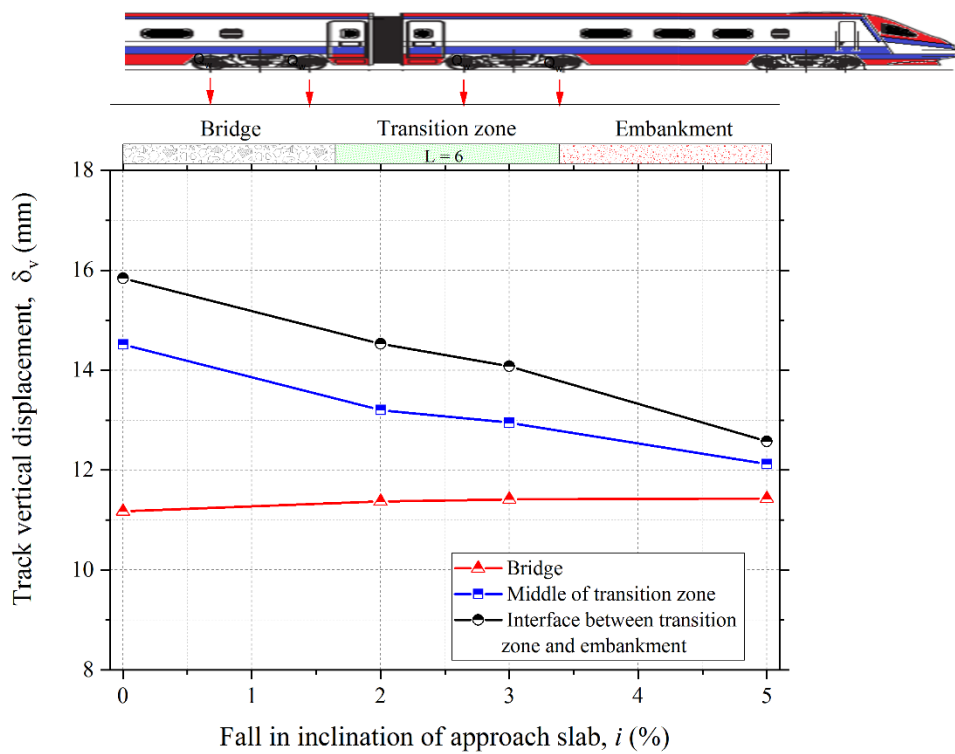


Fig. 4.10 Variation of Track Displacement with Fall in Inclination of Approach Slab.

4.4.5 Backfill Soil Type

The backfill soil type is varied to simulate the loose, medium, and dense states to assess its impact on the track performance. Table 4.3 gives the details of properties of backfill soils considered in the analysis. Figure 4.11 depicts the vertical displacement across the depth for different compaction states of the backfill soil.

Table 4.3 Material properties of different backfill soil types (Bowles, 1996).

| Material | Density, ρ (kg/m ³) | Young's Modulus, E (MPa) | Poisson's Ratio, ν | Friction Angle, ϕ' (°) | Dilation Angle, ψ (°) | Cohesion, c' (kPa) |
|-------------|--------------------------------------|----------------------------|------------------------|-----------------------------|----------------------------|----------------------|
| Loose sand | 1700 | 28 | 0.35 | 28 | - | 6 |
| Medium sand | 1800 | 35 | 0.35 | 38 | 8 | 6 |
| Dense sand | 2200 | 60 | 0.35 | 42 | 12 | 6 |

The maximum displacement occurs at the embankment section. The transition zone experiences the least displacement due to its immediate vicinity to the approach slab. The loose and dense sand backfills show the maximum and minimum vertical displacements, respectively. The track displacement at embankment is 18.07 mm for the case of medium sand, which is 9.12% lesser and 8.5% higher than the backfill comprising of loose and dense sands, respectively. Similarly, at the middle of the approach slab, the track displacement is 12.39 mm for medium sand, which is 5.87% lesser and 5.4% higher than that for loose and dense sands, respectively. Similarly, at the interface of transition zone and embankment, the track displacement is 14.19 mm for medium sand, which is 7.98% lesser and 7.46% higher than that for loose and dense sands, respectively. The maximum ballast settlement occurs at the bridge section and decreases at the embankment zone due to the efficient load transfer to the subgrade and in turn to the backfill. The ballast layer settlement at the middle of approach slab is 8.72 mm (70.43%), which is 3.9% lesser and 3.88% higher than that for dense and loose sands, respectively. The ballast layer settlement at the embankment is 7.34 mm (40.6%), which is 6.11% lesser and 4.43% higher than that for dense and loose sands, respectively. The effect of backfill soil type on ballast layer settlement is observed to be predominant at the interface of transition zone and embankment when compared to the rest of the track sections but lesser than the bridge section. The ballast layer at the bridge-transition zone rests over the rigid concrete section and undergoes more

settlement as compared to the embankment, where the ballast rests on the soil subgrade. At the embankment zone, the vertical displacement is more significant in the top of the backfill soil layer and decreases along the depth of the layer, as shown in Figure 4.8. However, beneath the transition zone, the difference in the vertical displacement is negligible between the top and bottom of the backfill soil layer. The minimum and maximum ballast settlements are observed for the case of loose and dense backfill soils.

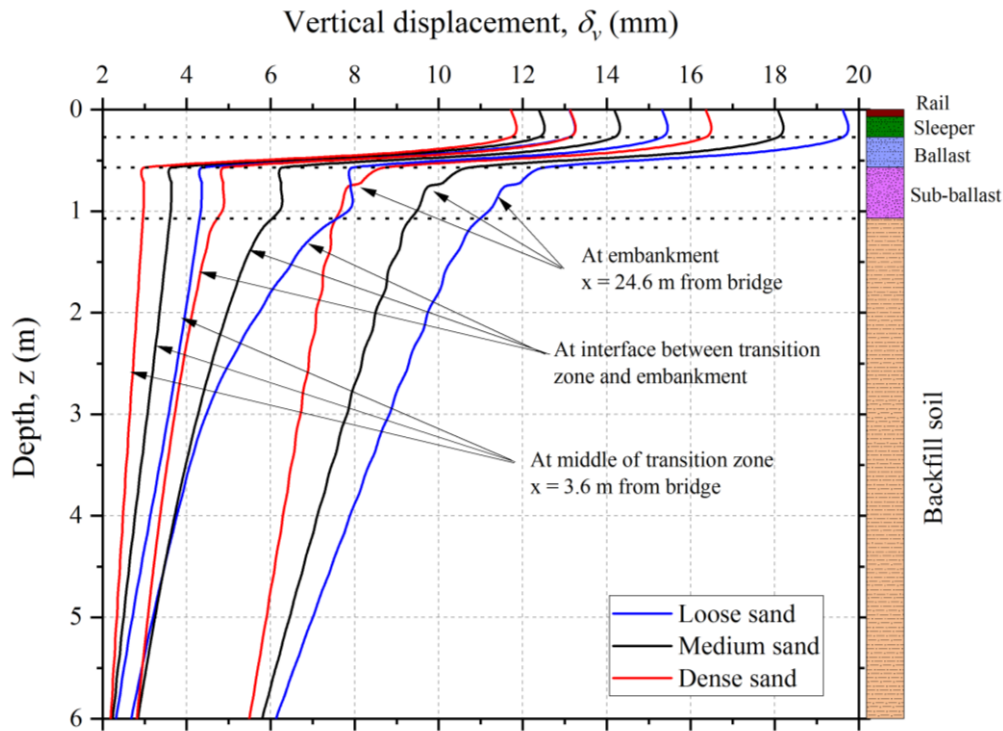


Fig. 4.11 Variation of Vertical Displacement with Depth for Different Backfill Soils.

4.5 EQUIVALENT DYNAMIC LOADING: SIMULATION AND RESULTS

The dynamic amplification factor (DAF) is a dimensionless dynamic impact factor used to simulate the dynamic effects of the moving train over the tracks. In the present study, the DAF values are evaluated for different train speeds such as 60, 100, 150, and 200 km/h. The past literature suggests several methods to calculate the value of DAF. The DAF value is evaluated by using the equivalent dynamic wheel load method (Shin *et al.*, 2002; RTRI, 1996) as

$$DAF = \left(1 + \frac{0.3V}{100}\right) (1 + C) \quad (4.9)$$

where V is the velocity of the train in km/h and C is the coefficient equal to 0.3. These amplification factors are multiplied with the static train wheel axle loading (Q_w) to simulate the dynamic train wheel axle loading effect. These equivalent coupled bogie loadings corresponding to different speeds are applied at the different locations such as embankment, transition zone and bridge in the FE domain and simulations are performed. Figure 4.12 shows the variation of ballast displacement across the length of the model from the bridge to the embankment. It is seen that the consideration of DAF in lieu of the train speed captured the dynamic loading effects. The comparison of displacements due to different train speeds highlights the predominant difference in the ballast settlement at the embankment, transition zone, and the bridge. The higher DAF results in higher displacement throughout the bridge structure. The results obtained in the present study are consistent with those reported in the previous studies (e.g., Coelho *et al.*, 2011). The effect of the dynamic train coupled bogie loading on the track displacement is also evaluated for different thickness and fall in the inclination of the approach slab.

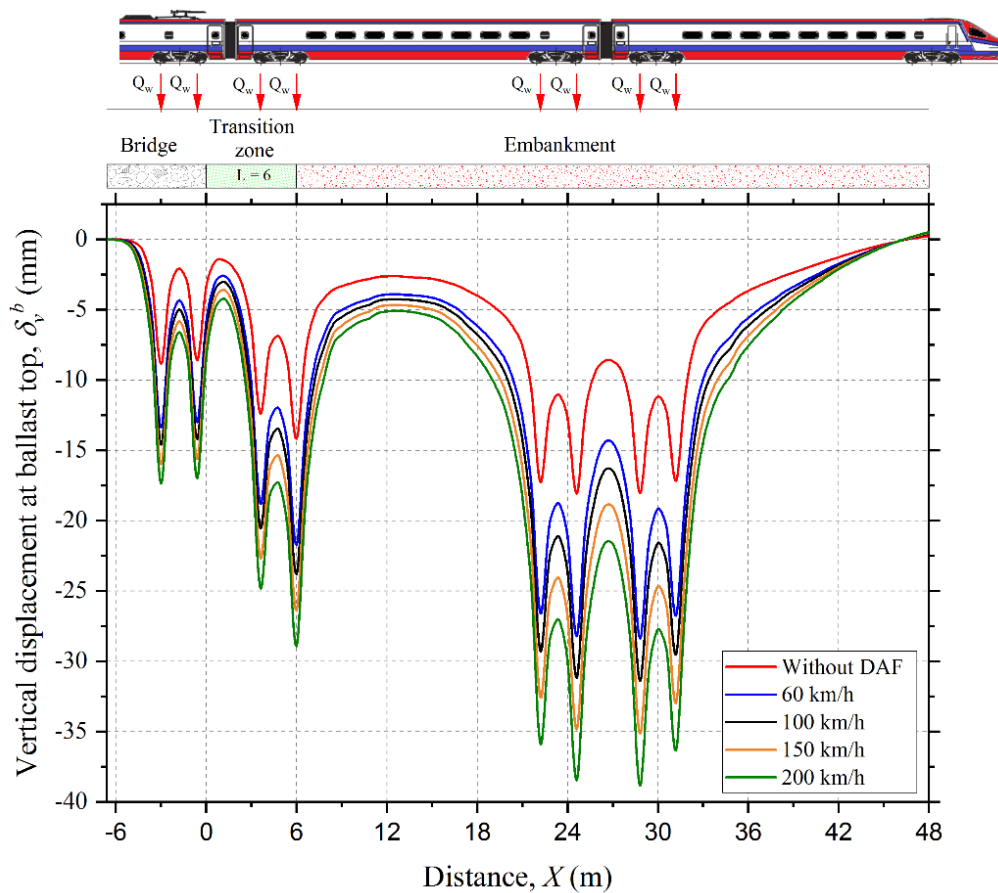
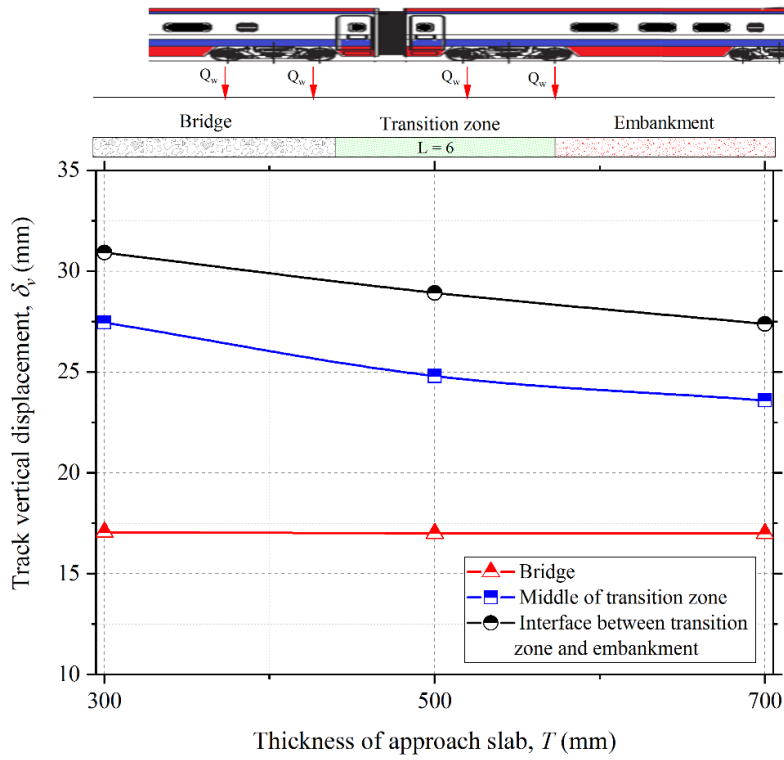


Fig. 4.12 Variation of Displacement at the Top of Ballast due to Change in Train Velocity.

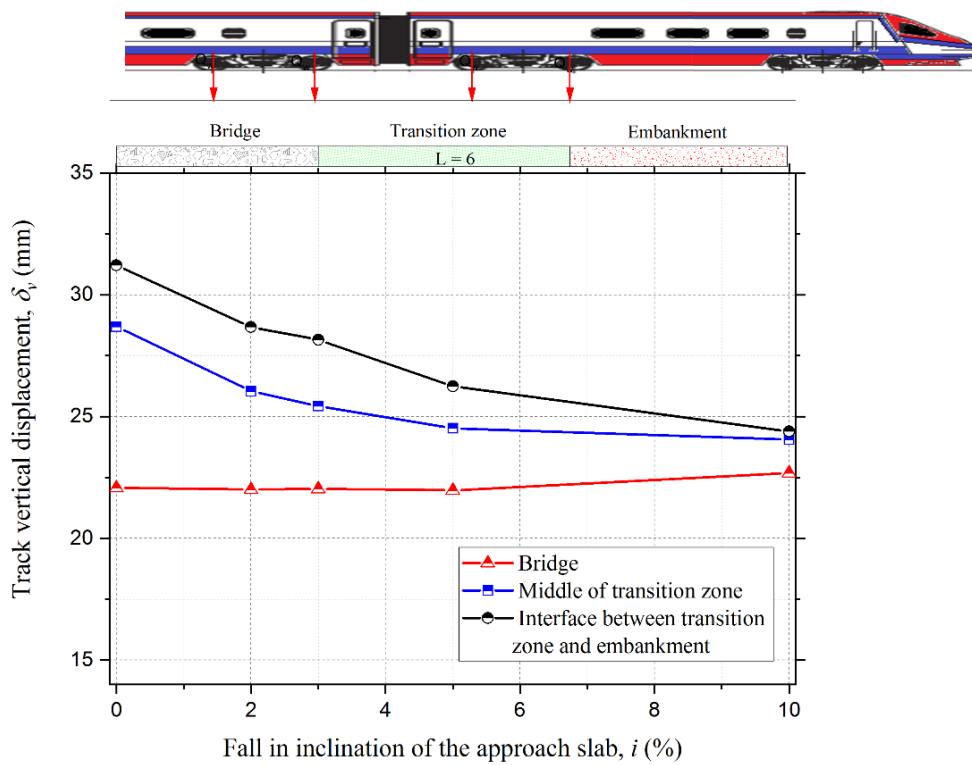
4.5.1 Variation in Thickness and Fall in Inclination of the Approach Slab

The track displacement for equivalent dynamic train coupled bogie loading is evaluated for different thicknesses of the approach slab and the results are depicted in Figure 4.13(a). The height of the integral abutment and length of the approach slab are kept constant as 5 m and 6 m, respectively. The backfill soil considered is the medium sand. The results show that the track displacement reduces with the increase in the thickness of the approach slab. A similar trend is observed earlier for the static train wheel loading (see Section 4.3.2), but the displacements are increased significantly due to the equivalent dynamic train coupled bogie loading. The track displacement at the bridge deck is shown in comparison with the transition zone. Since the geometric properties of the bridge deck section are not varied, hence the track displacement at the bridge deck is independent of the transition zone. The load coming on the bridge may change slightly due to variations in thickness of the approach slab at the transition zone. However, in the present study, the loading on the bridge deck is kept constant. The geometric properties of the transition zone are varied such as thickness and fall in inclination of the approach slab. At the bridge section, the rail and sleeper are supported on the ballast and the ballast is supported on the bridge deck. The load from the bridge deck is transferred to the abutment. At the transition zone, the ballast layer is supported on the approach slab, and in turn this approach slab is supported directly on the backfill soil. Because of this load transfer mechanism, the track displacement changes only in the transition zone area.

The fall in inclination of the approach slab is varied from 0% to 10%. Figure 4.13(b) shows the variation of the track displacement with the fall in inclination of the approach slab. The decrease in the track displacement is observed, similarly as in the case of static train loading (see Section 4.3.4). However, the magnitudes of the track displacement are much higher due to the equivalent dynamic train coupled bogie loading.



(a)



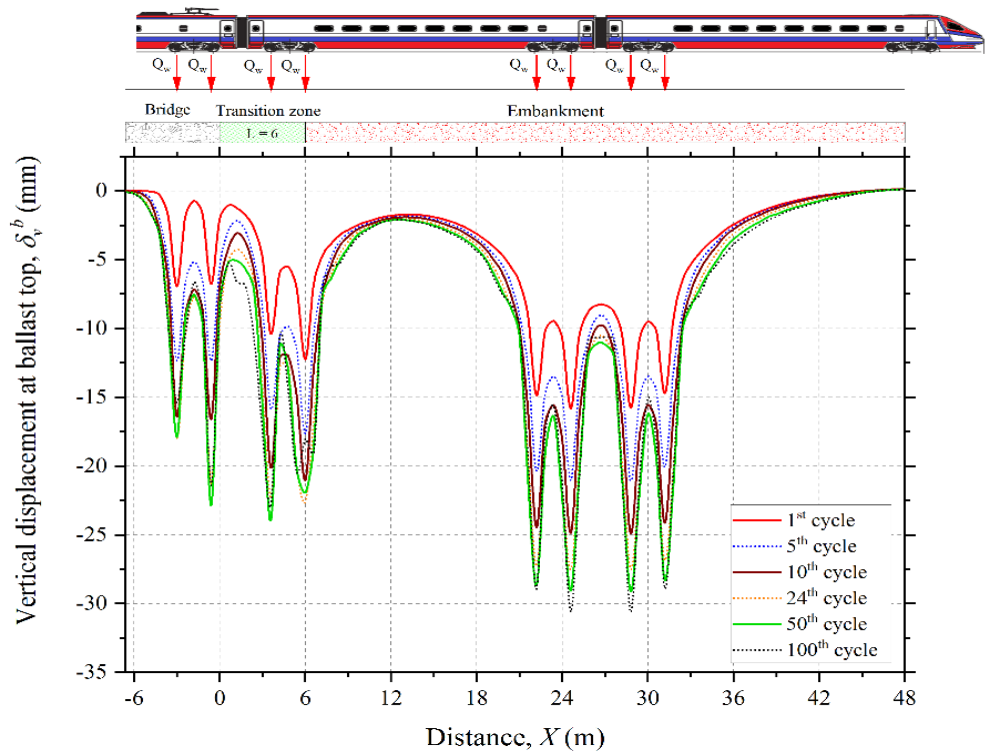
(b)

Fig. 4.13 Variation of Track Displacement with (a) Thickness, and (b) Fall in Inclination of Approach Slab.

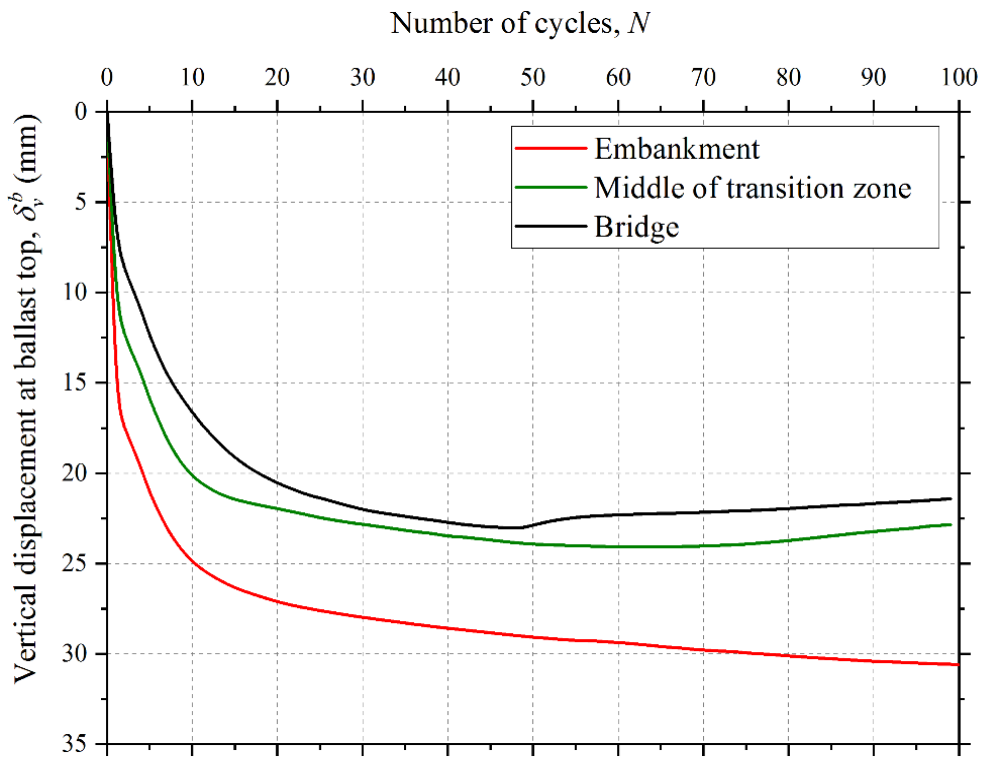
4.6 BEHAVIOUR OF IARB UNDER CYCLIC TRAIN WHEEL LOADING

The train wheel loading acts as the repetitive wheel loading during the entire train passage at a point on the rail track above the sleeper. The train wheel axle load for the entire train passage is simulated via a stationary cyclic (repetitive) wheel loading. These cyclic loading are applied in coupled bogie loading configuration at the bridge, the middle of the transition zone, the interface of the transition–embankment, and the embankment. The magnitude of the applied individual train wheel axle load (Q_w) is 100 kN. The frequency of train wheel axle loading is considered as 1 Hz. The effect of cyclic train wheel axle loading on the displacement of the ballast layer increases as the number of cycles of train loading increases. Figure 4.14(a) depicts the ballast displacement for the entire stretch of the FE model after the 1st, 5th, 10th, 24th, 50th, and 100th cycles of train loading. Due to the cyclic train loading, the ballast displacement increases rapidly for the first ten cycles, then slowly increases for the remaining cycles of the train loading.

Figure 4.14(b) shows the displacement at the top of the ballast layer at the bridge, transition zone, and the embankment after 100 cycles of train wheel loading. It is observed that the displacement at the top of the ballast layer stabilizes and remains almost constant after 100 cycles of loading. Similar trend is observed in the displacement at the top of the ballast layer for the center of the transition zone. The value of displacement at the top of the ballast layer for the bridge and the middle of the transition zone are closer. At the embankment zone, with the increase in the number of cycles of train loading, the displacement at the top of the ballast layer is found to increase as in Figure 4.14(b).



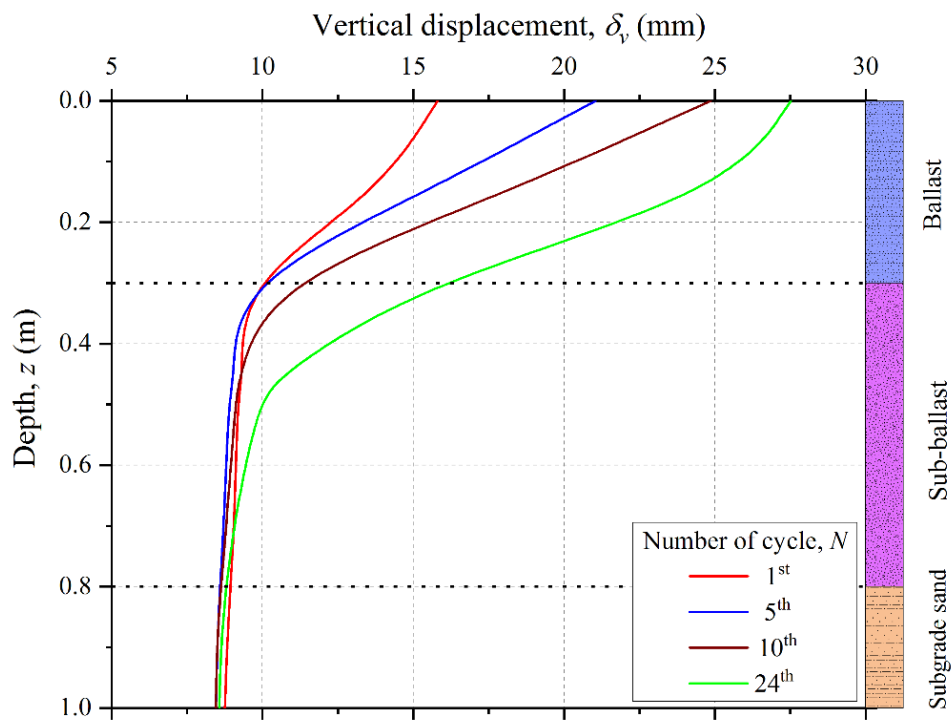
(a)



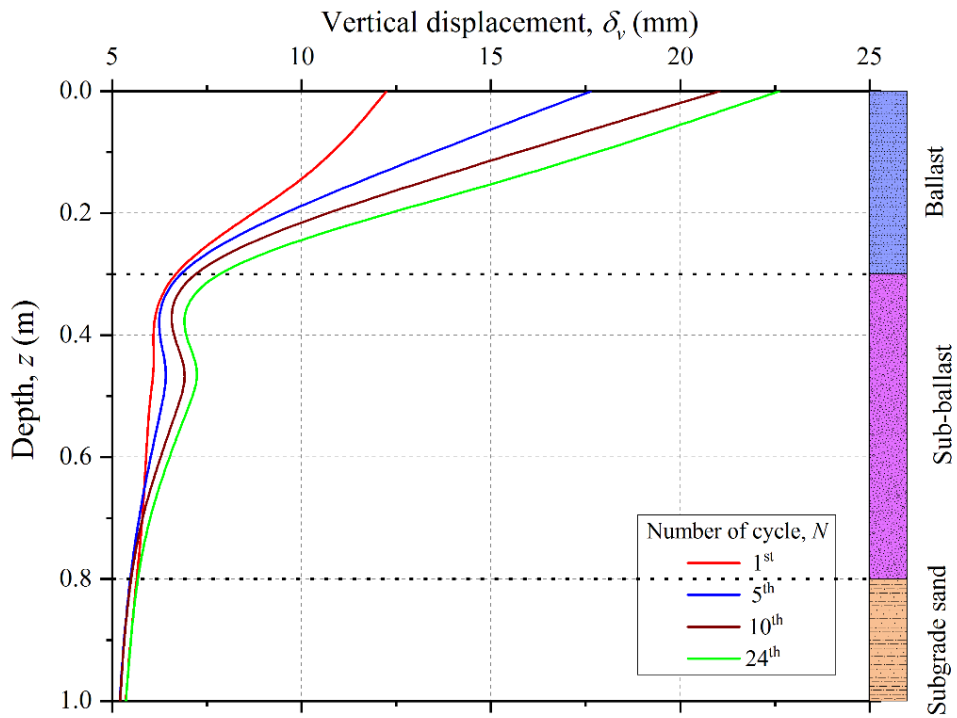
(b)

Fig. 4.14 Variation of Ballast Displacement (a) at 1st, 5th, 10th, 24th, 50th, and 100th Cycle across the FE Domain, and (b) with Number of Cycles of Loading.

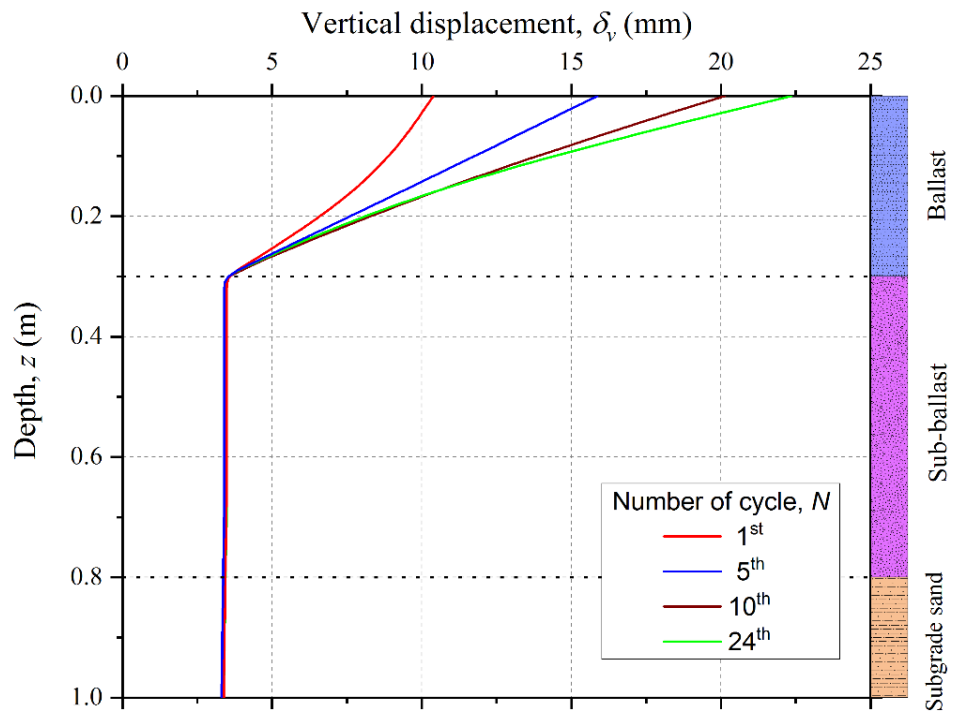
The vertical displacement profiles across the depth at different sections such as the embankment, the interface between the transition zone and embankment, and the middle of the transition zone are shown in Figure 4.15(a) – (c) for different cycles of train loading. It is noted that the increase in the number of loading cycles increases the vertical displacement of the track. For the 24th cycle of train loading, the vertical displacement profiles up to a depth of 3 m are only shown in Figure 4.16. From the results, it is seen that the vertical displacement is maximum at the embankment and minimum at the bridge.



(a)



(b)



(c)

Fig. 4.15 Variation of Vertical Displacement with Depth at Different Locations along the Track at (a) Embankment, (b) Interface between the Embankment and Transition Zone, and (c) Middle of the Transition Zone.

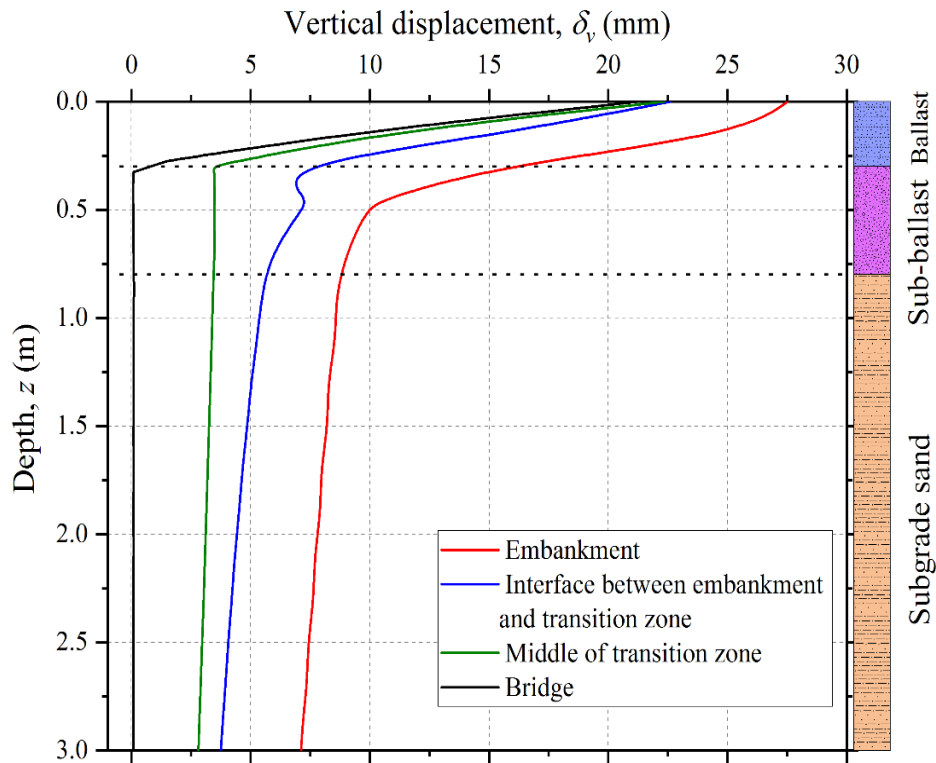


Fig. 4.16 Variation of Vertical Displacement with Depth at Different Locations along the Track for 24th Cycle of Train Loading.

4.7 SUMMARY

The 2D FE analysis of the transition zone of the IARB is performed using ABAQUS software under the static and cyclic train coupled bogie loadings. Firstly, the FE model is successfully validated with the published field data. Subsequently, parametric studies are conducted to explore the behaviour of the track transition under varying approach slab geometry such as the length, thickness and fall in the inclination of the approach slab, height of the integral abutment and backfill soil type. These parametric studies are conducted under the static train wheel axle loading applied as coupled bogie load configuration at the specific locations such as the embankment, transition zone and bridge section in the FE model. The dynamic effects of the variation of train speed are simulated using dynamic amplification factors. The variation in the thickness and fall in the inclination of the approach slab for the equivalent dynamic train coupled bogie loading is investigated. The repetitive cycles of train wheel axle loadings at specific points are simulated as cyclic train wheel axle loadings. The FE simulations are performed for a total of 100 cycles of train wheel axle loadings, and the corresponding results are presented.

In the next chapter, the 2D FE analysis of the IARB with approach slab under realistic moving train loading is carried out and the results are presented.

CHAPTER 5

DYNAMIC BEHAVIOUR OF INTEGRAL ABUTMENT BRIDGE TRANSITION UNDER MOVING TRAIN LOADS

5.1 INTRODUCTION

In the previous chapter, the behaviour of the IARB with approach slab subjected to equivalent train loading is studied. The train loadings were applied as the static ones as opposed to the actual moving loads imposed by the train movement. It is noted that most of the existing studies on the behaviour of transition zones of the IARBs have considered the equivalent static loads. The studies pertaining to the realistic dynamic behaviour of the IARBs with approach slab under the moving train loads are limited. In this chapter, the dynamic behaviour of the transition zone of the IARB under moving train loads is evaluated using the 2D plane-strain FE analyses.

Firstly, the FE model is validated by comparing its response with the field data reported in the published literature. Subsequently, the influence of varying approach slab geometry (length, thickness, inclination, and shape) on the performance of the transition zone of the IARB is explored. Finally, the influence of the backfill soil type, train movement direction and train speed on the behaviour of track-transition zone is investigated. The key novelty in the present study is the more realistic consideration of the moving train loads on the behaviour of the IARB-embankment transition zones, as opposed to the existing studies that considered only the equivalent static loading. Other key features include: (a) the simulation of complex stress distribution in the track substructure layers, which involves a reversal of the direction of shear stresses as the wheel moves along the track, (b) investigation on the influence of train movement direction on the response of the track in the transition zone, and (c) prediction of differential movement along the length of the track. This chapter contributes immensely to enhance the current understanding of the behaviour of IARBs subjected to moving train loading and identifies the parameters that influence performance of the IARBs.

5.2 FINITE ELEMENT MODELLING OF IARB

The 2D plane-strain FE analysis has been adopted in the present study instead of two-and-half-dimensional (2.5 D) or three-dimensional (3D) approaches to limit the required computational time, while providing reasonably accurate results. Indeed, there are some limitations associated with the 2D modelling approach, such as, inability to realistically simulate the track conditions (complex geometry and 3D loading), dynamic wave propagation and lateral spreading of the granular substructure layers. However, the 2D models are generally simple, require less computational resources and can readily be used by the practising engineers on a routine basis.

5.2.1 Description of Geometry

In this study, an IARB with an approach slab is modelled using FE based program ABAQUS. Figure 5.1 shows the 2D plane-strain FE model of the IARB used in the analyses. The geometry and dimensions of the various components of the IARB are selected based on the published data on the existing railway bridge transitions (Al-Qarawi *et al.*, 2020).

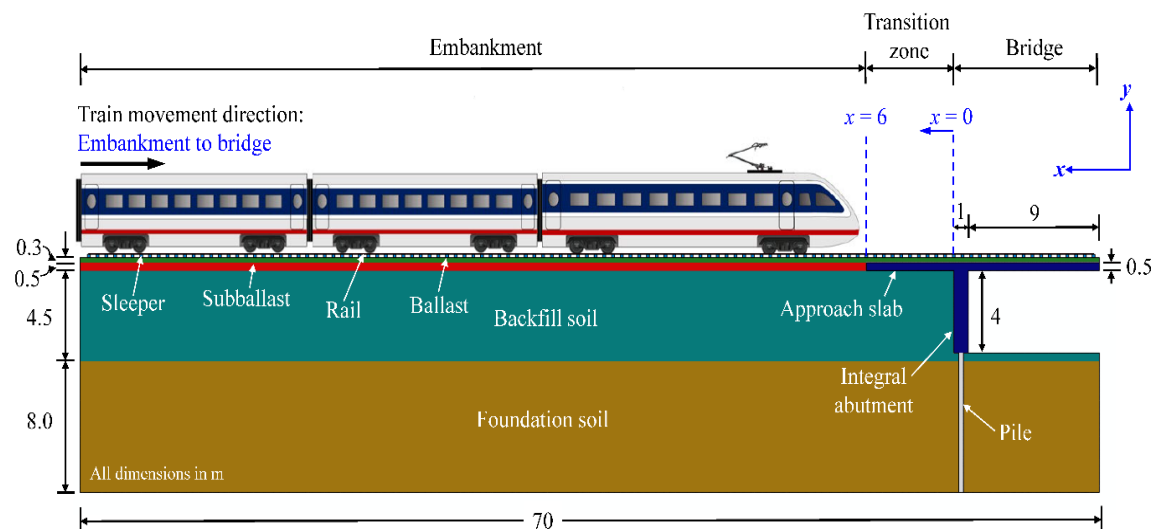


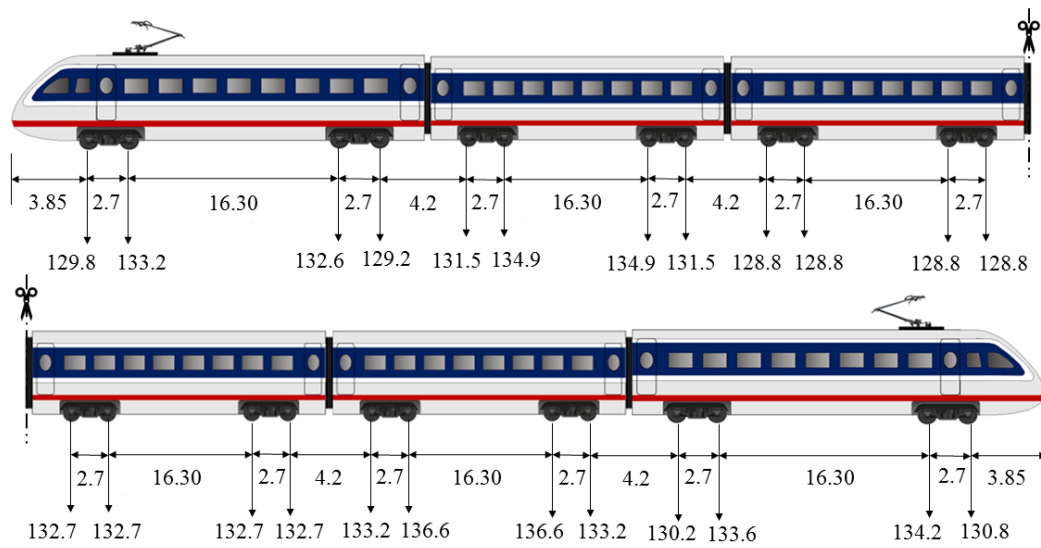
Fig. 5.1 Schematic Geometry of Integral Abutment Railway Bridge.

The total length of the model is 70 m, with 116 sleepers equally spaced at 0.6 m intervals. An approach slab is provided to allow a smooth transition of the track stiffness. The IARB consists of a steel girder of 1.5 m depth, a deck slab of 0.5 m thickness, and the integral abutment is supported on the HP pile. The width and height of the abutment are taken as 1 m and 4 m, respectively. The H-pile is 8 m long and is

firmly socketed into the bedrock. The railway track comprises a steel rail supported by concrete sleepers resting on the ballast bed, which overlies the subballast layer, approach slab or deck slab, depending on the location. The rail is modelled as a rectangle with a moment of inertia equivalent to that of a 60 kg/m rail. The height and width of concrete sleepers are taken as 0.2 m and 0.2 m, respectively. The substructure of the railway track in the embankment portion consists of ballast, subballast, backfill and foundation soils. The thickness of the ballast and subballast layers are considered as 0.3 m and 0.5 m, respectively.

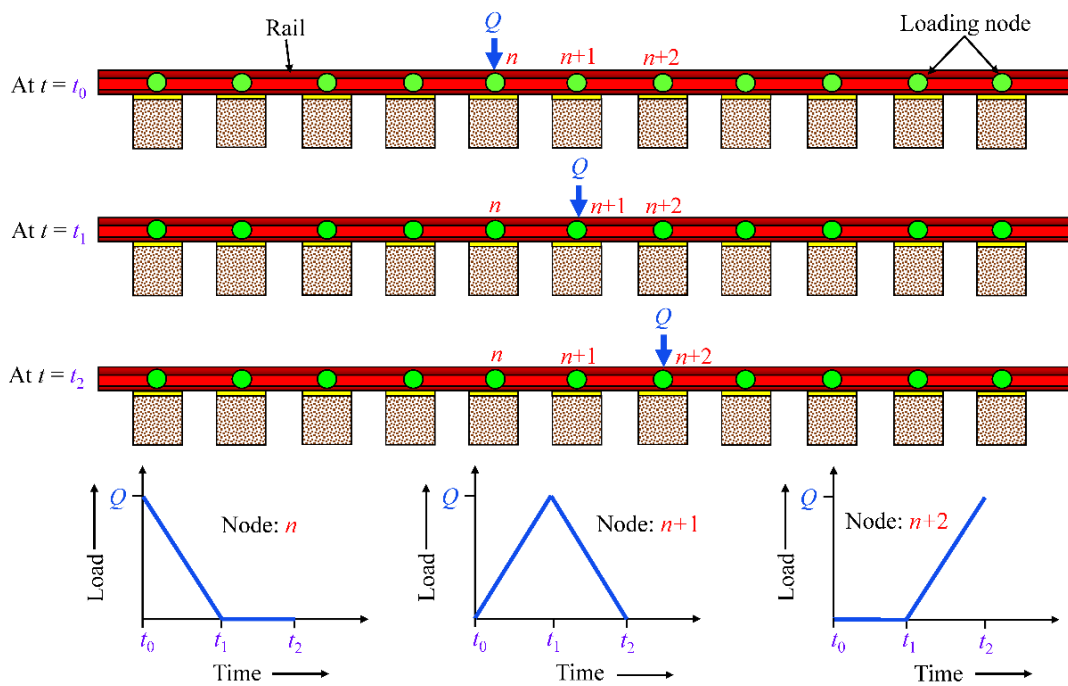
5.2.2 Moving Train Load Simulation

Figure 5.2(a) shows the configuration of the Alfa Pendular train, which is used to replicate the moving train loads (Paixao *et al.*, 2014). In this study, the moving load is simulated by applying a point load at the top of the rail above each sleeper (known as loading node), as shown in Figure 5.2(b), whose magnitude varies with time depending on the train configuration and speed (Hall, 2003; Punetha *et al.*, 2021). The point loads are triangular pulses distributed between three nodes. These triangular pulses are moved from node to node by a time step equal to the node spacing of the loading node divided by the speed of the moving train. The magnitude of the point load at a loading node increases as the train wheel moves towards it. It reaches a maximum value when the wheel is exactly above the loading node, and then decreases as the wheel moves away from the node. This variation in magnitude of load is applied to each loading node as load-time history which is calculated for different train speeds. The load-time history is calculated for all the loading nodes. The dynamic behaviour of the track is evaluated for a single passage of Alfa Pendular train running at a speed of 200 km/h (unless otherwise specified), and the corresponding results are presented in Section 5.3.



All dimensions and loads are in m and kN, respectively. Not to scale

(a)



(b)

Fig. 5.2 (a) Alfa Pendular Train Configuration with Distance between Axles (in m) and approximate Axle Loads (in kN) (Paixao *et al.*, 2014), and (b) Variation of Wheel Load with Time at Different Loading Nodes.

5.2.3 Material Properties and Constitutive Model

Table 5.1 lists the values of the material properties used in the FE simulations. These values are chosen based on the existing literature and the published technical reports. The rail, sleeper, integral abutment, approach slab and H-pile are modelled using the linear elastic model. The behaviour of the backfill and foundation soils is simulated using the MC model. The behaviour of the ballast and subballast is simulated using the Drucker-Prager model with a non-associated flow rule (Li *et al.*, 2018; Leshchinsky and Ling, 2013). The material damping in the FE model is captured using Rayleigh damping, and the values of damping coefficients, ' α ' and ' β ' for each of the track materials are determined. The evaluation procedure of Rayleigh damping coefficient is given in Section 4.2.2 (Chapter 4). Table 5.2 gives the dynamic parameters of various layers considered in the FE simulation. The natural frequencies of the ballast and subballast layers are very high due to their smaller thicknesses, which result in higher damping in the initial frequency range closer to the loading frequency. Hence, the target frequencies of 3 and 20 Hz are adopted for the ballast and subballast layers (Shih *et al.*, 2017).

Table 5.1 Material properties used in the FE simulation (data sourced from ¹Li *et al.* 2018; ²Al-Qarawi *et al.* 2020; ³Indraratna and Nimbalkar 2013).

| Component | Material Model | Density, ρ (kg/m ³) | Young's Modulus, E (MPa) | Poisson's Ratio, ν | Friction Angle, ϕ' (°) | Dilation Angle, ψ (°) | Cohesion, c' (kPa) |
|---|----------------|--------------------------------------|----------------------------|------------------------|-----------------------------|----------------------------|----------------------|
| Rail (steel) ¹ | LE | 7,700 | 206,000 | 0.30 | – | – | – |
| Sleeper (concrete) ¹ | LE | 2,350 | 25,500 | 0.20 | – | – | – |
| Ballast ¹ | DP | 1,700 | 200 | 0.25 | 50 | 20 | 1 |
| Subballast ³ | DP | 1,800 | 140 | 0.35 | 45 | 5 | 1.42 |
| Backfill soil ² | MC | 1,835 | 35 | 0.35 | 38 | 8 | 6 |
| Foundation soil ² | MC | 1,682 | 30 | 0.30 | 20 | 1 | 20 |
| Integral abutment (concrete) ² | LE | 2,385 | 30,000 | 0.25 | – | – | – |
| HP pile (steel) ² | LE | 7,951 | 200,000 | 0.30 | – | – | – |
| Approach slab (concrete) ² | LE | 2,385 | 30,000 | 0.25 | – | – | – |

Note: LE: Linear elastic; DP: Drucker-Prager; MC: Mohr-Coulomb.

Table 5.2 Parameters used in dynamic FE simulation.

| Material | Thickness of Layer, H | Shear Wave Velocity, V_s (m/s) | Damping Ratio, D_R (%) | Angular Frequencies | | Rayleigh Coefficients | |
|--------------------------|-------------------------|----------------------------------|--------------------------|---------------------|--------------------|-----------------------------|-------------|
| | | | | ω_1 (rad/s) | ω_3 (rad/s) | α (s ⁻¹) | β (s) |
| Ballast | 0.3 | 216.93 | 4 | 18.85 | 125.66 | 1.31 | 0.0005 |
| Subballast | 0.5 | 169.72 | 4 | 18.85 | 125.66 | 1.31 | 0.0005 |
| Backfill soil | 4.5 | 84.05 | 5 | 29.33 | 146.69 | 2.44 | 0.0005 |
| Foundation soil/Subgrade | 8 | 82.82 | 5 | 16.26 | 81.31 | 1.355 | 0.001 |

5.2.4 Interface Interactions

The soil-structure interaction between the integral abutment-backfill soil, pile-foundation soil, sleeper-ballast, and approach slab-ballast is simulated using the Coulomb friction model available in ABAQUS. The normal and tangential contact behaviours are simulated using surface-to-surface interaction by employing the master-slave concept. The normal contact behaviour is simulated as ‘*hard contact*’ in which the normal stresses are transferred under compression. The tangential contact is simulated using a penalty friction algorithm for which the interface friction coefficient between the two surfaces is evaluated by Equations 4.6 and 4.7 (see Chapter 4, Section 4.2.3).

5.2.5 FE Mesh Discretisation, Boundary Conditions and Modelling Procedure

The 2D plane-strain FE model of the transition zone of the IARB is discretised using a 4-noded bilinear plane-strain element with reduced integration (CPE4R) and hourglass control, as shown in Figure 5.3. The entire FE mesh consists of 69,224 elements. A finer mesh is used for the rail, sleeper, ballast and subballast layers. The slightly coarser mesh is used for the backfill and foundation soils. The final mesh configuration is selected based on the results of the mesh sensitivity analyses, as shown in Figure 5.4. Based on the mesh sensitivity analysis, element size of 0.05 m is assigned to the rail, sleeper, ballast, subballast, approach slab and integral abutment. An element of size of 0.1 m is used for the backfill and foundation soils. A finer discretisation near the loading region and a progressively coarser meshing away from this zone provided a trade-off between the computational time and the desired accuracy. The standard boundary conditions are adopted for the FE model in which the nodes along the bottom boundary

are considered fixed. The roller support and symmetric boundary conditions are provided at the vertical boundaries towards the left (embankment side) and right side of the model (IAB side), respectively. An implicit FE analysis is performed to study the behaviour of the transition zone of the IARB under moving train loads in the following steps: (a) a geostatic stress field is applied to generate the initial effective stresses in the model, and (b) moving train loads are applied on the loading nodes. The validation of the FE model is performed by comparing its response with the field data reported in the published literature. (Chapter 4, Section 4.2)

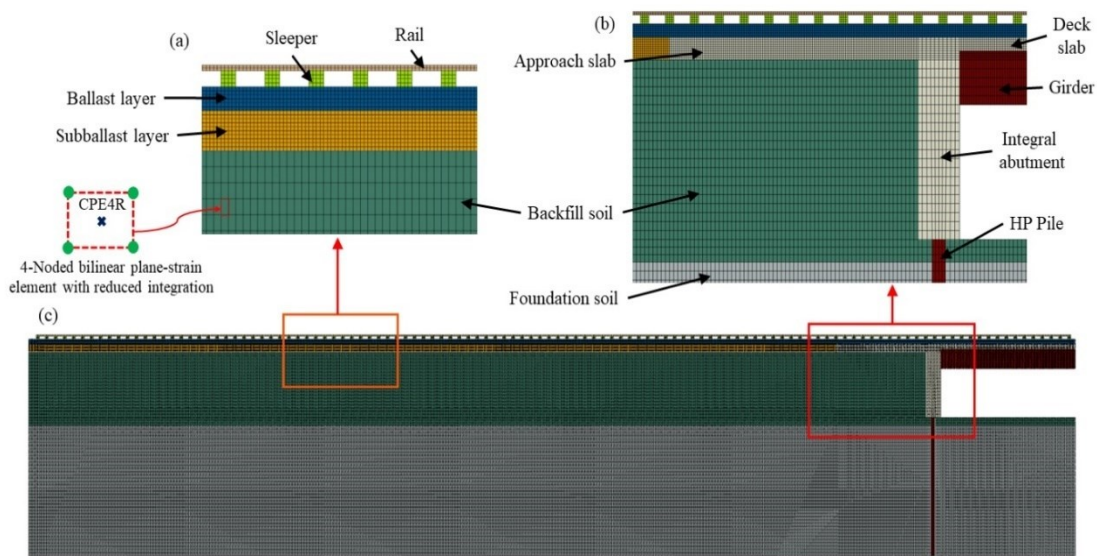


Fig. 5.3 FE Mesh of the Typical IARB with Approach Slab.

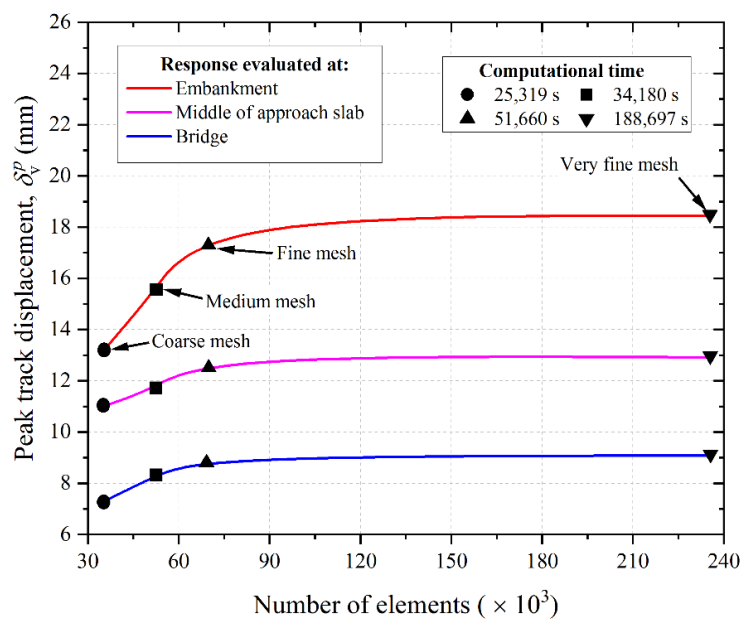


Fig. 5.4 Mesh Sensitivity Analysis for IARB Model.

5.3 RESULTS AND DISCUSSION

A parametric analysis is conducted using the FE model of the transition zone of the IARB to understand its behaviour comprehensively under moving train loads. The influence of parameters such as approach slab geometry (length, thickness, inclination, and shape), backfill soil type, and train movement direction on the dynamic behaviour of the track is investigated. Table 5.3 gives the nominal values and range of the parameters considered in the analyses. The range of the parameters is selected based on the published data (see e.g., Asghari *et al.*, 2021; Sharpe *et al.*, 2002; Varandas *et al.*, 2016). The value of only one parameter is varied in each analysis, and the other parameters are assigned nominal values to single out the influence of the varying parameter. This study is essential to highlight the factors that significantly affect the dynamic response of the railway tracks of the IARBs. It is to be noted that the peak track displacement refers to the maximum value of the total displacement (which includes both the elastic and inelastic components) during one complete passage of the train loading which is equivalent to Alfa Pendular train loading.

Table 5.3 Nominal values and range of parameters considered in parametric studies.

| Parameter | Range or Value |
|-------------------------------|---|
| Approach slab length (m) | 3 – 12 (6) |
| Approach slab thickness (m) | 0.3 – 0.7 (0.5) |
| Approach slab inclination (%) | 0 – 10 (0) |
| Approach slab shape | Rectangular, trapezoidal, and stepped |
| Backfill soil type | Loose, medium, and dense sand |
| Train movement direction | Embankment to bridge and bridge to embankment |

5.3.1 Influence of Approach Slab Geometry

5.3.1.1 Length

The length of the approach slab (L) is varied between 3 and 12 m to analyse its effect on the performance of the railway track transition. This range has been selected based on the recommended values of L by several organisations. The minimum value of L in a transition usually differs from one organisation to another. The Indian Ministry of Railways specifies a minimum length of 4 m (Indian railway bridge manual, 1998), and the American Railway Engineering and Maintenance-of-Way Association (AREMA)

recommends a minimum length of 6 m for the approach slab (Smith *et al.*, 2003). No limit is specified for the maximum length of the approach slab by these organisations.

Figure 5.5 shows the variation of vertical track displacement with distance along the track for different L values. It is apparent that the approach slab provides a gradual transition of vertical displacement from the softer side (embankment) towards the stiffer side (bridge). The track displacements at the embankment, middle of the approach slab and bridge are 7.6 mm, 1.7 mm to 5.2 mm (depending on L), and 0.5 mm, respectively. The displacement gradient (change in track displacement per unit length) decreases with the increase in L , implying that the longer approach slabs provide a more gradual change in the displacement as compared to the shorter slabs. Figure 5.6 depicts the variation of contact stress above the backfill soil along the length of the track. The increase in L leads to a reduction in stress transmitted to the backfill soil due to an increment in the contact length between the slab and the backfill soil. As evident from Figure 5.6, the peak contact stresses below the approach slab are much lower than that below the subballast. Therefore, the deformation in the backfill soil near the bridge approach decreases with the increase in value of L . It can be noted that there is a stress concentration below the free end of the approach slab, which may cause significant localised deformation. Hence, a sleeper slab must be provided at the free end of the approach slab to prevent this localised deformation.

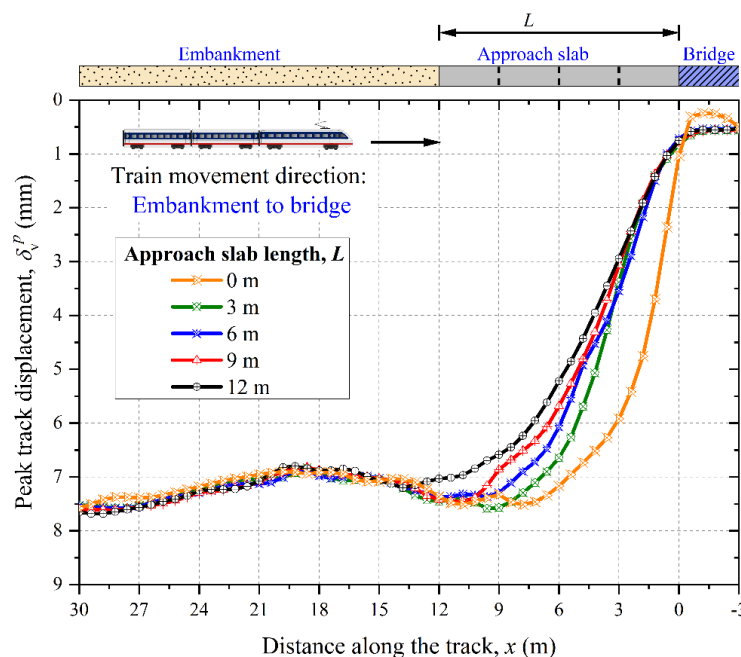


Fig. 5.5 Variation of Vertical Displacement with Distance along the Track for Different Lengths of Approach Slab.

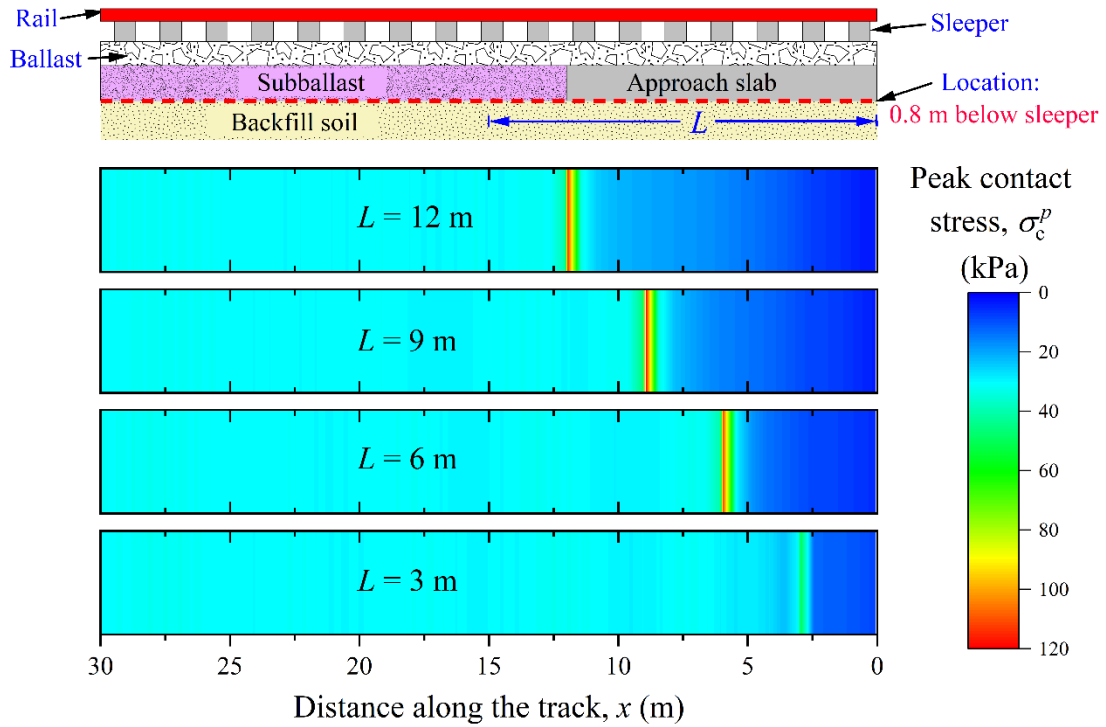


Fig. 5.6 Variation of Contact Stress above Backfill along the Track for Different Lengths of Approach Slab.

Figure 5.7 depicts the variation of peak tensile stress on the rail along the length of the track. It can be observed that the peak rail stresses are lower in the transition zone compared to that in the embankment region. This is due to a larger bending of the rail in the embankment region as compared to the transition zone. In the absence of approach slab, the rail stress at the interface of the bridge and embankment zone is the maximum. With the introduction of the approach slab, this stress reduces and shifts to the embankment-approach slab interface. Nevertheless, the length of the approach slab has a small effect on the magnitude of rail stresses. This observation is consistent with the previous studies (e.g., Asghari *et al.*, 2021).

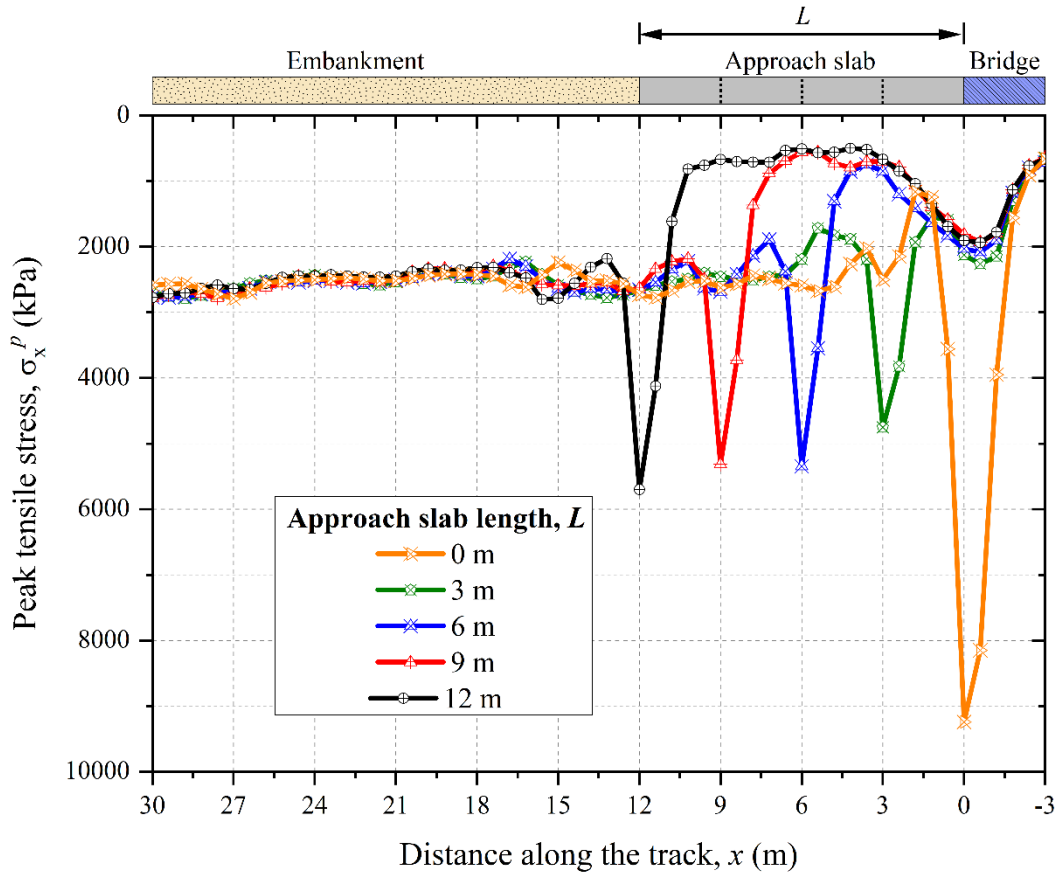


Fig. 5.7 Variation of Peak Tensile Stress on the Rail along the Length of the Track for Different Lengths of Approach Slab.

5.3.1.2 Thickness

The approach slab thickness (T) is varied between 300 mm and 700 mm to investigate its influence on the performance of railway track transition. Figure 5.8 shows the variation of peak vertical track displacement with distance along the slab (normalised with respect to L) for different T values. It is observed from the figure that the track displacement decreases with the increase in T . The track displacement at the middle of the approach slab ($x/L = 0.5$) decreases by 14.3%, 22.4%, 28.3% and 34.1% for the increase in the slab thickness from the base value of 300 mm to 400 mm, 500 mm, 600 mm, and 700 mm, respectively. This observation is attributed to the increased rigidity of the slab due to the increased approach slab thickness. Moreover, the required thickness of the backfill soil also decreases with the increase in T , thereby contributing less to the track displacement.

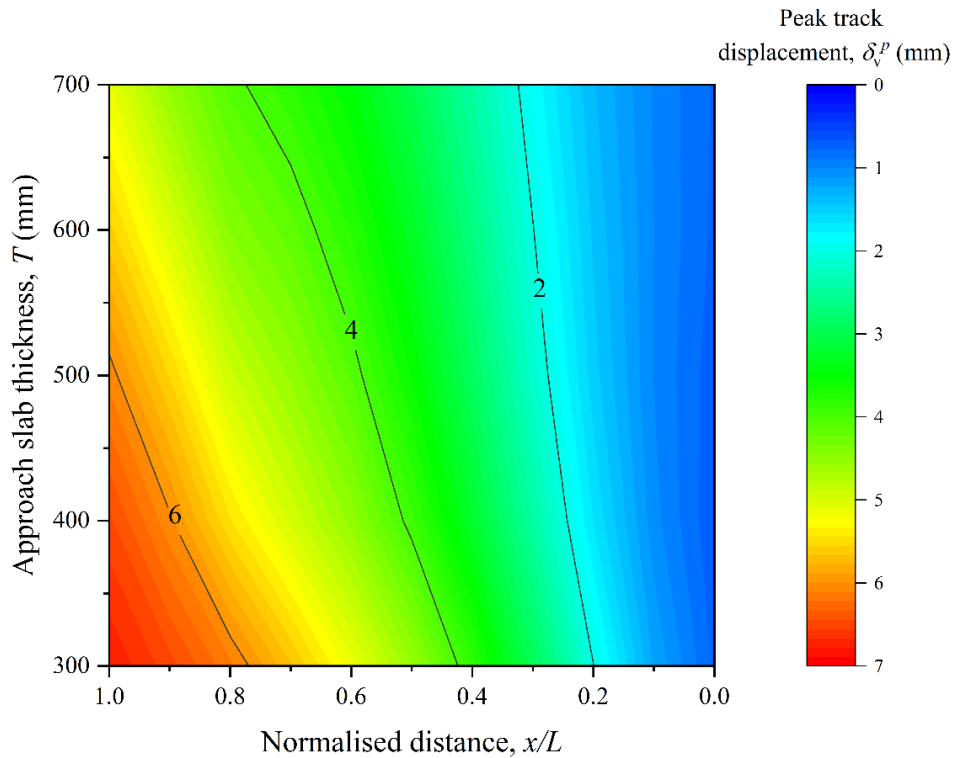


Fig. 5.8 Variation of Peak Track Displacement along the Approach Slab Length for Different Thicknesses.

5.3.1.3 Inclination

The fall in inclination (i) of the approach slab is varied from 0% to 10% to investigate its influence on the performance of the track transition. In the analysis, the thickness of the approach slab (h_a) is kept constant, and the thickness of the ballast layer at the free end of the slab (h_b) is increased by Δh (see Figure 4.9 in Chapter 4, Section 4.3.4). It can be observed from Figure 5.9 that the peak track displacement decreases with the increase in the value of i . In the middle of the approach slab, the peak track displacement decreases by 1.9% to 8.9% as compared to the nominal case (i.e., at $i = 0\%$) in which i is increased from 2% to 10%. One of the reasons for such behaviour is the stress reduction within the ballast layer with increasing i . This can be visualised in Figures 5.10(a) – 5.10(c), which depict the variation of peak vertical stress along the depth of the ballast layer at different locations of the transition zone ($x = 1.2$ m, 3 m, and 4.8 m) for different i values. It can be observed that the peak vertical stress at all the three locations typically reduced with an increase in the inclination of the approach slab. Another possible reason is that the thickness of the backfill soil below the approach slab is decreased with the increase in i , thereby contributing less to the total track displacement.

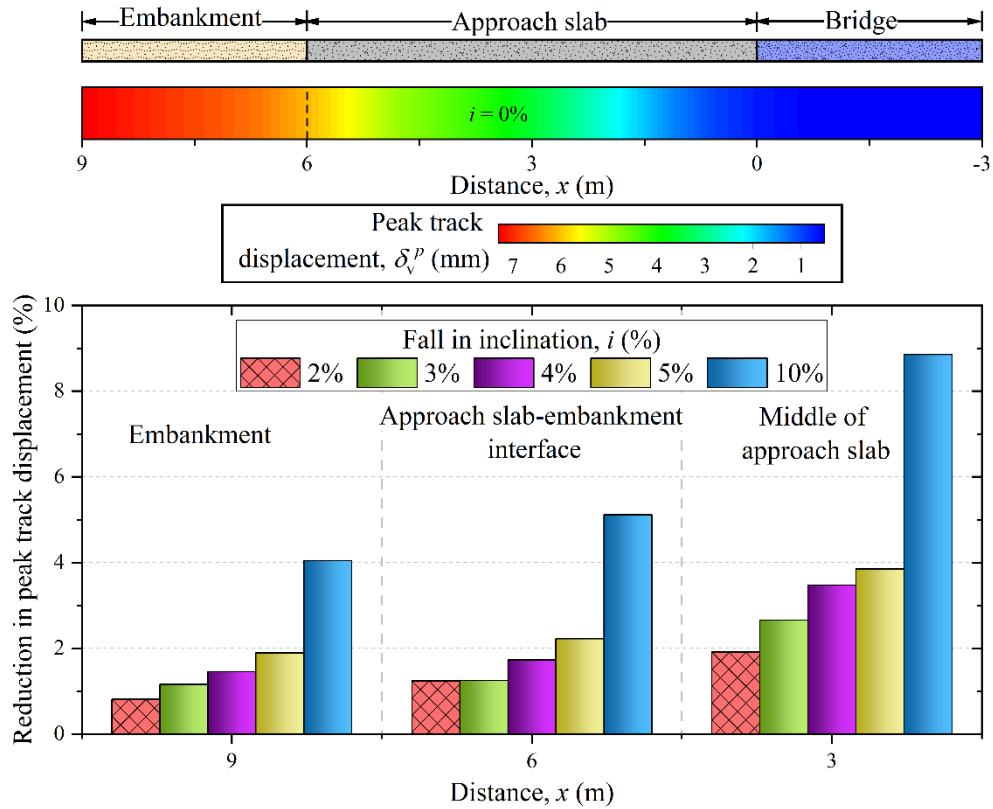


Fig. 5.9 Reduction in Peak Track Displacement for Different Fall in Inclination of Approach Slab.

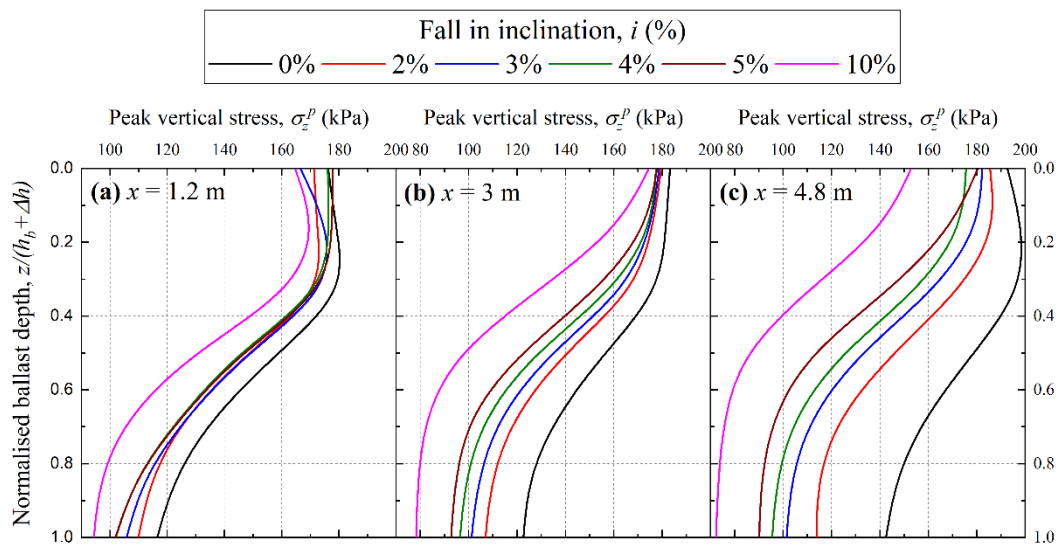


Fig. 5.10 Variation of Vertical Stress along the Depth of Ballast Layer at: (a) $x = 1.2$ m, (b) $x = 3$ m, and (c) $x = 4.8$ m.

5.3.1.4 Shape

In this section, the influence of the shape of the approach slab on the response of track transition is investigated. Three different shapes of the approach slab are considered, namely, rectangular, trapezoidal, and stepped (see Figure 5.11). For the rectangular shape, three different cases are considered: $T = 300$ mm, $T = 500$ mm, and $T = 700$ mm (R_1 , R_2 and R_3 , respectively). For the trapezoidal shape, three cases are considered: (i) thicknesses at the bridge side (T_b) and embankment side (T_e) are 500 mm and 300 mm, respectively, with slope at the bottom portion (T_1); (ii) $T_b = 700$ mm, $T_e = 500$ mm with slope at bottom portion (T_2); and (iii) $T_b = 500$ mm, $T_e = 300$ mm with slope at top portion (T_3) (see Figure 5.11). For the stepped case, T_b and T_e are considered as 500 mm and 300 mm, respectively with the steps provided in the top portion of the slab (S_1). The width of each step is taken as 1 m, and a total of six steps are considered. The variation of vertical displacement along the length of the track for different shapes of the approach slab is depicted in Figure 5.11. The results indicate that the track response in the case of R_3 and T_2 configurations is nearly identical, which suggest that the trapezoidal slabs are as effective as the rectangular slabs. Moreover, the trapezoidal slab (T_2) is more economical as its construction cost is less compared to the rectangular slab (R_3). Similarly, the responses of R_2 , T_1 and T_3 configurations are also similar. In addition, the track response remained the same on replacing the inclined surface (T_3) with steps (S_1). Thus, the trapezoidal shape is the most effective shape of the approach slab considered in this study in terms of construction cost. Apart from the construction cost, the trapezoidal approach slab can facilitate efficient water drainage by preventing the accumulation of water on the bridge approaches and reduces the risk of soil erosion. The trapezoidal configuration facilitates a gradual and smooth rise in track stiffness leading to the bridge, thereby reducing the stresses at the fixed end of the approach slab in relation to its dead weight. The above results also demonstrate the utility of the FE method in assessing the adequacy of different shapes of approach slabs in mitigating the differential movement at the embankment-IARB transition and selecting the most appropriate shape.

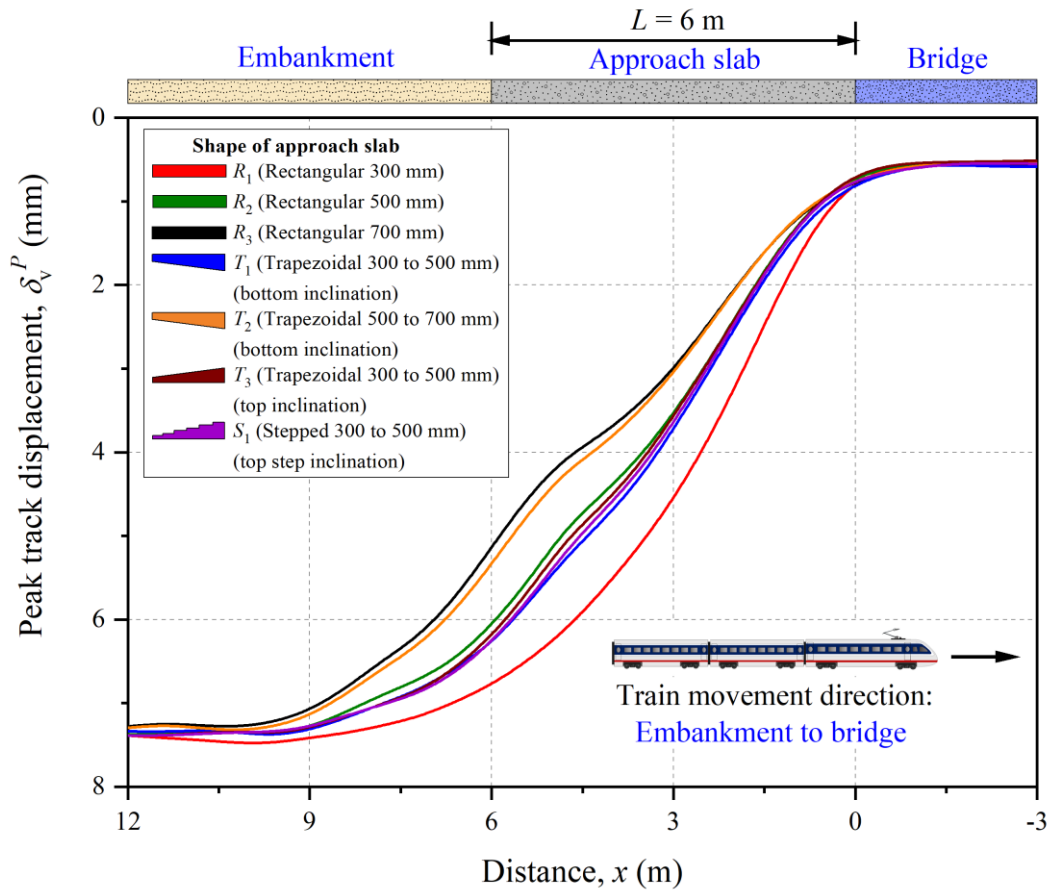


Fig. 5.11 Variation of Vertical Displacement along the Length of Track for Different Shapes of the Approach Slab.

5.3.1.5 Stresses at the fixed end of the approach slab

Figure 5.12 shows the variation of peak tensile stress at the fixed end of the approach slab for different approach slab thicknesses. It can be observed that the peak tensile stress for $T = 300$ mm and 400 mm exceeds the tensile strength of M40 grade concrete [taken as $0.7\sqrt{f_{ck}}$, where f_{ck} is the characteristic compressive strength (Indian railway bridge manual, 1998)]. Therefore, the use of M40 grade concrete to construct the 300 mm and 400 mm thick approach slab may lead to poor performance. Thus, the adequate selection of the grade of concrete (hence the strength) is essential to ensure that the approach slab performs satisfactorily.

Table 5.4 gives the peak tensile stress at the fixed end of approach slab for different approach slab lengths. It can be observed that the peak tensile stress for all the lengths considered in the study is less than the tensile strength of M40 grade concrete (4.43 MPa). Nonetheless, the compressive stresses at the fixed end of the approach slab are found to be negligible compared to the compressive strength of the concrete. The shear

stresses at the fixed end of the approach slab are also within the limits $[0.75\sqrt{f_{ck}} \text{ or } 4.75 \text{ N/mm}^2 \text{ whichever is lower (Indian railway bridge manual, 1998)}]$.

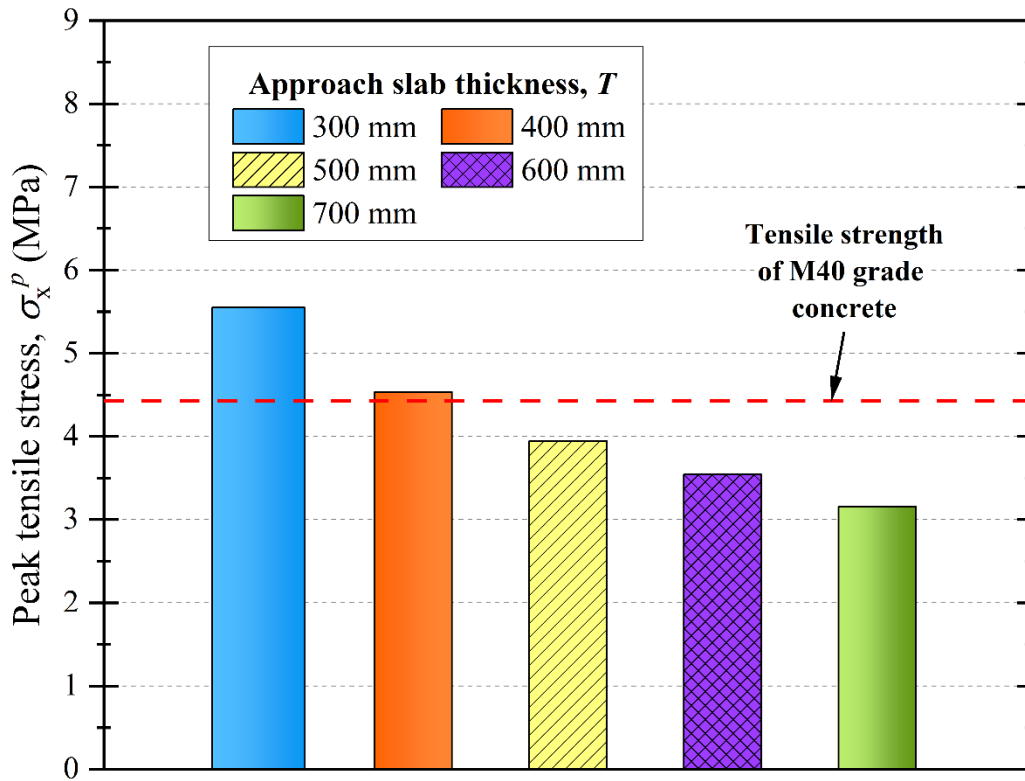


Fig. 5.12 Variation of Peak Tensile Stress at the Fixed End of Approach Slab for Different Thicknesses.

Table 5.4 Variation of peak tensile stress for different parameters.

| Parameter | | Peak Tensile Stress, σ_x^p (MPa) |
|-----------------------------|------|---|
| Approach slab length, L (m) | 3 | 4.37 |
| | 6 | 3.94 |
| | 9 | 3.61 |
| | 12 | 3.29 |
| E_{cc}/E_c ratio | 1 | 3.94 |
| | 0.83 | 3.69 |
| | 0.67 | 3.41 |
| | 0.5 | 3.11 |

A parametric study is also conducted by varying the Young's modulus of concrete to simulate the behaviour of uncracked and cracked approach slabs. Four damage levels are considered by taking the ratio of the Young's modulus of the cracked (E_{cc}) concrete to the uncracked one (E_c), (E_{cc}/E_c), equal to 1, 0.83, 0.67 and 0.5. The ratio, $E_{cc}/E_c = 1$ represents the uncracked concrete and $E_{cc}/E_c = 0.5$ represents significantly cracked concrete. Table 5.4 provides the peak tensile stresses at the fixed end of the approach slab for different damage levels. It can be observed that the peak tensile stress decreases with the increase in the damage level. However, it can be observed that the peak tensile stress for different damage levels considered in the study is less than the tensile strength of M40 grade concrete (4.43 MPa). For the four damage levels, decrease in E_{cc}/E_c ratio from 1 to 0.83, 0.67 and 0.5 is found to increase the peak track displacement at the middle of the approach slab by 2.65 %, 5.11 % and 9 % respectively.

5.3.2 Influence of Backfill Soil Type

The effect of backfill soil type on the performance of railway track in a transition zone is investigated by considering three different backfills, namely, loose sand, medium sand, and dense sand. Table 5.5 gives the properties of the backfill soils considered in the analyses. Figure 5.13 shows the track displacement along the length of the track for three types of backfill soils. The track displacement in the embankment and approach slab region is maximum and minimum for the loose and dense sands, respectively. This observation is obvious as the dense sand has a much higher stiffness and strength compared to the loose sand. As expected, the track displacement for the medium sand is intermediate to that of the loose and dense sands. At the embankment, the track displacement is 7.5 mm for the case of medium sand, which is 9% lesser and 22% higher than the backfill comprising of the loose and dense sands, respectively. Similarly, at the middle of the approach slab, the track displacement is 3.5 mm for medium sand, which is 10% lesser and 17% higher than that for loose and dense sands, respectively. Furthermore, the approach slab provides a more gradual change in the track displacement for the dense sand backfill compared to the medium and loose sand backfills. These results highlight the importance of a well-compacted dense backfill for providing the stable foundation, and thereby, improving the performance of a railway track, especially at the transitions of the IARBs.

Table 5.5 Material properties of different backfill soils (Bowles, 1996).

| Material | Density, ρ (kg/m ³) | Young's Modulus, E (MPa) | Poisson's Ratio, ν | Friction Angle, ϕ' (°) | Dilation Angle, ψ (°) | Cohesion, c' (kPa) |
|-------------|--------------------------------------|----------------------------|------------------------|-----------------------------|----------------------------|----------------------|
| Loose sand | 1700 | 28 | 0.35 | 28 | - | 6 |
| Medium sand | 1800 | 35 | 0.35 | 38 | 8 | 6 |
| Dense sand | 2200 | 60 | 0.35 | 42 | 12 | 6 |

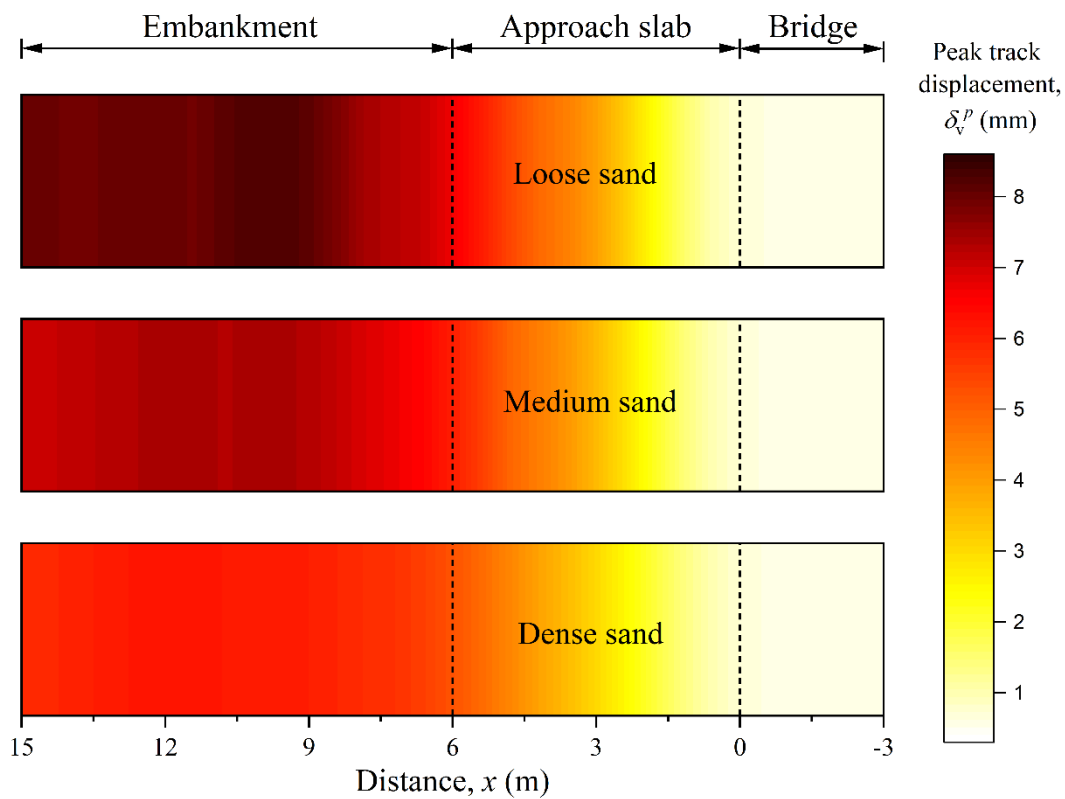


Fig. 5.13 Variation of Track Displacement along the Length of Track for Different Backfill Soils.

5.3.3 Influence of Train Speed

The train speed is varied between 100 km/h and 200 km/h to investigate its influence on the behaviour of the transition zone of the IARB. Figures 5.14(a) – 5.14(c) show the vertical track displacement-time history at the embankment ($x = 30$ m), middle of the approach slab ($x = 3$ m) and bridge ($x = -0.6$ m), respectively, for different train speeds. It can be observed that the track displacement increases with the increase in the train speed throughout the softer side of the track. For 200 km/h train speed, the peak vertical

track displacements at the embankment, middle of the approach slab and bridge are 8 mm, 3.9 mm, and 0.31 mm, respectively. For 150 km/h train speed, the peak vertical track displacements at the embankment and middle of the approach slab are 22% and 29% lesser than that corresponding to 200 km/h train speed, respectively. Similarly, the peak track displacements at the embankment and middle of the approach slab reduce by 1.1%, for the decreasing train speeds from 150 km/h to 100 km/h. The increase in the track displacement with train speed may be attributed to various reasons, such as the sleeper passing frequency and the relative speed of the train with respect to the wave-propagation speed of the track-foundation system (Esveld, 2001; Kaynia *et al.*, 2000). At the bridge, the vertical track displacement shows a similar trend for all the train speeds considered in the study.

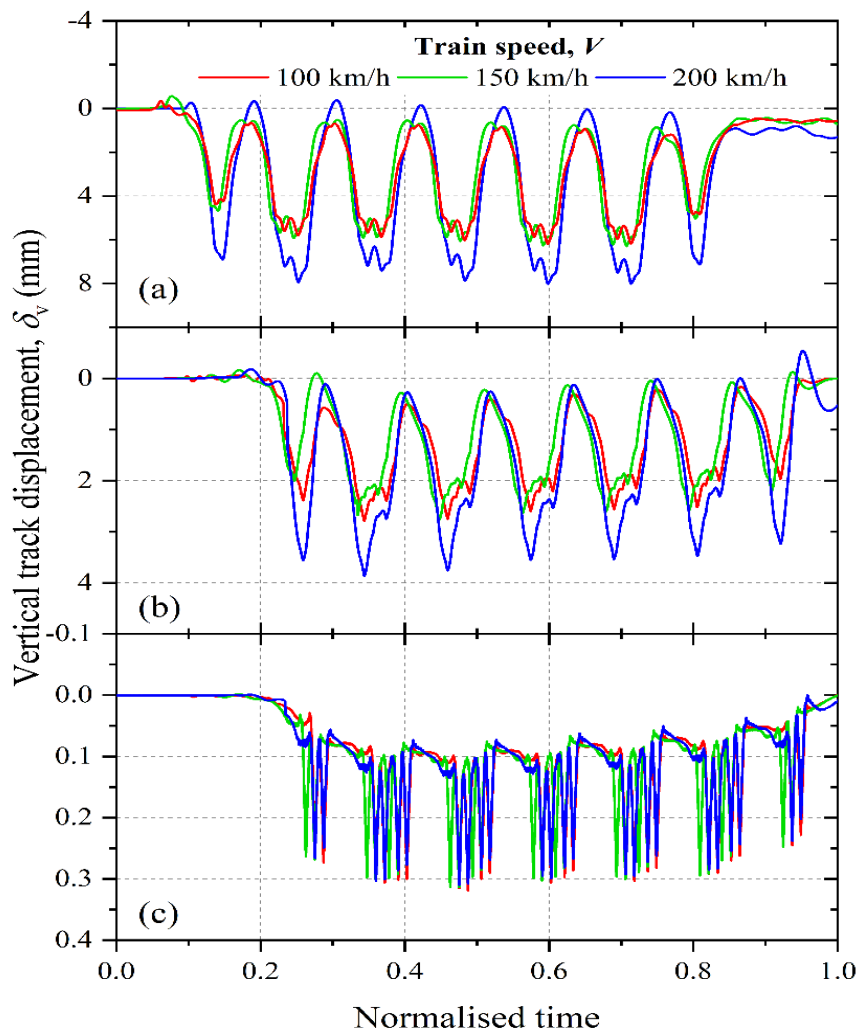


Fig. 5.14 Effect of Train Speed on Track Displacement at (a) Embankment, (b) Middle of Approach Slab, and (c) Bridge.

5.3.4 Influence of Train Movement Direction

The direction of train movement also influences the behaviour of the transition zone. Therefore, the response of transition of the IARB is investigated by considering two different cases of train movement: (a) when the train is moving from the bridge to embankment (BE) and (b) when the train is moving from the embankment to bridge (EB). Figure 5.15 depicts the variation of peak track displacement along the length of the track for the BE and EB cases. It can be observed that the track displacement along the approach slab and near the interface between the embankment and approach slab is lower for the BE case as compared to the EB case. In addition, the transition of track displacement between the embankment and the approach slab is more gradual for the BE case than the EB case. This result is in line with the previous investigations, which revealed that the train movement from the softer to the stiffer side (EB case) is more problematic as compared to the opposite case (see e.g., Wang and Markine, 2018; Namura and Suzuki, 2007). Figure 5.16 shows the variation of peak vertical stress along the length of the track for the two cases (BE and EB). It can be observed that the peak vertical stress near the free end of the approach slab is lower for the BE case as compared to the EB case.

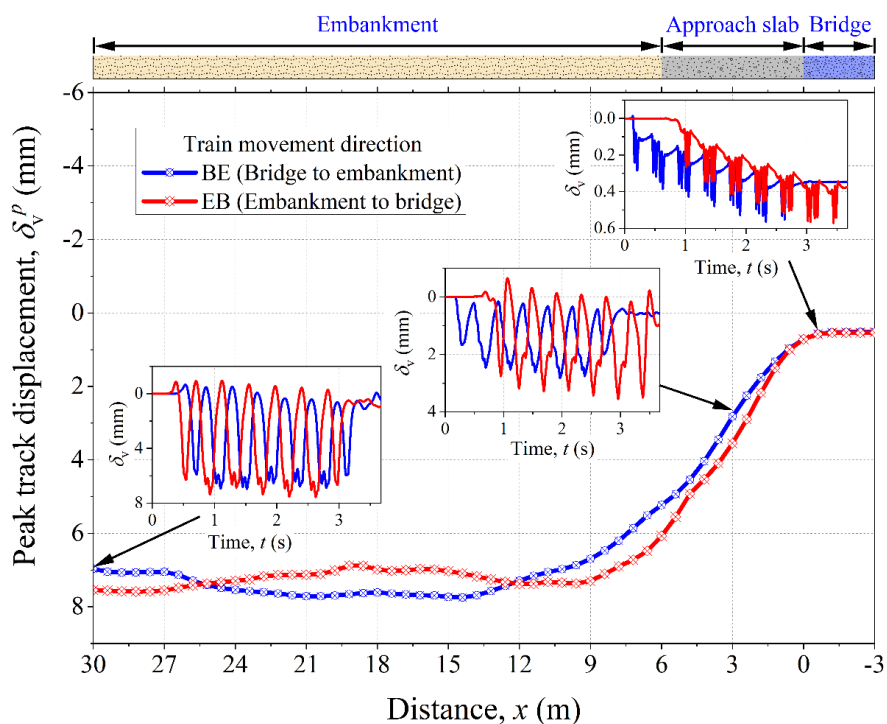


Fig. 5.15 Variation of Track Displacement along the Length of Track for Different Train Movement Directions.

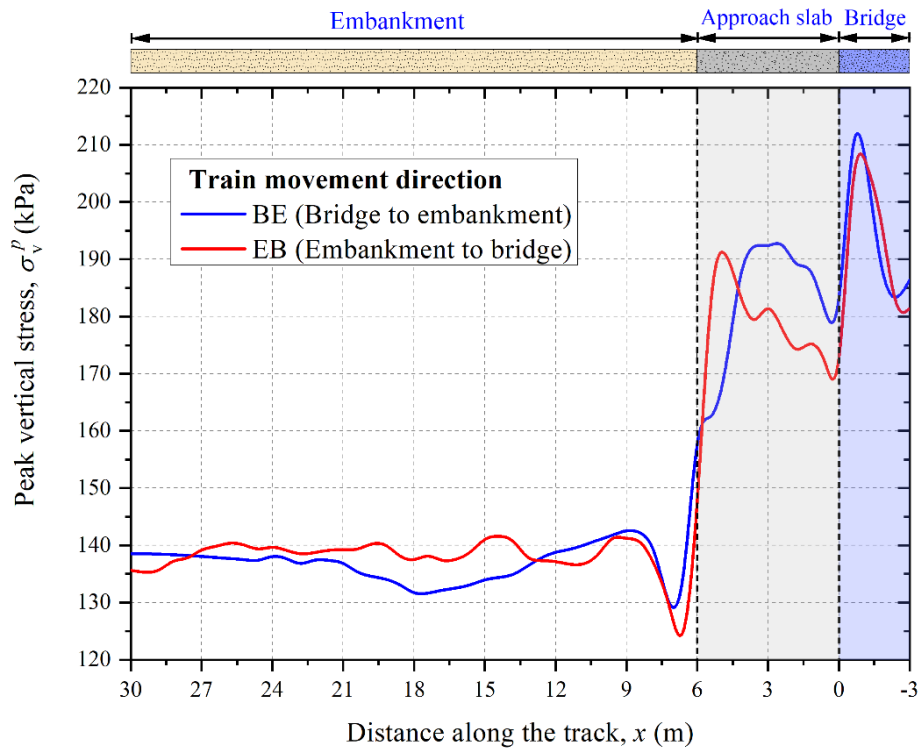


Fig. 5.16 Variation of Peak Vertical Stress along the Length of Track for Different Train Movement Directions.

5.3.5 Influence of Multiple Axle Passages

The effect of multiple passages of the Alfa Pendular train loading on the track displacement in the transition zone of the IARB is investigated. A total of 105 multiple axle passages (i.e., 15 complete train passages having six bogies) are simulated. Figure 5.16 shows the variation of track displacement at the embankment ($x = 30$ m), middle of the approach slab ($x = 3$ m), and bridge ($x = -0.6$ m) for multiple passages of the train. The total track displacement is represented by solid lines and the settlement (plastic or irrecoverable component) is denoted by dashed lines. The multiple train passages are represented in terms of tonnage, which is calculated as the product of axle load and the number of axles. It can be observed from Figure 5.17 that the track settlement accumulates with the tonnage. The cumulative settlement is the highest in the embankment and lowest in the bridge. Moreover, the cumulative settlement at the approach slab is intermediate to that of the embankment and the bridge, suggesting that the approach slab reduces the differential settlement.

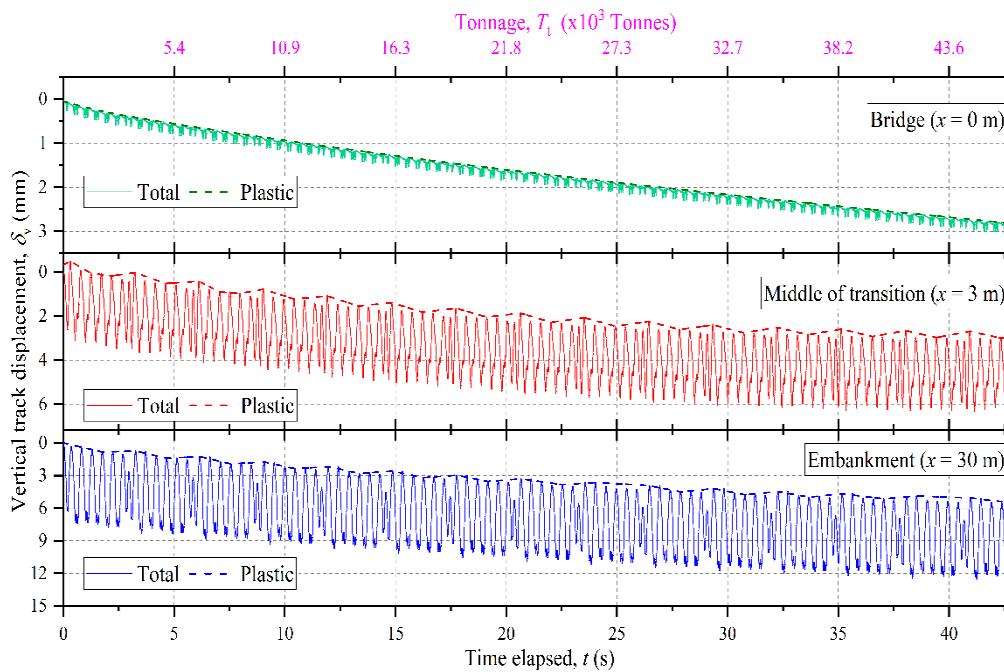


Fig. 5.17 Variation of Vertical Track Displacement in Embankment, Bridge, and Middle of Transition Zone for Multiple Axle Passages.

5.4 SUMMARY

The response of the transition zone of the IARB and embankment is investigated under moving train loading using the 2D FE analysis. Firstly, the FE model is validated with the published field data. The mesh sensitivity analysis for the FE model is also carried out to select the optimum size for obtaining desired accuracy in the results. The moving train loading configuration used in the present study is of Alfa Pendular train. Subsequently, parametric studies are conducted to explore the behaviour of track transition under varying approach slab geometry, backfill soil type, train speed (100 km/h, 150 km/h and 200 km/h) and train movement directions (bridge to embankment and vice versa). The behaviour of the transition under repeated train passages is also explored.

In the next chapter, the results of the seismic behaviour of the typical IAB are presented. The PSDMs and fragility curves for the IAB are also developed and presented.

CHAPTER 6

RESPONSE OF INTEGRAL ABUTMENT BRIDGE UNDER SEISMIC LOADS

6.1 INTRODUCTION

Most widely adopted probabilistic seismic risk assessment approach, such as the performance-based earthquake engineering (PBEE) framework developed by Pacific Earthquake Engineering Research (PEER) and its corresponding framework equation (Equation 2.19) are presented in Chapter 2. The hazard curves for EDP, DM, and DV can be evaluated by de-aggregating the PBEE framework Equations 2.21(a) – 2.21(c). In the present study, the performance-based seismic analysis is carried out for the pile-supported IAB at the response level implementation within the PBEE framework. This chapter outlines the development of fragility curves for the pile-supported IAB. Fragility curves offer an efficient method for assessing the design alternatives, especially when examining the influence of changes in the design and detailing on the vulnerability of various components and accounting for performance uncertainties. The framework employed in this context encompasses distinct assessment modules that are interconnected through pinch point variables, including intensity measures (IMs) and engineering demand parameters (EDPs). The framework consists of essential components such as selection of ground motion suite, FE modelling of pile-supported IAB, capacity and demand estimates and fragility formation. The methodology of the development of fragility curves is presented in the beginning and later the fragility curves established for the typical IAB and presented.

6.2 METHODOLOGY

The methodology adopted for the fragility analysis of the pile-supported integral abutment bridge is depicted schematically in Figure 6.1. The methodology adopted in the present study is as follows:

1. Selection of ground motions: According to IS 1893 (Part 3): 2019, the minimum number of ground motions for time-history analysis is three. In the present study, ten different ground motions including seven pulse type events and three

broadband type events are selected from the PEER strong motion database. The ground motions are selected such that their mean acceleration spectrum of the chosen seismic records is compatible with the design spectrum for Type I rock or hard soil of seismic Zone IV as per the Indian Standards.

2. Scaling of ground motions: The selected ten unscaled ground motions are scaled to represent the different peak ground accelerations (PGAs) varying from 0.1g to 1.2g. In total, eighty two ground motions including the scaled and unscaled intensities (PGAs) are used in the seismic analysis of the pile-supported IAB.
3. Finite element analysis (FEA) of pile-supported IAB: A 2D FE model of the pile-supported IAB supported on the rock layer with infinite elements at the left and right boundaries, is developed in the ABAQUS. These eighty two ground motions are applied one at a time at the bottom of the FE model and simulations are performed.
4. Development of PSDMs: The EDPs considered in the study are permanent vertical displacement of the backfill, approach fill settlement and longitudinal displacement of the abutment-backfill system. These EDPs for the IAB are evaluated considering for all the eighty two ground motions. Using these results, the PSDMs are developed.
5. Development of fragility curves: The limit threshold values for different damage states corresponding to the considered EDPs are established using the guidelines available in the literature. The probability of exceedance or failure for each damage state is evaluated for the IM ranging from 0.1g to 1.2g. A plot of the relation between the probability of failure corresponding to the damage state for the range of PGA values is termed as fragility curve. The fragility curves for all the EDPs are evaluated for the pile-supported IAB.

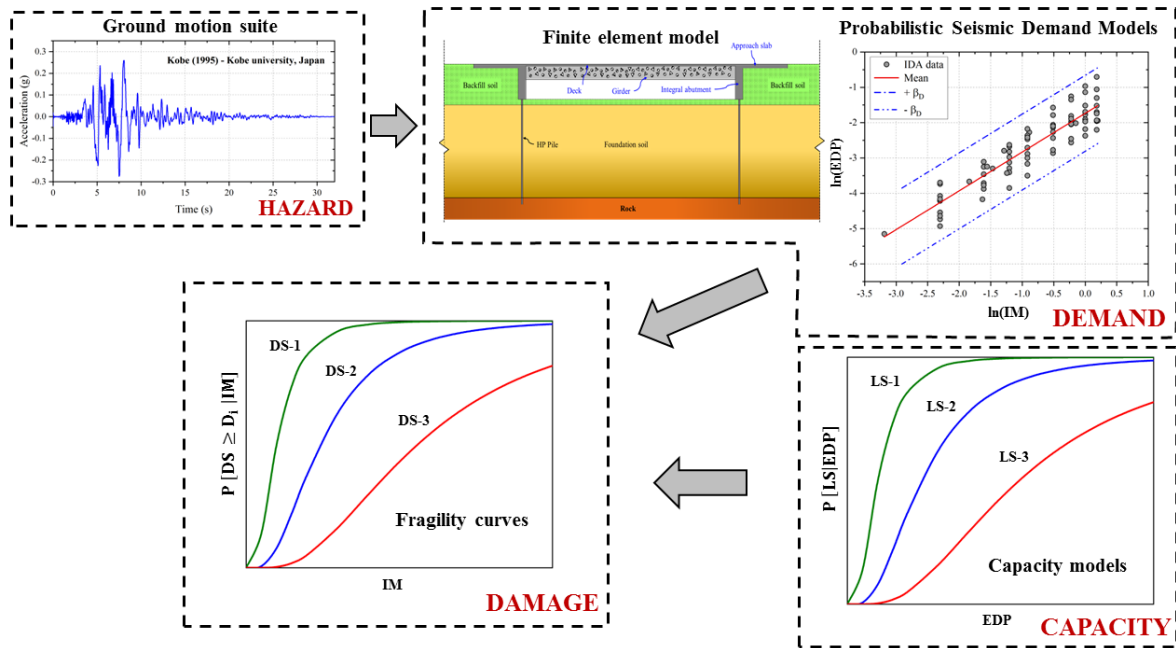


Fig. 6.1 Schematic of the Fragility Analysis Procedure.

6.3 FRAGILITY ANALYSIS

6.3.1 Selection and Scaling of Ground Motions

Generally, for the seismic response analysis of the structure, it is advised to select 10 – 20 separate ground motion records (Shome and Cornell, 1999). In the present study, ten earthquake records are obtained from the PEER ground motion database matching the target response spectrum (5% damping) of IS 1893 (Part 1): 2021 for Type I rock or hard soil sites for seismic Zone IV. These earthquake records have been selected to include the wide range of occurrence of earthquakes considering the different characteristics of the earthquake such as magnitude (M_w), fault mechanism, rupture distance and location of epicentre and average shear wave velocity (V_{s30}) to a depth of 30 m. Figure 6.2 depicts the response spectra of all the ten ground motions which match the response spectrum of IS in the average sense along with \pm one standard deviation response spectra. Table 6.1 provides the detailed characteristics of the selected ground motion records. The time-histories of pulse and broadband type ground motions are shown in Figures 6.3 and 6.4. In the incremental dynamic analysis (IDA), these ground motions are scaled to different peak ground acceleration (PGA) levels such as 0.1g, 0.2g, 0.3 g, 0.4g, 0.6g, 0.8g, 1g and 1.2g. The scaled and unscaled ground motions are applied at the base of the FE model of the pile-supported IAB and accordingly the response calculations are performed.

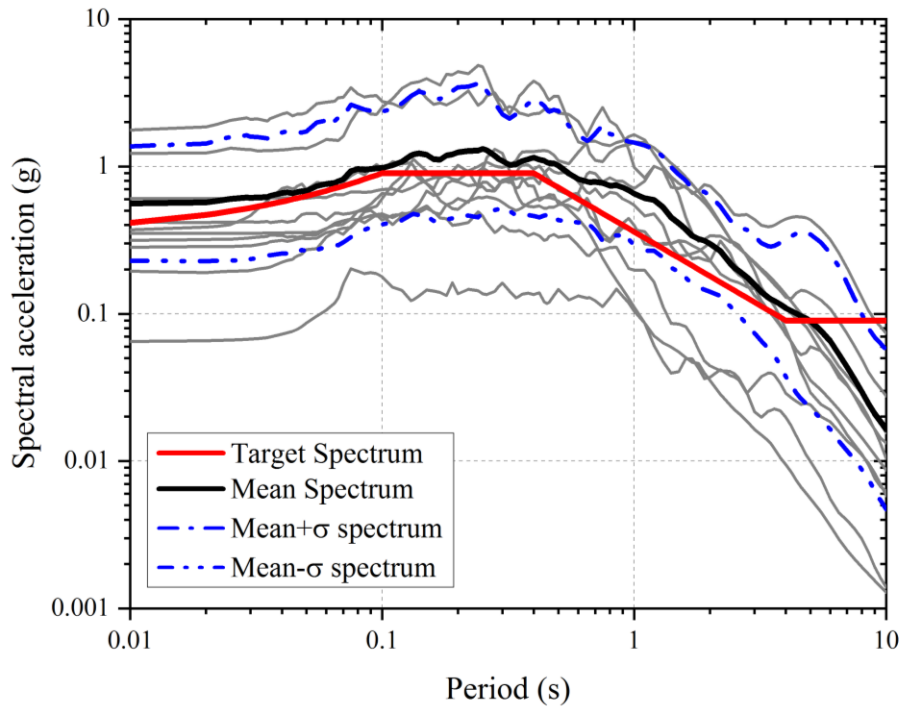


Fig. 6.2 Average Response Spectrum and Response Spectra of the Ten Selected Ground Motions.

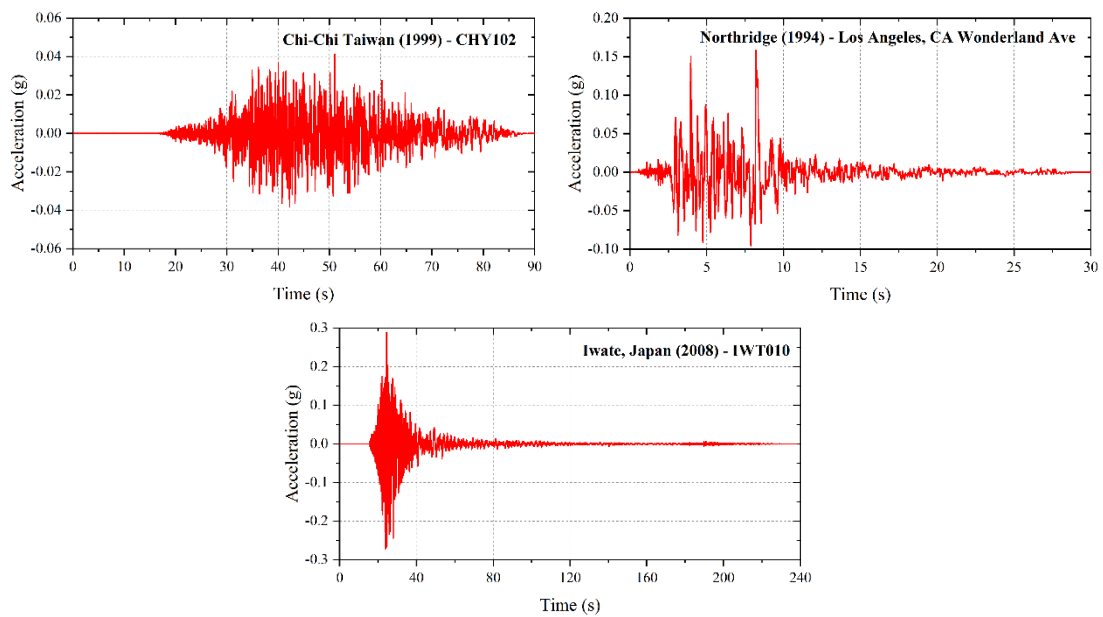


Fig. 6.3 Time-Histories of the Selected Broadband Type Ground Motions.

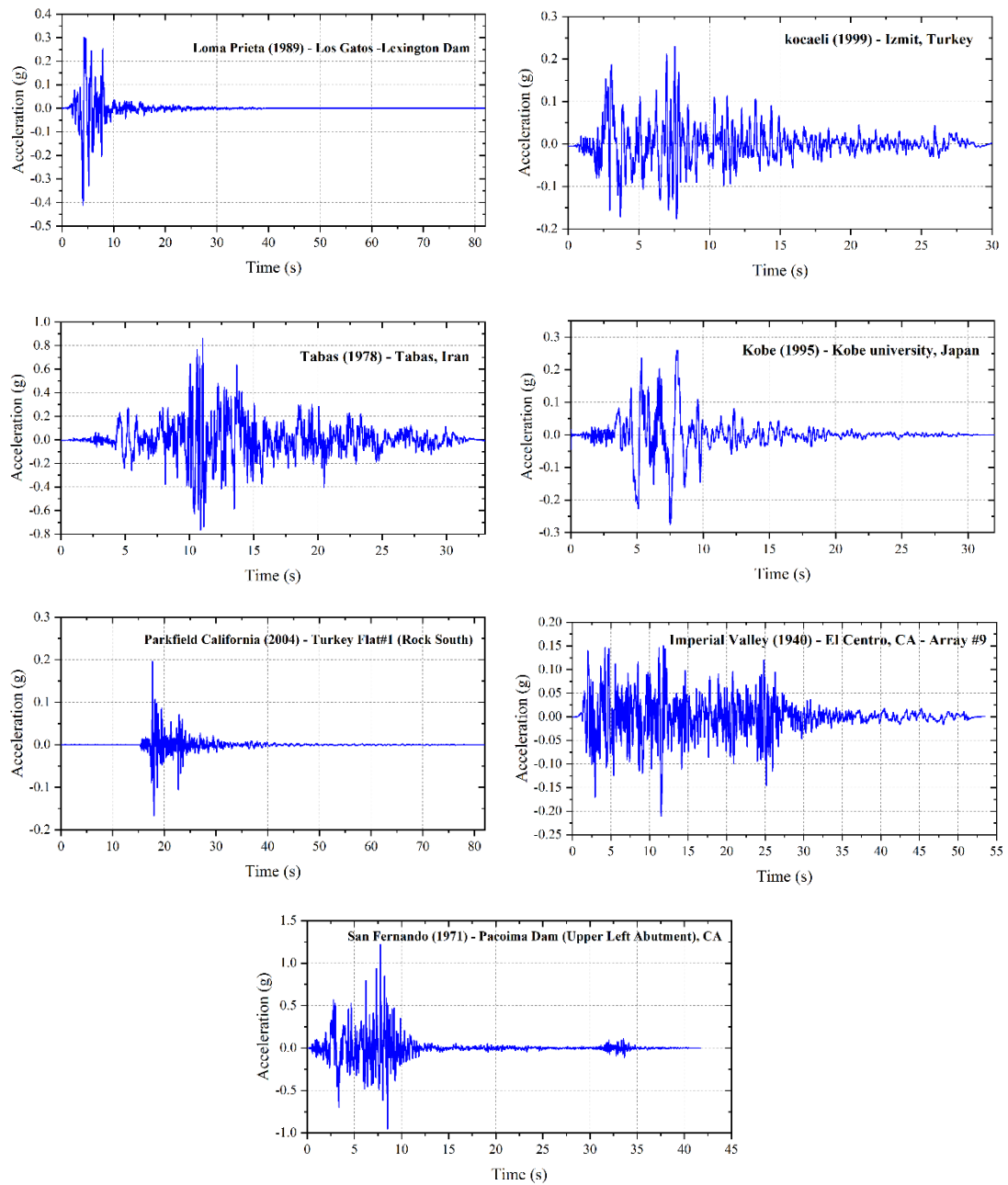


Fig. 6.4 Time-Histories of the Selected Pulse Type Ground Motions.

Table 6.1 Characteristics of acceleration time-histories selected for the study.

| Earthquake Type | Name | Year | Station Name | Faulting Mechanism | Rupture Distance (km) | M_w | V_{s30} (m/s) | PGA (g) |
|------------------------|----------------------|-------------|--|---------------------------|------------------------------|----------------------|------------------------------|----------------|
| Pulse | Loma Prieta | 1989 | Los Gatos – Lexington Dam | Reverse oblique | 5.02 | 6.93 | 1070.34 | 0.41 |
| | Kocaeli | 1999 | Izmit | Strike slip | 7.21 | 7.51 | 811 | 0.23 |
| | Tabas | 1978 | Tabas | Reverse | 2.05 | 7.35 | 766.77 | 0.86 |
| | Kobe | 1995 | Kobe University | Strike slip | 0.92 | 6.9 | 1043 | 0.27 |
| | Parkfield California | 2004 | Parkfield – Turkey Flat#1 (rock south) | Strike slip | 5.29 | 6 | 906.96 | 0.19 |
| | Imperial Valley | 1940 | El Centro, CA - Array#9 | Strike slip | 6.09 | 6.95 | 213.44 | 0.21 |
| | San Fernando | 1971 | Pacoima dam (upper left abutment), CA | Reverse | 1.81 | 6.61 | 2016.13 | 1.21 |
| Broadband | Chi-Chi Taiwan | 1999 | CHY102 | Reverse oblique | 37.72 | 7.62 | 804.36 | 0.04 |
| | Northridge | 1994 | Los Angeles, CA Wonderland Ave | Reverse | 20.29 | 6.69 | 1222.52 | 0.16 |
| | Iwate Japan | 2008 | IWT010 | Reverse | 16.27 | 6.9 | 825.83 | 0.28 |

6.3.2 Parameters of Fragility Function

6.3.2.1 Intensity measure

In the case of development of fragility curves for pile-supported IABs, the choice of earthquake IMs must align closely with the unique characteristics of these structures. The Applied Technology Council report, ATC-63/FEMA P-695 (2008) uses the spectral acceleration at the fundamental period of the structure as the preferred IM. The risk assessment software package, HAZUS-MH (2011) uses the PGA, peak ground displacement (PGD) and spectral acceleration at 1.0 s. Padgett *et al.* (2008) investigated the use of IMs in the context of bridge portfolios with geometric variability. Their findings indicated that among the various IMs, the PGA emerged as the most suitable choice for the probabilistic seismic demand analysis of different classes of bridges, considering the criteria such as sufficiency, practicality, proficiency, efficiency, and hazard computability. In the present study, the PGA is used as the IM to develop the PSDMs and fragility curves for the pile-supported IAB.

6.3.2.2 Engineering demand parameters

The EDPs signify the vital component responses, the failure of which can impair the bridge's operational or functional capabilities. These component responses are observed throughout the seismic events to analyse the seismic performance and establish the connection between the peak response and IM of the ground motion. The EDPs for the IAB which are vulnerable to seismic forces are presented in Table 6.2 (Argyroudis and Mitoulis, 2021; Ahmed and Dasgupta, 2022). In the present study, the EDPs considered are the permanent vertical displacement of the backfill, approach fill settlement and longitudinal displacement of the abutment-backfill system.

Table 6.2 Components of bridge failure modes and relevant EDPs (Argyroudis and Mitoulis, 2021; Ahmed and Dasgupta, 2022).

| Component | Failure Type | Engineering Design Parameters |
|----------------------------|--------------|--|
| Foundation soil | GEO | Settlement |
| Deep foundation | GEO & STR | Pile yielding BM, pile cap failure (BM, SF), rotation, cracking width |
| Shallow foundation | GEO & STR | Uniform and/or differential settlement, BM and/or SF, rotation, cracking width |
| Backfill and approach slab | GEO | Settlement |
| Abutment and wing walls | GEO & STR | Drift ratio, yielding BM, cracking width |
| Pier | STR | Drift ratio, tilting, yielding BM, cracking width |
| Deck | STR | Yielding BM, cracking BM, permanent deflection |
| Bearing | STR | Shear and axial (compressive or tensile) strains, rotation and combinations |

Note: GEO: Geotechnical; STR: Structural; BM: Bending moment; SF: Shear force

6.3.3 Definition of Damage States

The damage states assess the limit state thresholds for the different EDPs of the deck, abutments, piers, approach fill, foundation and backfill soils. The IAB may experience different levels of damage depending on the intensity of shaking. A few damage states for the bridges are defined based on the extent of settlement or ground offset (NIBS, 2004; Argyroudis and Kaynia, 2015). The damage states for backfill settlement or heaving behind the bridge abutment or retaining walls due to seismic loading for the highways and railways have been adopted from Argyroudis and Kaynia (2014) and the corresponding limit states thresholds are given in Table 6.3. The damage states are classified into three states such as minor, moderate, and extensive/complete damage for the permanent vertical displacement of the backfill (δ_v) and the corresponding serviceability status is given in the table. The damage states for the abutment-backfill system (ABS) are set with limit state thresholds for backfill maximum longitudinal displacement (δ_h) as a fraction of the height of the integral abutment (H). From the literature, the backfill maximum longitudinal displacement is $0.06H$ (Martin and Yan, 1995; Ahmed and Dasgupta, 2022). In the study, the damage states of Ahmed and Dasgupta (2022) are adopted, and the corresponding limit state thresholds and

serviceability are given in Table 6.4. The five damage states are considered for the approach fill settlement namely, observable, minor, moderate, major, and severe. The damage states and limit state thresholds for each damage states are adopted from Shao *et al.*, (2022) and are given in Table 6.5.

Table 6.3 Damage states and limit state thresholds for highways and railways assets (Argyroudis and Kaynia, 2014).

| Typology | Damage State | Permanent Vertical Backfill Displacement (m) | | | Serviceability |
|----------|----------------------|--|------|------|--|
| | | Min. | Max. | Mean | |
| Highways | Minor | 0.02 | 0.08 | 0.05 | Open, reduced speeds or partially closed during repair |
| | Moderate | 0.08 | 0.22 | 0.15 | Closed or partially closed during repair works |
| | Extensive / Complete | 0.22 | 0.58 | 0.4 | Closed during repair works |
| Railways | Minor | 0.01 | 0.05 | 0.03 | Open, reduced speeds |
| | Moderate | 0.05 | 0.10 | 0.08 | Closed during repair works |
| | Extensive / Complete | 0.01 | 0.30 | 0.2 | Closed during reconstruction works |

Table 6.4 Damage states and limit state thresholds for abutment-backfill system (Ahmed and Dasgupta, 2022).

| Damage State | Limit State Threshold (m) | Serviceability |
|--------------|---------------------------|------------------------------------|
| Slight | 0.1 $\delta_h = 0.021$ | Repairable minor functional damage |
| Extensive | 0.35 $\delta_h = 0.073$ | Repairable major functional damage |
| Ultimate | $\delta_h = 0.21$ | Replacement required |

Table 6.5 Damage states and limit state thresholds for approach fill settlement (Shao *et al.*, 2022)

| Damage State | Limit State Threshold (cm) |
|-------------------------------|----------------------------|
| Observable (LS ₁) | 2.79 |
| Minor (LS ₂) | 5.33 |
| Moderate (LS ₃) | 10.67 |
| Major (LS ₄) | 21.59 |
| Severe (LS ₅) | 43.18 |

6.3.4 FE Modelling of Pile-Supported Integral Abutment Bridge

In this study, a typical pile-supported IAB with approach slab is modelled using FE based program ABAQUS. Figure 6.5 shows the 2D plane-strain FE model of the pile-supported IAB used in the analyses. The geometry and dimensions of the various components of the IAB founded on rock are selected based on the published data (Al-Qarawi *et al.* 2020). A single span IAB of length 30 m and an approach slab of length 6 m supported by a 12 m steel H-pile socketed in the rock for a length of one meter is considered. The IAB with 0.2 m thick deck slab, 1.5 m deep steel girder, and an abutment of height 4 m and thickness of 1 m are adopted. The backfill has the dimensions of 4.5 m deep and 65.5 m long. This is followed by an embankment of 4.5 m height for the whole length of the model. The foundation soil has a thickness of 11.5 m and the bed rock has a thickness of 30 m as in the figure. The FE domain has a total length of 830 m out of which 200 m on either side is the region consisting of infinite elements. These infinite elements will simulate the semi-infinite media such that the effect of wave reflection is eliminated in the FE simulations.

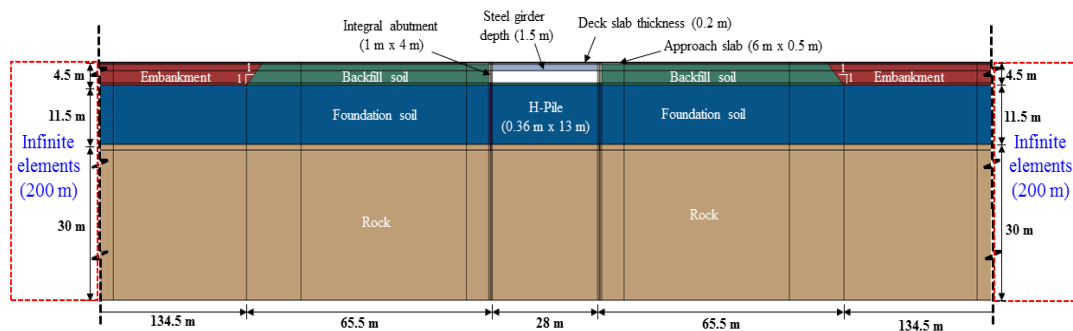


Fig. 6.5 Schematic Representation of Pile-Supported Integral Abutment Bridge.

Table 6.6 lists the values of the material properties used in the FE simulations. These values are chosen based on the published literature. The integral abutment, approach slab and H-pile are modelled using the linear elastic model. The behaviour of the backfill, embankment, foundation soil and bed rock is simulated using the MC material models. The material damping in the FE model is captured using Rayleigh damping, and the values of damping coefficients, ‘ α ’ and ‘ β ’ for each of the materials are determined using Equations 4.1 and 4.2 (Section 4.2.2, Chapter 4).

Table 6.6 Material properties used in the FE simulation (data sourced from ¹Al-qarawi *et al.*, 2020; ²Meena *et al.*, 2020; ³Gadicherla *et al.*, 2022).

| Component | Material Model | Density, ρ (kg/m ³) | Young's Modulus, E (MPa) | Poisson's Ratio, ν | Friction Angle, ϕ' (°) | Dilation Angle, ψ (°) | Cohesion, c' (kPa) | Rayleigh Coefficients | |
|--|----------------|--------------------------------------|----------------------------|------------------------|-----------------------------|----------------------------|----------------------|-----------------------------|-------------|
| | | | | | | | | α (s ⁻¹) | β (s) |
| Backfill soil ¹ | MC | 1,835 | 35 | 0.35 | 38 | 8 | 6 | 2.44 | 0.0005 |
| Foundation soil ¹ | MC | 1,682 | 30 | 0.3 | 20 | 1 | 20 | 0.94 | 0.0014 |
| Embankment ² | MC | 1,730 | 50 | 0.35 | 24 | 0 | 30 | 1.55 | 0.0008 |
| Rock ³ | MC | 2,100 | 720 | 0.35 | 21 | 1 | 115 | - | - |
| Integral abutment, deck and approach slab (reinforced concrete) ¹ | LE | 2,385 | 30,000 | 0.25 | – | – | – | – | – |
| HP pile (steel) ¹ | LE | 7,951 | 200,000 | 0.3 | – | – | – | – | – |

Note: LE: Linear elastic; MC: Mohr-Coulomb.

The soil-structure interaction between the integral abutment-backfill soil, pile-foundation soil, and approach slab-backfill soil is simulated using the Coulomb friction model available in ABAQUS. The normal and tangential contact behaviours are simulated using surface-to-surface interaction by employing the master-slave concept. The normal contact behaviour is simulated as ‘*hard contact*’ in which the normal stresses are transferred under compression. The tangential contact is simulated using a penalty friction algorithm for which the interface friction coefficient between the two surfaces is evaluated by Equations 4.6 and 4.7 (Section 4.2.3, Chapter 4).

The 2D plane-strain FE model of the IAB is discretised using a 4-noded bilinear plane-strain element with reduced integration (CPE4R) and hourglass control as shown in Figure 6.6. The lateral boundaries are modelled using CINPE4 elements. The CINPE4 element is a 4-node linear, one-way plane-strain infinite element. The entire FE mesh consists of 35,072 elements. Near the IAB, the elements have the size of 0.5 m on an average and farther away and right up to the beginning of the infinite elements, the size of the elements is 1 m on an average. The standard boundary conditions are adopted for the FE model in which the nodes along the bottom boundary are considered as fixed. The pinned boundary conditions are provided at the vertical boundaries of the infinite elements on both sides of the FE model. The bottom boundary is at 46 m from the top of the integral abutment and the seismic input motion is applied at that level.

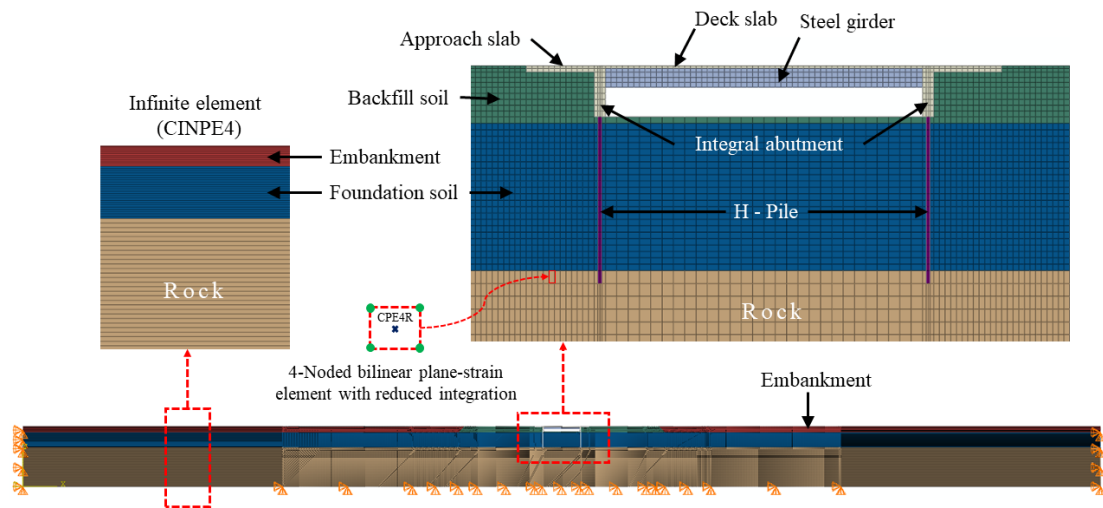


Fig. 6.6 FE Mesh of the Pile-Supported Integral Abutment Bridge.

The FE analysis is performed adopting the following steps: (a) a geostatic stress field is applied to generate the initial effective stresses in the model, and (b) dynamic implicit analysis is carried out for each of the chosen ground motions applied at the base of the FE model. The fundamental frequency of the structure is in the acceleration sensitive region of the response spectrum. The PGA values adopted in the IDA are obtained for each the ground motions. The PGA values used in the IDA are 0.1, 0.2, 0.3, 0.4, 0.6, 0.8, 1.0 and 1.2g. A total of 82 FE simulations are carried out for the pile-supported IAB for all the three EDPs and the results are used in the development of PSDMs and fragility curves.

6.3.5 Development of PSDMs

The probabilistic seismic demand analysis (PSDA) encompasses the development of seismic demand models, frequently described as probabilistic models representing the structural responses based on the seismic intensity measure (IM). The result of PSDA is a probabilistic seismic demand model (PSDM). In the present study, the seismic demand (D or d) is related to the permanent vertical displacement of the backfill, approach fill settlement and longitudinal displacement of the abutment-backfill system and PGA is the IM. Cornell *et al.* (2002) presented the relationship between the seismic demand and IM, termed as the PSDM expressed by two parameter lognormal distribution as in Equation 6.1 and the same is adopted in the study:

$$P[D \geq d | IM] = 1 - \Phi\left(\frac{\ln(d) - \ln(S_D)}{\beta_D}\right) \quad (6.1)$$

where $\Phi(\cdot)$ is the standard normal cumulative distribution function, S_D is the median value of the seismic demand parameter in terms of IM and β_D is the lognormal standard deviation. The relationship between the S_D and IM is expressed in the power model form as

$$S_D = a (IM)^b \quad (6.2)$$

Equation 6.2 is transformed into linear space as in Equation 6.3 to perform a linear regression analysis to determine a and b :

$$\ln(S_D) = \ln(a) + b \ln(IM) \quad (6.3)$$

The parameter $\ln(a)$ is the vertical intercept and parameter b is the slope of the line and β_D is the standard deviation of the linear regression and is expressed as

$$\beta_D = \sqrt{\frac{\sum_{i=1}^N [\ln(d_i) - \ln(aIM^b)]^2}{N - 2}} \quad (6.4)$$

where N is the number of response history analysis and d_i and IM are the peak EDP and intensity measure (e.g., PGA) related to the i^{th} response history analysis.

The PSDMs are developed for the following EDPs: the permanent vertical displacement of the backfill (PVDB) (δ_v), approach fill settlement (AFS) (δ_{av}) and longitudinal displacement of abutment-backfill system (ABS) (δ_h). Figures 6.7 - 6.9 depict the

PSDMs corresponding to the above three EDPs. The scatter plots shown in the figures are fitted with the linear regression trend line to obtain the predictive relationships between the PVDB, AFS and ABS with the IM and the corresponding PSDMs for all the three EDPs are given as

$$y_{PVDB} = 1.0975x - 1.7359 \quad (6.5)$$

$$y_{AFS} = 1.2219x - 2.1494 \quad (6.6)$$

$$y_{ABS} = 0.8979x - 0.4334 \quad (6.7)$$

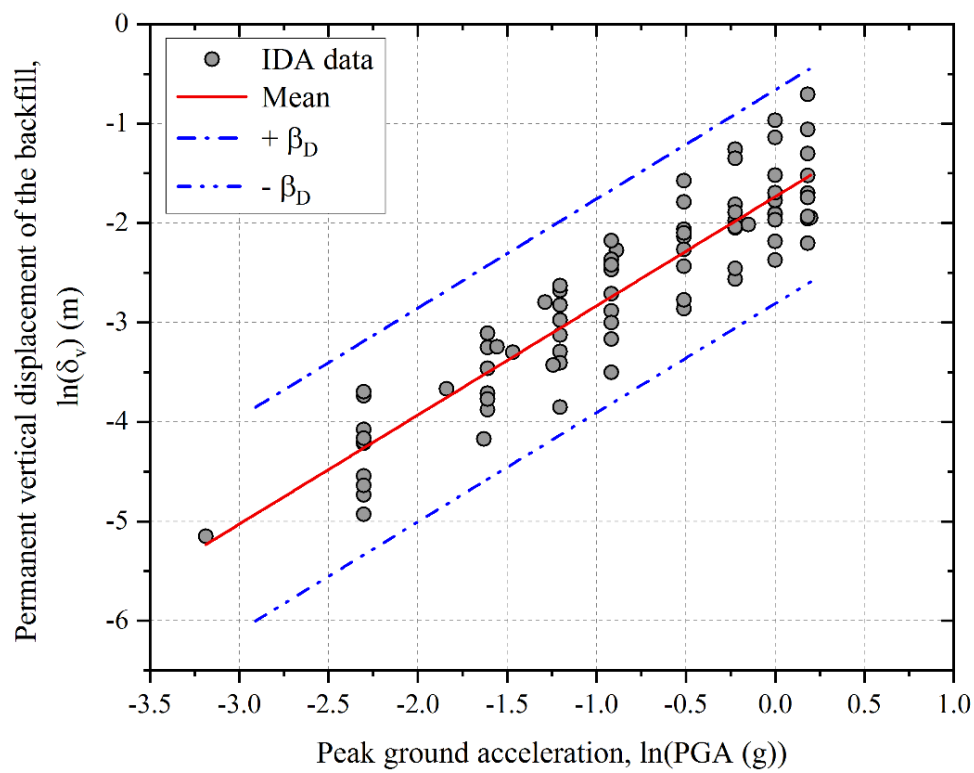


Fig. 6.7 PSDM for Permanent Vertical Displacement of Backfill of the IAB.

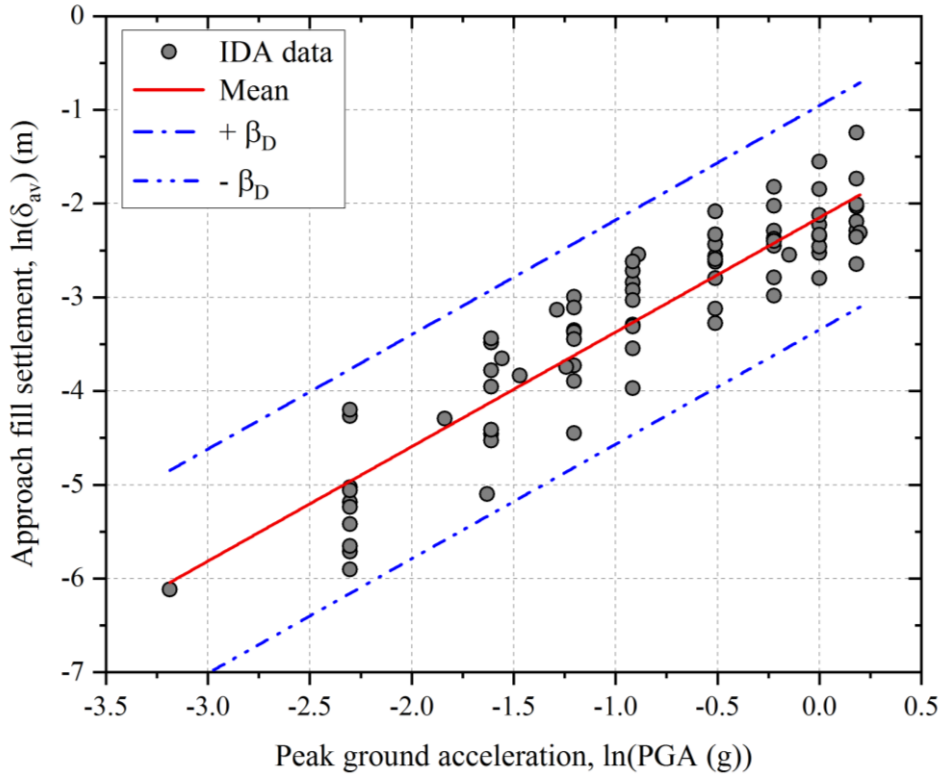


Fig. 6.8 PSDM for Approach Fill Settlement of the IAB.

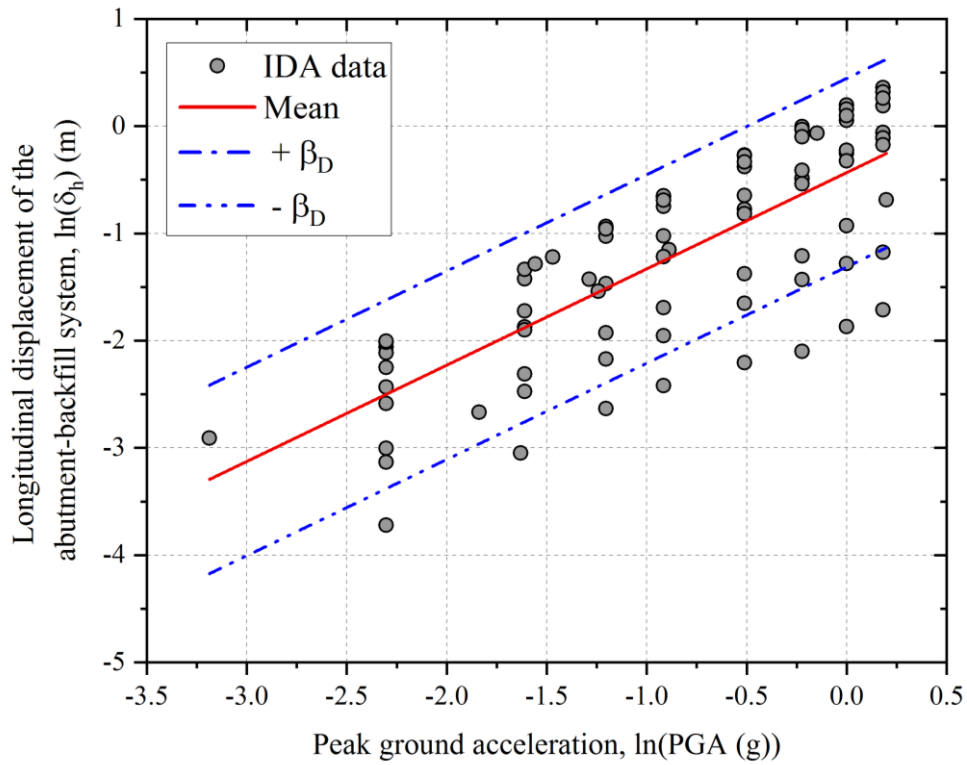


Fig. 6.9 PSDM for Longitudinal Displacement of Abutment-Backfill System.

6.3.6 Development of Fragility Curves

The fragility functions are the probabilities of exceeding different limit state thresholds for a given level of ground shaking expressed in PGA. The fragility curves are expressed using the lognormal probability distribution function as

$$P_f[DS \geq D_i | IM] = \Phi \left[\frac{1}{\beta_{tot}} * \ln \left(\frac{IM}{IM_i} \right) \right] \quad (6.8)$$

where $P_f(\cdot)$ is the probability of exceeding a particular damage state (DS) for a given seismic intensity measure (IM), Φ is the standard cumulative probability function, IM_i is the median intensity measure required to cause the i^{th} damage state D_i and β_{tot} is the total lognormal standard deviation. The development of fragility curves requires two parameters IM_i and β_{tot} .

The linear mean regression line of the PSDM is used to calculate the intensity measure (IM_i) required to cause the i^{th} damage state (DS_i) based on the definition of damage indices defined in Tables 6.3 - 6.5. The HAZUS (2004) recommends three primary sources of uncertainty to be considered, namely the definition of damage state (β_{ds}), resistance capacity and response of the element (β_c), and the earthquake input motion demand (β_D). The total variability is represented by the amalgamation of the three factors, presuming their statistical independence and random variables following the lognormal distributions as

$$\beta_{tot} = \sqrt{\beta_{ds}^2 + \beta_c^2 + \beta_D^2} \quad (6.9)$$

The uncertainty associated with the definition of damage states (β_{ds}) due to lack of rigorous estimation is set equal to 0.4 as per HAZUS (2004). Based on engineering judgement, the uncertainty in capacity and response of element (β_c) is set equal to 0.3 as per Argyroudis *et al.* (2013). The uncertainty associated with the seismic demand (β_D) is evaluated from the developed PSDM. The seismic demand values evaluated for the PVDB, AFS and ABD are 0.395, 0.438 and 0.614, respectively. The total variability is evaluated using Equation 6.9 and the corresponding values are 0.637, 0.664 and 0.792 for the PVDB, AFS and ABD respectively.

Using the above results, the fragility curves for the permanent vertical displacement of the backfill for highway and railway infrastructure are developed and are shown in

Figures 6.10 and 6.11. The fragility curves developed in the present study are found to have similar characteristics as reported by Argyroudis *et al.* (2013; 2018). Argyroudis *et al.* (2013) have reported the damages to the bridges based on the settlement of the approach fills after the 2007 Niigata-Chuetsu Oki earthquake in Japan. These reported damages are based on the qualitative description and range of observed settlements in the backfill. However, it is to be noted that the features of the abutment are unknown and many uncertainties exist in the characterization of soil type. The findings of the current study on the fragility curves of the pile-supported IAB have identified some notable agreements with the reported data. It is to be stated that, despite various uncertainties involved in the analysis, the present study can evaluate the seismic vulnerability of the IAB in terms of the backfill settlement as the damage state.

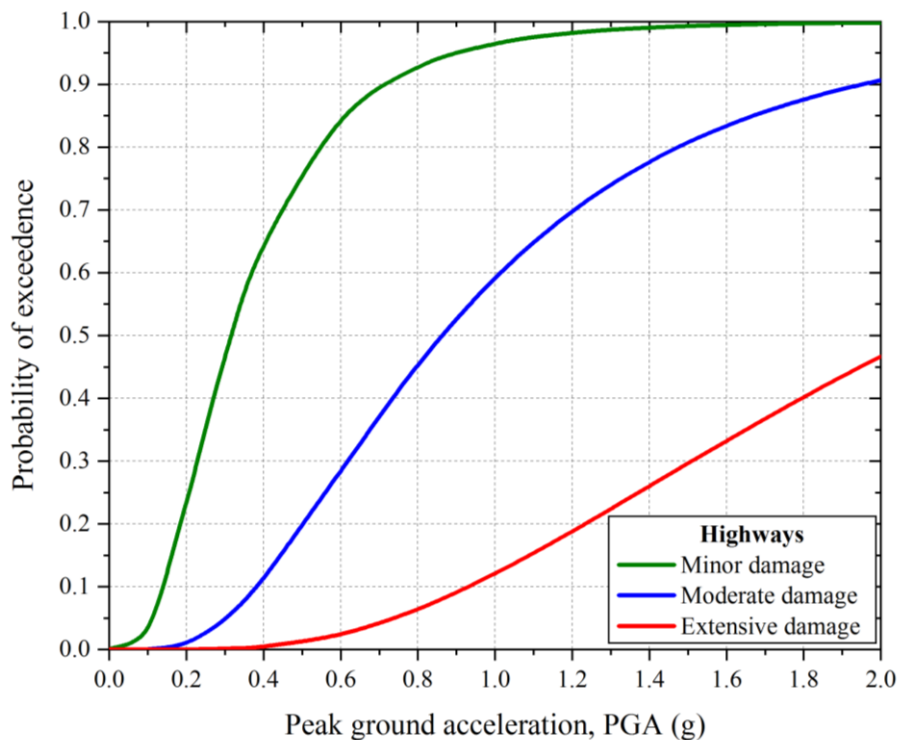


Fig. 6.10 Fragility Curves for Pile-Supported IAB for PVDB: Highway Infrastructure.

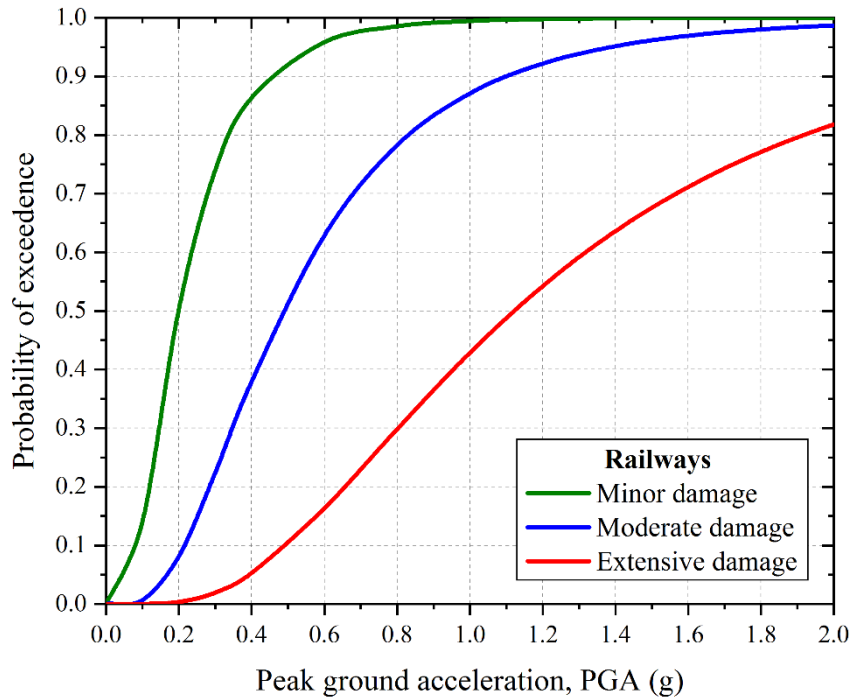


Fig. 6.11 Fragility Curves for Pile-Supported IAB for PVDB: Railway Infrastructure.

The fragility curves for the approach fill settlement and longitudinal displacement of the abutment-backfill system are also developed using the results of IDA and are shown in Figures 6.12 and 6.13.

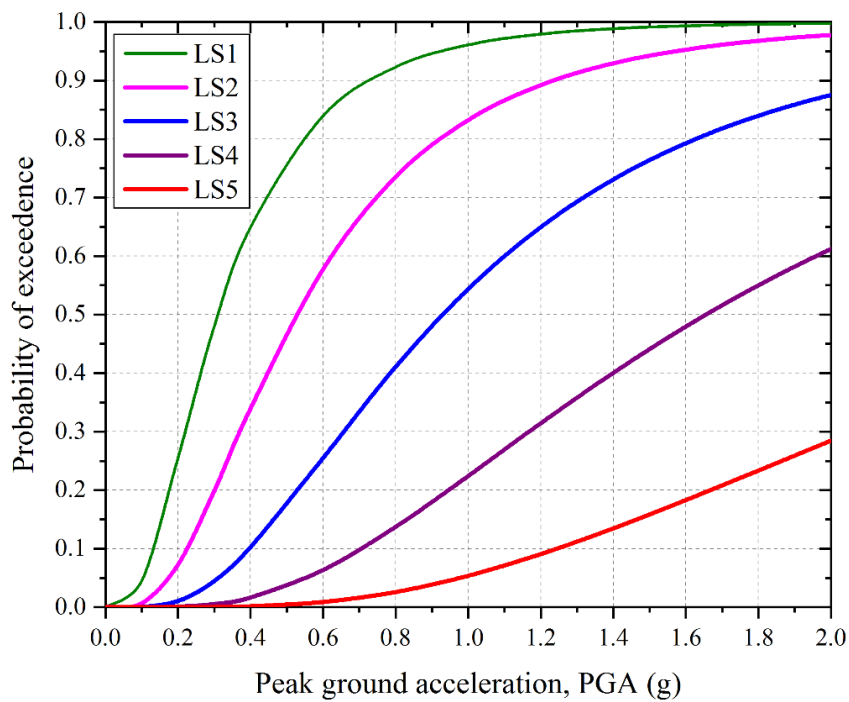


Fig. 6.12 Fragility Curves for Pile-Supported IAB for Approach Fill Settlement.

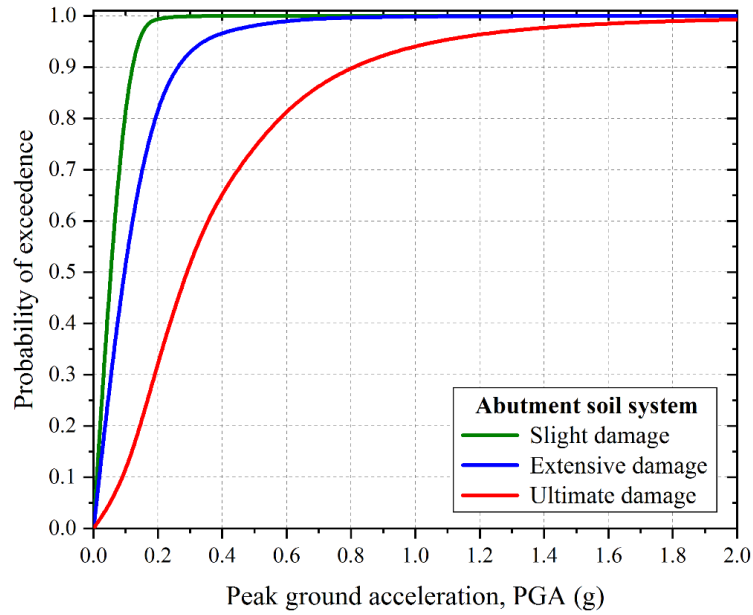


Fig. 6.13 Fragility Curves for Pile-Supported IAB for Longitudinal Displacement of Abutment-Backfill System.

6.4 SEISMIC EARTH PRESSURE ON INTEGRAL ABUTMENT

A variation of seismic earth pressure behind the integral abutment is evaluated for a total of 82 scaled and unscaled earthquake ground motions. The variation of mean peak soil pressure behind the left and right integral abutments of the IAB for all the ground motions is shown in Figure 6.14 along with \pm one standard deviation. The trend in the variation of the soil pressure behind the integral abutment is found to be similar with those reported in the published literature.

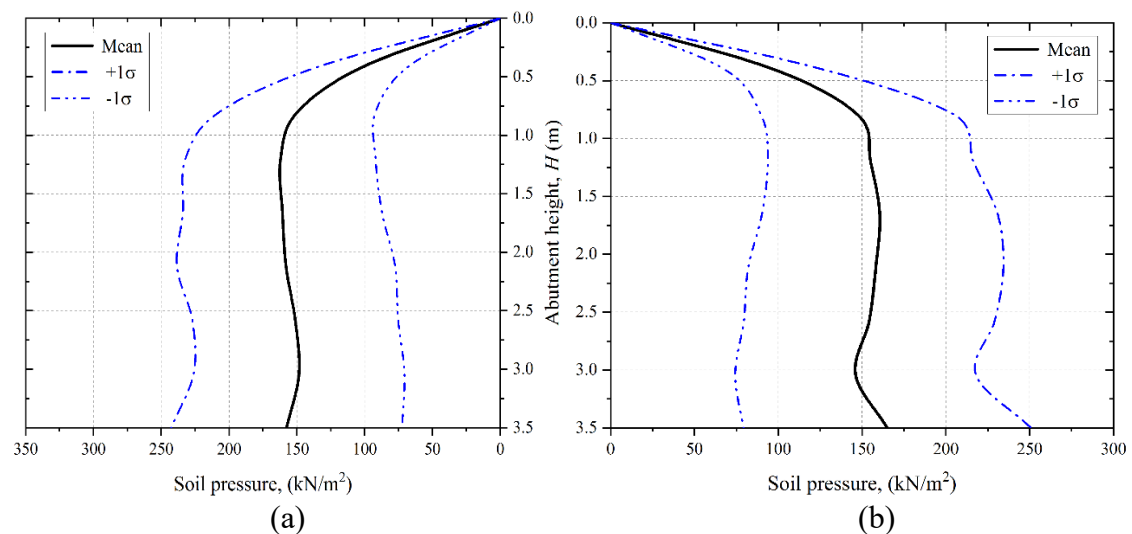


Fig. 6.14 Variation of Soil Pressure on (a) Left Integral Abutment, and (b) Right Integral Abutment.

6.5 HORIZONTAL SEISMIC COEFFICIENT FOR PILE SUPPORTED IAB

The design horizontal seismic force acting on the bridge is evaluated by the product of horizontal seismic coefficient and combined dead load and appropriate live load as per IRC – 6: 2017. The horizontal seismic coefficient (k_h) can be evaluated as per IS 1893 (Part 1): 2021. In the present study, the k_h is evaluated from the maximum passive earth pressure generated behind the integral abutment for different PGA values of the ground motions. Using the values of maximum passive earth pressure, height of the integral abutment and unit weight of the backfill soil, the k_h is evaluated. The k_h values are evaluated for all the PGA values of the 82 ground motions. Figure 6.15 show the scattered plot of the variation of k_h with PGA. A nonlinear regression curve fitting by the power law function is adopted to obtain the relationship between the k_h and PGA and is expressed as

$$k_h = 6.3602 (PGA)^{0.4871} \quad (6.10)$$

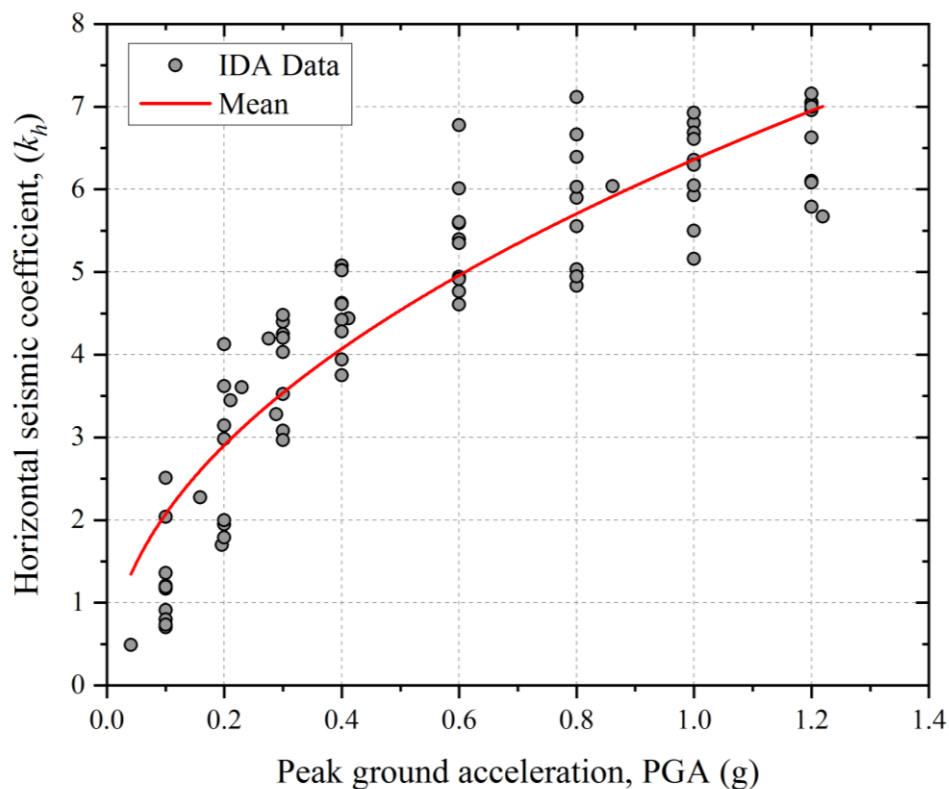


Fig. 6.15 Variation of Horizontal Seismic Coefficient with PGA for the Typical Pile-Supported IAB.

Kavazanjian *et al.* (2011) recommended that the design horizontal seismic coefficient shall be determined by the basis of the site class adjusted peak acceleration at the ground

surface. Equation 6.10 can be used to evaluate the design k_h in case the guidelines are not available to evaluate this coefficient, especially for the preliminary seismic analysis of the pile-supported IAB. More detailed studies are needed to obtain the design k_h so that the properly evaluated design k_h will provide the displacement ductility for the IABs.

6.6 SUMMARY

Seismic response analysis of the pile-supported IAB is carried out using the incremental dynamic analysis. Ten ground motions from the PEER database are selected to match the target spectrum of the IS code. Using these ground motions, many other ground motions are obtained using the scaling procedure. The increasing intensities of PGA (i.e., IM) are considered in the analysis. Three EDPs of the IABs are considered to develop the PSDMs and fragility curves. The EDPs considered are the permanent vertical displacement of the backfill, approach fill settlement and longitudinal displacement of the abutment-backfill system of the IABs. The limit state thresholds for all the three EDPs are identified, and the corresponding damage states are identified. All the three EDPs of the IAB are evaluated for the increasing values of PGA. Using these results, the PSDMs and fragility curves are developed. The PSDMs and fragility curves are very useful in the seismic vulnerability assessment of the pile-supported IABs. A nonlinear regression curve is obtained between the horizontal seismic coefficient and PGA. This curve can be used to evaluate the design horizontal seismic force on the IAB.

In the next chapter, a summary of the present study undertaken is given followed by the conclusions. A scope for further research is also presented.

CHAPTER 7

SUMMARY AND CONCLUSIONS

7.1 SUMMARY

The integral abutment bridges (IABs) are widely accepted and adopted over the conventional bridges due to better performance and maintenance cost. The construction of IABs across the world have increased in numbers and yet a lack of proper understanding exists with respect to the behaviour of IABs. Guidelines and standards related to the design of IABs are also lacking in the literature. Several researchers have conducted field monitoring and numerical simulation studies on the IABs. Numerical studies conducted on the analysis of the behaviour of IABs have adopted nonlinear Winkler spring models to simulate the behaviour of the soil surrounding the bridge superstructure and substructure. A very few studies have incorporated the continuum model for simulation of the soil behaviour and SSI effects. The aim of the present study is to predict the behaviour of the IAB using numerical simulation technique incorporating the nonlinear behaviour of the soil and SSI effects subjected to static, cyclic and thermal loadings. The other loadings such as static coupled bogie loading, moving train loading and seismic loading are also considered in the performance assessment of the IABs. The FE models of the IABs and IARBs are developed using ABAQUS software. The published literature is consulted to obtain the dimensions of the bridge components and soil parameters.

The 2D plane-strain FE model of the pile-supported integral abutment bridge with approach slab is developed and the response is analysed under static, cyclic, and thermal loadings. The nonlinear hysteresis behaviour of the backfill is simulated using hypoplastic sand constitutive model. The hypoplastic constitutive model is validated with triaxial test results of Toyoura and Karlsruhe sands. The FE results are also validated with the large-scale field tests conducted on the abutment backwall involving cyclic loading to establish the passive force-displacement relationship. Additionally, the FE model of the pile group with a Mohr-Coulomb material model for the backfill soil is validated using the large-scale field tests on the pile group for passive force-displacement relationship.

The developed FE model of the field-tested abutment backwall is used to obtain the passive force-displacement relationships under pure translation and pure rotation. Similarly, for the pile-supported abutment-backfill system, the passive force-displacement relationship is obtained under lateral translation. Based on the results, it is noted that the behaviour of the pile-supported abutment-backfill system matches well with the behaviour of abutment backwall under pure translation. The length of the approach slab, backfill soil type and foundation soil stiffness are varied, and the passive force-displacement relationships are obtained. The ambient seasonal temperature fluctuation induces expansion and contraction of the bridge superstructure. This thermal loading is simulated in the FE model by applying the temperature fluctuation in the model and accordingly the response of the IAB is analysed. The thermally induced displacements are obtained from the actual field monitored data on the integral abutment and the same are simulated and the corresponding responses are compared. The field measured displacements are varying and are simulated considering cyclic sinusoidal displacement equal to thermal expansion and contraction equivalent of 20 mm for 20 cycles. The effect of backfill soil type on the generated passive pressure and settlement of the backfill soil is assessed for these number of cycles of thermal loading. The occurrence of soil ratcheting phenomenon is also investigated.

The response of an embankment-IARB transition zone is investigated under static and cyclic coupled bogie loading and moving train loading using the 2D FE analysis. The FE model is validated with the published field data. Subsequently, parametric sensitivity analyses are conducted to explore the behaviour of track transition under different approach slab geometry (length, thickness, inclination, and shape), height of the integral abutment, backfill soil type (loose, medium, and dense sand), train speed (100 km/h, 150 km/h and 200 km/h) and train movement directions (embankment to bridge and bridge to embankment). In the coupled bogie loading simulations, the variation in train speeds (60 km/h, 100 km/h, 150 km/h and 200 km/h) is simulated by using dynamic amplification factor in the FE model and applied at a specific locations of the FE domain. The behaviour of the transition under repeated cyclic coupled bogies loading and moving train passages are investigated. Results show that the behaviour of IARB is sensitive to the length of the approach slab, backfill soil type and train speed.

These findings will enhance the current understanding of the behaviour of IARBs subjected to moving train loading and identify the important parameters that influence their performance.

Seismic response analysis of the pile-supported IAB is carried out using incremental dynamic analysis (IDA) to develop the PSDMs and fragility curves within the framework of PBEE. In the present study, ten earthquake ground motions are selected from the PEER ground motion database. These ground motions are selected by matching the target response spectrum of seismic Zone IV of IS 1893 (Part1): 2021 for Type I rock or hard soil sites. In the IDA, these selected earthquake records are scaled to the required range of the intensity measure. The intensity measure considered in this study is the peak ground acceleration (PGA) which has a range varying from 0.1 to 1.2g. The engineering design parameters (EDPs) considered in the study are permanent vertical displacement of the backfill, settlement of the approach fill and longitudinal displacement of the abutment-backfill system. The limit state thresholds for all the three EDPs are identified, and the corresponding damage states are defined. Total of 82 earthquake ground motions are simulated and the corresponding responses for the EDPs are evaluated. Based on the responses of the EDPs of the IAB, the probabilistic seismic demand models (PSDMs) are developed. The fragility curves are also generated from the PSDMs for the each of the limit state thresholds. These fragility curves can be used to evaluate the losses associated with the pile-supported integral abutment bridges in future seismic events. Based on the estimated losses, the retrofiting strategies can be adopted and accordingly the bridges can be rehabilitated.

7.2 CONCLUSIONS

The following conclusions are arrived at from the present study:

Behaviour of integral abutment bridge under static, cyclic and thermal loadings

- The passive force-displacement relationship evaluated for the pile-supported integral abutment subjected to lateral translation applied at the monolithic connection of the integral abutment, deck slab and steel girder is found to be matching well with the abutment backwall-soil system subjected to pure translation.

- The effect of variation in the length of the approach slab and foundation soil stiffness is minimum on the passive force-displacement relationship for the pile-supported integral abutment.
- The effect of backfill soil type on the passive force-displacement relationship is significant. The maximum and minimum passive forces on the abutment are generated in the case of dense and loose sand conditions, respectively.
- The presence of approach slab has moved the formation backfill heave at the end of the approach slab rather than behind the integral abutment. It is noted that with increase in the length of the approach slab the increase in the backfill heave is observed.
- The effect of approach slab on the vertical settlement of the backfill soil subjected to cyclic and thermal loadings is found to be higher at the end tip of the approach slab in the backfill.
- Number of cycles of cyclic thermal loading and thermally induced cyclic displacements have led to drastic increase in the vertical settlement of the backfill. The densification of the backfill soil behind the integral abutment is observed with the increase in the number of cycles of loading. The presence of dense sand backfill soil is found to reduce the vertical settlement of the backfill.
- The occurrence of soil ratcheting phenomenon is not observed in the FE simulation studies under cyclic thermal loading and for SR-18 bridge under field monitored cyclic displacements. The increase in passive pressure behind the abutment of SR-18 bridge is same as in the case of field monitored data. The soil ratcheting is found to occur in the initial three cycles of displacement loading as in the observed field data.
- The presence of soil ratcheting is observed even in the FE simulation studies of the cyclic sinusoidal displacement of amplitude ± 20 mm for 20 cycles. The soil ratcheting is more predominant in both the medium and dense sands backfill.

Behaviour of transition zone of IARB under static and cyclic coupled bogie loadings and moving train loading

- The behaviour of a railway track in the IARB transition zone is sensitive to the approach slab geometry. The track displacement at the transition decreases with increase in the length, thickness and inclination of the approach slab. The

approach slab provides a gradual transition in the displacement from the softer to the stiffer side and vice versa.

- In the middle of the approach slab, the peak track displacement for the case: (a) Length – decreases by 50% for any approach slab length compared to the case of without approach slab, (b) Thickness – decreases by 14.3% to 34.1% for the slab thickness varying from 300 mm to 700 mm, and (c) Inclination (i) – decreases by 1.9% to 8.9% for the i varying from 2% to 10% as compared to the nominal case (i.e., $i = 0\%$).
- The approach slab reduces the stresses transmitted to the backfill soil at the transition zone. However, the stress concentration occurs at the free end of the approach slab, which can be minimised by installing a sleeper slab at the free end of the approach slab.
- The effectiveness of the trapezoidal approach slab in mitigating the differential movements is identical to that provided by the rectangular slab suggesting that the shape of the approach slab has a marginal effect on the behaviour of track transitions. However, the other factors such as the construction cost and effective water drainage, may influence the selection of the most effective shape.
- The backfill soil type significantly influences the track displacement at the transition. The track displacement is found to be maximum and minimum for the loose and dense sands, respectively. This indicates that the effective compaction of the backfill soil from loose to dense condition will significantly reduce the track displacement (i.e., 31% and 27%) at the embankment and middle of the approach slab, respectively.
- Vertical displacement at the top of the backfill soil layer is found to be significant at the embankment section in comparison to the transition zone. The enhanced load transfer from the ballast to the approach slab in the transition zone has helped reduce the vertical displacement of the track.
- The train movement direction also influences the track behaviour. The track displacement along the approach slab and near its free end is lower for the case when the train moves from the bridge towards the embankment as compared with the case when the train moves in the opposite direction (i.e., from the embankment to the bridge).

- It is found that the interface between the embankment and the transition zone is susceptible to excessive vertical displacements under the static and cyclic coupled bogie loadings.
- The vertical track displacement increases with increase in the train speed. However, the variation of track displacement with the train speed at the middle of the approach slab and bridge is less than that at the embankment.
- The cumulative vertical settlement of the track increases with increase in the number of train passages with varying magnitude at the embankment, approach slab and bridge sections. The approach slab provides a gradual change in the settlement along the length of the track, thereby improving the performance of the transition zone.

Response of integral abutment bridge under seismic loads

- The seismic vulnerability of the IABs adopted for railways is higher compared to highways due to lower tolerance for the vertical displacement of the backfill.
- For the longitudinal displacement of the abutment-backfill system, the seismic vulnerability is very high for slight and extensive damages under lower PGA values. Based on the results of fragility analysis of IABs, the probability of observable and minor damages can occur in the approach fill at lower values of PGA.
- Higher magnitude earthquake having higher PGA values induce higher probability of ultimate damage to the abutment-backfill system and moderate to severe damage to the backfill.
- The PSDMs and fragility curves developed for the IABs are very useful to evaluate the damage states for different PGA values. Based on the damage states, the loss estimation can be made and accordingly the retrofiting strategies can be undertaken.

7.3 SCOPE FOR FURTHER RESEARCH

The following are the aspects that can be addressed in the future studies.

- The behaviour of integral abutment bridge superstructure is simulated as linear elastic. The effect of variation in different parameters such as skew angle, H-pile orientation in strong and weak axes, bridge span length and number of spans in the bridge are not taken into consideration in the present study.

- The wheel load is applied as a point load, which essentially acts as a line load in 2D plane-strain analysis. This will not realistically replicate the train-induced loading. The 2.5D or 3D numerical analysis can be employed for more accurate simulation of the train-induced loads.
- The vehicle-track interaction has been ignored and a constant value of wheel load is assumed. However, the train-induced loads may fluctuate as the train traverses along the transition with an abrupt change in the support conditions.
- The influence of fluctuations in moisture content and temperature on the response of the IARB-embankment transition zone has not been addressed.
- The consideration of crib ballast between the sleepers is ignored for the simplicity of finite element simulations. The crib ballast can be modelled explicitly in future studies.
- The train-loading has been considered only along the vertical direction. However, the real track is subjected to loads acting along the vertical, longitudinal, and transverse directions.
- Seismic fragility curves developed for the pile-supported integral abutment bridge under only one horizontal component of the earthquake ground motion along the longitudinal direction in the FE model. The response of the IAB under multi-directional ground motions will reveal the realistic interaction between different components of the bridge and as a consequence the global behaviour can be evaluated comprehensively.
- Uncertainties in the earthquake ground motions are not explicitly considered in the present study although a suite of ten ground motions are considered for the fragility analysis of the IAB. Explicit consideration of uncertainties in the ground motions will provide comprehensive understanding of the seismic performance of the IAB.

REFERENCE

1. **AASHTO** *Guide Specifications for LRFD Seismic Bridge Design*. American Association of State Highway and Transportation Officials, Washington, DC, 2015.
2. **ABAQUS/CAE** ABAQUS/CAE User's Guide, Dassault Systèmes, Providence, Rhode Island, USA, 2014.
3. **Abdel-Fattah, M. T., T. T. Abdel-Fattah, and A. A. Hemada** (2018) Nonlinear Finite-Element Analysis of Integral Abutment Bridges due to Cyclic Thermal Changes. *Journal of Bridge Engineering*, 23(2). [https://doi.org/10.1061/\(asce\)be.1943-5592.0001183](https://doi.org/10.1061/(asce)be.1943-5592.0001183)
4. **Abdullah, A., and H. El Naggar** (2023) Soil-Structure Interaction of Integral Abutments. *Transportation Geotechnics*, 38, 100900. <https://doi.org/10.1016/j.trgeo.2022.100900>
5. **Ahmed, B. F., and K. Dasgupta** (2022) Seismic Limit States of the Components in Reinforced Concrete Integral Abutment Bridges. *Bulletin of Earthquake Engineering*, 20(1), 477–516. <https://doi.org/10.1007/s10518-021-01210-0>
6. **Ahmed, B. F., and K. Dasgupta** (2023) A Methodology for Assessing the Component-Level Fragility Curves and Its Application to a Class of Integral Abutment Bridges. *ASCE-ASME Journal of Risk and Uncertainty in Engineering Systems, Part A: Civil Engineering*, 9(1), 04022056. <https://doi.org/10.1061/ajrua6.0001276>
7. **Al-qarawi, A., Leo, C., and D. S. Liyanapathirana** (2020) Effects of Wall Movements on Performance of Integral Abutment Bridges. *International Journal of Geomechanics*, 20(2), 04019157. [https://doi.org/10.1061/\(asce\)gm.1943-5622.0001559](https://doi.org/10.1061/(asce)gm.1943-5622.0001559)
8. **Applied Technology Council, ATC** *Quantification Seismic of Building Seismic Performance Factors*, ATC-63, Applied Technology Council, Redwood City, California, 2008.

9. **Argyroudis S.** and **A. M. Kaynia** (2014) Fragility Functions of Highway and Railway Infrastructure. In **K. Pitilakis, H. Crowley, and A. M. Kaynia** (eds.), *SYNER-G: Typology Definition and Fragility Functions for Physical Elements at Seismic Risk: Buildings, Lifelines, Transportation Networks and Critical Facilities* (pp. 299–326). Springer Netherlands. https://doi.org/10.1007/978-94-007-7872-6_10
10. **Argyroudis, S., A. M. Kaynia, and K. Pitilakis** (2013) Development of Fragility Functions for Geotechnical Constructions: Application to Cantilever Retaining Walls. *Soil Dynamics and Earthquake Engineering*, 50, 106–116. <https://doi.org/10.1016/j.soildyn.2013.02.014>
11. **Argyroudis, S., and A. M. Kaynia** (2015) Analytical Seismic Fragility Functions for Highway and Railway Embankments and Cuts. *Earthquake Engineering and Structural Dynamics*, 44(11), 1863–1879. <https://doi.org/10.1002/eqe.2563>
12. **Argyroudis, S., S. Mitoulis, A. M. Kaynia, and M. G. Winter** (2018) Fragility Assessment of Transportation Infrastructure Systems Subjected to Earthquakes. In *Geotechnical Earthquake Engineering and Soil Dynamics V* (pp. 174–183). <https://doi.org/10.1061/9780784481479.018>
13. **Arsoy, S.** (2004). Mobilization of Passive Earth Pressures Behind Abutments of Jointless Bridges. *Transportation Research Record: Journal of the Transportation Research Board*, 1868(1), 199–204. <https://doi.org/10.3141/1868-21>
14. **Asghari, K., S. Sotoudeh, and J. A. Zakeri** (2021) Numerical Evaluation of Approach Slab Influence on Transition Zone Behavior in High-Speed Railway Track. *Transportation Geotechnics*, 28, 100519. <https://doi.org/10.1016/j.trgeo.2021.100519>
15. **Banimahd, M.** (2008) *Advanced Finite Element Modelling of Coupled Train-Track Systems: A Geotechnical Perspective*, Doctoral Dissertation, Heriot-Watt University, Edinburgh, UK.
16. **Banimahd, M., P. K. Woodward, J. Kennedy, and G. M. Medero** (2012) Behaviour of Train-Track Interaction in Stiffness Transitions. *Proceedings of*

- the Institution of Civil Engineers: Transport*, 165(3), 205–214.
<https://doi.org/10.1680/tran.10.00030>
17. **Bloodworth, A. G., M. Xu, J. R. Banks, and C. R. I. Clayton** (2012) Predicting the Earth Pressure on Integral Bridge Abutments. *Journal of Bridge Engineering*, 17(2), 371–381. [https://doi.org/10.1061/\(ASCE\)BE.1943-5592](https://doi.org/10.1061/(ASCE)BE.1943-5592)
 18. **Bowles, J. E.** *Foundation Analysis and Design*, 5th Edition, The McGraw-Hill Companies, Inc., Singapore, 1996.
 19. **Breña, S. F., C. H. Bonczar, S. A. Civjan, J. T. DeJong, and D. S. Crovo** (2007) Evaluation of Seasonal and Yearly Behavior of an Integral Abutment Bridge. *Journal of Bridge Engineering*, 12(3), 296–305. <https://doi.org/10.1061/ASCE1084-0702200712:3296>
 20. **Briaud, J. L.** (1997) Settlement of Bridge Approaches: The Bump at the End of the Bridge, *Transportation Research Board*, 234. http://onlinepubs.trb.org/Onlinepubs/nchrp/nchrp_syn_234.pdf
 21. **Burdet, O., J. Einpaul, and A. Muttoni** (2015) Experimental Investigation of Soil-Structure Interaction for the Transition Slabs of Integral Bridges. *Structural Concrete*, 16(4), 470–479. <https://doi.org/10.1002/suco.201500018>
 22. **Bureau of Indian Standards, BIS** *Criteria for Earthquake Resistant Design of Structures, Part 1: General Provisions and Buildings*, IS 1893 (Part 1), Bureau of Indian Standards, New Delhi, 2016.
 23. **Bureau of Indian Standards, BIS** *Criteria for Earthquake Resistant Design of Structures, Part 3: Bridges and Retaining Walls*, IS 1893 (Part 3), Bureau of Indian Standards, New Delhi, 2016.
 24. **Burke Jr, M. P.** *Integral and Semi-integral Bridges*, John Wiley and Sons, Chichester, UK, 2009.
 25. **Cai, C. S., X. M. Shi, G. Z. Voyiadjis, and Z. J. Zhang** (2005) Structural Performance of Bridge Approach Slabs under Given Embankment Settlement. *Journal of Bridge Engineering*, 10(4), 482–489. <https://doi.org/10.1061/ASCE1084-0702200510:4482>
 26. **CALTRANS, S. D. C.** *Seismic Design Criteria. Version 1.7*. California Department of Transportation, Sacramento, CA, 2013.

27. **Choine, M. N., A. J. O’connor, and J. E. Padgett** (2015) Comparison between the Seismic Performance of Integral and Jointed Concrete Bridges. *Journal of Earthquake Engineering*, 19(1), 172–191. <https://doi.org/10.1080/13632469.2014.946163>
28. **Chopra, A. K.** *Dynamics of Structures: Theory and Applications to Earthquake Engineering*, Pearson Education Limited, Essex, England, 2014.
29. **Choudhury, D., and S. Nimbalkar** (2005) Seismic Passive Resistance by Pseudo-Dynamic Method. *Geotechnique*, 55(9), 699–702. <https://doi.org/10.1680/geot.2005.55.9.699>
30. **Civjan, S. A., C. Bonczar, S. F. Breña, J. DeJong, and D. Crovo** (2007) Integral Abutment Bridge Behavior: Parametric Analysis of a Massachusetts Bridge. *Journal of Bridge Engineering*, 12(1), 64–71. <https://doi.org/10.1061/ASCE1084-0702200712:164>
31. **Civjan, S. A., E. Kalayci, B. H. Quinn, S. F. Breña, and C. A. Allen** (2013) Observed Integral Abutment Bridge Substructure Response. *Engineering Structures*, 56, 1177–1191. <https://doi.org/10.1016/j.engstruct.2013.06.029>
32. **Clayton, C. R., M. Xu, and A. Bloodworth** (2006) A Laboratory Study of the Development of Earth Pressure behind the Integral Bridge Abutments. *Geotechnique*, 56(8), 561-571.
33. **Clough, G. W., and J. M. Duncan.** *Earth Pressures*. pp. 223–235. In **H-Y. Fang** (ed.) In *Foundation Engineering Handbook*, Van Nostrand Reinhold, New York, 1991.
34. **Coelho, B., P. Hölcher, J. Priest, W. Powrie, and F. Barends** (2011) An Assessment of Transition Zone Performance. *Proceedings of the Institution of Mechanical Engineers, Part F: Journal of Rail and Rapid Transit*, 225(2), 129–139. <https://doi.org/10.1177/09544097JRRT389>
35. **Cole, R. T., and K. M. Rollins** (2006) Passive Earth Pressure Mobilization during Cyclic Loading. *Journal of Geotechnical and Geoenvironmental Engineering*, 132(9), 1154–1164. <https://doi.org/10.1061/ASCE1090-02412006132:91154>

36. **Cornell, C. A., F. Jalayer, R. O. Hamburger, and D. A. Foutch** (2002) Probabilistic Basis for 2000 SAC Federal Emergency Management Agency Steel Moment Frame Guidelines. *Journal of Structural Engineering*, 128(4), 413–555. <https://doi.org/10.1061/ASCE0733-94452002128:4526>
37. **Cosgrove, E. F., and B. M. Lehane** (2003) Cyclic Loading of Loose Backfill Placed Adjacent to Integral Bridge Abutments. *International Journal of Physical Modelling in Geotechnics*, 3(3), 9–16. <https://doi.org/10.1680/ijpmg.2003.030302>
38. **Dahlberg, T.** (2010). Railway Track Stiffness Variations – Consequences and Countermeasures. *International Journal of Civil Engineering*, 8(1), 1–12. <http://ijce.iust.ac.ir/article-1-420-en.html>
39. **David, T. K., J. P. Forth, and J. Ye** (2014) Superstructure Behavior of a Stub-Type Integral Abutment Bridge. *Journal of Bridge Engineering*, 19(6), 04014012. [https://doi.org/10.1061/\(asce\)be.1943-5592.0000583](https://doi.org/10.1061/(asce)be.1943-5592.0000583)
40. **Dauids, W. G., T. Sandford, S. Ashley, J. DeLano, and C. Lyons** (2010) Field-Measured Response of an Integral Abutment Bridge with Short Steel H-Piles. *Journal of Bridge Engineering*, 15(1), 32–43. <https://doi.org/10.1061/ASCE1084-0702201015:132>
41. **Dhar, S., and K. Dasgupta** (2019) Seismic Soil Structure Interaction for Integral Abutment Bridges: A Review. *Transportation Infrastructure Geotechnology*, 6(4), 249–267. <https://doi.org/10.1007/s40515-019-00081-y>
42. **Di Donna, A., A. Ferrari, and L. Laloui** (2016) Experimental Investigations of the Soil–Concrete Interface: Physical Mechanisms, Cyclic Mobilization, and Behaviour at Different Temperatures. *Canadian Geotechnical Journal*, 53(4), 659–672. <https://doi.org/10.1139/cgj-2015-0294>
43. **Dicleli, M.** (2005) Integral Abutment-Backfill Behavior on Sand Soil-Pushover Analysis Approach. *Journal of Bridge Engineering*, 10(3), 354–364. <https://doi.org/10.1061/ASCE1084-0702200510:3354>
44. **Dicleli, M., P. Eng, and S. M. Albhaisi** (2003) Maximum Length of Integral Bridges Supported on Steel H-piles Driven in Sand. *Engineering Structures*, 25(12), 1491–1504. [https://doi.org/10.1016/S0141-0296\(03\)00116-0](https://doi.org/10.1016/S0141-0296(03)00116-0)

45. **Duncan, J. M., and C. Y. Chang** (1970) Nonlinear Analysis of Stress and Strain in Soils. *Journal of the Soil Mechanics and Foundations Division*, 96(5), 1629–1653. <https://doi.org/10.1061/JSFEAQ.0001458>
46. **Duncan, M. J., and R. L. Mokwa** (2001) Passive Earth Pressures: Theories and Tests. *Journal of Geotechnical and Geoenvironmental Engineering*, 127(3), 248–257. [https://doi.org/10.1061/\(ASCE\)1090-0241\(2001\)127:3\(248\)](https://doi.org/10.1061/(ASCE)1090-0241(2001)127:3(248))
47. **England, G. L., N. C. M. Tsang, and D. Bush**, *Integral Bridges - A Fundamental Approach to the Time Temperature Loading Problem*, ICE Publishing, London, 2000.
48. **Erhan, S., and M. Dicleli** (2014) Effect of Dynamic Soil-Bridge Interaction Modeling Assumptions on the Calculated Seismic Response of Integral Bridges. *Soil Dynamics and Earthquake Engineering*, 66, 42–55. <https://doi.org/10.1016/j.soildyn.2014.06.033>
49. **Esveld, C.** *Modern railway track*, MRT-Productions, Delft, The Netherlands, 2001.
50. **Faraji, S., J. M. Ting, D. S. Crovo, and H. Ernst** (2001). Nonlinear Analysis of Integral Bridges: Finite-Element Model. *Journal of Geotechnical and Geoenvironmental Engineering*, 127(5), 454–461. [https://doi.org/10.1061/\(ASCE\)1090-0241\(2001\)127:5\(454\)](https://doi.org/10.1061/(ASCE)1090-0241(2001)127:5(454))
51. **Farooq, M. A., S. Nimbalkar, and B. Fatahi** (2021) Three-Dimensional Finite Element Analyses of Tyre Derived Aggregates in Ballasted and Ballastless Tracks. *Computers and Geotechnics*, 136, 104220. <https://doi.org/10.1016/j.compgeo.2021.104220>
52. **Federal Emergency Management Agency, FEMA P – 695.** *Quantification of Building Seismic Performance Factors*. Washington, DC, 2009.
53. **Fennema, J. L., J. A. Laman, and D. G. Linzell** (2005) Predicted and Measured Response of an Integral Abutment Bridge. *Journal of Bridge Engineering*, 10(6), 666–677. <https://doi.org/10.1061/ASCE1084-0702200510:6666>
54. **Franke, B. W.** (2013). *Passive Force on Skewed Abutments with Mechanically Stabilized Earth (MSE) Wingwalls Based on Large-Scale Tests*, Doctoral

- Dissertation, Brigham Young University, Provo, Utah, USA.
<https://scholarsarchive.byu.edu/etd/3909>
55. **Frosch, R. J., M. E. Kreger, and A. M. Talbott.** *Earthquake Resistance of Integral Abutment Bridges*, Indiana Department of Transportation, Indianapolis, USA, 2009. <https://doi.org/10.5703/1288284313448>
 56. **Gadicherla, V., G. R. Dodagoudar, and M. P. Anumolu** (2022) Seismic Fragility Analysis of a Two Bay Two Storey Underground Metro Station: A Case Study. *International Journal of Advances in Engineering Sciences and Applied Mathematics*, 14(3–4), 80–93. <https://doi.org/10.1007/s12572-022-00323-2>
 57. **Giannakos, K., and S. Tsoukantas** (2012) Transition Zone between Ballastless and Ballasted Track: Influence of Changing Stiffness on Acting Forces. *Procedia - Social and Behavioral Sciences*, 48, 3548–3557. <https://doi.org/10.1016/j.sbspro.2012.06.1318>
 58. **Gudehus, G.** (1996) A Comprehensive Constitutive Equation for Granular Materials. *Soils and Foundations*, 36(1), 1–12. <https://doi.org/10.3208/sandf.36.1>
 59. **Hall, L.** (2003) Simulations and Analyses of Train-Induced Ground Vibrations in Finite Element Models. *Soil Dynamics and Earthquake Engineering*, 23(5), 403–413. [https://doi.org/10.1016/S0267-7261\(02\)00209-9](https://doi.org/10.1016/S0267-7261(02)00209-9)
 60. **Hassiotis, S., and K. Xiong** (2007) Field Measurements of Passive Pressures Behind an Integral Abutment Bridge. *7th FMGM 2007: Field Measurements in Geomechanics*. [https://doi.org/10.1061/40940\(307\)9](https://doi.org/10.1061/40940(307)9)
 61. **Herle, I., and G. Gudehus** (1999) Determination of Parameters of a Hypoplastic Constitutive Model from Properties of Grain Assemblies. *Mechanics of Cohesive-Frictional Materials*, 4(5), 461–486. [https://doi.org/10.1002/\(SICI\)1099-1484\(199909\)4:5<461::AID-CFM71>3.0.CO;2-P](https://doi.org/10.1002/(SICI)1099-1484(199909)4:5<461::AID-CFM71>3.0.CO;2-P)
 62. **Huang, J., C. K. Shield, and C. E. W. French** (2008) Parametric Study of Concrete Integral Abutment Bridges. *Journal of Bridge Engineering*, 13(5), 511–526. <https://doi.org/10.1061/ASCE1084-0702200813:5511>

63. **Huang, J., C. K. Shield, and C. French** (2005) Time-Dependent Behavior of a Concrete Integral Abutment Bridge. *Transportation Research Record: Journal of the Transportation Research Board*, 11s, 299–309. <http://dx.doi.org/10.3141/trr.11s.f114879181v878t1>
64. **Huang, Y. H., C. Lin, and J. G. Rose** (1984) Asphalt Pavement Design: Highway versus Railroad. *Journal of Transportation Engineering*, 110(2), 276–282. [https://doi.org/10.1061/\(ASCE\)0733-947X\(1984\)110:2\(276\)](https://doi.org/10.1061/(ASCE)0733-947X(1984)110:2(276))
65. **Huntley, S. A., and A. J. Valsangkar** (2013). Field Monitoring of Earth Pressures on Integral Bridge Abutments. *Canadian Geotechnical Journal*, 50(8), 841–857. <https://doi.org/10.1139/cgj-2012-0440>
66. **Huntley, S. A., and A. J. Valsangkar** (2014) Behaviour of H-piles supporting an integral abutment bridge. *Canadian Geotechnical Journal*, 51(7), 713–734. <https://doi.org/10.1139/cgj-2013-0254>
67. **Huntley, S. A., and A. J. Valsangkar** (2018). Nine-Year Field-Monitoring Data from an Integral-Abutment Bridge. pp. 101–111, In **X. Zhang, P. J. Cosentino, and M. H. Hussein** (eds.), *Innovations in Geotechnical Engineering*. <https://doi.org/10.1061/9780784481639.005>
68. **Hwang, H., J. Jernigan, and Y. Lin**, (2000) Evaluation of Seismic Damage to Memphis Bridges and Highway Systems. *Journal of Bridge Engineering*, ASCE, 5(4), 322-330.
69. **Indian Railway Standard: Bridge Manual**. Research Designs and Standard Organization, Ministry of Railways, Government of India, Lucknow, 1998.
70. **Indian Railway Standard: Code of Practice for Plain, Reinforced, and Prestressed Concrete for General Bridge Construction**, Research Designs & Standards Organization, Ministry of Railways, Government of India, Lucknow, 1997.
71. **Indian Roads Congress, IRC Criteria Standard Specifications and Code of Practice for Road Bridges, Section II: Loads and Load Combinations**, IRC 6, Indian Roads Congress, New Delhi, 2017.
72. **Indraratna, B., and S. Nimbalkar** (2013) Stress-Strain Degradation Response of Railway Ballast Stabilized with Geosynthetics. *Journal of Geotechnical and*

- Geoenvironmental Engineering*, 139(5), 684–700.
[https://doi.org/10.1061/\(asce\)gt.1943-5606.0000758](https://doi.org/10.1061/(asce)gt.1943-5606.0000758)
73. **Jeong, S.** and **A. Elnashai** (2007) Probabilistic Fragility Analysis Parameterized by Fundamental Response Quantities. *Engineering Structures*, 29(6), 1238-1251.
74. **Jessee, S. J.** (2012) *Skew Effects on Passive Earth Pressures Based on Large-Scale Tests*, Doctoral Dissertation, Brigham Young University, Provo, Utah, USA. <https://scholarsarchive.byu.edu/etd/3202>
75. **Kalayci, E.** (2012) *Performance Monitoring and Analysis of Integral Abutment Bridges*, Doctoral Dissertation, University of Massachusetts - Amherst. <https://doi.org/10.7275/5694961>
76. **Kalayci, E., S. A. Civjan,** and **S. F. Breña** (2012) Parametric Study on the Thermal Response of Curved Integral Abutment Bridges. *Engineering Structures*, 43, 129–138. <https://doi.org/10.1016/j.engstruct.2012.05.007>
77. **Kavazanjian E., J. Wang, G. Martin, A. Shamsabadi, I. Lam, S. E. Dickenson,** and **C. J. Hung.** *LRFD Seismic Analysis and Design of Transportation Geotechnical Features and Structural Foundations - NHI Course No. 130094 Reference Manual Geotechnical Engineering Circular No. 3.* FHWA-NHI-11-032, National Highway Institute, Federal Highway Administration, Washington, D.C., 2011. <https://rosap.nhl.bts.gov/view/dot/40372>
78. **Kaynia, A. M., C. Madshus,** and **P. Zackrisson** (2000) Ground Vibration from High-Speed Trains: Prediction and Countermeasure. *Journal of Geotechnical and Geoenvironmental Engineering*, 126(6), 495–582. [https://doi.org/10.1061/\(ASCE\)1090-0241\(2000\)126:6\(531\)](https://doi.org/10.1061/(ASCE)1090-0241(2000)126:6(531))
79. **Kerokoski, O.** (2006). *Soil-Structure Interaction of Long Jointless Bridges with Integral Abutments*, Doctoral Dissertation, Tampere University of Technology, Tampere, Finland.
80. **Khasawneh, Y. A.** (2014). *Soil Structure Interaction of Integral Abutment Bridges*, Doctoral Dissertation, Purdue University, West Lafayette, Indiana. <https://docs.lib.purdue.edu/dissertations/AAI3669413/>

81. **Khodair, Y. A., and S. Hassiotis** (2005) Analysis of Soil-Pile Interaction in Integral Abutment. *Computers and Geotechnics*, 32(3), 201–209. <https://doi.org/10.1016/j.compgeo.2005.01.005>
82. **Khodair, Y., and A. Ibrahim** (2013) Seismic Analysis of Integral Abutment Bridges Considering Soil-Structure Interaction. *Structures Congress 2013: Bridging Your Passion with Your Profession*, 2895–2903. <https://doi.org/10.1061/9780784412848.252>
83. **Kim, W. S., and J. A. Laman** (2010) Integral Abutment Bridge Response under Thermal Loading. *Engineering Structures*, 32(6), 1495–1508. <https://doi.org/10.1016/j.engstruct.2010.01.004>
84. **Kim, W., and J. A. Laman** (2012) Seven-Year Field Monitoring of Four Integral Abutment Bridges. *Journal of Performance of Constructed Facilities*, 26(1), 54–64. [https://doi.org/10.1061/\(asce\)cf.1943-5509.0000250](https://doi.org/10.1061/(asce)cf.1943-5509.0000250)
85. **Kirupakaran, K., and K. K. Muraleetharan** (2017) Parametric Study for Understanding the Behavior of Integral Abutment Bridges. In *Geotechnical Frontiers 2017*, pp. 164–173. <https://doi.org/10.1061/9780784480465.017>
86. **Kirupakaran, K., B. Hanlon, K. K. Muraleetharan, and G. A. Miller** (2012) Field-Measured Response of an Integral Abutment Bridge. *GeoCongress 2012: State of the Art and Practice in Geotechnical Engineering*, 2157–2166. <https://doi.org/10.1061/9780784412121.221>
87. **Kirupakaran, K., K. K. Muraleetharan, and G. A. Miller** (2015) Soil-Structure Interactions in a Skewed Integral Abutment Bridge. *IFCEE 2015*, 309–318. <https://doi.org/10.1061/9780784479087.031>
88. **Kolymbas, D.** *Introduction to Hypoplasticity: Advances in Geotechnical Engineering and Tunnelling 1*, (1st ed.). CRC Press, London, 2000. <https://doi.org/10.1201/9781482283785>
89. **Kong, B., C. S. Cai, and X. Kong** (2015) Field Monitoring Study of an Integral Abutment Bridge Supported by Prestressed Precast Concrete Piles on Soft Soils. *Engineering Structures*, 104, 18–31. <https://doi.org/10.1016/j.engstruct.2015.09.004>

90. **Kozak, D. L., L. A. Fahnestock, and J. M. LaFave** (2022) Seismic Behavior Assessment for Design of Integral Abutment Bridges in Illinois. *Earthquake Engineering and Engineering Vibration*, 21(2), 573–589. <https://doi.org/10.1007/s11803-022-2104-5>
91. **Kramer, S. L.** *Geotechnical Earthquake Engineering*, Prentice-Hall, Upper Saddle River, New Jersey, 1996.
92. **Kramer, S.** (2014) Performance-based design methodologies for geotechnical earthquake engineering. *Bulletin of Earthquake Engineering*, 12(3), 1049-1070. <https://doi.org/10.1007/s10518-013-9484-x>
93. **Kunin, J., and S. Alampalli** (2000) Integral Abutment Bridges: Current Practice in United States and Canada. *Journal of Performance of Constructed Facilities*, 14(3), 87–131. [https://doi.org/10.1061/\(ASCE\)0887-3828\(2000\)14:3\(104\)](https://doi.org/10.1061/(ASCE)0887-3828(2000)14:3(104))
94. **LaFave, J. M., J. K. Riddle, M. W. Jarrett, B. A. Wright, J. S. Svatora, H. An, and L. A. Fahnestock** (2016) Numerical Simulations of Steel Integral Abutment Bridges under Thermal Loading. *Journal of Bridge Engineering*, 20(10), 04016061-. [https://doi.org/10.1061/\(ASCE\)](https://doi.org/10.1061/(ASCE))
95. **Lemnitzer, A., E. R. Ahlberg, R. L. Nigbor, A. Shamsabadi, J. W. Wallace, and J. P. Stewart** (2009) Lateral Performance of Full-Scale Bridge Abutment Wall with Granular Backfill. *Journal of Geotechnical and Geoenvironmental Engineering*, 135(4), 506–514. <https://doi.org/10.1061/ASCE1090-02412009135:4506>
96. **Leshchinsky, B., and H. Ling** (2013) Effects of Geocell Confinement on Strength and Deformation Behavior of Gravel. *Journal of Geotechnical and Geoenvironmental Engineering*, 139(2), 340–352. [https://doi.org/10.1061/\(asce\)gt.1943-5606.0000757](https://doi.org/10.1061/(asce)gt.1943-5606.0000757)
97. **Li, D., and D. Davis** (2005) Transition of Railroad Bridge Approaches. *Journal of Geotechnical and Geoenvironmental Engineering*, 131(11), 1392–1398. <https://doi.org/10.1061/ASCE1090-02412005131:111392>
98. **Li, L., S. Nimbalkar, and R. Zhong** (2018) Finite Element Model of Ballasted Railway with Infinite Boundaries Considering Effects of Moving Train Loads

- and Rayleigh Waves. *Soil Dynamics and Earthquake Engineering*, 114, 147–153. <https://doi.org/10.1016/j.soildyn.2018.06.033>
99. **Lovell, M. D.** (2010) *Long-Term Behavior of Integral Abutment Bridges*, Doctoral Dissertation, Purdue University, West Lafayette, Indiana. http://www.purdue.edu/policies/pages/teach_res_outreach/viii_3_1.html
 100. **Mackie, K. R.** and **B. Stojadinovic**, *Fragility basis for California Highway Overpass Bridge Seismic Decision Making*, PEER, Report 2005/02, University of California, Berkeley, USA, 2005.
 101. **Mangalathu, S.** (2017) *Performance Based Grouping and Fragility Analysis of Box-Girder Bridges in California*, Doctoral Dissertation, Georgia Institute of Technology, Atlanta, Georgia. <http://hdl.handle.net/1853/58291>
 102. **Maroney, B.** (1995) *Large Scale Bridge Abutment Test to Determine Stiffness and Ultimate Strength under Seismic Loading*, Doctoral dissertation, University of California, Davis, CA.
 103. **Marsh, A. K.** (2013) *Evaluation of Passive Force on Skewed Bridge Abutments with Large-Scale Tests*, Doctoral Dissertation, Brigham Young University, Provo, Utah, USA. <https://scholarsarchive.byu.edu/etd/3921>
 104. **Marsh, A., K. Rollins, B. Franke, J. Smith, and K. Palmer** (2013) Passive Force-Deflection Behavior for 0° and 30° Skewed Abutments. *Transportation Research Record: Journal of the Transportation Research Board*, 2363(1), 12–20. <https://doi.org/10.3141/2363-02>
 105. **Martin G. R.** and **L. Yan** (1995) Modeling Passive Earth Pressure for Bridge Abutments. Earthquake-Induced Movements and Seismic Remediation of Existing Foundations and Abutments, *ASCE 1995 Annual National Convention, Geotechnical Special Publication*, San Diego, California, 55.
 106. **Maruri, R. F.** and **S. H. Petro** (2005) Integral Abutments and Jointless Bridges (IAJB) 2004 Survey Summery, *Proceedings The 2005-FHWA Conference, Baltimore, Maryland*.
 107. **Matsuoka, H.** and **T. Nakai** (1974) Stress deformation and strength characteristics of soil under three different principal stresses. *Proceedings of the Japanese Society of Civil Engineers*, 232, 59–70.

https://doi.org/10.2208/jscej1969.1974.232_59

108. **Meena, N. K., S. Nimbalkar, B. Fatahi, and G. Yang** (2020) Effects of Soil Arching on Behavior of Pile-Supported Railway Embankment: 2D FEM Approach. *Computers and Geotechnics*, 123, 103601. <https://doi.org/10.1016/j.compgeo.2020.103601>
109. **Mei, G., Q. Chen, and L. Song** (2009) Model for Predicting Displacement-Dependent Lateral Earth Pressure. *Canadian Geotechnical Journal*, 46(8), 969–975. <https://doi.org/10.1139/T09-040>
110. **Mistry, V. C.** (2005) Integral Abutment and Jointless Bridges, *Proceedings The 2005-FHWA Conference, Baltimore, Maryland*.
111. **Mitoulis, S. A.** (2020) Challenges and Opportunities for the Application of Integral Abutment Bridges in Earthquake-Prone Areas: A Review. *Soil Dynamics and Earthquake Engineering*, 135, 106183. <https://doi.org/10.1016/j.soildyn.2020.106183>
112. **Mylonakis, G., P. Kloukinas, and C. Papantonopoulos** (2007) An Alternative to the Mononobe-Okabe Equations for Seismic Earth Pressures. *Soil Dynamics and Earthquake Engineering*, 27(10), 957–969. <https://doi.org/10.1016/j.soildyn.2007.01.004>
113. **Namura, A., and T. Suzuki** (2007) Evaluation of Countermeasures against Differential Settlement at Track Transitions. *Quarterly Report of RTRI*, 48(3), 176–182. <https://doi.org/10.2219/rtriqr.48.176>
114. **Ni, P., S. Mangalathu, L. Song, G. Mei, and Y. Zhao** (2018) Displacement-Dependent Lateral Earth Pressure Models. *Journal of Engineering Mechanics*, 144(6). [https://doi.org/10.1061/\(asce\)em.1943-7889.0001451](https://doi.org/10.1061/(asce)em.1943-7889.0001451)
115. **NIBS HAZUS-MH: Technical Manuals**, Federal Emergency Management Agency and National Institute of Building Science, Washington, DC, USA, 2004.
116. **Nielson, B. G.** (2005) *Analytical Fragility Curves for Highway Bridges in Moderate Seismic Zones*, Doctoral dissertation, Georgia Institute of Technology, Atlanta, Georgia.

117. **Nimbalkar, S., B. Indraratna, S. K. Dash, and D. Christie** (2012) Improved Performance of Railway Ballast under Impact Loads Using Shock Mats. *Journal of Geotechnical and Geoenvironmental Engineering*, 138(3), 281–294. [https://doi.org/10.1061/\(asce\)gt.1943-5606.0000598](https://doi.org/10.1061/(asce)gt.1943-5606.0000598)
118. **Ooi, P. S. K., X. Lin, and H. S. Hamada** (2010a). Field Behavior of an Integral Abutment Bridge Supported on Drilled Shafts. *Journal of Bridge Engineering*, 15(1), 4–18. <https://doi.org/10.1061/ASCEBE.1943-5592.0000036>
119. **Ooi, P. S. K., X. Lin, and H. S. Hamada** (2010b). Numerical Study of an Integral Abutment Bridge Supported on Drilled Shafts. *Journal of Bridge Engineering*, 15(1), 19–31. <https://doi.org/10.1061/ASCEBE.1943-5592.0000037>
120. **Padgett J. E., B. G. Nielson and R. DesRoches** (2008) Selection of Optimal Intensity Measures in Probabilistic Seismic Demand Models Of Highway Bridge Portfolios. *Earthquake Engineering and Structural Dynamics*, 37, 711–725.
121. **Paixão, A., E. Fortunato, and R. Calçada** (2014) Transition Zones to Railway Bridges: Track Measurements and Numerical Modelling. *Engineering Structures*, 80, 435–443. <https://doi.org/10.1016/j.engstruct.2014.09.024>
122. **Pak, D., H. Bigelow, and M. Feldmann** (2017) Design of Composite Bridges with Integral Abutments. *Steel Construction*, 10(1), 23–30. <https://doi.org/https://doi.org/10.1002/stco.201710006>
123. **Paul, M., J. A. Laman, and D. G. Linzell** (2005) Thermally Induced Superstructure Stresses in Prestressed Girder Integral Abutment Bridges. *Transportation Research Record: Journal of the Transportation Research Board*, 287–297. https://engineering.unl.edu/downloads/civil/trb_bridgeconf_2005.pdf
124. **Potyondy, J. G.** (1961) Skin Friction between Various Soils and Construction Materials. *Géotechnique*, 11(4), 339–353. <https://doi.org/10.1680/geot.1961.11.4.339>
125. **Pugasap, K., W. Kim, and J. A. Laman** (2009) Long-Term Response Prediction of Integral Abutment Bridges. *Journal of Bridge Engineering*, 14(2), 129–139. <https://doi.org/10.1061/ASCE1084-0702200914:2129>

126. **Punetha, P.** (2022). *Dynamic Behaviour of Ballasted Railway Track with Special Reference to Transition Zones*, Doctoral Dissertation, University of Technology Sydney, Sydney.
127. **Punetha, P., K. Maharjan, and S. Nimbalkar** (2021) Finite Element Modeling of the Dynamic Response of Critical Zones in a Ballasted Railway Track. *Frontiers in Built Environment*, 7. <https://doi.org/10.3389/fbuil.2021.660292>
128. **Quinn, B. H., and S. A. Civjan** (2017) Parametric Study on Effects of Pile Orientation in Integral Abutment Bridges. *Journal of Bridge Engineering*, 22(4). [https://doi.org/10.1061/\(asce\)be.1943-5592.0000952](https://doi.org/10.1061/(asce)be.1943-5592.0000952)
129. **Rodriguez, J., F. Martinez, and J. Marti** (2011) Integral Bridge for High-Speed Railway. *Structural Engineering International*, 21(3), 297–303. <https://doi.org/10.2749/101686611X13049248219881>
130. **Rollins, K. M., and A. Sparks** (2002) Lateral Resistance of Full-Scale Pile Cap with Gravel Backfill. *Journal of Geotechnical and Geoenvironmental Engineering*, 128(9), 711–801. <https://doi.org/10.1061/ASCE1090-02412002128:9711>
131. **Rollins, K. M., and R. T. Cole** (2006) Cyclic Lateral Load Behavior of a Pile Cap and Backfill. *Journal of Geotechnical and Geoenvironmental Engineering*, 132(9), 1143–1153. <https://doi.org/10.1061/ASCE1090-02412006132:91143>
132. **Rollins, K. M., and S. J. Jessee** (2013) Passive Force-Deflection Curves for Skewed Abutments. *Journal of Bridge Engineering*, 18(10), 1086–1094. [https://doi.org/10.1061/\(asce\)be.1943-5592.0000439](https://doi.org/10.1061/(asce)be.1943-5592.0000439)
133. **Rollins, K. M., E. Scott, and A. Marsh** (2017) Geofoam Inclusions for Reducing Passive Force on Bridge Abutments Based on Large-Scale Tests. In *Geotechnical Frontiers 2017*, pp. 59–68. <https://doi.org/10.1061/9780784480465.007>
134. **Romstad, K., B. Kutter, B. Maroney, E. Vanderbilt, M. Griggs, and Y. H. Chai.** *Experimental Measurements of Bridge Abutment Behavior*. Report No. UCD-STR-95, 1, Dept. of Civil and Environmental Engineering, University of California, Davis, CA, 1995.

135. **Rowe, P. W.** (1954) A Stress-Strain Theory for Cohesionless Soil with Applications to Earth Pressures at Rest and Moving Walls. *Geotechnique*, 4(2), 49–90. <https://doi.org/10.1680/geot.1954.4.2.70>
136. **RTRI** (1996) *A study on reasonable design methods for reinforcing railroad roadbed*, Special Report No. 6 (in Japanese), Japan Railway Technical Research Institute.
137. **Sañudo, R., L. Dell’Olio, J. A. Casado, I. A. Carrascal, and S. Diego** (2016) Track Transitions in Railways: A Review. *Construction and Building Materials*, 112, 140–157. <https://doi.org/10.1016/j.conbuildmat.2016.02.084>
138. **Shamsabadi, A.** (2007) *Three-Dimensional Nonlinear Seismic Soil-Abutment-Foundation-Structure Interaction Analysis of Skewed Bridges*, Doctoral dissertation, University of Southern California, Los Angeles. https://cee.usc.edu/wp-content/uploads/2017/02/Dissertation_Shamsabadi2007.pdf
139. **Shamsabadi, A., and K. M. Rollins** (2014) Three-Dimensional Nonlinear Continuum Seismic Soil-Structure Interaction Analysis of Skewed Bridge Abutments. *NUMGE 2014, 8th European Conference on Numerical Methods in Geotechnical Engineering*, 2, 933–938. <https://doi.org/10.1201/b17017-166>
140. **Shamsabadi, A., K. M. Rollins and M. Kapuskar** (2007) Nonlinear Soil-Abutment-Bridge Structure Interaction for Seismic Performance-Based Design. *Journal of Geotechnical and Geoenvironmental Engineering*, 133(6), 707–720. <https://doi.org/10.1061/ASCE1090-02412007133:6707>
141. **Shamsabadi, A., M. Kapuskar, and G. R. Martin** (2006). Three-Dimensional Nonlinear Finite Element Soil-Abutment Structure Interaction Model for Skewed Bridges. *Fifth National Seismic Conference on Bridges & Highways*, B15, San Francisco, CA.
142. **Shamsabadi, A., P. Khalili-Tehrani, J. P. Stewart, and E. Taciroglu** (2010) Validated Simulation Models for Lateral Response of Bridge Abutments with Typical Backfills. *Journal of Bridge Engineering*, 15(3), 302–311. <https://doi.org/10.1061/ASCEBE.1943-5592.0000058>

143. **Shan, Y., B. Albers, and S. A. Savidis** (2013) Influence of Different Transition Zones on the Dynamic Response of Track-Subgrade Systems. *Computers and Geotechnics*, 48, 21–28. <https://doi.org/10.1016/j.compgeo.2012.09.006>
144. **Shao, Y., Y. Xie, C. J. Roblee, and J. Zhang** (2022) Seismic Fragility of Approach Backfill Differential Settlement for Statewide Bridges in California. *Soil Dynamics and Earthquake Engineering*, 153. <https://doi.org/10.1016/j.soildyn.2021.107049>
145. **Sharpe, P., R. J. Armitage, W. G. Heggie, and A. Rogers** (2002) Innovative Design of Transition Zones. *Proceedings of International Conference on Railway Engineering*, 12, London.
146. **Shih, J. Y., D. J. Thompson, and A. Zervos** (2017) The Influence of Soil Nonlinear Properties on the Track/Ground Vibration Induced by Trains Running on Soft Ground. *Transportation Geotechnics*, 11, 1–16. <https://doi.org/10.1016/j.trgeo.2017.03.001>
147. **Shin, E. C., D. H. Kim, and B. M. Das** (2002) Geogrid-Reinforced Railroad Bed Settlement due to Cyclic Load. *Geotechnical and Geological Engineering*, 20, 261–271. <https://doi.org/10.1023/A:1016040414725>
148. **Shome, N., and C. A. Cornell**, *Probabilistic Seismic Demand Analysis of Nonlinear Structures: Reliability of Marine Structures*, Program Report No. RMS-35, Department of Civil and Environmental Engineering, Stanford University, Stanford, California, 1999.
149. **Simon, J., and L. G. Vigh** (2016) Seismic Fragility Assessment of Integral Precast Multi-Span Bridges in Areas of Moderate Seismicity. *Bulletin of Earthquake Engineering*, 14(11), 3125–3150. <https://doi.org/10.1007/s10518-016-9947-y>
150. **Smith, K. M.** (2014) *Passive Force on Skewed Bridge Abutments with Reinforced Concrete Wingwalls Based on Large-Scale Tests*, Doctoral Dissertation, Brigham Young University, Provo, Utah, USA. <https://scholarsarchive.byu.edu/etd/5577>
151. **Smith, L., B. Doe, D. Li, D. Otter, and S. Uppal**, *Study of Bridge Approach and Track Transition Degradation: Factors and Mitigation*, U.S. Department of Transportation, Federal Railroad Administration, Washington, DC, OMB

No. 0704-0188, 2003.

152. **Steedman, R. S., and X. Zeng** (1990) The Influence of Phase on the Calculation of Pseudo-Static Earth Pressure on a Retaining Wall. *Geotechnique*, 40(1), 103–112. <https://doi.org/10.1680/geot.1990.40.1.103>
153. **Stewart, J. P., E. Taciroglu, J. W. Wallace, E. R. Ahlberg, A. Lemnitzer, C. Rha, P. K. Tehrani, S. Keowen, R. L. Nigbor, and A. Salamanca**, *Full Scale Cyclic Testing of Foundation Support Systems for Highway Bridges. Part II: Abutment Backwalls*, UCLA-SGEL Report 2007/02, 2007. <https://escholarship.org/uc/item/5ch0f8mg>
154. **Terzaghi K.** *Theoretical Soil Mechanics*. John Wiley and Sons, New York, 1943.
155. **Tsinidis, G., M. Papantou, and S. Mitoulis** (2019) Response of Integral Abutment Bridges under a Sequence of Thermal Loading and Seismic Shaking. *Earthquake and Structures*, 16(1), 11–28. <https://doi.org/10.12989/eas.2019.16.1.011>
156. **Varandas, J. N., P. Hölscher, and M. A. G. Silva** (2011) Dynamic Behaviour of Railway Tracks on Transitions Zones. *Computers and Structures*, 89(13–14), 1468–1479. <https://doi.org/10.1016/j.compstruc.2011.02.013>
157. **Verdugo, R., and K. Ishihara** (1996) The Steady State of Sandy Soils. *Soils and Foundations*, 36(2), 81–91. https://doi.org/10.3208/sandf.36.2_81
158. **Von Wolffersdorff, P. A.** (1996). Hypoplastic Relation for Granular Materials with a Predefined Limit State Surface. *Mechanics of Cohesive-Frictional Materials*, 1(3), 251–271. [https://doi.org/10.1002/\(SICI\)1099-1484\(199607\)1:3<251::AID-CFM13>3.0.CO;2-3](https://doi.org/10.1002/(SICI)1099-1484(199607)1:3<251::AID-CFM13>3.0.CO;2-3)
159. **Wang, H., and V. L. Markine** (2018) Methodology for the Comprehensive Analysis of Railway Transition Zones. *Computers and Geotechnics*, 99, 64–79. <https://doi.org/10.1016/j.compgeo.2018.03.001>
160. **White II, H., H. Pétursson, and P. Collin** (2010). Integral Abutment Bridges: The European Way. *Practice Periodical on Structural Design and Construction*, 15(3), 201–208. <https://doi.org/10.1061/ASCESC.1943-5576.0000053>

161. **Wilson, P. R.** (2009). *Large Scale Passive Force-Displacement and Dynamic Earth Pressure Experiments and Simulations*, Doctoral Dissertation, University of California, San Diego, USA.
162. **Wilson, P., and A. Elgamal** (2009) Full-Scale Shake Table Investigation of Bridge Abutment Lateral Earth Pressure. *Bulletin of the New Zealand Society for Earthquake Engineering*, 42(1), 39–46. <https://doi.org/10.5459/bnzsee.42.1.39-46>
163. **Wilson, P., and A. Elgamal** (2010) Large-Scale Passive Earth Pressure Load-Displacement Tests and Numerical Simulation. *Journal of Geotechnical and Geoenvironmental Engineering*, 136(2), 1634–1643. <https://doi.org/10.1061/ASCEGT.1943-5606.0000386>
164. **Wood, J. H.** (2015) Earthquake Design of Bridges with Integral Abutments. *6th International Conference on Earthquake Geotechnical Engineering*, Christchurch, New Zealand.
165. **Wu, W., E. Bauer and D. Kolymbas** (1996) Hypoplastic Constitutive Model with Critical State for Granular Materials. *Mechanics of Materials*, 23, 45–69. [https://doi.org/10.1016/0167-6636\(96\)00006-3](https://doi.org/10.1016/0167-6636(96)00006-3)
166. **Xu, M., C. R. I. Clayton, and A. G. Bloodworth** (2007) The Earth Pressure behind Full-Height Frame Integral Abutments Supporting Granular Fill. *Canadian Geotechnical Journal*, 44(3), 284–298. <https://doi.org/10.1139/T06-122>
167. **Zakeri, B., J. E. Padgett, and G. G. Amiri** (2014) Fragility Analysis of Skewed Single-Frame Concrete Box-Girder Bridges. *Journal of Performance of Constructed Facilities*, 28(3), 571–582. [https://doi.org/10.1061/\(asce\)cf.1943-5509.0000435](https://doi.org/10.1061/(asce)cf.1943-5509.0000435)
168. **Zakeri, J. A., and V. Ghorbani** (2011) Investigation on Dynamic Behavior of Railway Track in Transition Zone. *Journal of Mechanical Science and Technology*, 25(2), 287–292. <https://doi.org/10.1007/s12206-010-1202-x>
169. **Zamiran, S. and A. Osouli** (2018) Seismic Motion Response and Fragility Analyses of Cantilever Retaining Walls with Cohesive Backfill. *Soils and Foundations*, 58(2), 412-426.

170. **Zhao, Q., R. Vasheghani-Farahani, and E. G. Burdette** (2011) Seismic Analysis of Integral Abutment Bridges Including Soil-Structure Interaction. *Structures Congress 2011*, 289–303. [https://doi.org/10.1061/41171\(401\)26](https://doi.org/10.1061/41171(401)26)
171. **Zordan, T., B. Briseghella, and C. Lan** (2011) Parametric and Pushover Analyses on Integral Abutment Bridge. *Engineering Structures*, 33(2), 502–515. <https://doi.org/10.1016/j.engstruct.2010.11.009>

CURRICULUM VITAE

1. **NAME** : Akshay Sakhare

2. **DATE OF BIRTH** : _____

3. **EDUCATIONAL QUALIFICATIONS**

Bachelor of Engineering **2012**

Institution : Visvesvaraya Technological University, Belagavi

Specialisation : Civil Engineering

Master of Technology **2015**

Institution : National Institute of Technology Warangal,
Warangal

Specialisation : Geotechnical Engineering

Doctor of Philosophy **2024**

Institution : Indian Institute of Technology Madras, Chennai
University of Technology Sydney, Sydney

Specialisation : Civil Engineering - Geotechnical Engineering

4. **WORK EXPERIENCE** **August – December 2015**

Organisation : B. L. D. E. A's Dr. P. G. Halakatti College of
Engineering and Technology, Vijayapura

Position : Assistant Professor

5. **FELLOWSHIPS/AWARDS**

Collaborative Degree UTS President's Scholarship (COLUTSP) – UTS

Collaborative International Research Scholarship (COLIRS) - UTS

DOCTORAL COMMITTEE

- CHAIRPERSON:** **Dr. Benny Raphael**
Professor and Head of the Department
Department of Civil Engineering, IIT Madras, Chennai
- Dr. Gayathri Danasamy**
Senior Lecturer
School of Civil and Environmental Engineering, UTS, Sydney
- GUIDE (S):** **Dr. G. R. Dodagoudar**
Professor
Department of Civil Engineering, IIT Madras, Chennai
- Dr. Sanjay Nimbalkar**
Associate Professor
School of Civil and Environmental Engineering, UTS, Sydney
- MEMBERS:** **Dr. S. T. G. Raghukanth**
Professor
Department of Civil Engineering, IIT Madras, Chennai
- Dr. B. N. Rao**
Professor
Department of Civil Engineering, IIT Madras, Chennai
- Dr. K. V. Nagendra Gopal**
Professor
Department of Aerospace Engineering, IIT Madras, Chennai
- Dr. Behzad Fatahi**
Professor
School of Civil and Environmental Engineering, UTS, Sydney
- Dr. Hadi Khabbaz**
Professor
School of Civil and Environmental Engineering, UTS, Sydney
- Dr. Xuzhen He**
Senior Lecturer
School of Civil and Environmental Engineering, UTS, Sydney

